REPORT DOCUMENTATION PAGE

Form Approved
OMB NO. 0704-0188

1. AGENCY USE ONLY (Leave Blank)	2. REPORT DATE 31 October 2004	3. REPORT TYPE AND DATES COVERED Final report for 1 August 00 to 31 July 04

4. TITLE AND SUBTITLE **Center of Excellence for Propulsion Systems at the Engine Research Center**	5. FUNDING NUMBERS DAAD19-00-1-0487
6. AUTHOR(S) P. Farrell	
7. PERFORMING ORGANIZATION NAME(S) AND ADDRESS(ES) University of Wisconsin-Madison Research and Sponsored Programs 750 University Ave, Madison, WI 53706	8. PERFORMING ORGANIZATION REPORT NUMBER 1
9. SPONSORING / MONITORING AGENCY NAME(S) AND ADDRESS(ES) U. S. Army Research Office P.O. Box 12211 Research Triangle Park, NC 27709-2211	10. SPONSORING / MONITORING AGENCY REPORT NUMBER 41347.2-EG

11. SUPPLEMENTARY NOTES

The views, opinions and/or findings contained in this report are those of the author(s) and should not be construed as an official Department of the Army position, policy or decision, unless so designated by other documentation.

12 a. DISTRIBUTION / AVAILABILITY STATEMENT Approved for public release; distribution unlimited.	12 b. DISTRIBUTION CODE

13. ABSTRACT (Maximum 200 words)

This project began August 1, 2000, and involves faculty and students at three institutions (University of Wisconsin-Madison, Michigan Technical University, and the University of Minnesota) in three research thrust areas. The research thrust areas are:

- Transient Engine Experiments,
- Engine Simulation and Powertrain Modeling, and
- Detailed Chemical Characterization of Diesel Engine Exhaust.

A detailed description of the progress to-date in each of these thrust areas is given in the following pages, with a separate section for each of the thrusts. The initial program period ended July 31, 2003, and we were given a one-year no-cost extension to July 31, 2004.

14. SUBJECT TERMS IC engines; diesel engines; CFD modeling in engines;	15. NUMBER OF PAGES 194
	16. PRICE CODE

17. SECURITY CLASSIFICATION OR REPORT **UNCLASSIFIED**	18. SECURITY CLASSIFICATION ON THIS PAGE **UNCLASSIFIED**	19. SECURITY CLASSIFICATION OF ABSTRACT **UNCLASSIFIED**	20. LIMITATION OF ABSTRACT **UL**

NSN 7540-01-280-5500

Standard Form 298 (Rev.2-89)
Prescribed by ANSI Std. 239-18
298-102

Center of Excellence for Propulsion Systems at the Engine Research Center

Final Progress Report

DAAD19-00-1-0487

October 31, 2004

P. V. Farrell
Engine Research Center
Department of Mechanical Engineering
University of Wisconsin-Madison

Table of Contents

(4) Statement of Problem Studied:

This program is intended to address current and future powertrain issues of interest to the Army and its suppliers. The focus of the program is on diesel engine powertrain power density, performance, fuel economy, and related emissions and control issues. A goal of the work is to provide fundamental research results that will allow future Army vehicles to have a smaller size powertrain with increased power, reduced fuel consumption, minimal emission signature, and increased reliability and durability.

Specifically, we recognize:

- Diesel engines are the only powerplant that offers the potential fuel economy, power density, robustness, and versatility required for Army ground mobility systems.
- Understanding of many of the fundamental thermal, fluid, and chemical processes involved in diesel engine combustion systems is incomplete.
- Current commercial development is almost completely directed at meeting current and pending emission regulations.

In developing a thorough detailed fundamental understanding of the combustion phenomena, we will need to assess the impact of emission-driven modifications on relevant performance characteristics of the engine and how current design and development of diesel engine systems will impact potential performance of engines needed for Army ground mobility systems. If control strategies are implemented to override emission controls for certain situations, we need to understand how the engine will perform and whether the resulting emissions will present a significant detection issue.

The incorporation of aftertreatment systems into commercial engines may actually facilitate their application into Army ground mobility systems. It is important to understand the interaction between the engine and the aftertreatment system to see how this connection can be exploited.

Engine emissions may be considered a combustion metric. The power density limit of many engines is determined by the smoke limit—an air utilization and emission issue, the importance of which may differ between civilian and military use.

The specific goals of this program are:

- Develop and apply the means to measure transient engine characteristics (Thrust 1) with an emphasis on high power density engine configurations.
- Develop research-based modeling of combustion process and overall powertrain system behavior so these models can be applied to future engine design and operation (Thrust 2)
- Explore the fundamental relationships among engine performance (power, bsfc), emission quantity (g/kw-hr), and detailed emission characteristics (e.g. particulate size distribution). (Thrust 3)

This program is a joint effort among the UW-Madison Engine Research Center, the UW-Madison Powertrain Control Research Lab (PCRL), UW-Madison Department of Civil Engineering and the State of Wisconsin Hygiene Laboratory, Michigan Technological University (MTU), and the University of Minnesota (UMinn).

(5) Summary of most important results

Thrust 1: Transient Engine Measurements

1.1.1 Introduction

This thrust is aimed at developing and applying a method for making transient measurements of engine performance, primarily for smaller displacement high-speed diesel engines. Future Army powertrains may employ smaller displacement higher speed engines which can provide higher power density output for smaller and lighter future vehicles, with a potential for improved fuel economy as well. As these powertrains are likely to operate under highly transient conditions, understanding of the characteristics and limits of transient operation is important.

Under development at the University of Wisconsin are a high bandwidth hydrostatic engine dynamometer, high data rate diagnostics, and a format for evaluating engine control inputs in light of real-time engine data. At MTU, the focus is on developing piston measurement systems that can accurately describe the state of the piston, which is often a limit in pushing towards higher power density.

1.1.2 Engine and Transient Dynamometer System

The transient engine dynamometer is a hydraulic-based dynamometer system, similar to those constructed by Prof. Moskwa and his students in the PCRL at UW-Madison. Figure 1.1.1 shows a schematic of the system. This system has been described in detail in previous reports, so will not be discussed here.

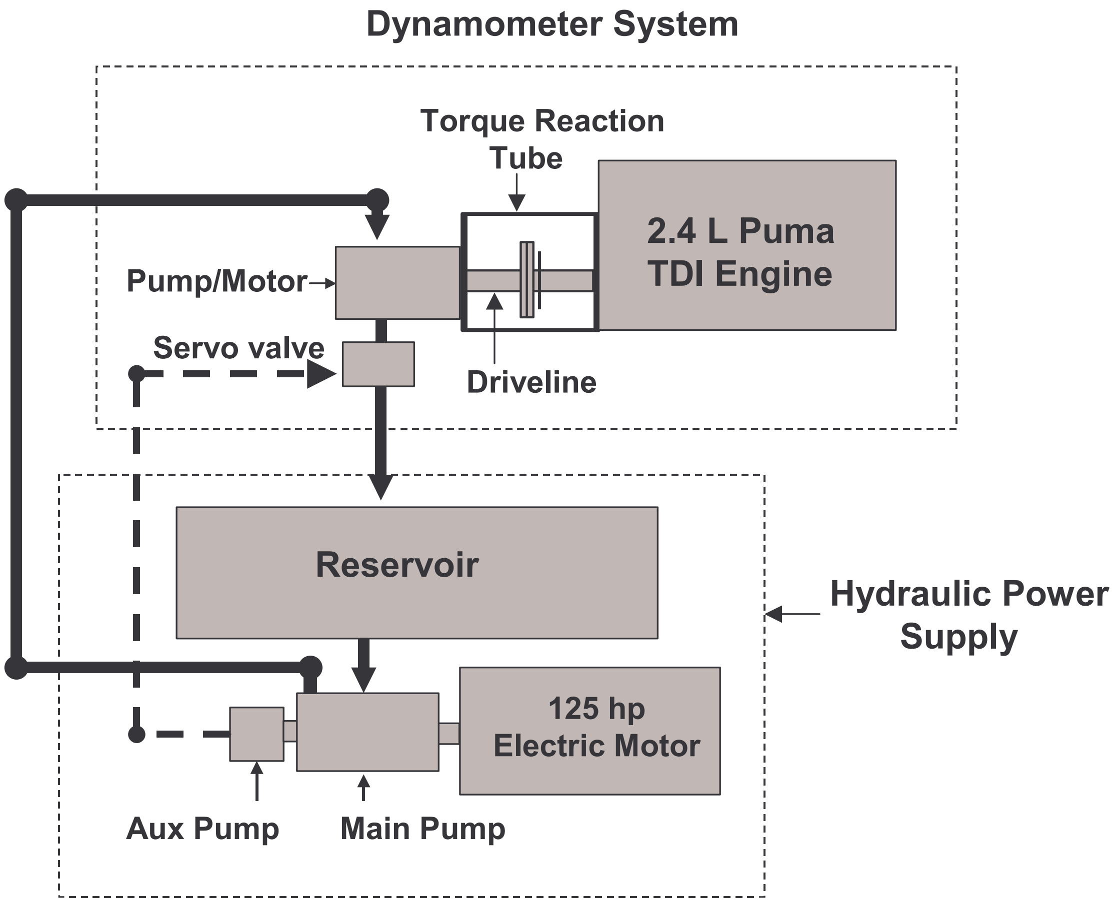

Figure 1.1.1 Schematic of transient dynamometer system.

•

The results for the system in its current state are illustrated in figs 1.1.2, and 1.1.2. Figure 1.1.2 shows the system response to a step change in torque request when operating in a motored condition. The measured torque follows the torque request with some rise time delay. The oscillations in the measured torques signal are artifacts of the torque variation as each of the 4 cylinders goes through a compression stroke. At higher torque values, these oscillations are not as evident.

Figure 1.3 shows a trace for the dynamometer with a step change in speed requested. The measured speed follows the request with a time lag. Note also the torque spike needed to rapidly adjust the speed to match the request. The final values of the measured speed compares well with the request value.

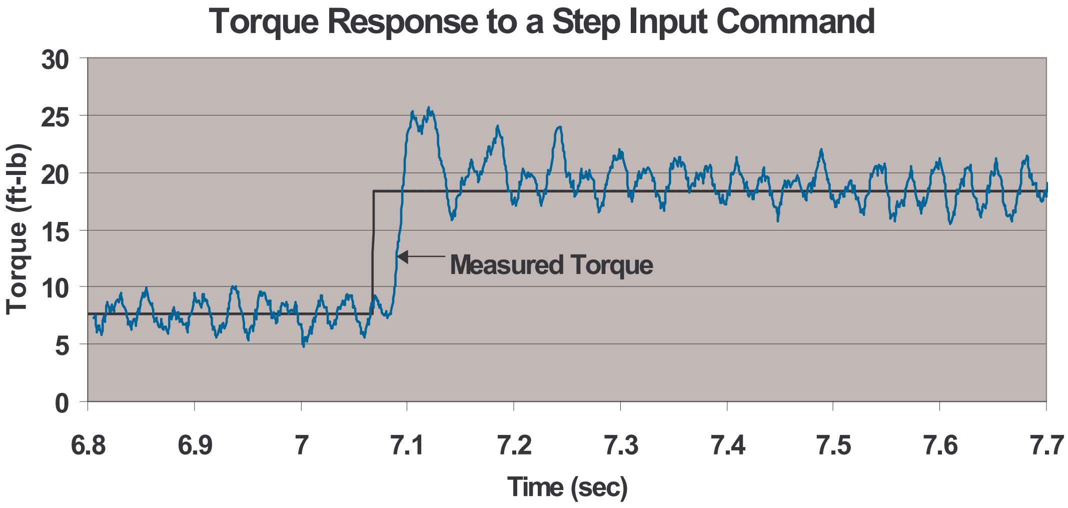

Figure 1.1.2. Torque response of the motored dynamometer to a step change request.

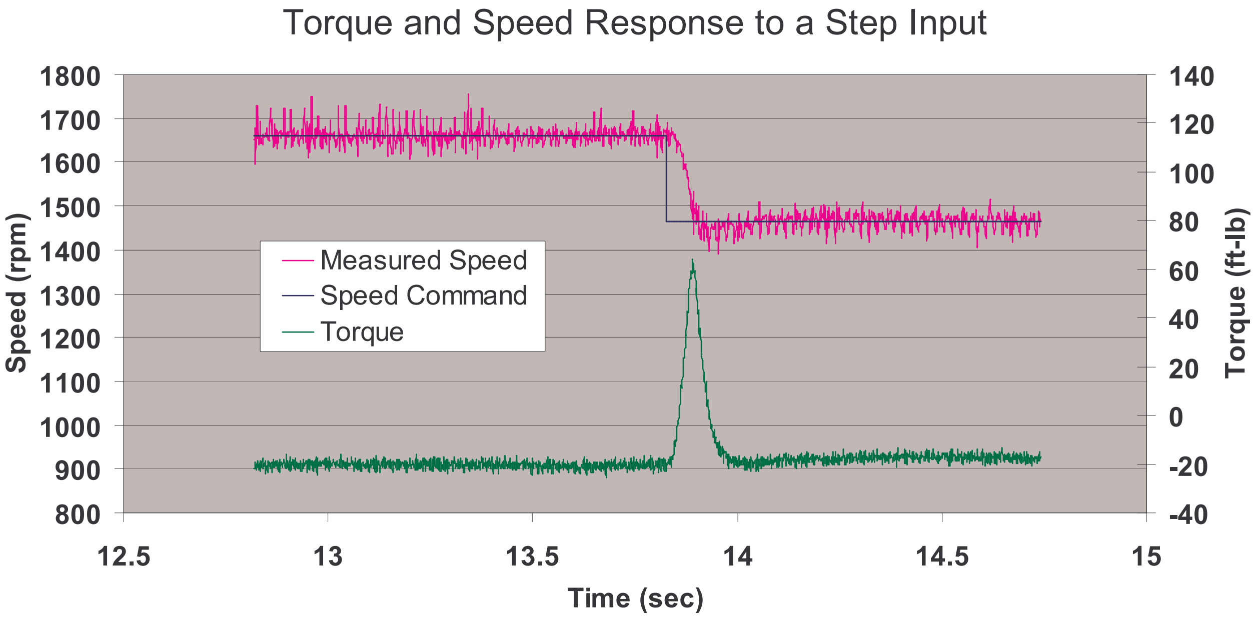

Figure 1.1.3. Time-varying speed request and response.

The major focus of effort for the past year has been to develop the capabilities of the transient dynamometer system and to expend the operating envelope of the engine and dyno system. This effort has been made challenging by the fact that the PCU (Powertrain Control Unit) for this engine is a vehicle PCU (not a dyno PCU) so a number of vehicle sensors need to be present and operating for the engine to operate over a wide range of speeds and loads. The primary electronic controls in the engine PCU affect the behavior of the high pressure pump. The engine uses a pump-line system for injection, with electronic control of pressure, SOI, and duration at the pump. Communication from the PCU to the pump is via CANBus, so direct intervention is not possible. We have obtained a CANBus controller (ATI) to interrogate and change PCM commands to the pump. With this system in place we are now able to operate the engine over from idle to about 2000 RPM (current dyno limit) and a range of loads from idle to about 75% of rated load.

While the CANBus system was being debugged, we installed the necessary connections for direct measurement of exhaust gas with the high speed HC and NOx systems. We expect to have results of dynamic operation with these measurement systems shortly.

1.2 Transient Engine Experiments - In-cylinder Temperature Measurements

1.2.1 Background

There continues to be a need for smaller, lighter, more efficient engines for automotive and military applications. The diesel engine can meet this need through increased power density, such as that achieved by high speed diesels being developed in Europe. When engine speeds increase, the time available for a combustible mixture to form is reduced. Additionally, the time between combustion events is reduced, thus increasing the thermal load on the piston. One solution to improve combustible mixture formation is to increase fuel penetration, thus increasing fuel/air mixing. This increased fuel penetration, along with small bore diameters, can lead to the spray contacting or “impinging” on the piston surface. This in turn can lead to negative effects on the combustion process and hence the emission of pollutants. Repeated contact of the spray on the piston can lead to increased thermal loading and premature piston failure. Thus, as engine speeds increase, the piston becomes even more of a critical component.

Traditionally, piston thermal loading investigations have focused on the average heat flux. Preliminary numerical results show that the piston surface acts as a semi-infinite solid in terms of heat transfer on an instantaneous basis. Additionally, spray impingement has been measured in bench top experiments, predicted in computational models and observed in optically accessible engines. Indirect evidence of impingement is inferred from emissions data and from visual inspection of the piston (scorch marks). Crank angle resolved, instantaneous temperature and heat flux for a piston has yet to be published in great quantity and even further, direct measurement of impingement in a running diesel engine has not been reported to date.

1.2.2 Students

Scott A. Miers - Ph.D. Candidate - Spray Impingement – Graduation: December 2004
Koray Inal - Ph.D. Candidate - Thermal Loading – Graduation: May 2005

1.2.3 Test Engine Specifications

The engine used for this research was a 2001 Ford Puma 2.0L direct injection diesel. The engine was donated to Michigan Technological University, through Ford US. The actual engine is produced and marketed for Ford Europe, thus making part acquisition and service challenging. However, the engine provided the particular characteristics (high speed, advanced fuel delivery system), desired for the research objectives. The engine specifications are shown in Table 1.2.1.

Table 1.2.1: Diesel Engine Specifications

Model	2001 Ford Puma 130 PS
Type	Four Stroke Diesel
No. of Cylinders / Configuration	4, in-line
Piston Configuration	Bowl-in-piston, with oil cooling gallery
Bore x Stroke	86 mm x 86 mm
Intake/Exhaust Valve Layout	2 Intake, 2 Exhaust per cylinder
Displacement	1.98 liters
Compression Ratio	19:1
Aspiration	Variable Geometry Turbocharger with Air to Water Intercooler
Fuel Delivery System	High Pressure Common Rail
Maximum Rail Pressure	1750 bar
Injection Details	Pilot (40° BTDC to 10° ATDC) Main (20° BTDC to 20° ATDC)
Rated Power	97 kW @ 3800 rpm
Peak Torque	330 N-m @ 1800 rpm
Power Density (Power/Displacement)	49 kW/liter (1.1 hp/in^3)
Power Density (Power/Weight)	0.045 kW/N (0.268 hp/lbf)

1.2.5 Laboratory Build

A complete engine test facility was created for this specific research. Figure 1.2.1 shows the test cell schematic and related sub-sections that make up the test facility.

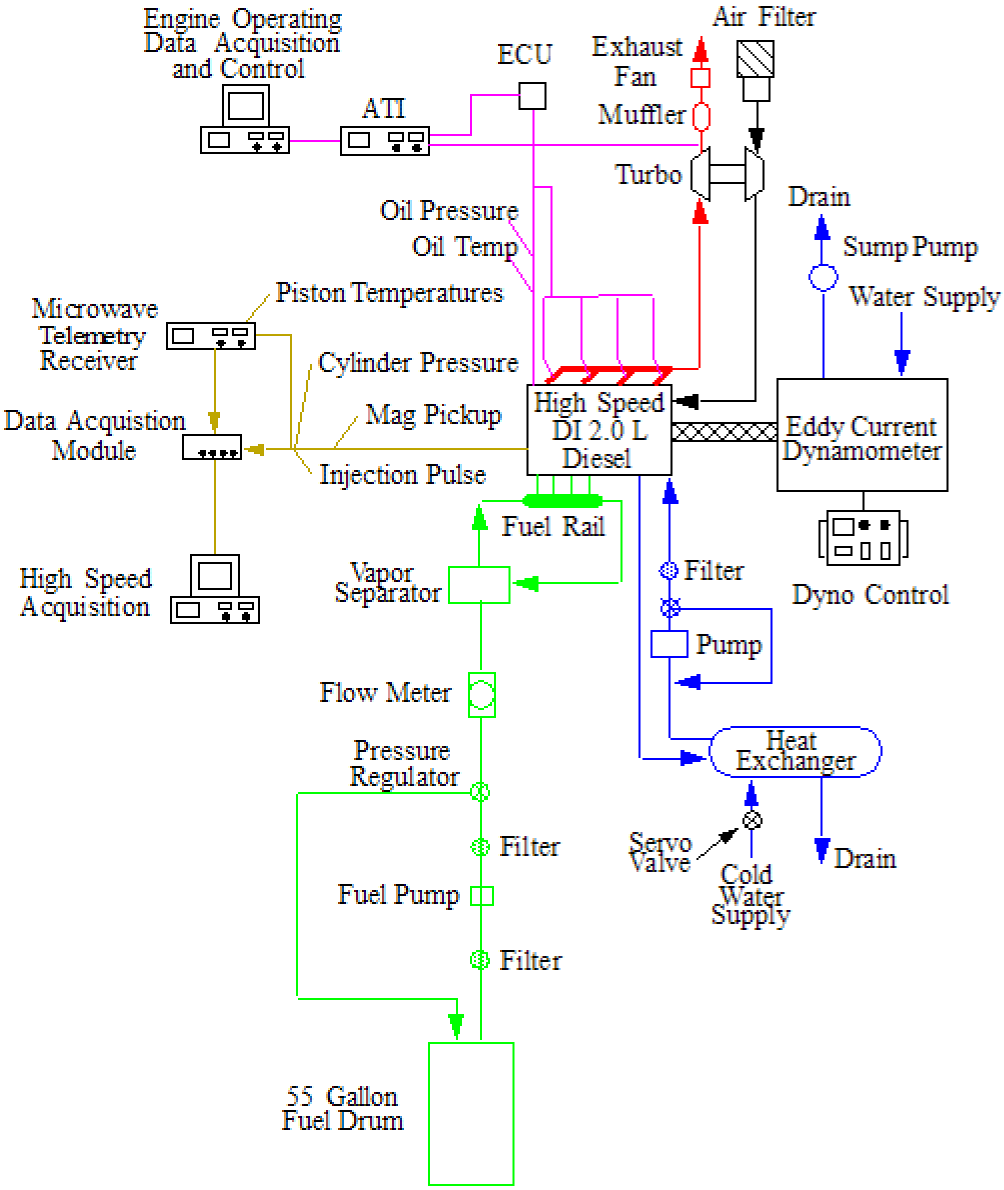

Figure 1.2.1: Test cell schematic showing cooling, fuel, exhaust and acquisition systems.

Laboratory construction began with the acquisition of a 6’ x 12’ bedplate. Custom engine mounting brackets were then fabricated to attach and isolate the bedplate from the engine.

1.2.6 Fuel System

The fuel system draws diesel from a remote, 55 gallon drum, filters it to 2 microns, and regulates the pressure to 5 psi. The fuel flow rate is measured by a Pierburg PLU 126-120 flow meter. The flow meter is a positive displacement unit, with zero pressure drop and can measure flow rates from 0.6 L/hr to 120 L/hr. A vapor separator is utilized to remove vapor from the fuel and transfer the fuel to the high pressure pump on the engine. The vapor separator does not allow transient fuel flow rate measurements. Figure 1.2.2 shows the fuel system cabinet.

Figure 1.2.2: Fuel delivery system.

Cooling System

The cooling system utilizes a heat exchanger that permits a 50/50 ethylene glycol mix to be used as the engine coolant, thus reducing internal corrosion and improving heat transfer. The open loop side of the heat exchanger utilizes the building cold water supply. Electronically controlled proportioning values regulate temperature and flow rate of engine coolant, to ensure complete control over the cooling system. Figure 1.2.3 shows the heat exchanger, pump, and proportioning valves, as installed in the lab.

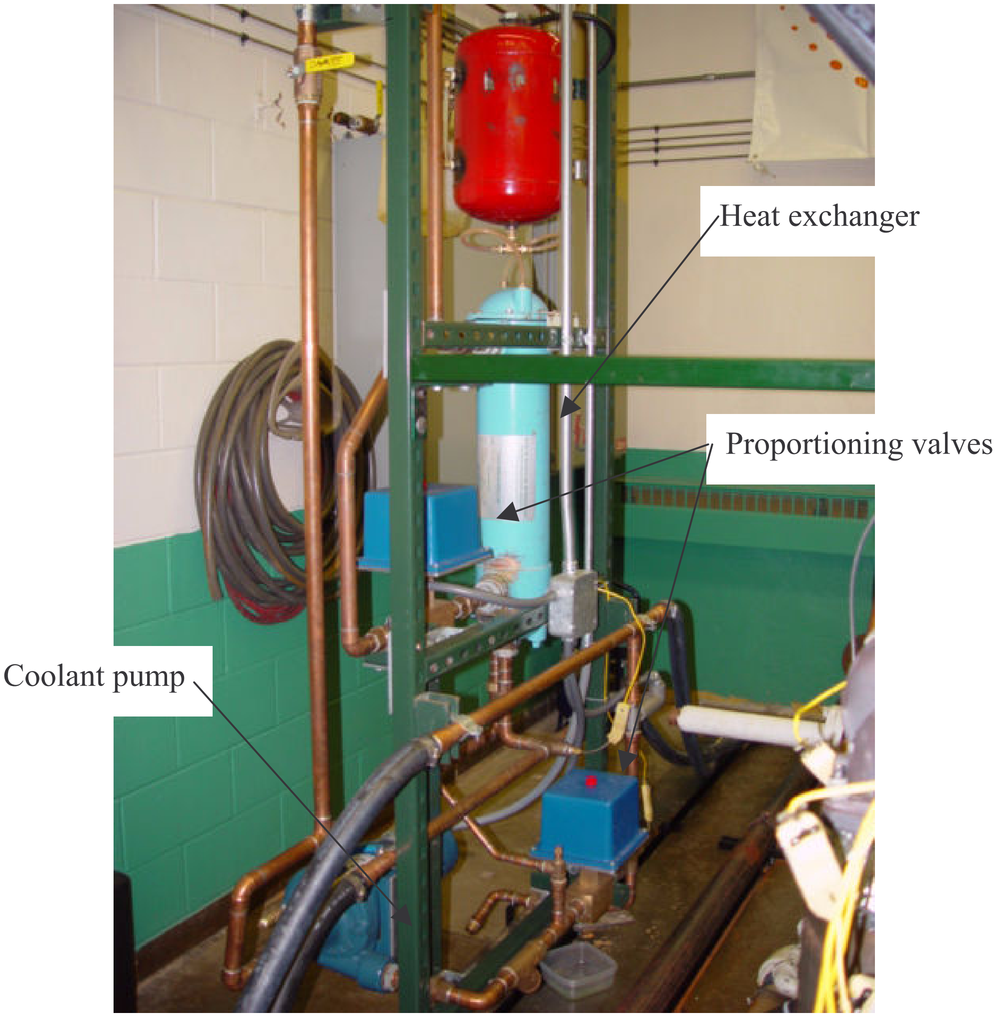

Figure 1.2.3: Cooling system components.

A separate electrical panel was constructed to contain the engine ECU, laboratory data acquisition system, control relays, and signal conditioners. Figure 1.2.4 shows the electrical cabinet, as installed and utilized in the lab.

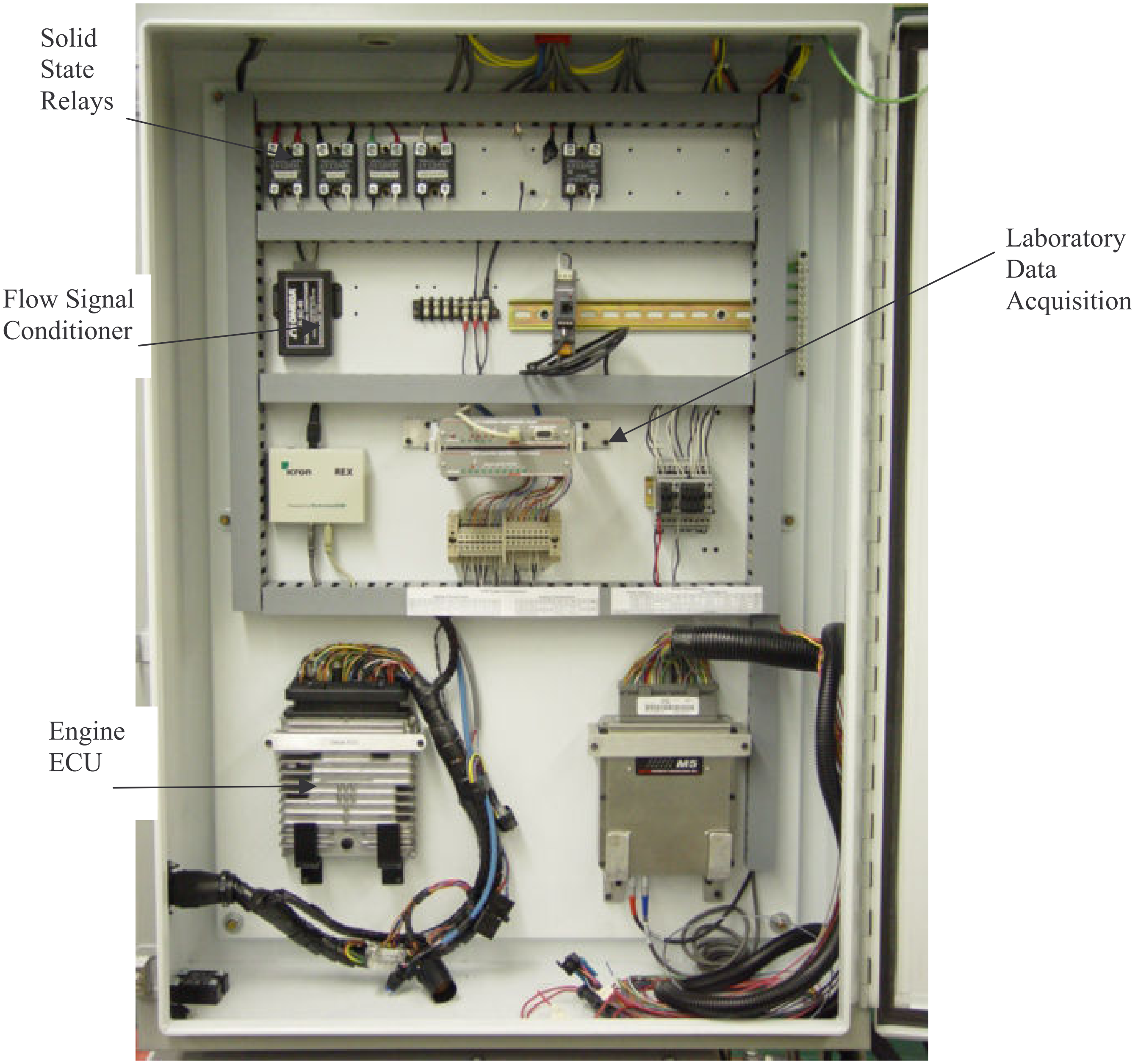

Figure 1.2.4: Electrical cabinet.

The data is transferred from the electrical cabinet to the control room via a high speed Ethernet connection. To properly operate the engine test cell, an instrument rack was installed in an adjacent control room. Dynamometer and engine control are performed from the control room, as well as general laboratory acquisition. As shown in Figure 1.2.5, the control room is well equipped and convenient for engine testing.

Figure 1.2.5: Control room.

The engine is mounted to the bedplate at three locations and is isolated by rubber dampers installed between the engine supports and elephant feet. A Centa Corporation CentaFlex driveshaft was chosen to connect the engine output to the dynamometer. The driveshaft utilizes flexible, rubber couplings, which ensure long life and quiet operation. The dynamometer is a 170 hp, 10,000 rpm Dynamatic Eddy Current system by Eaton. Figure 1.2.6 shows the engine, driveshaft guard and dynamometer installed on the bedplate. Above the dynamometer is the starting battery box and electrical cabinet.

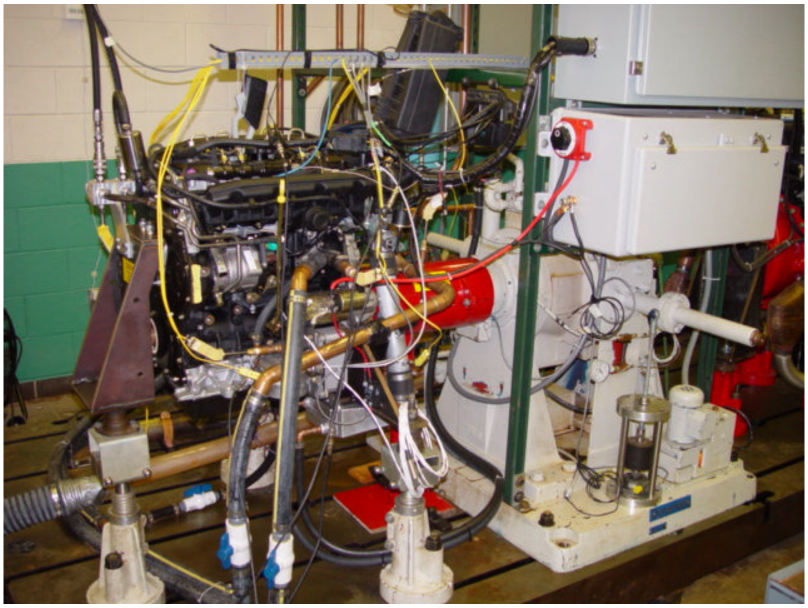

Figure 1.2.6: Diesel engine connected to dynamometer.

1.2.6 Instrumentation – Laboratory/Engine

Additional instrumentation included a cylinder pressure sensor from Optrand, Inc. The modified glow plug sensor had a pressure range of 0-3,000 psi, a frequency response range of 0.1 Hz to 25 kHz and a sensitivity of 1.49mV/psi. An Omega Corporation oil pressure sensor was utilized to monitor engine oil pressure. The pressure was 0-200 psi, with a 20 ms response time and an accuracy of 1% full-scale. The electrical pulse to the injector was recorded using a Simpson Amp-Clamp model 150 inductive pickup. The engine position was recorded by a magnetic pick-up, installed 0.025” from the flywheel teeth. There were 58 teeth on the flywheel, with 2 missing to identify TDC. K type, stainless steel sheathed thermocouples were used to record various temperatures on the engine; including coolant supply and return, exhaust gas, fuel supply and return, and oil temperature. Sheath diameters varied from 1/8” to 1/4”, depending on significance of response time.

1.2.7 Microwave Telemetry

Successfully capturing data from a piston in a running engine is not a trivial task. Typical diesel pistons can experience accelerations of 20,000 m/s^2, 2500 K combustion gas temperatures, 400°C surface temperatures and over 10,000 kPa of combustion gas pressure. In order to transmit the thermocouple information from the piston to a data acquisition system; a wireless, microwave telemetry technique was employed. The telemetry system consists of three main components; the transmitter, the inductive power unit and an external receiver. The transmitter attaches to the underside of the piston, receives data from 15 thermocouples and prepares the data for transmission out of the engine.

1.2.8 Signal Evolution

Thermocouples produce an emf signal that is input to a voltage-to-frequency converter. The thermocouple signal is converted to a frequency-modulated square wave in the 10-50 kHz range. The square wave is then used to modulate a microwave carrier wave (nominal frequency = 2.5 GHz) from a voltage controlled oscillator (VCO), and this signal is sent to the transmitting antenna. The entire transmitter package weighs less than 80 grams and is capable of multiplexing 15 transducer inputs. The multiplexer samples each thermocouple voltage for 500 ms, then switches to the next thermocouple. The 16th channel is reserved for a marker channel, to determine which thermocouple is being processed.

The transmitted signal is received by an antenna mounted in the engine block, which passes the high frequency signal to an external microwave receiver. The receiver demodulates the data to a square wave, and a frequency-to-voltage converter demodulates the square wave to the original analog signal. Figure 1.2.7 shows the evolution of the telemetry signal, from transducer to bench-top receiver output. The bandwidth of the telemetry system is 2,000 Hz, set by the internal filter during the final F/V conversion.

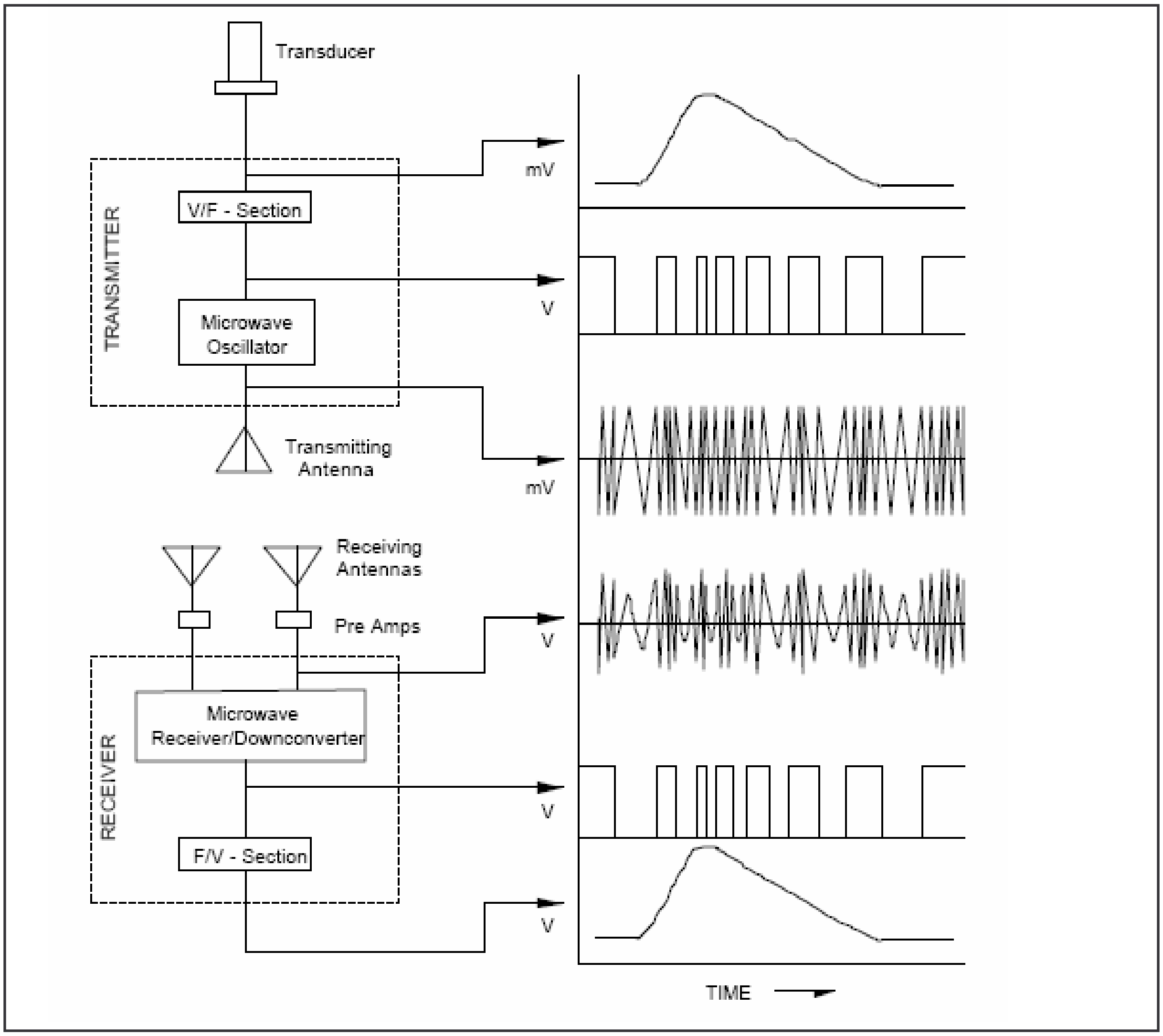

Figure 1.2.7: Wireless microwave telemetry signal evolution (IR Telemetrics 2003).

1.2.8 Telemetry Installation

The transmitter attaches to the underside of the piston, and receives signal from the fast response thermocouples. The inductive power unit attaches to the bottom of the piston pin boss, and provides wireless power to the transmitter. This eliminates the need for batteries, which can limit the operating speed of the engine. The inductive power unit receives power from a permanently mounted coil in the crankcase. The inductive coils "couple" at approximately 140^{o} ATDC, and have a "couple duration" of 80^{o}. Figure 1.2.8 shows the underside of the piston, with the transmitter, multiplexer, and inductive power unit installed.

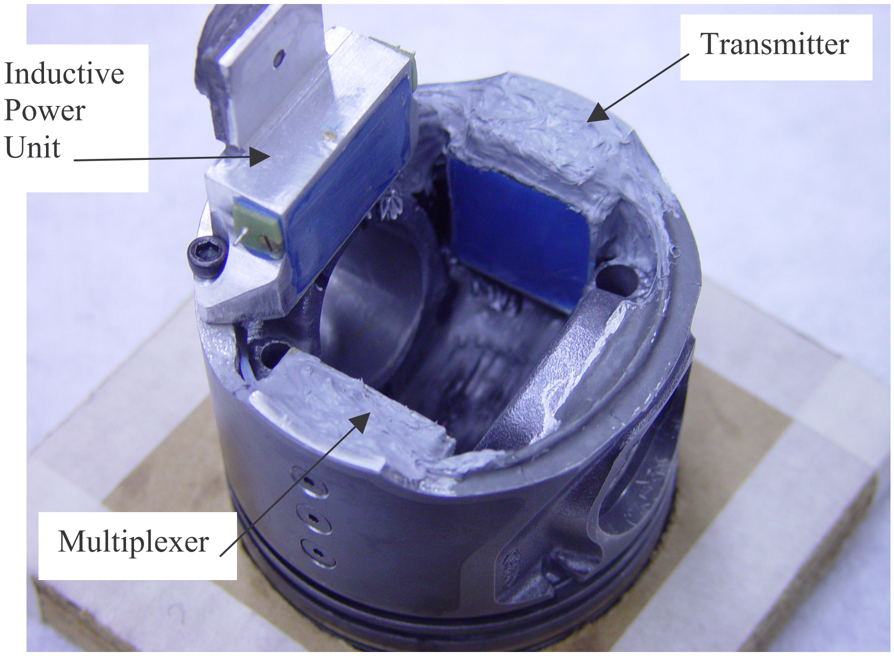

Figure 1.2.8: Microwave telemetry installed on piston.

1.2.9 Piston Thermocouple Installation

The #2 piston from the diesel engine was modified for 15 thermocouples. Eight fast-response surface thermocouples, five embedded thermocouples and two underside thermocouples were installed on the piston by Medtherm Inc. The fast-response surface thermocouples were 0.061" in diameter and press fit into 0.0605" holes. The electrical connection at the surface was accomplished through the application of a 2 micron thick, vacuum deposited layer of chromium. This particular installation technique produces a surface thermocouple with a response time of 1 μsec. Figure 1.2.9 shows a schematic layout of the tri-axial thermocouple used for measuring the surface temperature of the piston.

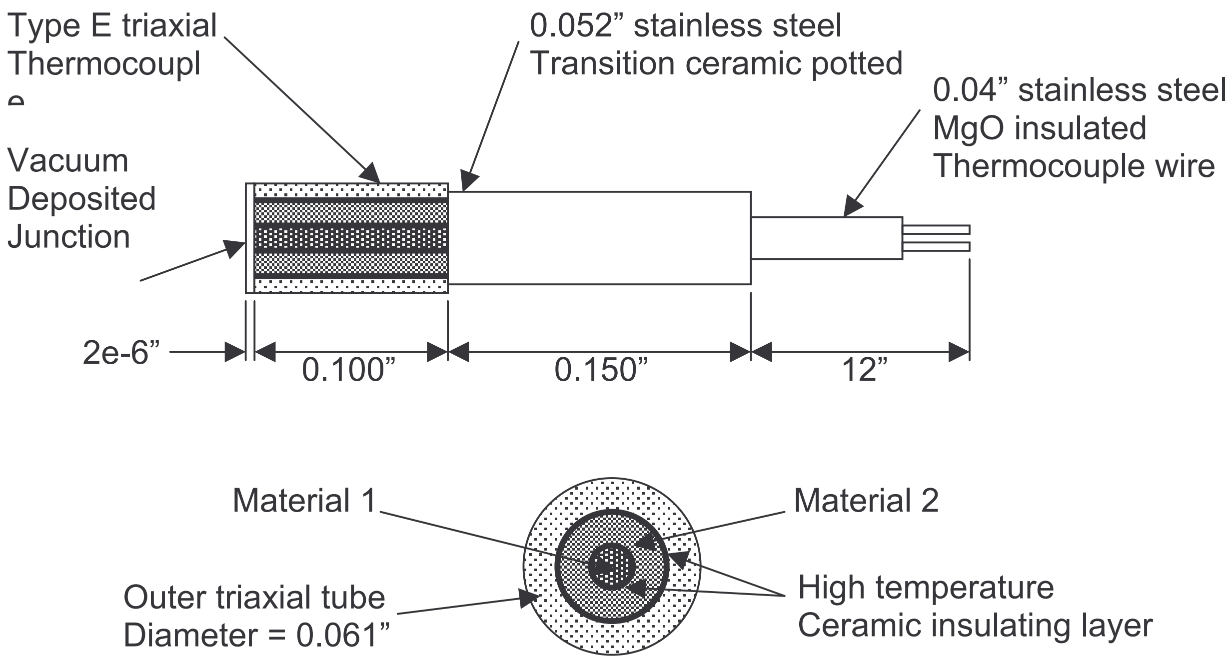

Figure 1.2.9: Triaxial thermocouple schematic.

Figure 1.2.10 shows the locations of the 15 thermocouples, on a piston cross-section and from a top view. Thermocouples 5, 14 and 15 are installed on the bowl lip, circumferentially 30° from each other.

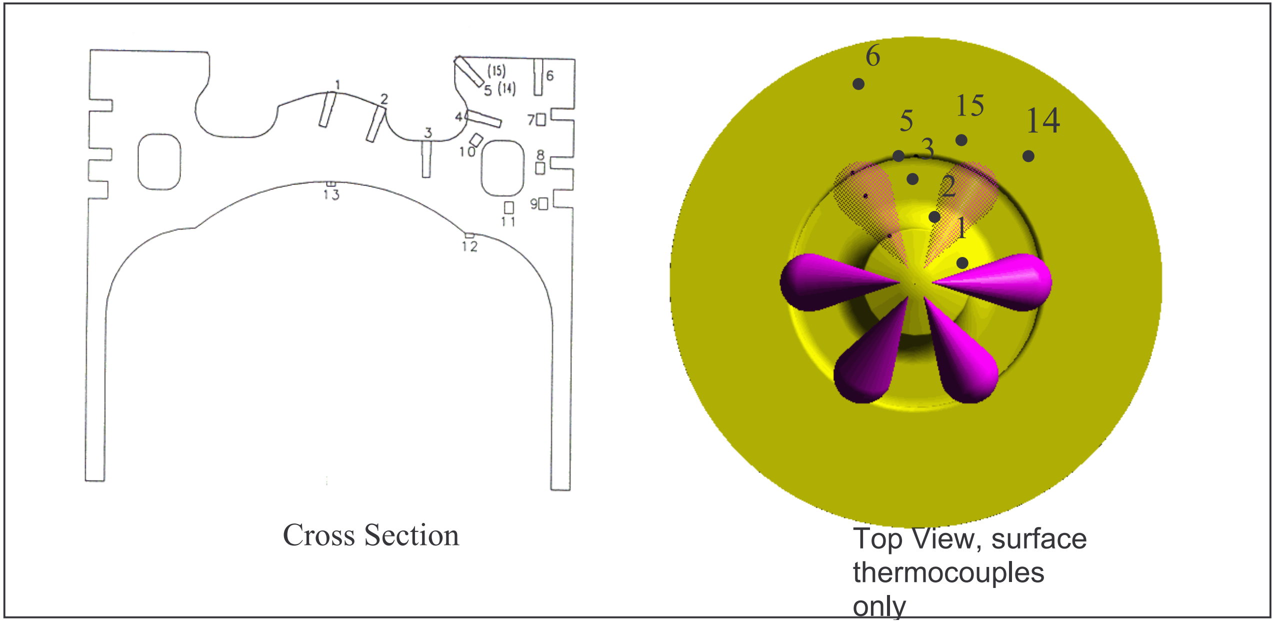

Cross Section

Top View, surface thermocouples only

Figure 1.2.10: Thermocouple location schematic.

1.2.9 Data Acquisition

Two major laboratory acquisition purchases were made to record engine operating conditions and piston temperature measurements.

1.2.9.1 General Laboratory Acquisition - Vision Software

The engine/lab operating parameters were recorded by Vision software, an Accurate Technologies Inc. (ATI) product. The Vision system allowed the user to monitor ECU activity, fully interrogate the ECU injection map and also monitor and record laboratory information. In addition, the software was used to control the laboratory equipment, using a voltage output module. The Vision system has a maximum sample rate of 1000 Hz. Table 1.2.2 and Table 1.2.3 list the input parameters and output parameters, respectively, controlled with the Vision software.

Table 1.2.2: Vision Input Parameters

Oil Pressure	Fuel Flow Rate	Coolant Flow Rate	Fuel Drum Level
Exhaust Gas Temperature, Cyl. 1	Exhaust Gas Temperature, Cyl. 2	Exhaust Gas Temperature, Cyl. 3	Exhaust Gas Temperature, Cyl. 4
Oil Temperature	Engine Coolant Temperature Out	Engine Coolant Temperature In	EGR Coolant Temperature Out
Intercooler Temperature In	Intercooler Temperature Out	Fuel Temperature Supply	Fuel Temperature Return
Fuel Temperature at Flow Meter	Heat Exchanger Temperature Supply	Heat Exchanger Temperature Return	

Table 1.2.3: Vision Output Parameters

ECU Power Relay	Fuel Cabinet Power Relay	Ignition Sense Relay	Starter Motor Relay	Coolant Pump Power Relay
Exhaust Fan Power Relay	Intercooler Solenoid Power Relay	Control Signal to Coolant Flowrate Valve	Control Signal to Coolant Temperature Valve	

1.2.9.2 High Speed Acquisition

Crankshaft position, cylinder pressure, injection pulse electrical signal and piston temperatures were recorded using a Siglab data acquisition system. The sample rate was set to 12,800 Hz in order to properly capture the magnetic pickup signal used to determine crankshaft position. The record length was varied for different rpm test conditions, to capture 100 combustion cycles.

1.2.10 Test Procedure

The engine was started under a no-load condition and then allowed to warm up for approximately 15 minutes. During the warm up period, the engine speed was maintained at 1500 rpm with a load of 50 N-m. The engine was considered warmed up when the engine coolant discharge temperature reached 85°C and the oil temperature was approximately 180°C. All test conditions were run at steady state. The engine was brought to a specific speed and load and held there for five minutes to stabilize piston temperatures. Exhaust gas temperature was monitored to verify the piston temperatures were stabilized. It was observed that typical coolant temperature fluctuations in the engine occurred during the acquisition of the piston temperatures. On average, the supply temperature would range from 80°C to 90°C, over a time interval of approximately 15 seconds. It was not believed to cause significant changes in the piston temperatures, over one engine cycle.

1.2.10.1 Test Matrix

Piston temperature data was recorded at multiple loads and speeds. In addition, two injector positions were tested, to determine the effect of rotating the spray plume 30°. Table 1.2.4 outlines the test matrix that was filled.

Table 1.2.4: Experimental Data Test Matrix.

Speed (rpm)	Load Range (N-m)	Load Range (% rated load at rpm)	Injector Rotation Angle (°)
890	5	3	0
1000	37-148	25-100	0 and 30
1350	33-165	16-80	0
1500	68-273	25-100	0 and 30
1800 (Peak torque)	33-165	10-50	0
2000	83-310	25-100	0 and 30
2500	78-300	25-100	0 and 30
3000	71-270	25-100	0 and 30
3800 (rated speed)	60-238	25-100	30

1.2.10.2 Injector Rotation

Dependency of the surface temperature profiles on injector location was of interest. The design of the common rail fuel injection system on the Ford Puma engine allowed the rotation of the injector by over 30° in either direction, without major modification of the system. This allowed the evaluation of the piston surface temperatures, at two unique injector locations. As shown in Figure 1.2.11, the #2 injector has been rotated 30°, prior to installing the high pressure pipes and electrical connections.

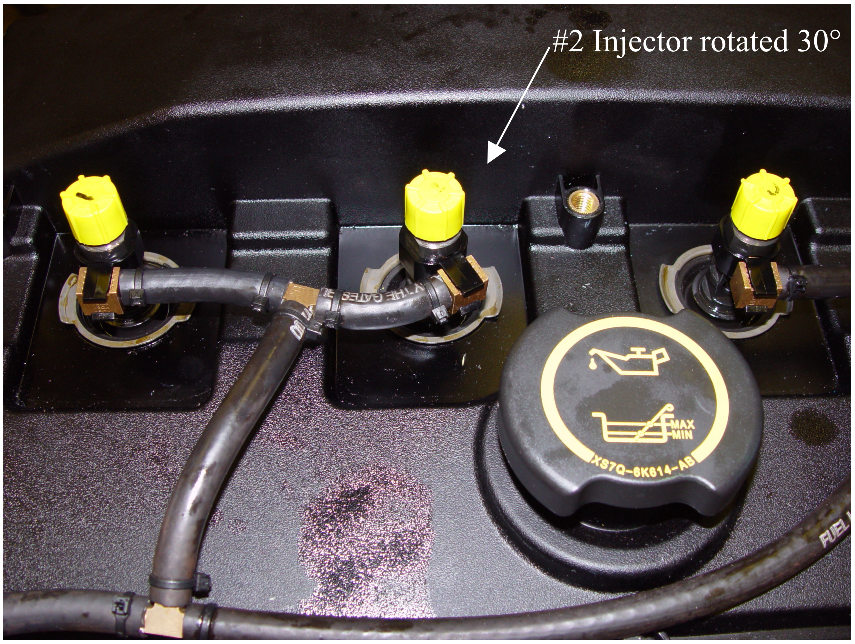

Figure 1.2.11: Injector #2 rotated 30°.

1.2.11 Experimental Results

1.2.11.1 Piston Thermal Loading

1.2.11.2 Objectives:

1. Acquire high speed temperature data from the piston.
2. Compute the thermal loading on the piston.
3. Compare analytical and finite element models that accurately solve for the heat transfer through the piston
4. Characterize the upper limit of useful frequency information of the temperature trace of the piston surface.

1.2.11.3 Heat Transfer

The piston surface is subjected to significant heat transfer. Temperature changes over the surface generated by the heat release form the boundary conditions for a heat transfer analysis through the piston cross section.

Three different tools, consisting two analytical models (based on semi-infinite solutions) and a FE model, have been developed to investigate piston heat transfer. FE model was chosen as the primary tool and results obtained from it are compared to the semi-infinite based solutions for verification of semi-infinite behavior of the piston surface.

Tool 1: Semi-Infinite Analysis with Fourier Series

This technique involves using the Fourier series coefficients of the boundary condition temperature trace as the periodic boundary conditions for a semi-infinite analysis. A frequency content analysis is required for the solution.

At a given RPM, engine speed is not perfectly constant and thus the data that lies in equidistant time steps from each other, doesn't lie in equidistant angle steps. Once the data is resampled for constant angular steps, the FFT analysis yields a clean plot with distinct peaks (Figure 1.2.12). "Order" is defined as number of occurrence of a certain signal in each 720 CAD, thus order 1 being the fundamental frequency of combustion at the corresponding RPM. For Figure 1.2.12, the first order corresponds to;

$$3800 RPM \cdot \frac{1\min}{60\sec} \cdot \frac{1 cycle}{2 revolutions} \cong 31.67 Hz = 1^{st}\ order$$

$$\frac{RPM \cdot n}{120} = n^{th} order$$

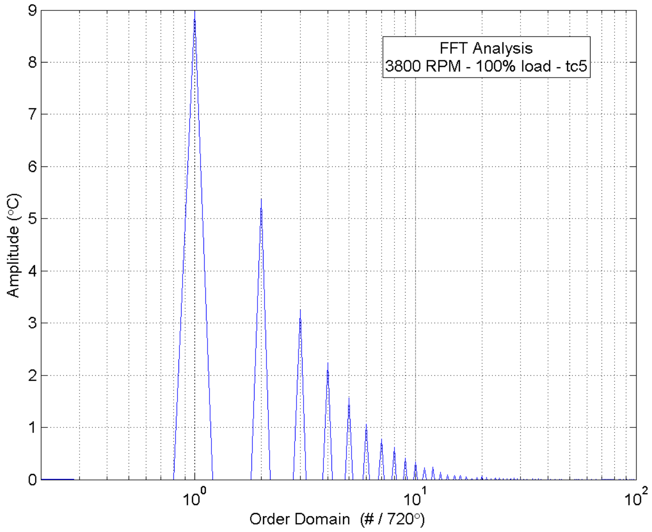

Figure 1.2.12 – FFT Analysis of thermocouple 5 temperature trace

Using the angular domain and defining the order domain in this way helps to examine data from different RPMs and loads over the same scale and also easily identify CAD positioned phenomena in the data. Figure 1.2.12 shows that the frequency content of the temperature trace becomes insignificant with the increasing harmonics.

The heat flux exact solutions for Sine and Cosine periodic boundary conditions applied over a semi-infinite surface are defined by Equation 1.2.1. First two equations define the periodic Cosine boundary condition and the corresponding surface heat flux solution. Latter equations define this relation for periodic Sine boundary condition. These are the main components of the solution that will translate each frequency component of the temperature trace into heat flux components.

$$T(x=0,t)=T_O\cdot\cos(w\cdot t)$$
$$q''(x=0,t)=k\cdot T_O\cdot\sqrt{\frac{w}{2\cdot\alpha}}\cdot(\cos(w\cdot t)-\sin(w\cdot t))$$
$$T(x=0,t)=T_O\cdot\sin(w\cdot t)$$
$$q''(x=0,t)=k\cdot T_O\cdot\sqrt{\frac{w}{2\cdot\alpha}}\cdot(\sin(w\cdot t)+\cos(w\cdot t))$$

Equation 1.2.1 – Semi-infinite Surface Temperature Gradient Functions

The real and imaginary coefficients of the FFT analysis define the amplitudes (To) for cosine and sine functions, respectively at their corresponding frequencies. Each frequency component of the temperature trace contributes to the overall heat flux trace. Adding up all resulting heat flux equations for each frequency component (Equation 1.2.2), yields the final form the heat flux solution. The solution is time based, thus the orders needs to be converted into frequencies by Equation 1.2.1. This approach can be applied to any periodic temperature trace like engine combustion temperature trace.

$$q''(t)=-k\cdot\sum_{w=0}^{\infty}\left[\sqrt{\frac{w}{2\cdot\alpha}}\cdot\left[real(w)\cdot(Sin(w\cdot t)-Cos(w\cdot t))+imag(w)\cdot(Sin(w\cdot t)+Cos(w\cdot t))\right]\right]$$

Equation 1.2.2: Heat Transfer as a function of Fourier Series

$$T(t)=\sum_{w=0}^{\infty}\left[real(w)\cdot Cos(w\cdot t)-imag(w)\cdot Sin(w\cdot t)\right]$$

Equation 1.2.3 – Temperature trace as a function of Fourier Series

As mentioned before by using the angular domain, it’s possible to obtain very clean and distinct peaks from the FFT analysis (Figure 1.2.12), which is very beneficial in evaluating heat transfer equation. It is also helpful in determining the significant harmonics of a temperature trace.

Equation 1.2.2 and Equation 1.2.3 point out that while constructing the heat transfer by the Fourier series, the magnitude of heat flux contributed by each frequency component is a direct function of amplitude (To) and square root of frequency. However, when reconstructing the temperature trace by Fourier series (inverse FFT), amplitudes (To) are the only important criteria. This is an important detail in choosing the right method for determining the significant harmonics in a temperature trace. According to the Equation 1.2.2, if any two frequency components of a temperature trace satisfy Equation 1.2.4, than their surface heat fluxes have the same magnitude, but with different frequencies. This relation plays a significant role in determining the significant harmonics.

$$\sqrt{w_1}\cdot T_{O,w_1}=\sqrt{w_2}\cdot T_{O,w_2}$$

Equation 1.2.4 – Frequency, amplitude and heat flux amplitude relation

Two different analyses can be followed at this point to reveal the significant harmonics;

- The amplitudes of all harmonics can be normalized to the amplitude of the 1st order (the most significant one) to find the frequency with the normalized amplitude below 1% (an arbitrary value). This means that the contribution of that and the higher harmonics to the reconstruction of the temperature trace will be less than 1% of the contribution of the most significant 1st order.

- The amplitudes of the surface heat fluxes of all harmonics can be normalized to the amplitude of the surface heat flux of the 1st order to find the harmonics with the normalized heat flux amplitude of 1%.

Figure 1.2.13 shows the normalization curve for the first method lying at the amplitude of the most significant, 1st order. Dividing the FFT curve with the normalization curve yields the Significance curve, Figure 1.2.14. At about 13th order, the significance curve passes 1% line (insignificance point), which means in reconstruction of the temperature trace with Equation 1.2.3, harmonics of 13th order and higher will contribute less than 1% of the 1st order.

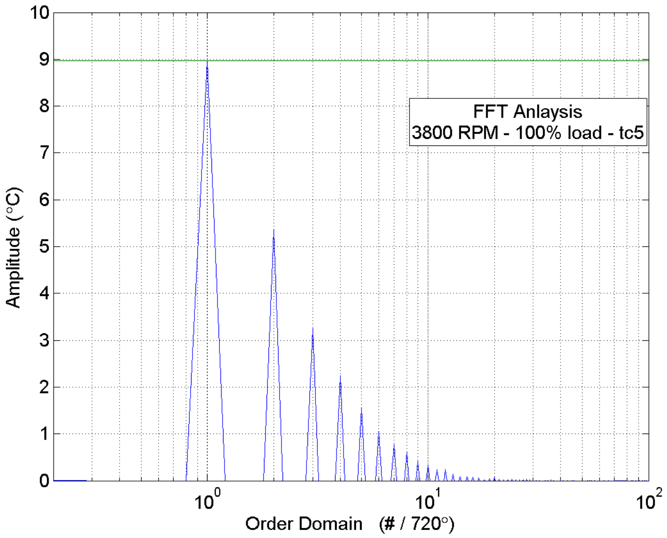

Figure 1.2.13 – FFT Analysis along with the significance curve for method one.

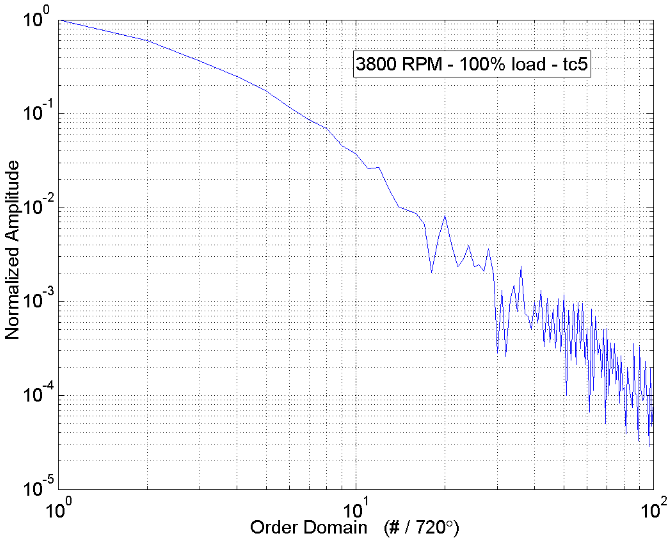

Figure 1.2.14 – Significance Analysis for method one

Equating Equation 1.2.4 to a constant, it's possible to obtain a normalization curve (Equation 1.2.5) for heat flux criteria. Figure 1.2.15 shows the FFT of the temperature trace along with the curve, constant evaluated at the 1st order. The curve points to the amplitude that a frequency component should have in order to yield the same surface heat flux amplitude as the 1st order. It's possible to see the difference between the two methods by comparing Figure 1.2.13 and Figure 1.2.15. Division of the FFT curve with the normalization curve yields the significance curve as in Figure 1.2.16 where the insignificance point is now drawn towards 25th order. Second method is chosen in determining insignificance point as it's more appropriate with the purpose of this study.

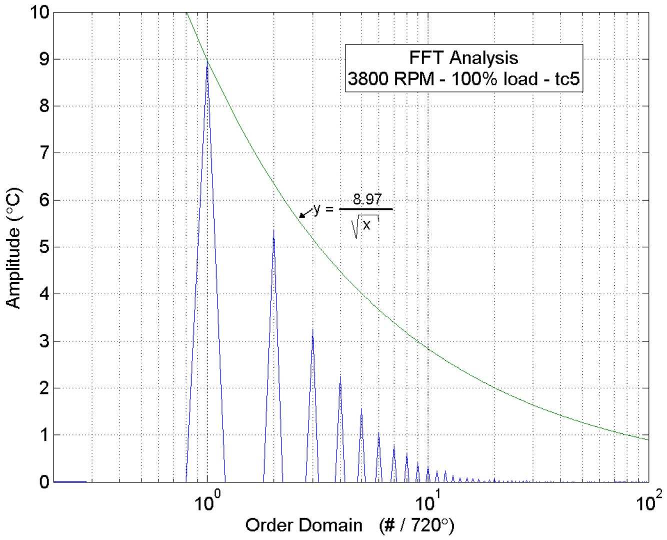

Figure 1.2.15 – FFT Analysis along with the significance curve of method two

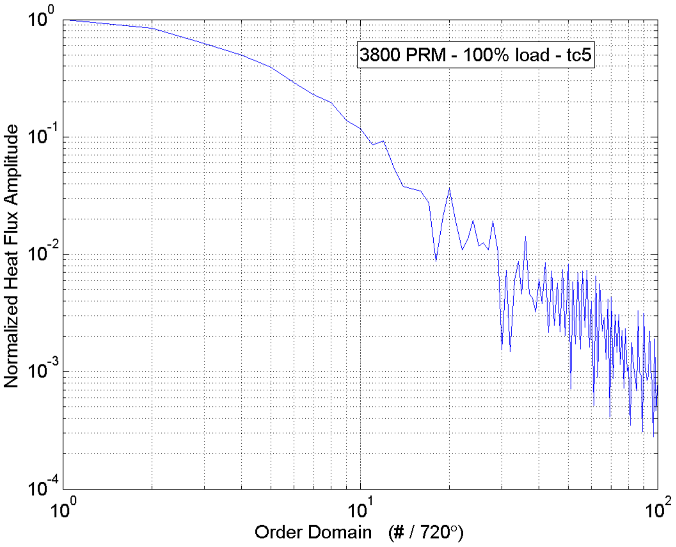

Figure 1.2.16 – Significance Analysis for method two

Figure 1.2.17 shows the change of insignificant harmonics compiled for various RPM. Converting each harmonics to their corresponding frequency values by Equation 1.2.1,

Figure 1.2.18 can be obtained where it's possible to see the effect of RPM on significant frequency. The results are useful in determining the optimization limits in heat transfer FE model.

$$\sqrt{w} \cdot T_{O,w} = \text{constant}$$

Equation 1.2.5 – (Refer to 'heat transfer' section for derivation)

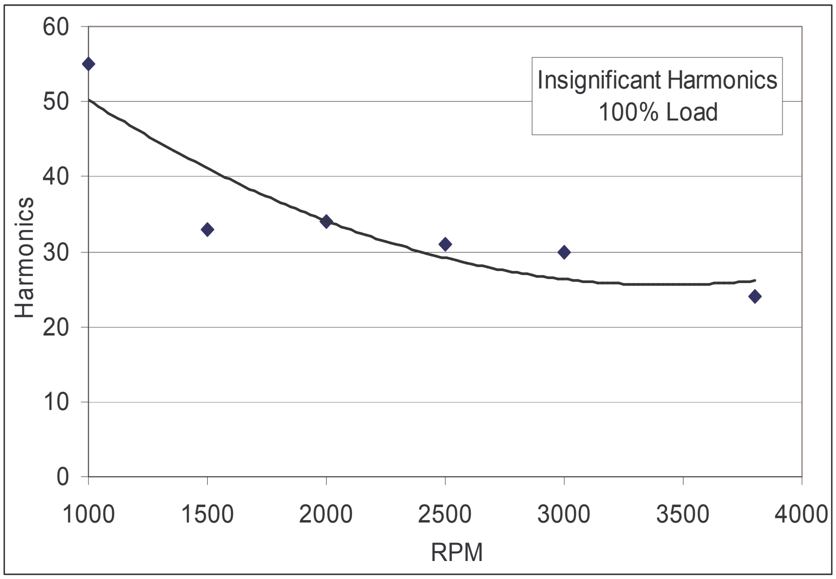

Figure 1.2.17 – Insignificant Harmonics at different RPMs

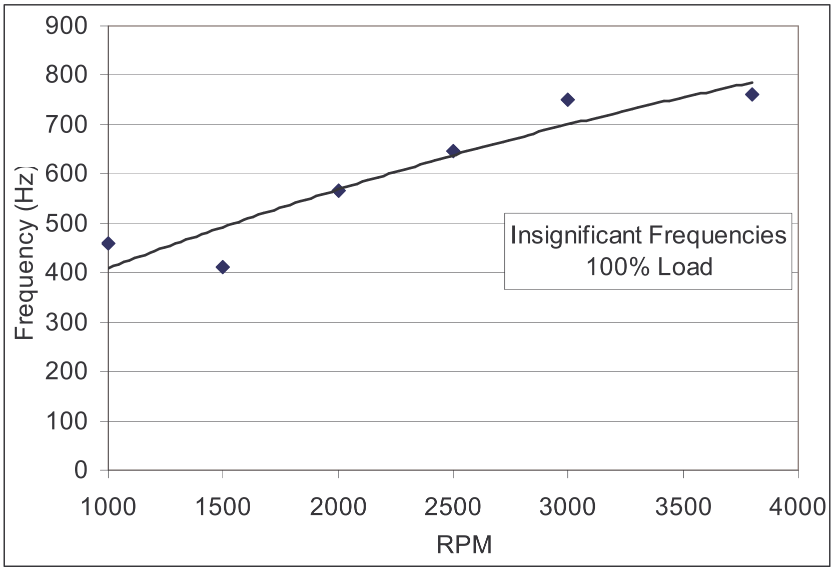

Figure 1.2.18 – Insignificant Frequencies at different RPMs.

The significant frequency content of the temperature trace is also affected by thermocouples and the telemetry system. The response time of a thermocouple is defined by Equation 1.2.6. Treating every discrete data point as a step change over the previous one, with a similar study to step change semi-infinite heat flux analysis, it's possible to model the behavior of the thermocouple with dynamic temperature traces at different frequencies. Accordingly, the frequency response of a 1 μsec thermocouple yields a frequency of about 53 kHz where the gain drops down to 95% (Figure 1.2.19).

$$\frac{T(t)-T_i}{T_s-T_i}=1-\frac{1}{e^{t/RC}}$$

Equation 1.2.6 – Thermocouple response function for a step change

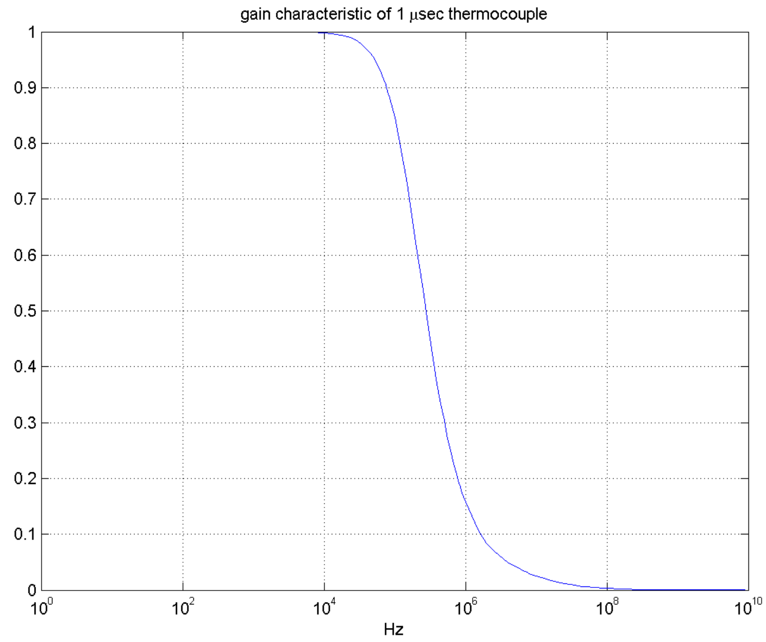

Figure 1.2.19 – Frequency Response of a 1 μsec thermocouple.

The telemetry system frequency response is shown in Figure 1.2.20, yielding a drop off at ~650 Hz at 95% gain (2 kHz at -3dB or 70% gain). It can also be said that the telemetry system has a time constant of about 80μsec. Thus the significant frequency content of the boundary condition data and the telemetry system together define the highest frequency content of the data and the maximum optimization point for FE model.

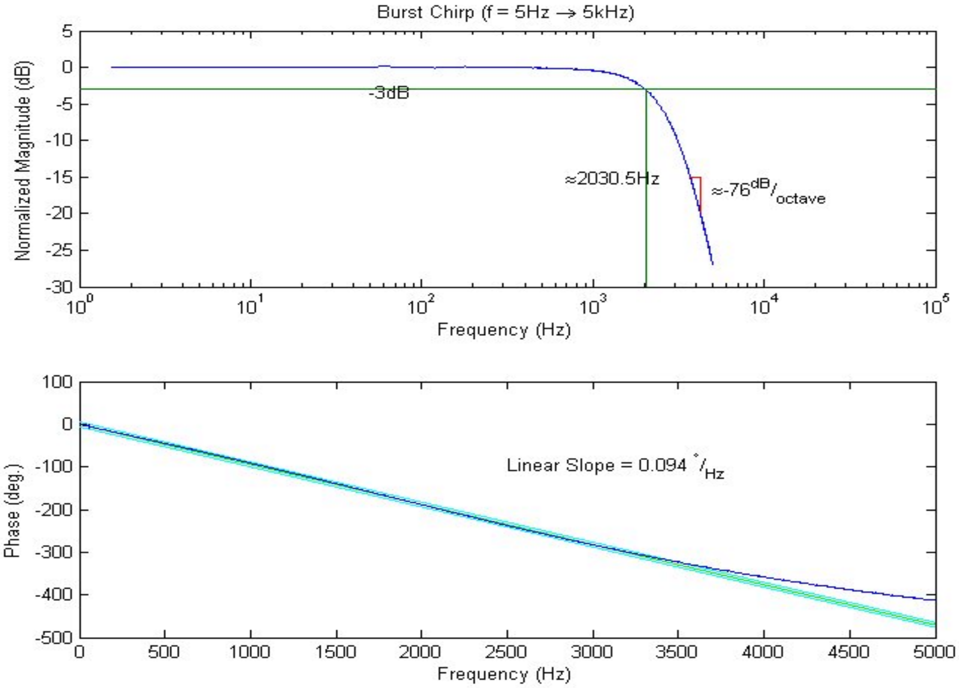

Figure 1.2.20 – Frequency Response function of the telemetry system

Tool 2: Semi-Infinite Modeling with Step Change Response Solution

This method is similar to Duhamel's superposition principle and consists of treating every consecutive data point as a step change over the previous one, and calculates the average heat flux during the time between the two data points. Semi-infinite behavior to a step change is defined by the error function and the resulting heat flux solutions can be seen in Equation 1.2.7.

$$\frac{T(x,t)-Ts}{Ti-Ts}=erf\left(\frac{x}{2\sqrt{\alpha\cdot t}}\right)$$

$$q''(x=0,t)=\frac{-k\cdot(Ti-Ts)}{\sqrt{\pi\cdot\alpha\cdot t}}$$

$$\overline{q}''(x=0,\Delta t)=\frac{\int_0^{\Delta t} q''(x=0,t)}{\Delta t}=\frac{-2\cdot k\cdot(Ti-Ts)}{\sqrt{\pi\cdot\alpha\cdot\Delta t}}$$

Equation 1.2.7 – Step-Change Semi-infinite solutions

When a step change in temperature occurs over a surface, a large amount of heat is initially transferred through the surface that diminishes by the time. Thus in every time step of the discrete data, there's heat flow generated by the most current step change as well as less significant heat flow generated by past step changes. In every step, the method calculates the average heat flux during the time of the current step, and in addition, the average heat fluxes still being contributed from previous steps by integrating the heat flux equation over the time interval since a past step change. In other words, method has to keep a track of the history of data. The resulting function is defined by Equation 1.2.8.

$$q''(x=0,t)=\sum_{i=-\infty}^{0}\frac{2\cdot k\cdot\left(T(i+1)-T(i)\right)}{\sqrt{\pi\cdot\alpha}\cdot\Delta t}\cdot\left(\sqrt{t(0)-t(i)+\Delta t}-\sqrt{t(0)-t(i)}\right)$$

Equation 1.2.8 – Heat Transfer modeling with Semi-infinite step change solution

Both “Fourier series” and “superposition principle” methods yield the same results with different approaches of semi-infinite analysis. “Superposition” modeling converges to its final shape as with more history taken into consideration, thus requiring more processor power. For the purpose of this study, Fourier series analysis is rather easier as the maximum attainable frequency is limited by the sampling rate and the insignificance of frequencies higher than about 30th order. The advantage of step change analysis is that it can be applied to any discrete temperature data whether it’s periodic or not. Some initialization time is required for enough history information to be processed. With enough processing power and buffering, the method can even be used real time during data acquisition, obtaining heat flux results from temperature measurements.

Tool 3: FEM Modeling

The method consists of developing an FEM solution for modeling piston heat transfer with the least amount of elements possible. The optimization technique of the model is developed around the variables of expected frequency ranges and material physical properties.

A solid model of the piston was generated for the FE model in IDEAS by taking measurements from a piston. Measurements were taken by a 3D coordinate measurement system at 0.0001” accuracy.

Earlier studies have prompted us to ask “how much of the piston surface behaves as a semi-infinite solid in terms of absorbing the heat flux”. One-dimensional semi-infinite exact solutions can predict the decay and phase of a temperature fluctuation at any depth and time. Depending on the frequency (w) of the fluctuation, the penetration depths vary as lower frequencies decay deeper than higher frequencies. This also depends on the thermal conductivity, specific heat and density. Equation 1.2.9 (Figure 1.2.21) defines the penetration depth as function of frequency (w) and material diffusivity (α), where the amplitude decays down to 1% of the surface amplitude.

$$\delta_{1\%}=-Ln(0.01)\cdot\sqrt{\frac{w}{2\cdot\alpha}}$$

Equation 1.2.9 – Penetration Depth

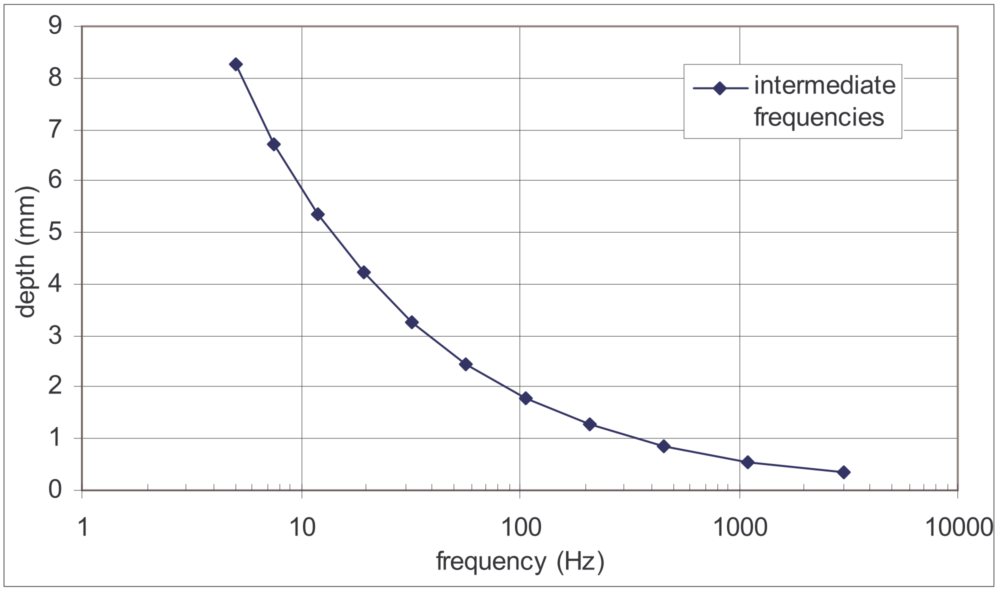

Figure 1.2.21 – Penetration Depth as a function of frequency

The piston is made of hyper-eutectic aluminum alloy which has a silicon content of between 16% - 18%. This helps reduce the crown cracking, improving the life span of the piston. Material properties are taken to be constant and isotropic.

Density: 2760 kg / m^3
Conductance: 127 W / m.K
Specific Heat: 913 J / kg.K

The penetration depth is chosen as the starting point for the development of the FE model. 1D FE models are built and meshed with different mesh distribution methods and periodic boundary conditions are applied at the surface. The results are compared with the periodic boundary condition semi-infinite exact solutions to establish accuracy.

The nature of the semi-infinite heat transfer phenomenon causes an exponential decay of the amplitude with the distance into the surface. Using this as a guideline, it's been tested and established that 50 elements placed in a 1% decay penetration depth for a certain frequency, exponentially getting smaller towards surface yields more than 99% accuracy with the least amount of elements. Equation 1.2.10 defines the node locations from 1% decay penetration depth towards surface, where n is the node number from 0 (bottom of the 1% decay penetration depth) to 50 (surface).

$$node(n) = \delta_{1\%} \cdot \ln\left(\left(\frac{e-1}{50} \cdot n\right) + 1\right)$$

Equation 1.2.10 – Node location for exponential element distribution

Figure 1.2.22 shows an example 1D FE model result comparison with the exact solution. In this example, a 1D semi-infinite model is built to accommodate the 1% decay penetration depth of 100Hz, and 50 elements are placed according to Equation 1.2.10. A periodic boundary condition of 100 Hz with 45^O phase and 50^OC amplitude is applied over the surface.

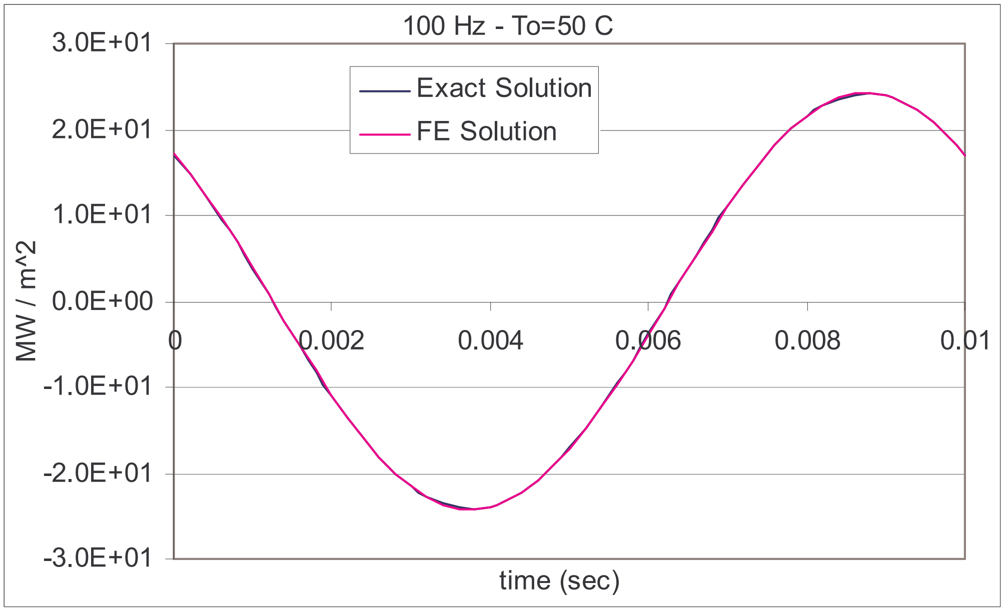

Figure 1.2.22: Transient surface heat flux comparison

The dynamic temperature change over the piston surface has a range of frequencies as discussed before. The lowest frequency is the fundamental frequency of the engine combustion related with the RPM and the highest frequency is about 800 Hz. A FE model to accurately solve for all frequency components is achieved by choosing ten intermediate frequencies (Figure 1.2.21) between the range limits and superimposing the individual FE models over each other. Equation 1.2.11 calculates the best distribution of intermediate frequencies as lower frequencies have larger penetration depth differences.

$$f(n) = \frac{f_{\max}}{\left(\frac{e-1}{10} \cdot n + 1\right)^{\ln\left(\frac{f_{\max}}{f_{\min}}\right)}}$$

Equation 1.2.11 – Intermediate frequency calculator

Figure 1.2.23 shows the final FE model before and after meshing. The $f_{\max}$ and $f_{\min}$ values are 3 kHz and 5 Hz in this example. Figure 1.2.24 is the final form of the technique after it's meshed over the piston cross section. Rest of the piston cross section after the 1% decay penetration depth of the lowest frequency is meshed with free coarse mesh as the heat flow and temperature distribution will be steady state over this area.

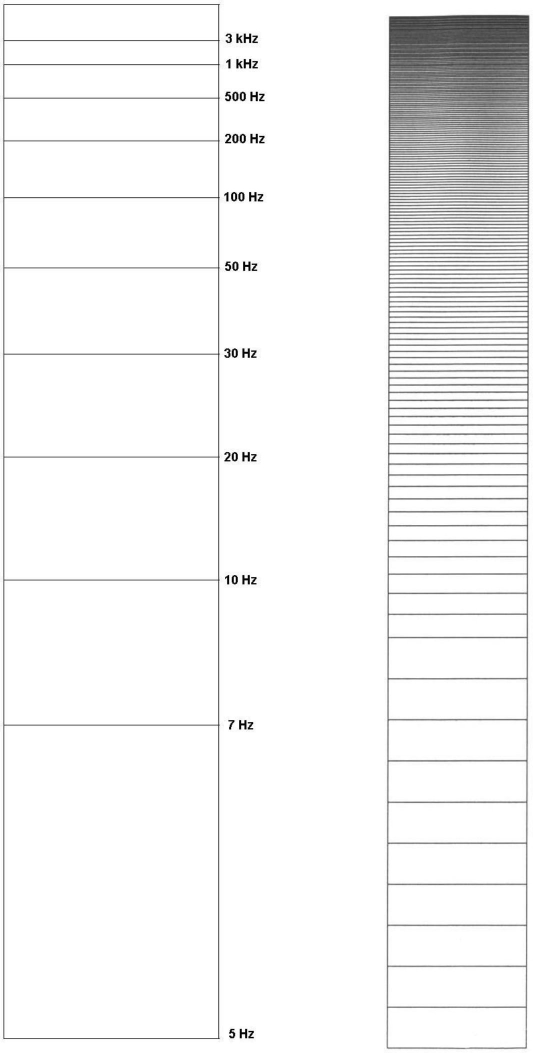

Figure 1.2.23 – 1% decay penetration depths of all intermediate frequencies superimposed over each other and final meshed FE model.

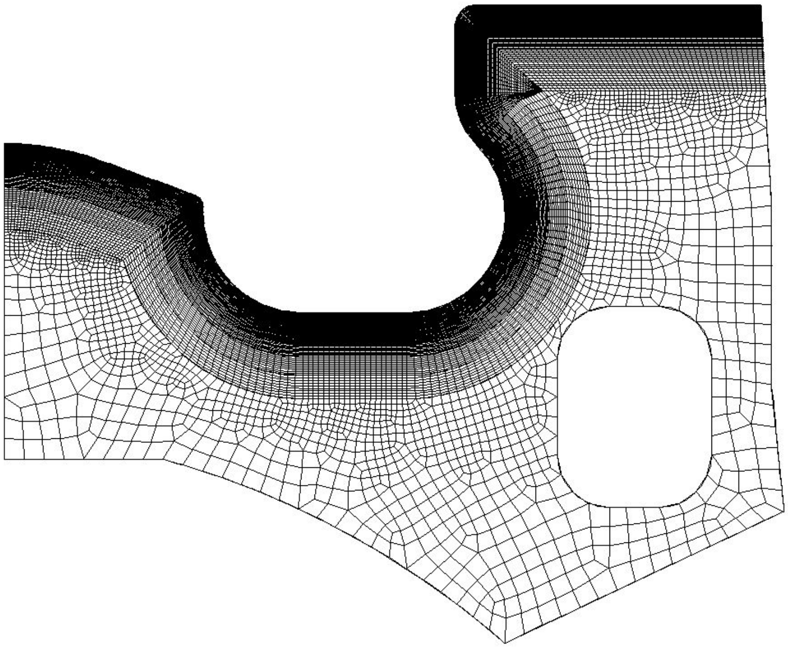

Figure 1.2.24 – Meshed Piston Cross Section

1.2.12 Thermal Loading Results

Nine segments are defined around the piston cross section between thermocouples to better resolve the heat flux distribution. First five segments are the piston surface, and the sixth, seventh, eight and ninth segments are the rings, skirts, piston bottom and oil gallery, respectively. Each black tick mark on Figure 1.2.25 defines a thermocouple location. There are also two more thermocouples along segment six, thus having a thermocouple behind every ring groove.

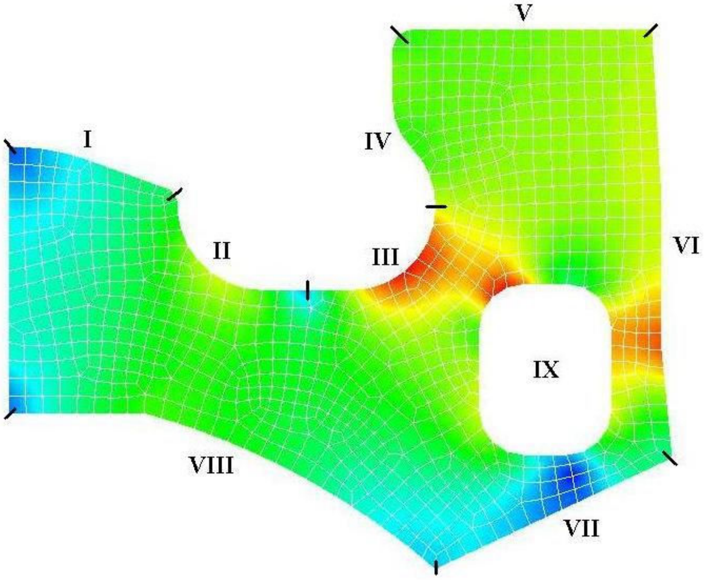

Figure 1.2.25 - Segments

One of the purposes of this study is to characterize the extent of semi-infinite behavior of the piston surface. To achieve this, results from the FE model are compared with the semi-infinite solutions. Both results yielded the same shape of the dynamic heat flux trace at the surface but with different offsets. As in 1.2.26, heat flux into the piston surface obtained from the FE model at the location of thermocouple five has the same shape but some offset from the heat flux obtained from semi-infinite analysis.

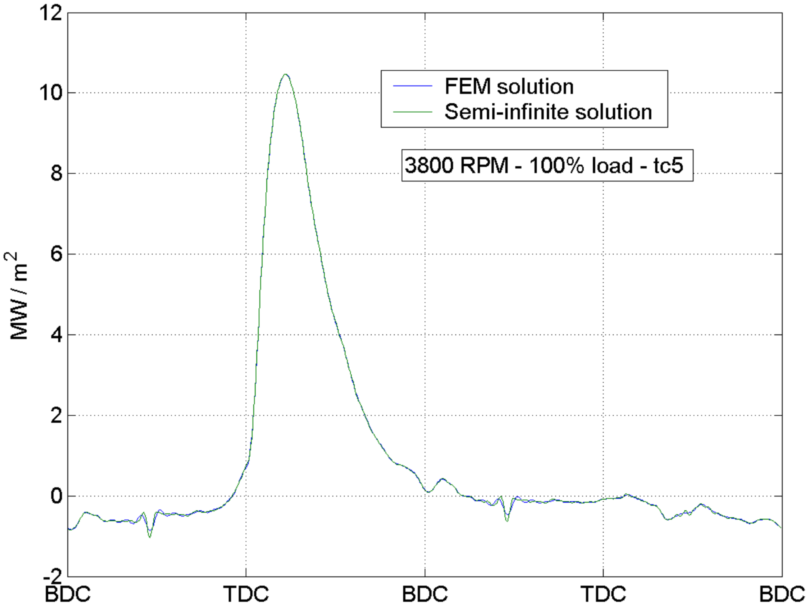

Figure 1.2.26 – Heat flux results comparison between Semi-infinite analysis and FE modeling

The heat flux calculated form the semi-infinite solutions need to be corrected by super-imposing the time averaged heat flux to it as shown in Equation 1.2.12. The results are shown in Figure 1.2.26 and compared to FEM results.

$$q''(t) = \overline{q}'' + q''(t)_{\text{semi-inf}}$$

Equation 1.2.12 – Overall form of semi-infinite transfer

At this point heat transfer can be calculated by either the FE model or the semi-infinite solutions. Differences between the two methods for this study are;

- The processing time (solution + post processing) for the transient FE model is significantly longer than the processing time for semi-infinite model. (10 hours to 1 hour for this study)
- The results for transient FE model create very large files and thus become hard to process due to large numbers of elements (the results being posted for each element at each time stamp). On the other hand, semi-infinite model requires a coarse meshed FE model for time averaged results, thus includes one set of results for a smaller number of elements. (10 gigabytes to 100 Kbytes for this study)

- The transient FE model includes constant and transient boundary conditions meeting each other at certain locations (i.e. location of thermocouple six), causing irregular heat flux results, thus introducing glitches in the solution.

The advantages and disadvantages change according to the structure of the model. For this study, choosing the second method is more advantageous over the first one.

Steady State Heat Transfer Results

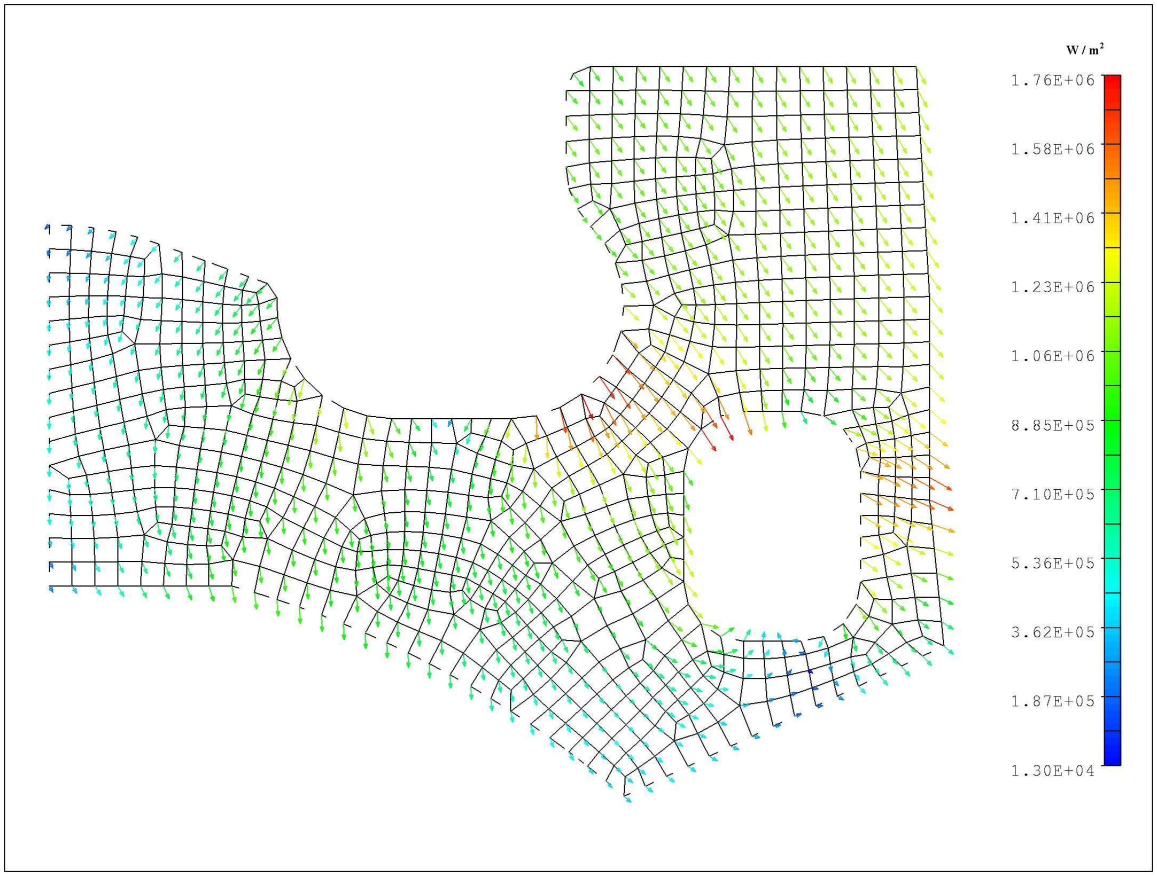

Figure 1.2.27 – Steady State Heat Transfer through the Piston at 3800 RPM – 100% load

Steady state heat transfer through the piston is calculated by a coarse meshed piston cross section as in Figure 1.2.27. A time averaged heat flux for each segment is also calculated by averaging the nodal heat fluxes over each segment. These are the time averaged heat transfer values that are super imposed on the semi-infinite solution heat flux results. The general flow scheme of heat transfer and relative magnitudes (general shape of Figure 1.2.27) is preserved for different load and rpm test conditions.

The oil gallery thermocouples are located 120^{O} away circumferentially from the oil gallery inlet. During its travel, the oil gets hot enough to start transferring heat towards rings, but still draws the largest average heat flux from segment three of piston surface. It also changes the direction of heat flow towards rings.

Segment four has one of the lowest average heat transfer rates as the downward direction of heat transfer from segment 5 causes the heat to flow towards surface especially at the lower sides of segment four (Figure 1.2.27).

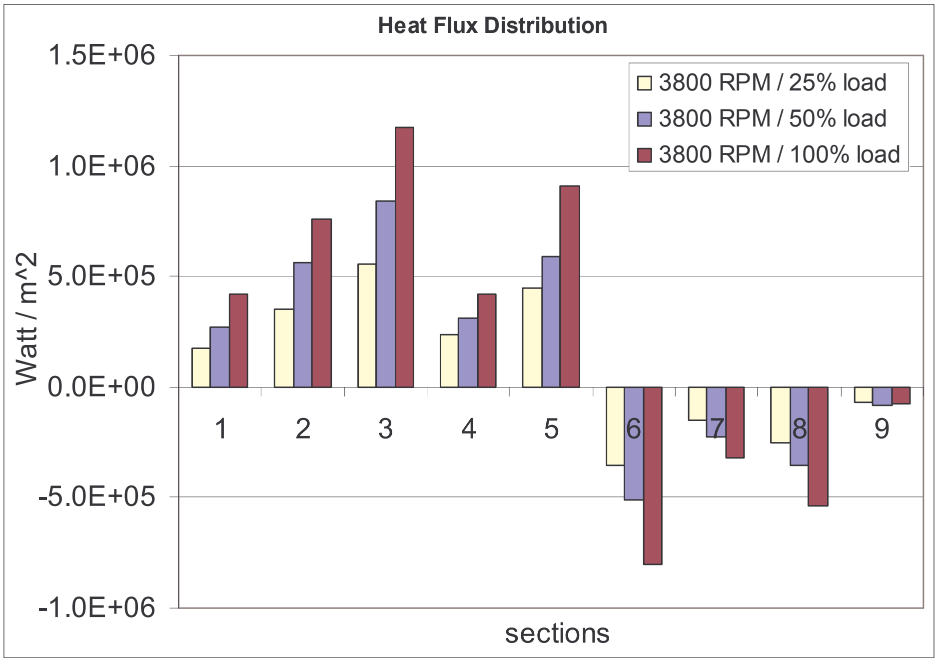

Figure 1.2.28 – Heat Flux at each segment at different load at 3800 RPM

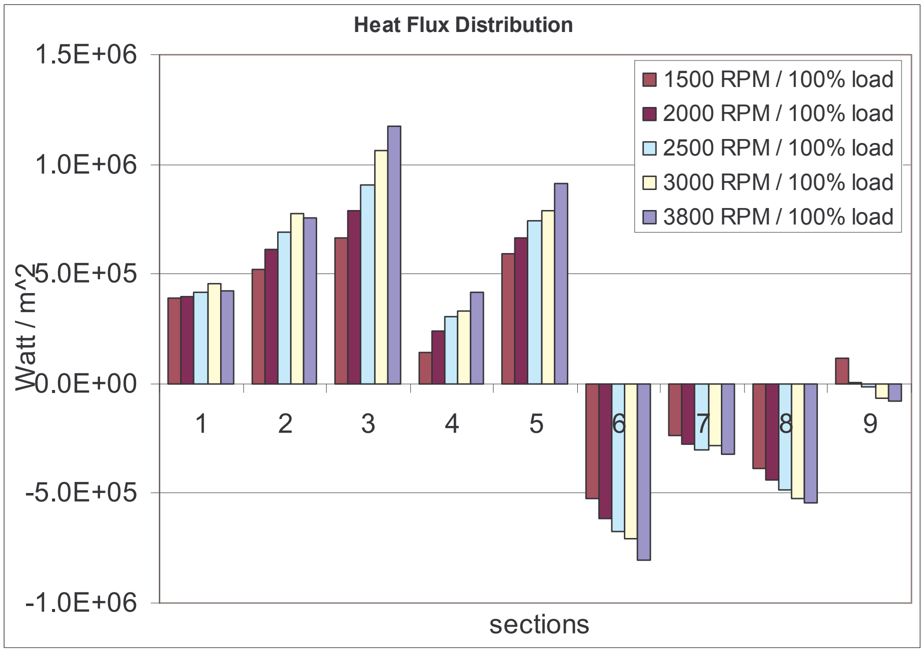

Figure 1.2.29 – Heat Flux at each segment at different RPMs at 100% load

Figure 1.2.28 and Figure 1.2.29 show the heat flux distribution at each segment. Positive and negative values indicate heat transfer into and out of the surface, respectively. Steady state heat transfer is a function of both load and RPM. The highest heat flux is seen at segment 3. Overall, the oil gallery does not experience high rates of heat transfer.

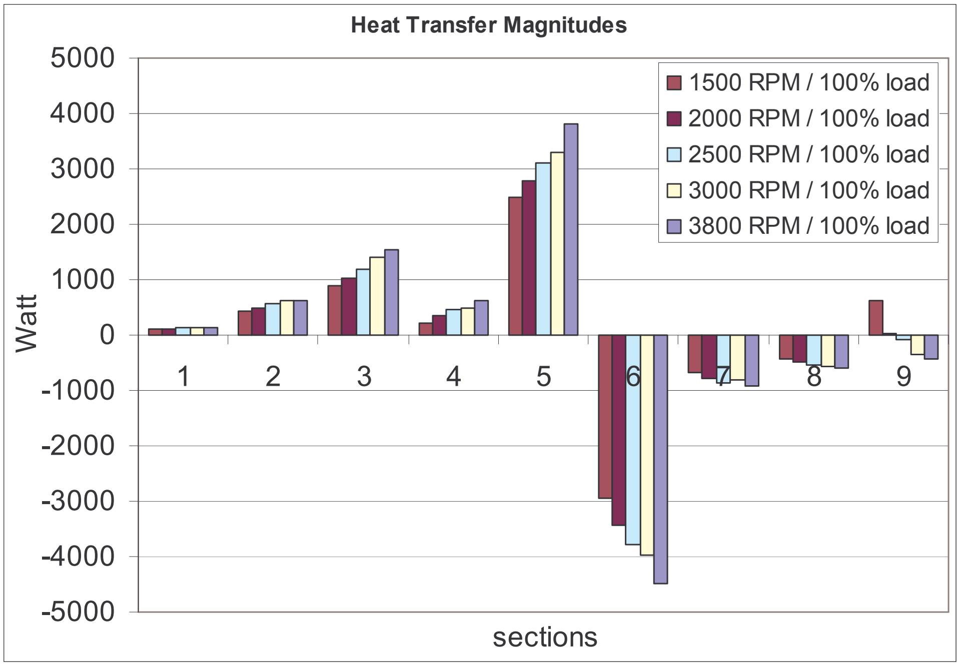

Figure 1.2.30 – Total Heat Transfers at each segment at different RPMs at 100% load

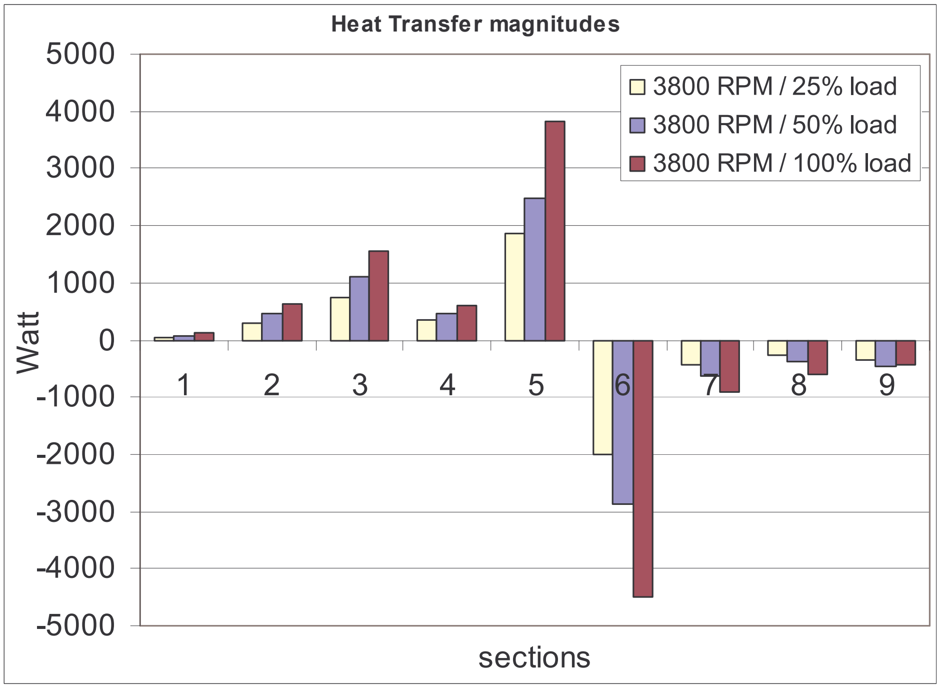

Figure 1.2.31 – Total Heat Transfers at each segment at different loads at 3800 RPM

Figure 1.2.30 and Figure 1.2.31 show the total heat transfer rates in to each segment. Due to its smaller surface area and lower heat flux value, segment one becomes more insignificant in this approach. Largest portions of the total heat are transferred through segments five and six. Segment six transfers most of the heat that enters the piston through segment five. Figure 1.2.32 and Figure 1.2.33 show the percentage of the heat transfer in each segment in the total heat transferred into the piston through first five segments. Speed and load is not an effective factor in the percentage distribution of heat transfer among segments.

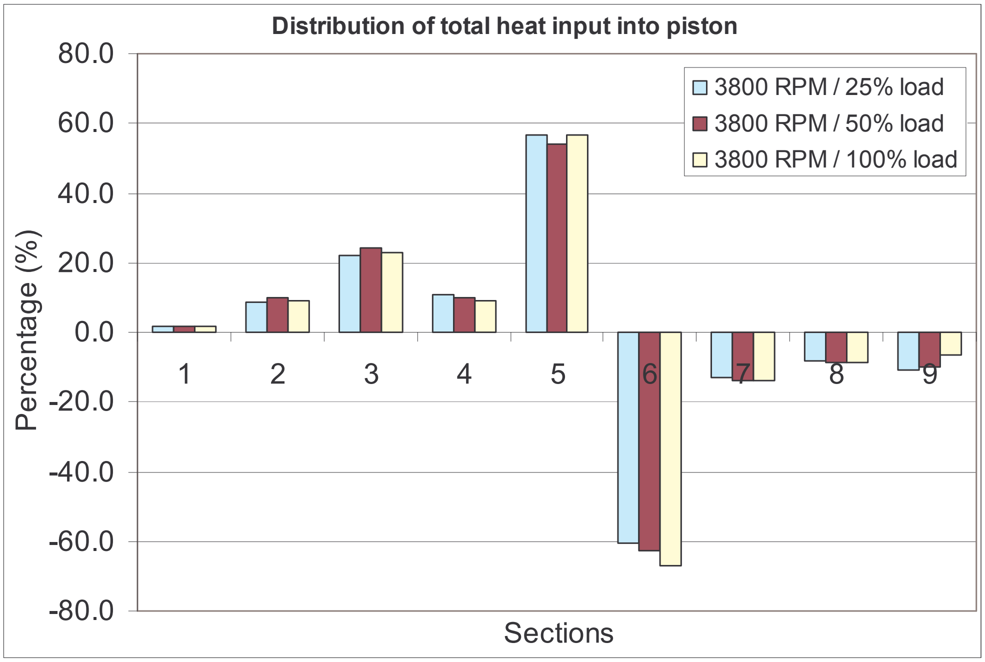

Figure 1.2.32 – Percentage distribution of heat transfers into each segment at different loads

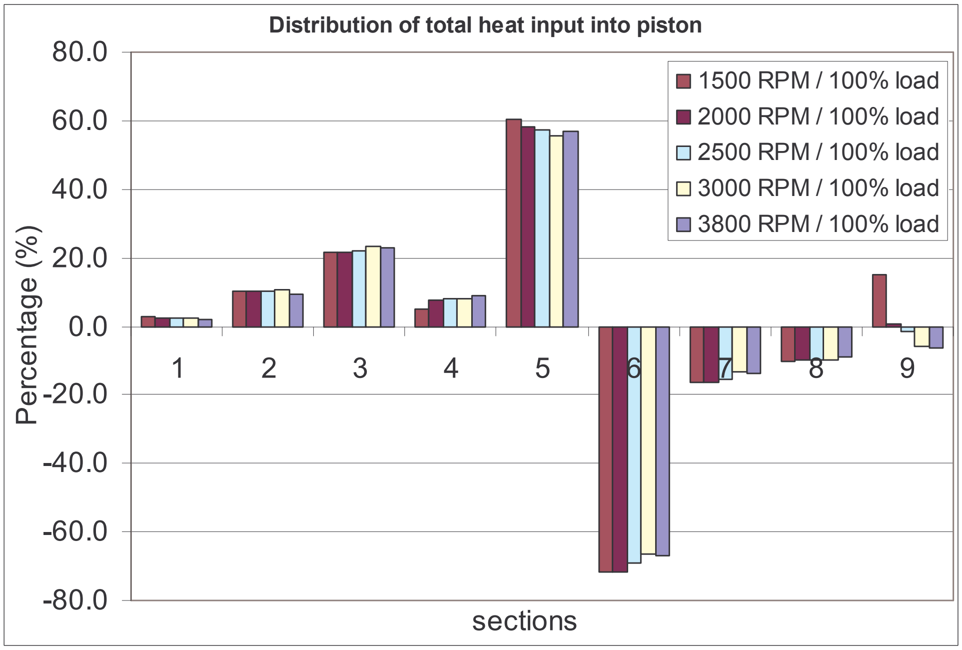

Figure 1.2.33 - Percentage distribution of heat transfers into each segment at different RPMs

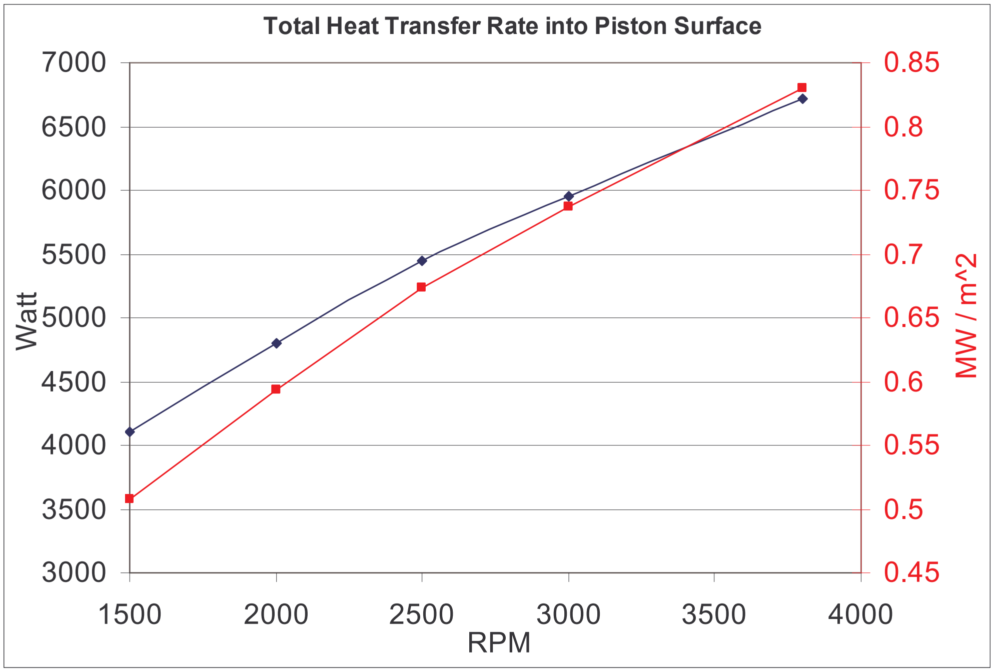

Figure 1.2.34 – Heat transfer and heat flux rates into the overall piston surface at 100% load

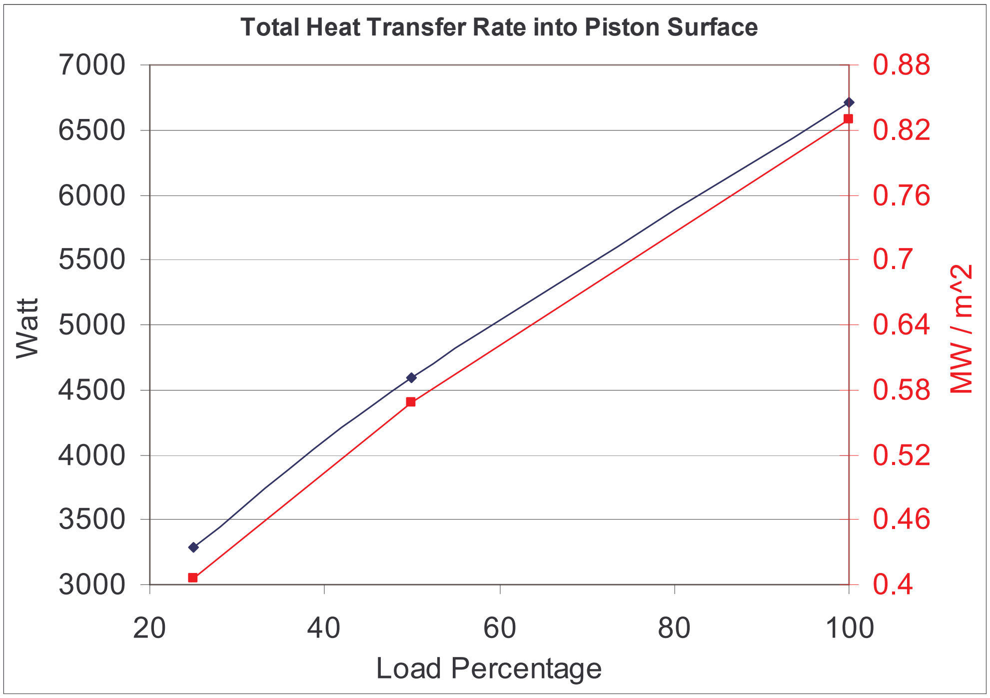

Figure 1.2.35 – Heat transfer and heat flux rates into the overall piston surface at 3800 RPM

The overall heat transfer and heat flux rate in to the piston surface are shown in Figure 1.2.34 and Figure 1.2.35. Both speed and load have close to linear relation with the steady state heat transfer rate into the piston surface.

1.2.12 Transient Heat Transfer Results

Transient heat transfer results are obtained by the semi-infinite model and corrected by superimposing the steady state FE model heat flux results. Figure 1.2.36 shows the general level of surface temperatures at each thermocouple location. Although magnitudes change for different test cases, relative positions of temperature traces to each other remain same.

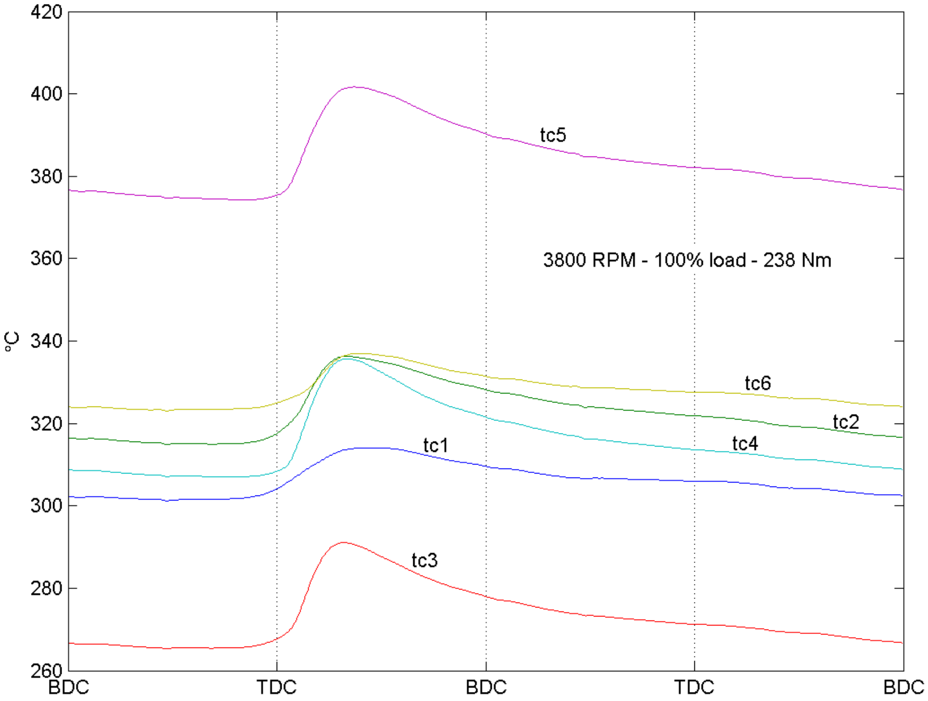

Figure 1.2.36 – Fast response surface thermocouple temperature measurements

Thermocouples three, four and five have the largest swings compared to the others. This causes the highest transient heat flux peaks to be created over segments three and four that are defined by these thermocouples. Segment five, which is defined by thermocouple five and six, have the highest time averaged temperature and thus have the highest time averaged heat flux. Segment one, have the lowest peak heat flux due to lower swings of thermocouples one and two that define it.

Figure 1.2.37 through Figure 1.2.41 show the heat fluxes at each segment at different loads of 3800 RPM. As segments three and five have the largest average heat transfer rates into the surface, there’s hardly a negative heat transfer form those segments. Segments one, two, and four transfer heat back in to the gas after combustion cycle.

Transient heat transfer in any segment is a strong function of load that can reach almost up to 12 MW / m^2 at the maximum output condition of the engine.

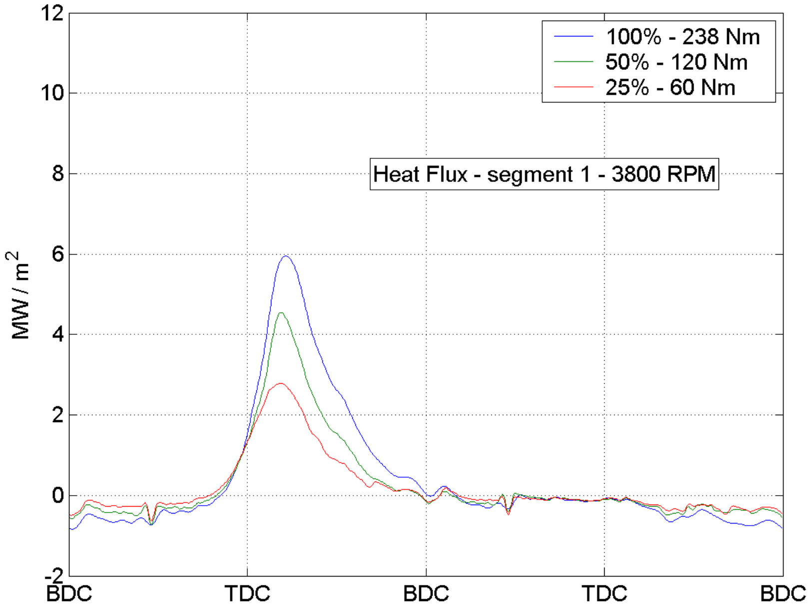

Figure 1.2.37 – Heat Flux at different loads at segment 1

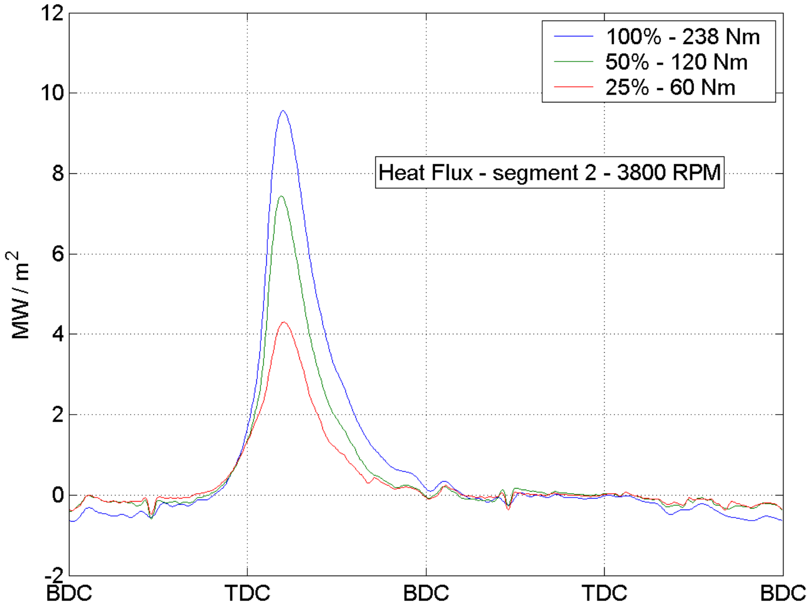

Figure 1.2.38 – Heat Flux at different loads at segment 2

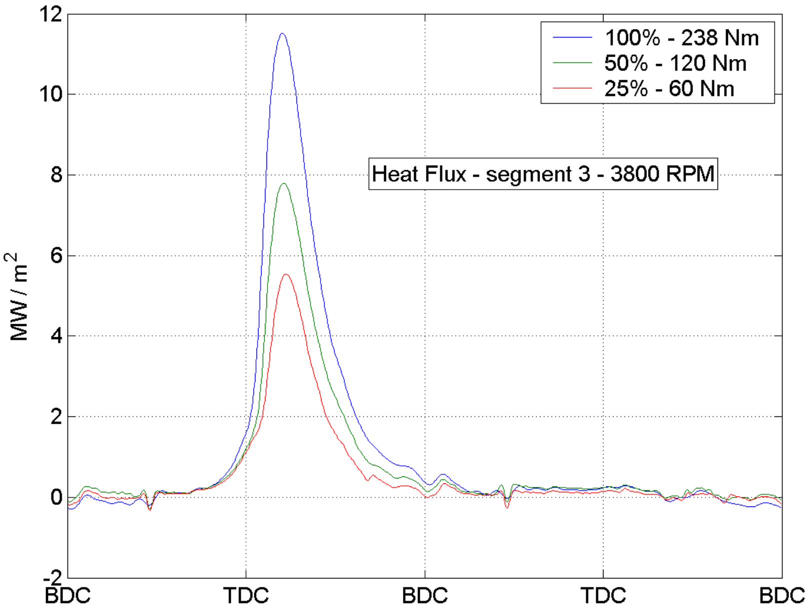

Figure 1.2.39 – Heat Flux at different loads at segment 3

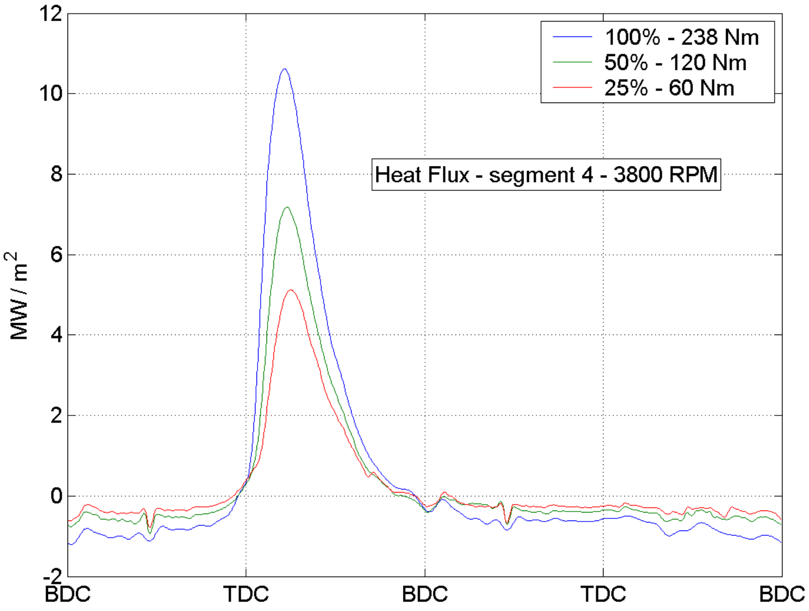

Figure 1.2.40 – Heat Flux at different loads at segment 4

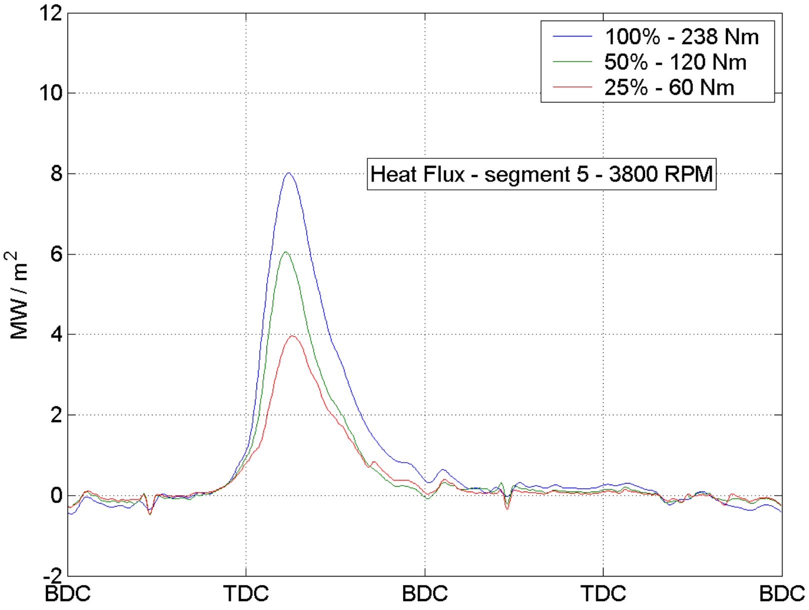

Figure 1.2.41 – Heat Flux at different loads at segment 5

Figure 1.2.42 through Figure 1.2.45 show the transient heat transfer at different speed settings at 100% load. In general, speed is a moderate factor on transient heat transfer especially on peak heat flux values.

The peak heat flux at segment one, decreases with engine speed. At segment two, the trend is not very clear. At segments three and four, peak heat flux increases with speed. The overall time averaged piston surface heat transfer increases with speed and load. At lower end of the speed range (1500 PRM), segment one has a higher heat flux peak compared to the other speed cases. Where as on segments three and four, where the spray is most likely to hit, peak heat flux value for 1500 RPM is lower than the others. At 3800 PRM, the peak heat flux is the lowest in segments one and two and highest in segments three and four. With the increasing speed, higher injection pressures and amounts dominate the turbulent effects and the peak heat flux sweeps towards the segments that the injectors are pointed towards.
In each figure, it's also possible to see the phase of the peak heat flux with the increasing speed. There's about 30^O phase between 1500 RPM peak heat flux location and 3800 RPM peak heat flux location.

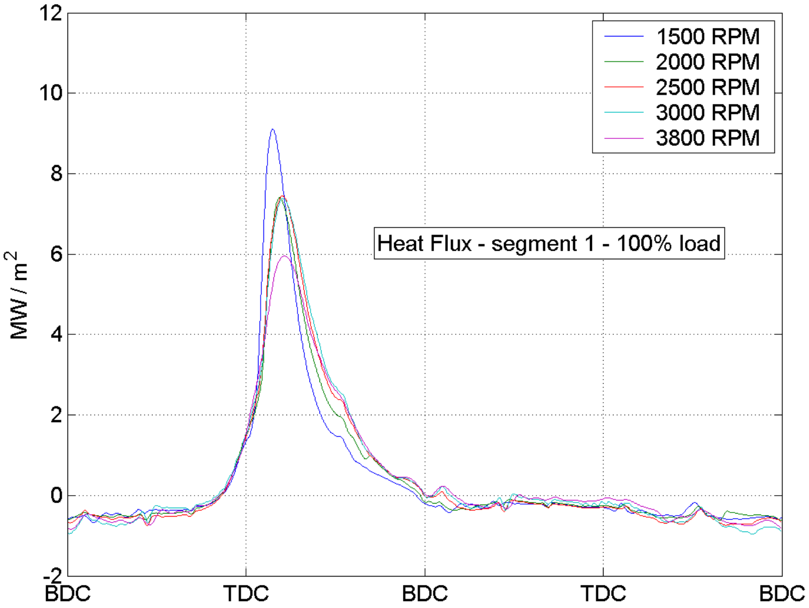

Figure 1.2.42 – Heat Flux at different RPMs at segment 1

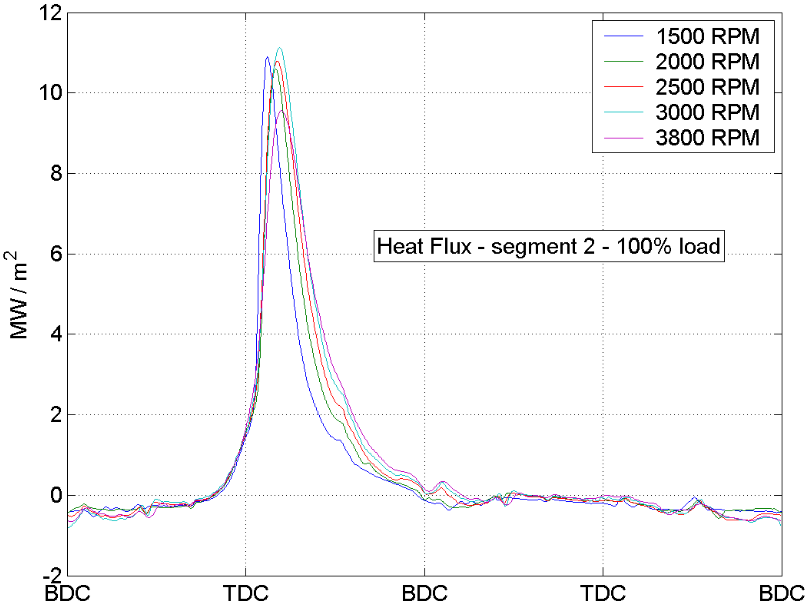

Figure 1.2.43 – Heat Flux at different RPMs at segment 2

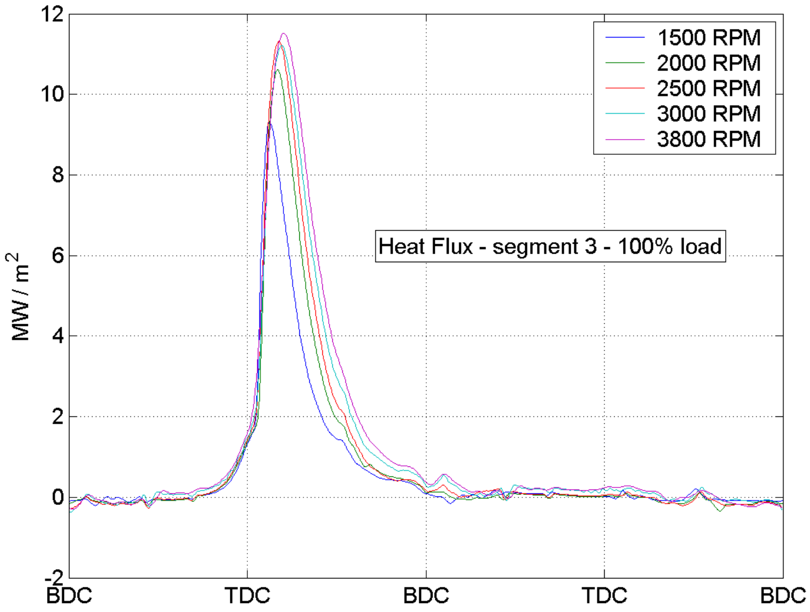

Figure 1.2.44 – Heat Flux at different RPMs at segment 3

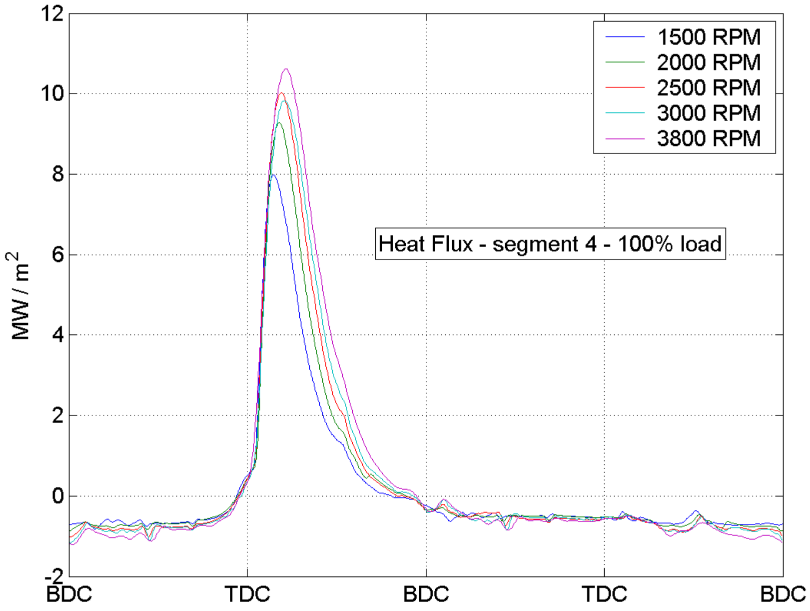

Figure 1.2.45 – Heat Flux at different RPMs at segment 4

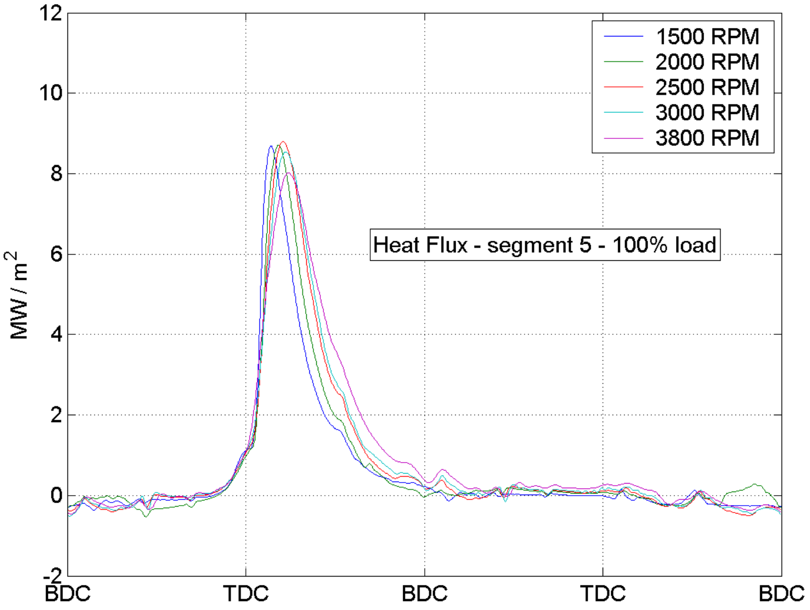

Figure 1.2.46 – Heat Flux at different RPMs at segment 5

1.2.13 Impingement Signatures

1.2.13.1 Objectives:

1. Measure instantaneous piston surface temperatures using fast response, triaxial surface thermocouples.
2. Develop a technique to identify the impingement of either liquid spray or flame on the piston surface, utilizing the surface temperature trace, under varying engine operating conditions.
3. Characterize the identified impingement signature using cylinder pressure traces, injection signals, rate of piston surface temperature change, and heat release.

1.2.13.2 Identification of Impingement Signatures

A typical set of surface temperature traces are shown in Figure 1.2.47. The data is from thermocouple 5, on the piston bowl lip, with the injector in the 0° orientation. From the figure it can be seen that as engine load increases, piston surface temperature increases, as expected. Additionally, the thermocouples recorded a surface temperature swing of 33°C at 1800 rpm, 165 N-m of load.

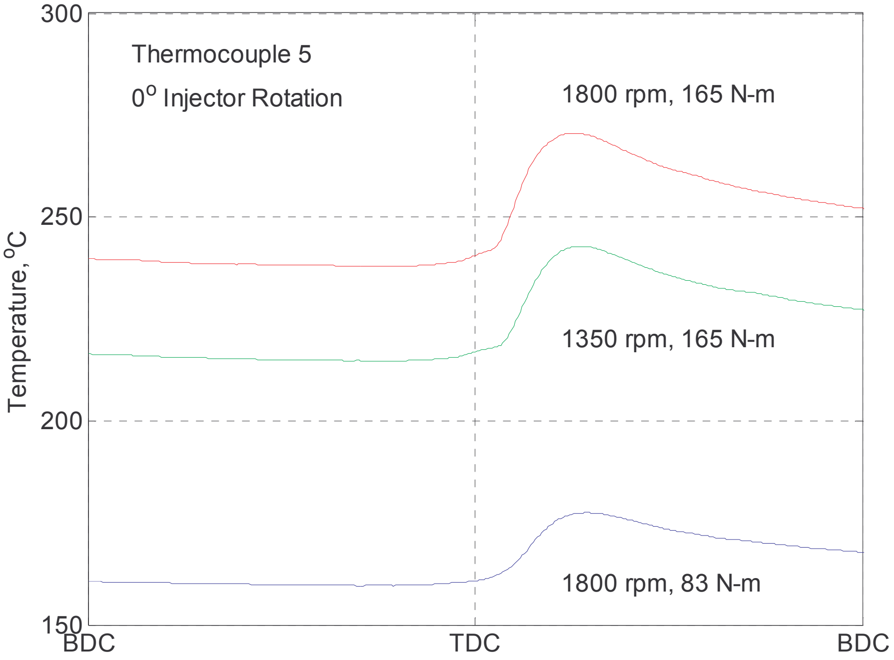

Figure 1.2.47: Typical piston surface temperature trace: thermocouple 5, 0° injector rotation.

It is interesting to look at another thermocouple location, under the same speed and load conditions. Piston surface temperature data from thermocouple 15, with the injector in the 0° orientation, is shown in Figure 1.2.48. Again, piston surface temperatures increase with increasing load, as expected. However, at the higher load, a distinct temperature feature around TDC appears at this thermocouple location and injector orientation. Note that at the lower load condition, the temperature feature does not exist. The temperature feature around TDC appears to be influenced by thermocouple location and engine operating condition.

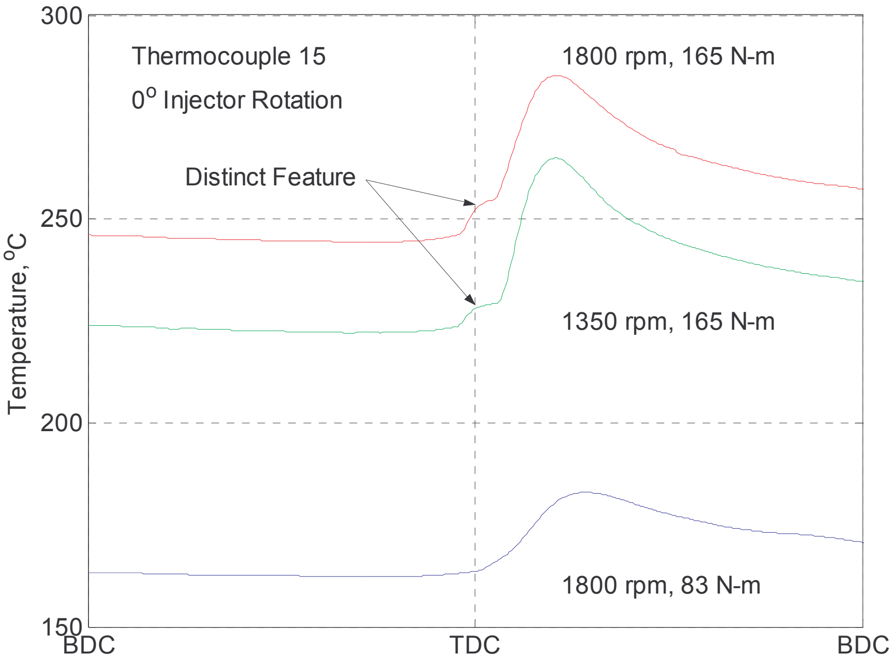

Figure 1.2.48: Distinct feature in temperature trace: thermocouple 15, 0° injector rotation.

To understand the feature appearing in Figure 1.2.48, the cylinder pressure and injection pulse traces were superimposed on the temperature trace. The magnitudes of the cylinder pressure and injection pulse are not to scale.

Figure 1.2.49 shows the unique temperature signal occurs after the pilot injection but before the main injection event begins. The relationship between the injection event and the temperature trace define the pilot injection event as the source of the distinct feature. From the figure it can also be seen that the main injection event does not cause a unique signal in the temperature trace. The shape of the temperature trace, in the vicinity of the unique feature, is similar to the pressure trace; however the temperature trace lags the pressure trace response. The pressure trace shape is highly governed by the combustion events in the cylinder. There are two unique slope changes in the pressure trace, caused by the pilot combustion and the main combustion events. The location and shape of the unique temperature feature tends to suggest flame impingement at the thermocouple location versus spray (liquid drop) impingement.

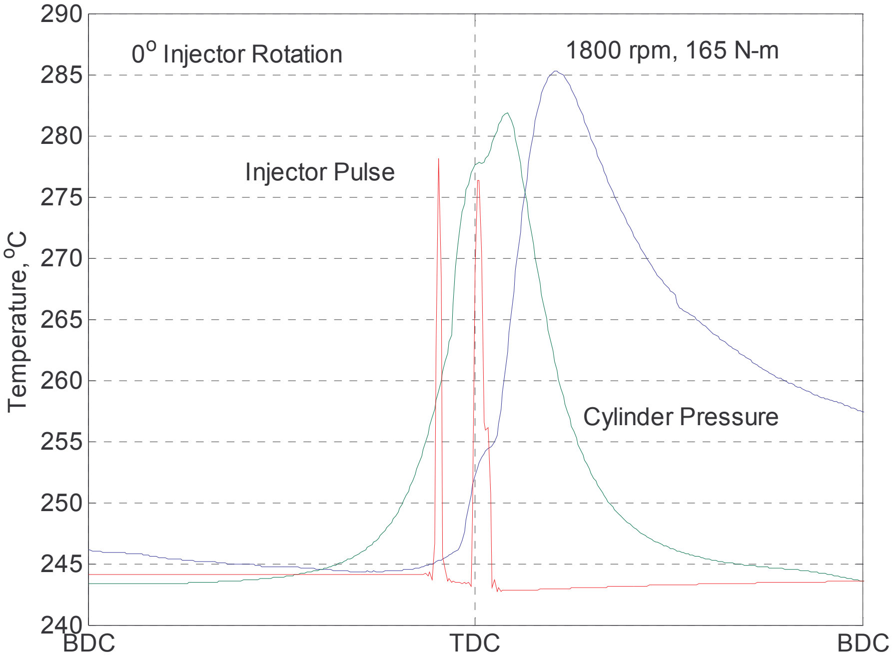

Figure 1.2.49: Thermocouple 15 with scaled cylinder pressure and injection pulse for reference.

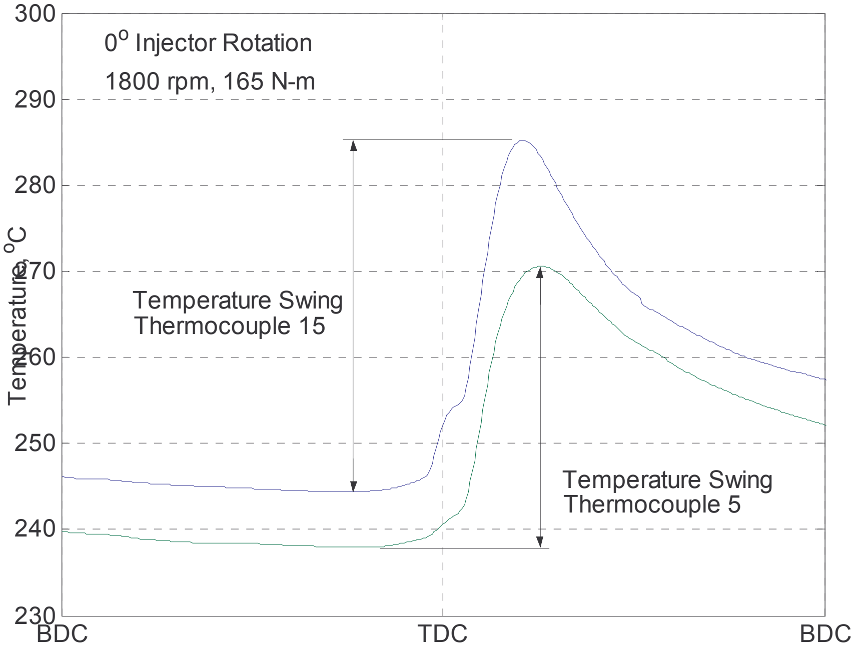

Figure 1.2.50: Determination of temperature swing.

It was also observed that when the unique signature was present in the temperature data around TDC, the temperature swing was noticeably increased. Temperature swing is defined as the difference in the temperature, from the peak value to the lowest value within the same temperature trace. This is shown in Figure 1.2.50.

Figure 1.2.51 shows the increase in temperature swing for two test conditions. The non-impinging location, TC 5, is shown to have a 20-30% lower temperature swing as compared to TC 15. The increase in the temperature swing is caused by a combination of factors within the combustion chamber. One may be increased heat transfer through an increased heat transfer coefficient. The heat transfer coefficient would be increased if the fuel spray disturbed the boundary layer on the piston surface. Additionally, if the burning spray contacted the piston surface directly at thermocouple location 15, it would expose the piston surface to 1500-2000 K temperatures. The temperature of the surface at these locations would be expected to rise above those that did not experience direct flame contact.

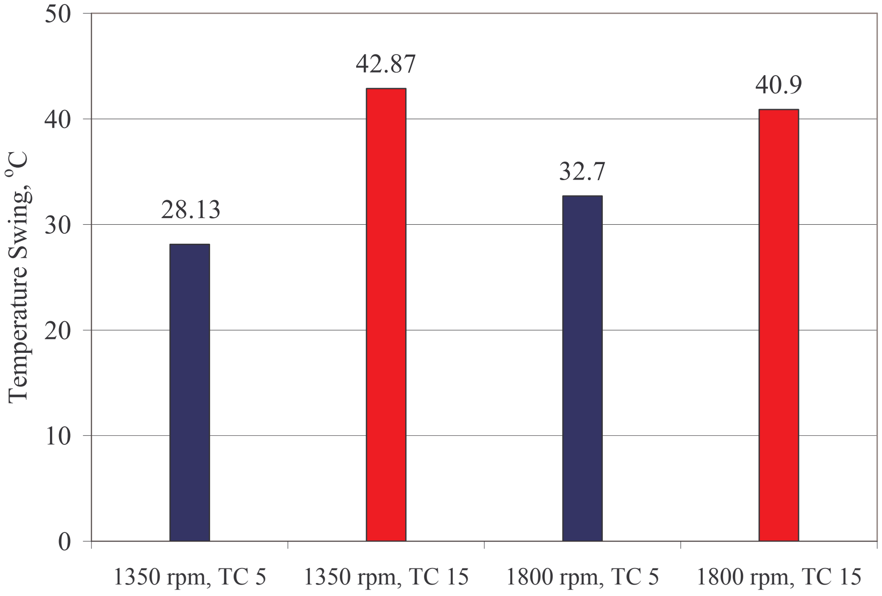

Figure 1.2.51: Effect of impingement on temperature swing: 0° injector rotation.

As stated earlier, the test matrix included two injector rotation angles, 0° and 30°, for each speed and load condition tested. To provide further proof that the observed signature was injection related, surface temperature versus crank angle position for thermocouple 15, was plotted for the different injector positions. For each injector orientation, the load and engine speed were held constant.

From Figure 1.2.52, it is observed that the unique temperature event occurs when the injector is in the 0° position, but does not occur in the 30° rotated position. It specifically defines a direct relationship between the injector and the observed signal. From this point forward, the signal will be identified as impingement. Note that no determination has yet been made to characterize the impingement as spray (liquid drop) or flame.
The overall surface temperature profiles of the two injector orientations are significantly different. When the injector is in the 0° orientation, a strong temperature feature shows up

around TDC and influences the peak surface temperature of the piston. The 30° orientation produces a significantly cooler temperature history, for the same thermocouple location. Peak temperature is reduced 23°C. These results are consistent with the results published by Wolf and Cheng (1989). They found that impingement of a burning spray resulted in a significant increase in heat flux to the wall, compared to a non-impinging burning spray.

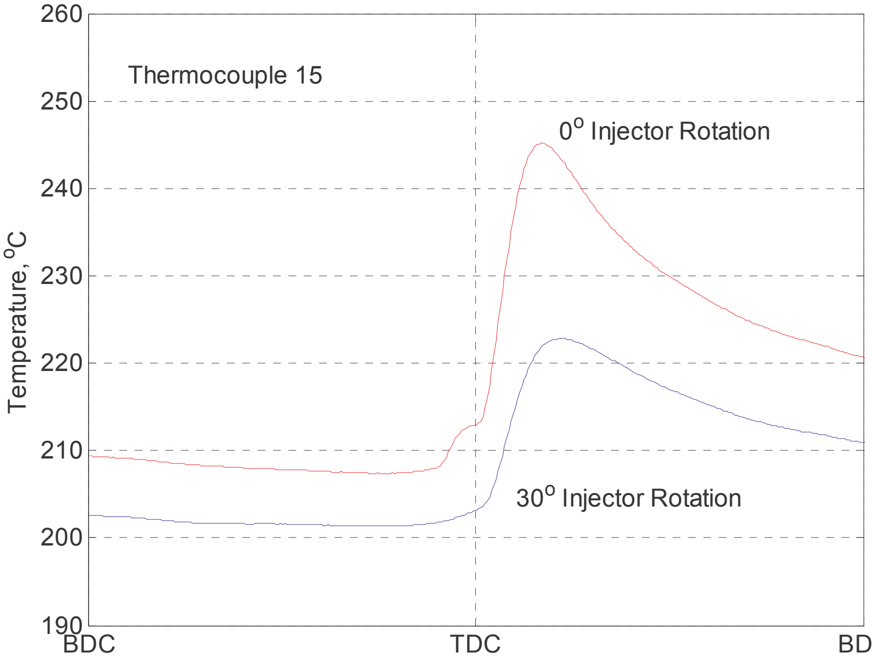

Figure 1.2.52: Temperature versus CAD for 0° and 30° injector rotations, showing effect of injector position on piston temperature.

A simple yet effective method for identifying impingement in the time domain is to calculate the derivative of the temperature trace, with respect to crank angle position. The derived quantity is the rate of change of surface temperature with respect to crank angle position. The impingement signature in the temperature trace is transformed into a "spike", prior to the main combustion "spike". Figure 1.2.53 shows the results for thermocouple location 5, 0° injector rotation, under varying speed and load conditions. A small "spike" is visible, before the main combustion event. The large spike is the result of the main combustion event and rapid rise in piston surface temperature.

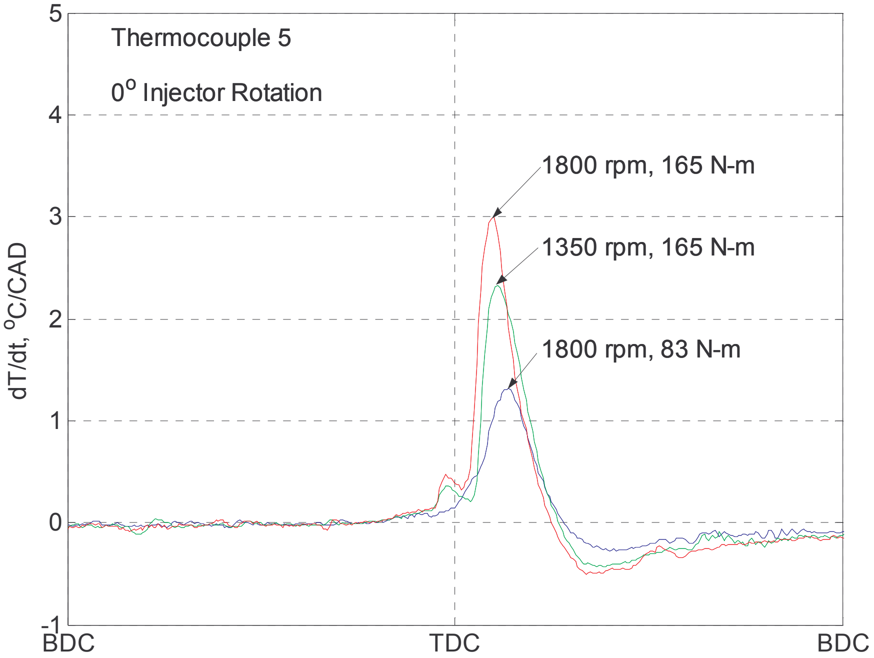

Figure 1.2.53: Rate of change of surface temperature, dT/dt: thermocouple 5, 0° injector rotation.

When the rate of change of surface temperature is computed for thermocouple 15, the impingement spike is clearly identified, as shown in Figure 1.2.54. The magnitude of the impingement spike is directly related to the rate at which the temperature change occurs. The more significant the impingement event is, the larger the impingement spike. Note that the identification of the impingement event is quite easy when the rate of temperature change is analyzed. The benefit of analyzing the data using this technique shows up in specific cases where impingement might be more difficult to identify in the original temperature trace.

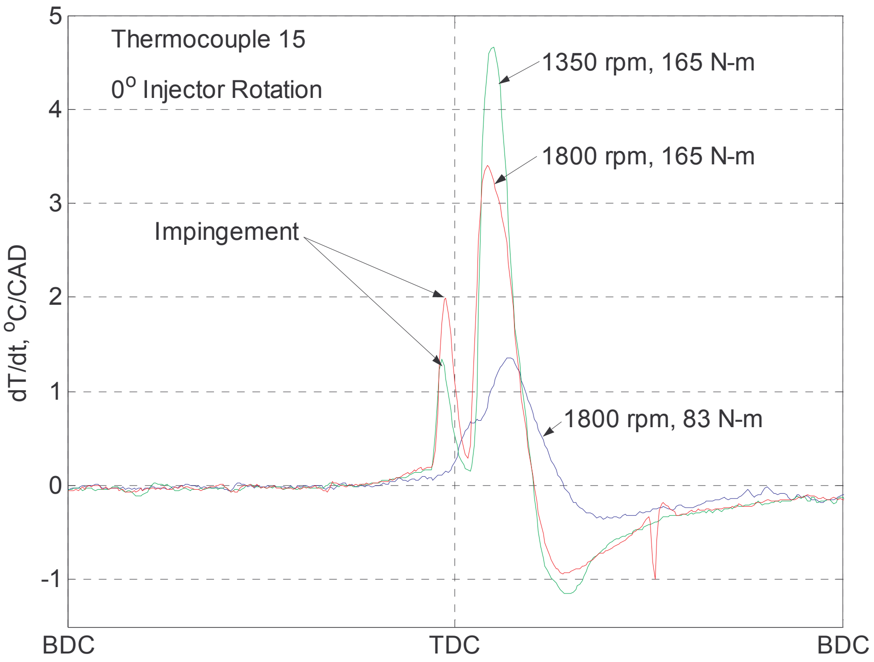

Figure 1.2.54: dT/dt identifies impingement at 1800 rpm/165 N-m load and 1350 rpm/165 N-m load: thermocouple 15, 0° injector rotation.

1.2.14 Characterization of Impingement Results

The technique of computing the rate of change of surface temperature vs. crank angle position appears to be very effective at identifying impingement in the temperature data. Because of this desirable characteristic, it was used as a visual tool to determine when impingement existed at each test condition. This allowed the separation of all the temperature data into two groups; those operating conditions with impingement and those without.

Previously, Figure 1.2.52 identified the strong dependence of the impingement location on injector orientation for the temperature versus CAD plots. Similar results were obtained for the rate of change of surface temperature, as expected. The 0° and 30° injector rotations are plotted for constant load and speed in Figure 1.2.55. From the figure it is observed that impingement occurs when the injector is in the 0° position, but does not occur when the injector is rotated 30°. Both test conditions use thermocouple 15 temperature data.

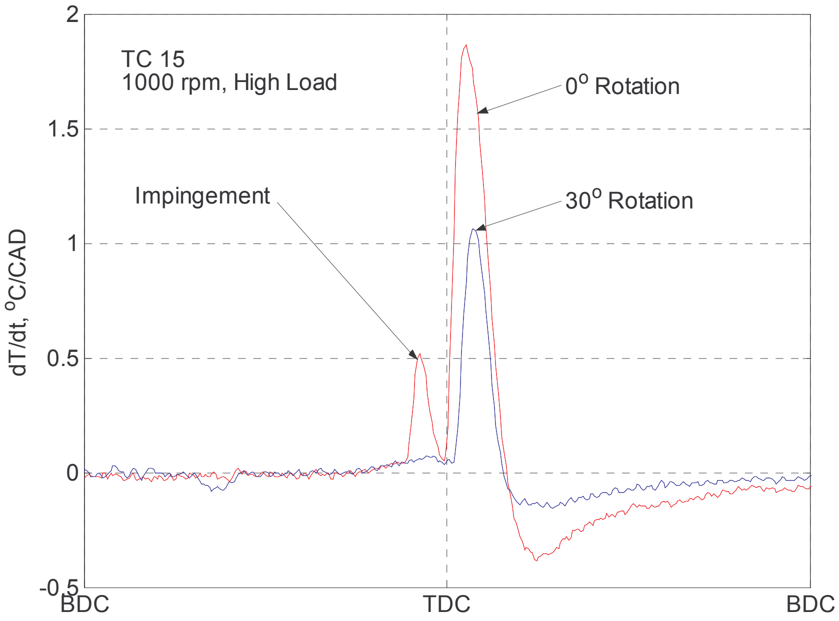

Figure 1.2.55: dT/dt for thermocouple 15 identifies impingement when the injector is at 0° rotation and does not identify it when the injector is at 30°.

When thermocouple 14 is observed, Figure 1.2.56, impingement occurs when the injector is rotated 30° and does not occur at 0° rotation. This verifies the dependence of impingement on injector location.

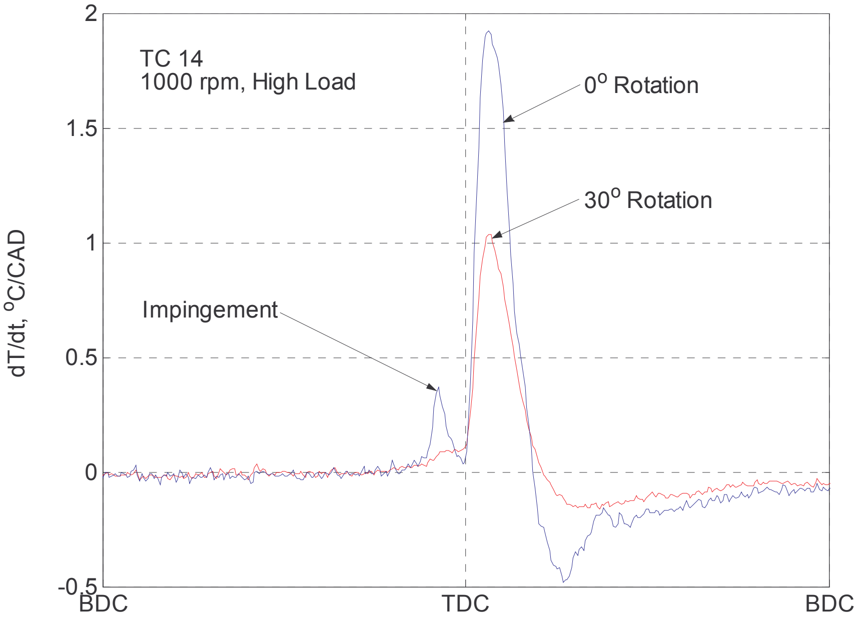

Figure 1.2.56: dT/dt for thermocouple 14 which shows no impingement when the injector is at 0° rotation and shows impingement when the injector is 30° rotated.

The data was categorized into impinging and non-impinging conditions by recording the magnitude of dT/dt at the impingement point, as shown in 1.2.57. The crank angle position at the maximum impingement value varied slightly for each operating condition. The peak value of the impingement signature, relative to zero, was recorded for all test conditions. A threshold value of 0.1 °C/CAD was used to separate impinging and non-impinging conditions. The maximum value of peak impingement was 0.8.

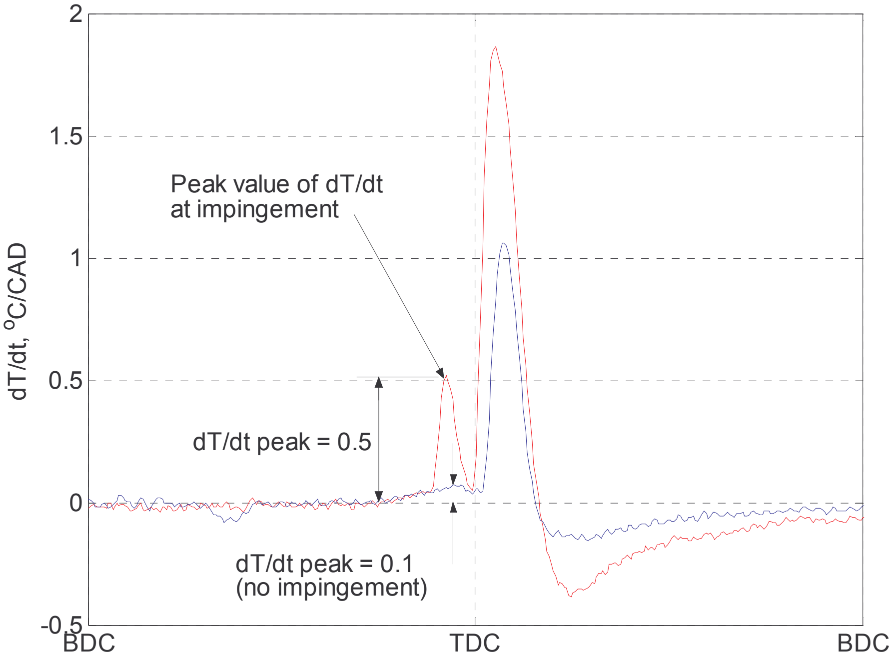

Figure 1.2.57: Explanation of impingement signature amplitude.

Plotting the magnitude of dT/dt peak versus engine speed for low, medium and high load cases, Figure 1.2.58, reveals two characteristics of the impingement signature. First, as engine speed rises above approximately 1800 rpm, impingement is no longer identified on the piston surface. Second, as engine load is increased, at constant engine speed, the magnitude of the impingement signature, in general, increases. The unexpected trend is the decrease in the magnitude of the impingement signal from a medium to a high load condition. This trend can be explained through the fuel injection scheme. At high loads above 1800 rpm, the pilot injection event is eliminated and only one, main injection event is utilized for fuel delivery. This eliminates the pilot combustion event and thus eliminates the piston surface impingement.

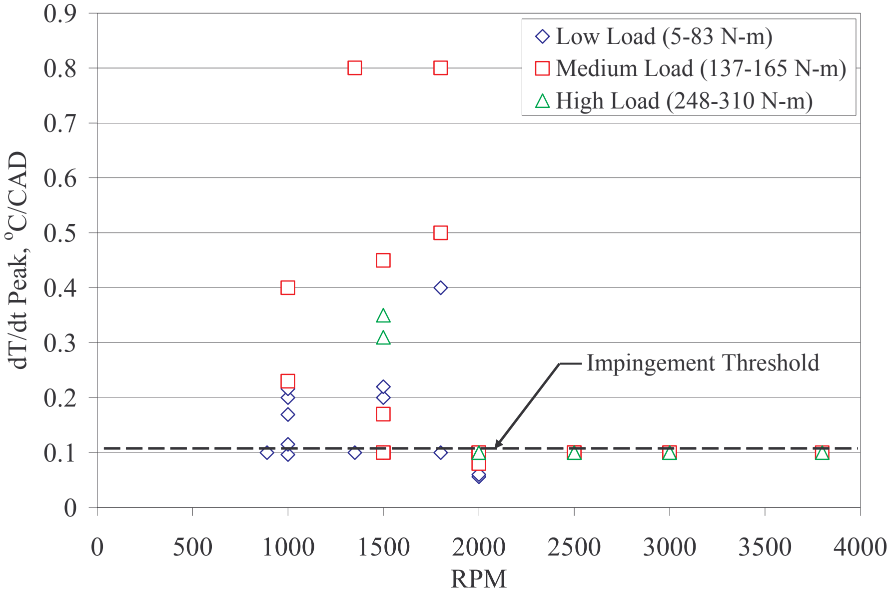

Figure 1.2.58: dT/dt peak vs. RPM for low, medium and high loads, showing dependency of impingement on speed.

Plotting dT/dt peak versus engine load for multiple engine speeds reveals a similar trend as observed above. Figure 1.2.59 shows that as engine load is increased at a given speed, the impingement signature increases in magnitude, except for cases above 1800 rpm. Note that while testing was conducted up to 3800 rpm, no impingement signature was identified above 1800 rpm, thus this data is not included in the plots.

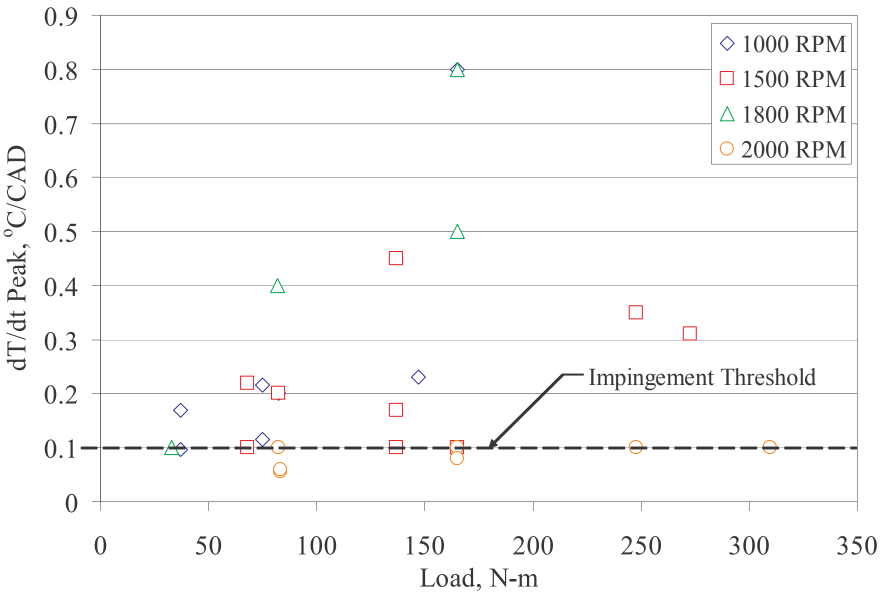

Figure 1.2.59: dT/dt signature vs. Load for 1000, 1500, 1800, 2000 RPM.

It is revealing to plot all of the test condition results on load versus rpm axis'. Figure 1.2.60 shows a very distinct transition between impinging and non-impinging data. The effect of engine speed appears to be a more significant factor compared to engine load in determining whether or not impingement occurs. However, before these trends are analyzed, an analysis to determine whether liquid spray or burning droplets are contacting the piston surface will be conducted.

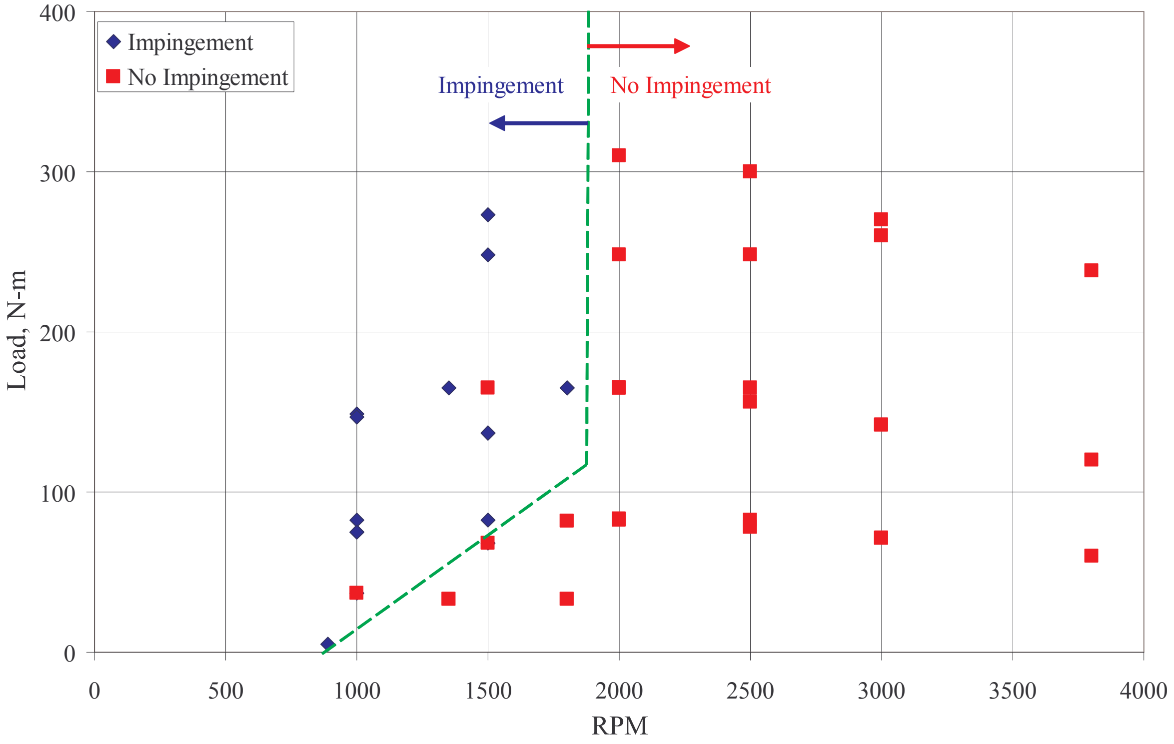

Figure 1.2.60: Load vs. rpm for impinging and non-impinging conditions.

1.2.15 Determination of Liquid or Flame Impingement

The determination of whether liquid spray or burning droplets are impinging on the piston surface begins with a heat release analysis. From the heat release analysis, the start of combustion can be determined. Knowing the pilot start of injection and start of combustion timing, a good estimation of liquid versus burning droplet impingement can be made.

1.2.15.1 Rate of Heat Release Study

The heat release analysis requires accurate cylinder pressure and cylinder volume data, along with their corresponding derivatives. A typical fired cylinder pressure trace is shown in Figure 1.2.61. Cylinder volume was calculated using an analytical model of the engine, developed in Matlab. The results are shown in Figure 1.2.62.

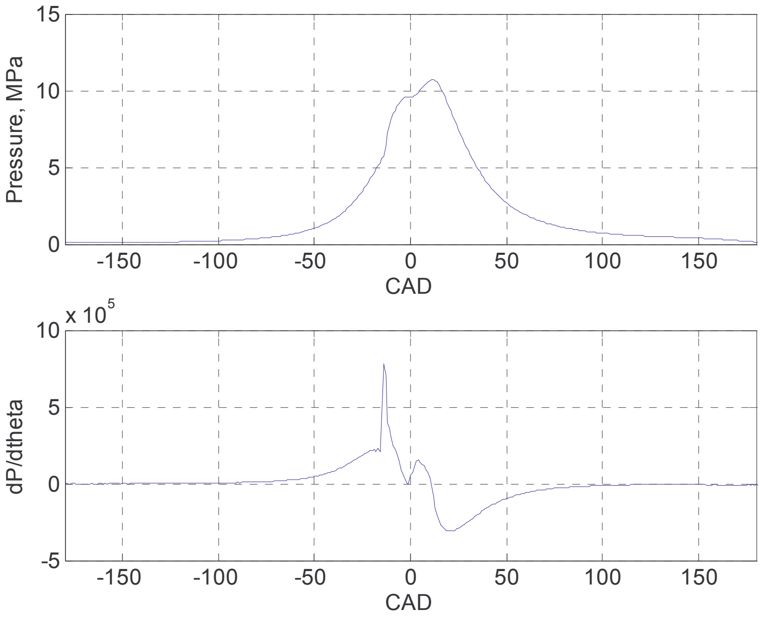

Figure 1.2.61: Fired cylinder pressure and corresponding rate of change of cylinder pressure for 1800 rpm/165 N-m load.

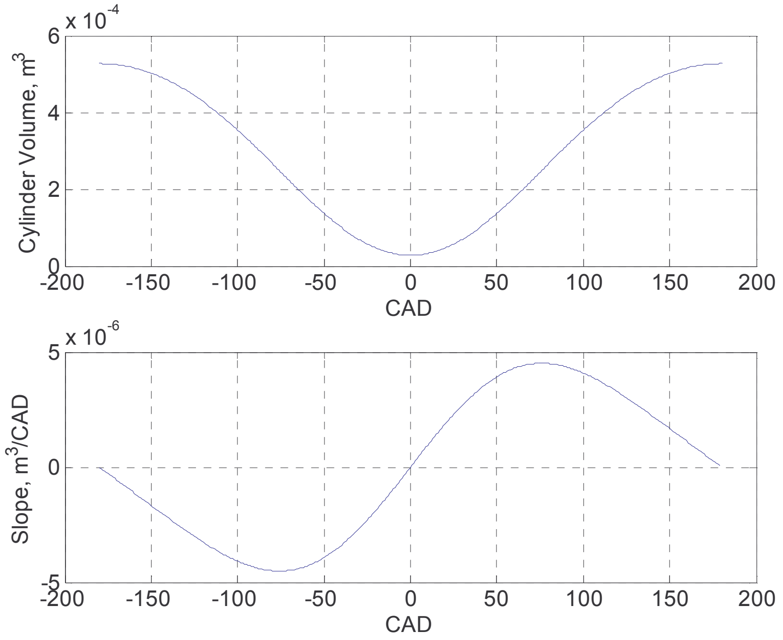

Figure 1.2.62: Cylinder volume and rate of change of cylinder volume versus CAD.

The apparent net heat release rate was calculated using a first law analysis, neglecting cylinder heat transfer and crevice volume effects. The resulting expression is shown in Equation 1.2.13.

$$\frac{dQ_n}{d\theta} = \frac{k}{k-1} \cdot P(\theta) \cdot \frac{dV(\theta)}{d\theta} + \frac{1}{k-1} \cdot V(\theta) \cdot \frac{dP(\theta)}{d\theta}$$

Equation 1.2.13

The apparent net heat release rate and corresponding injector pulse, for 1800 rpm and 165 N-m are shown in Figure 1.2.63. The expected pre-mixed combustion followed by the diffusion controlled combustion is clearly identified. Notice the early start of combustion, due to the pilot injection event in this particular case.

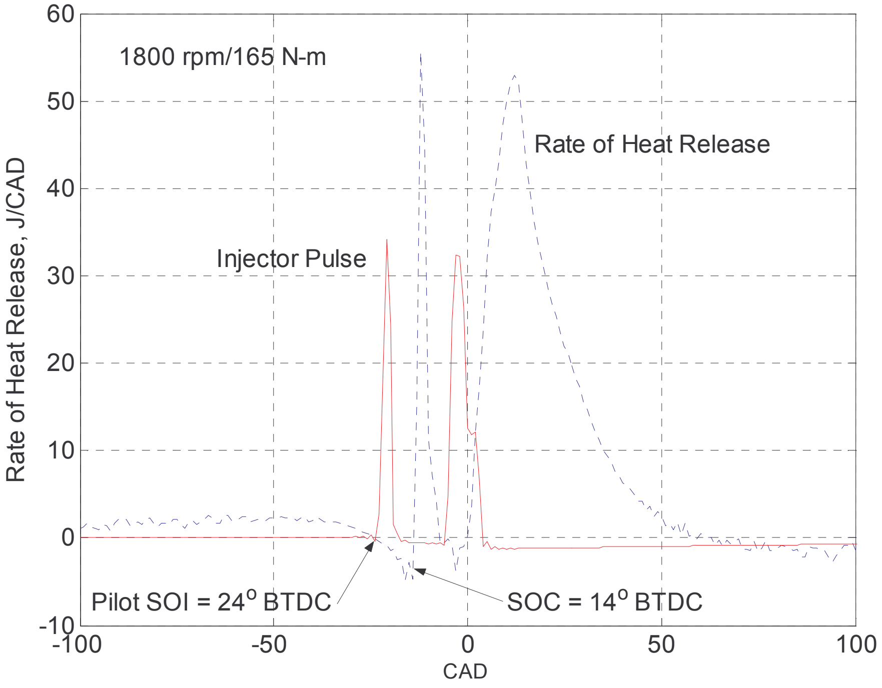

Figure 1.2.63: Rate of heat release and injection pulse signal, 1800 rpm, 165 N-m load.

For the 1800 rpm, 165 N-m case, the start of injection occurs 24° BTDC and the start of combustion occurs 14° BTDC. This corresponds to an ignition delay of approximately 1ms, which is consistent with typical published values. From Figure 1.2.49, it was identified that the temperature of the piston surface at thermocouple 15 did not record the impingement event until almost TDC. With combustion beginning 14° before the surface temperature records the impingement phenomena, the researcher's believe the identified signature is an impinging, burning spray instead of impinging liquid droplets.

If liquid impingement is occurring on the piston surface, the thermocouples closer to the center of the piston, 1, 2, 3 or 4 Figure 1.2.10, would record the event, as identified by Werlberger and Cartellieri (1987). They used an endoscope to view the fuel impingement and combustion events in a high speed diesel engine. Fuel impinged on the center of the piston while the start of combustion occurred farther down in the piston bowl. Initial investigations have produced no noticeable signal due to spray impingement at these locations in the current study.

1.2.16 Effect of Engine Speed and Pilot Timing on Impingement Trend

As engine speed is increased, in-cylinder turbulence is proportionally increased. This increase in turbulence reduces the localized effect of the combusting spray. The combustion event is spread-out over the piston surface. Additionally, as speed increases, the start of injection timing for the pilot injection is advanced, as shown in Figure 1.2.64. The advance in timing increases the distance from the injector tip to the piston surface by 32%, as shown in Figure 1.2.65. This effectively reduces the localized effect of the combusting spray. These two effects minimize the flame impingement event and thus it is not identifiable above 1800 rpm.

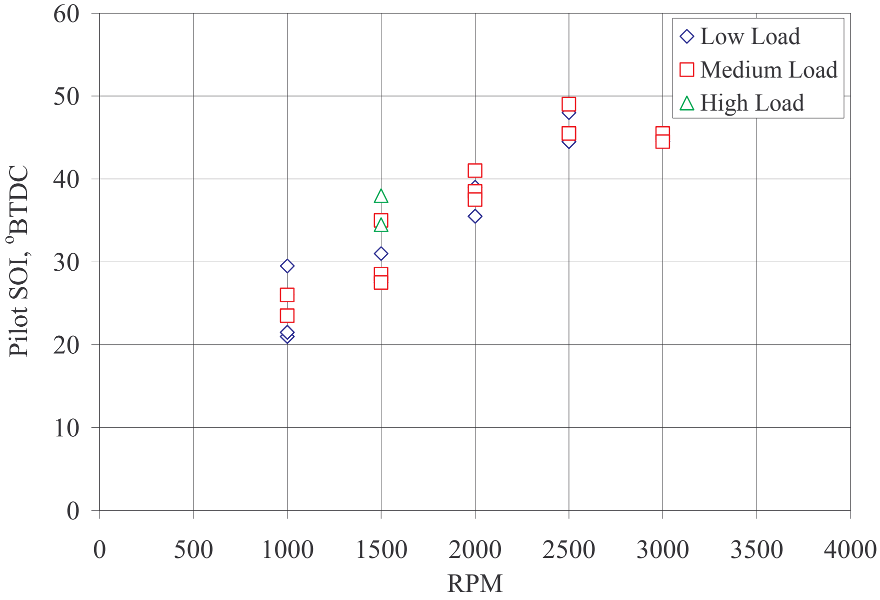

Figure 1.2.64: Change in Pilot SOI vs. RPM for low, medium and high load.

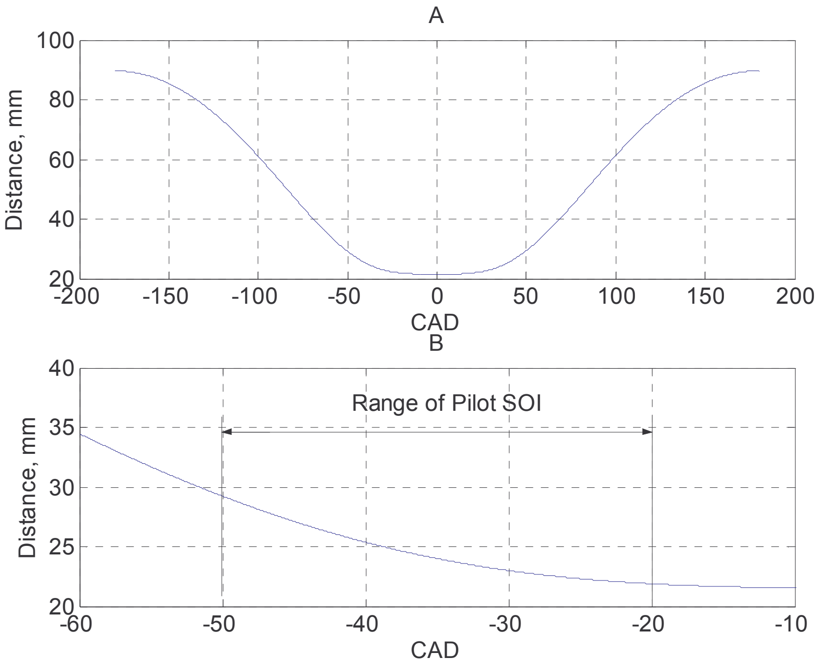

Figure 1.2.65: Distance from injector tip to piston bowl lip, mm.

1.2.17 Effect of Engine Load on Impingement Trend – Low Speed

The effect of engine load on the impingement signature at low engine speeds (less than 1800 rpm), is explained through the fuel rail pressure. As expected, fuel rail pressure increases with increasing load, as shown in Figure 1.2.66. Pressure increases 300% over the operating range of the engine. The increased fuel pressure directly increases the quantity of fuel delivered to the combustion chamber. Increased quantity of fuel leads to more flame impingement on the piston bowl lip and thus a larger impingement signature.

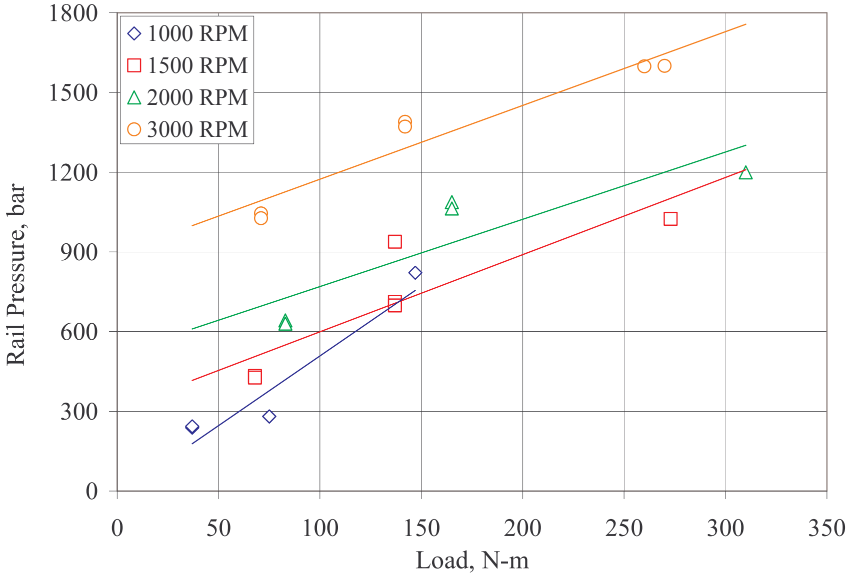

Figure 1.2.66: Rail pressure vs. Load for 1000, 1500, 2000 and 3000 rpm.

1.2.18 Conclusions

1.2.18.1 Thermal Loading

- Analytical and FE models were developed to calculate the steady state and transient heat transfers through the piston and successful results are obtained.
- Piston surface heat transfer was shown to behave as a semi-infinite heat transfer surface, but semi-infinite results need to be corrected by superimposing the time averaged heat fluxes.
- The significant frequencies that make up the transient temperature trace at the surface are related to engine speed. These frequencies do not exceed 800 Hz (30th order).
- Time averaged heat flux over the piston surface is a strong function of both speed and load.
- Peak transient heat flux is a strong function of load and a moderate function of speed.
- Highest transient heat flux peaks are observed around the thermocouples that have the largest sweeps. The highest time averaged heat fluxes are observed around the thermocouples with highest time averaged temperature readings.
- Heat transfer occurs from the piston bowl to the oil gallery, as expected. Additionally, heat transfer from the oil gallery to the ring area of the piston also occurs. This reduces the net heat transfer to the oil gallery.

1.2.18.2 Spray Impingement

- The identification of impingement on the piston surface has been accomplished through the use of fast response surface thermocouples.
- The effect can be observed in the piston surface temperature vs. crank angle degree trace, which has not previously been noted in the literature.
- The signature is highly localized on the piston surface and can cause significant temperature gradients across the piston surface.
- The impingement characteristics are highly circumferentially sensitive on the piston bowl lip. An angular displacement of 30° results in a surface temperature change of 15°C.
- The rate of change of piston surface temperature versus CAD is an effective, sensitive technique useful for identifying impingement.
- As engine speed was increased above 1800 rpm, the impingement signature was not identified.
- At engine speeds less than 1800 rpm, the signature was noticeable across a wide range of loads.
- A combination of larger distances between the injector tip to piston bowl lip (advanced pilot timing) and increased turbulence may explain the reduction in impingement signal, as engine speed increases.
- As load was increased at constant engine speed, the impingement event was shown to increase, due to an increase in fuel rail pressure and thus the quantity of delivered fuel.

- The circumferential temperature gradients that were identified on the piston surface cause concern over applying a single valued convective heat transfer coefficient for the piston surface.

1.2.19 Future Recommendations

1.2.19.1 Thermal Loading

Piston heat transfer depends also on circumferential location. Experimental work with more surface thermocouples would reveal improved overall surface heat flux information. These results would help better compare the fuel energy with the overall heat transfer into the piston. Thermodynamic cycle analysis of the combustion would reveal information about heat release and thus the combustion efficiency of fuel. Such a study would also help in estimating gas temperature and thus yielding the convective heat transfer coefficients at different locations over the piston surface. Dimensional analysis would provide a tool to correlate this information with different engine geometries.

1.2.19.2 Impingement

The clear dependence of the impingement signature on engine operating parameters suggests the possibility of developing a dimensionless number for predicting flame impingement. The analysis would use current research data as well as existing impingement data from previous studies in the literature. Correlating the conditions under which impingement occurs could then be scaled to larger bore engines.

Spray and flame impingement are active areas of research in engine modeling codes. Sophisticated sub-models are being created to accurately model wall heat transfer, drop/drop interaction, collisions, and post-impingement droplet behavior. Correlating the current impingement data from the 2.0L high speed diesel research engine with UW Madison computer models would be valuable for both programs.

1.2.20 References

1. Heywood, Internal Combustion Engines, McGraw Hill 1988.
2. Woschni G.A., Universally Applicable Equation for the Instantaneous Heat Transfer Coefficient in the internal combustion engine, SAE Technical Paper Series, 1967.
3. Kleeman A. P. & Gosman A. D., Heat transfer sensitivity Study for an Anvanced Diesel Engine, 2003-01-0561, SAE 2003.
4. Meingast U., Reichelt L., Renz U., Measuring Transient Wall Heat Flux under Diesel Engine Conditions, 2001.
5. Arpaci V., Conduction Heat Transfer, 1966.
6. IR Telemetrics, www.irtelemetrics.com, 2003.
7. Werlberger, P., Cartellieri, W.P., Fuel Injection and Combustion Phenomena in a High Speed DI Diesel Engine Observed by Means of Endoscopic High Speed Photography. SAE Technical Paper 870097, pp 1-11, 1987.
8. Wolf, R.S., Cheng, W.K., Heat Transfer Characteristics of Impinging Diesel Sprays. SAE Technical Paper 890439, 1989.

1.3 Transient Engine Experiments – Cavity Ringdown Spectroscopy for Soot Measurement

1.3.1 Introduction

Engine-out emissions can be used as indicators of combustion behavior in an engine as well as being used in their own right as measures of engine exhaust signature and compliance with relevant regulations. For transient engine experiments to be really useful, transient emission measurements are necessary. Commercial devices are available to measure HC and NOx with small time constants (~ 2 ms), but similar measures for particulates are not available. This project is aimed at developing a method for high speed particulate measurement, with possible extension to other engine out constituents.

The method under investigation is Cavity Ring-Down Spectroscopy (CRDS), which is a method employing light absorption in a multipass optical cell. The unique feature of CRDS is that the actual measurement is not total attenuation, but the rate of change of attenuation as a laser pulse is multi-passed through the cell and gradually decays due to absorption. A schematic of a simple CRDS system is shown in Figure 1.3.1.

Principle (empty cavity)

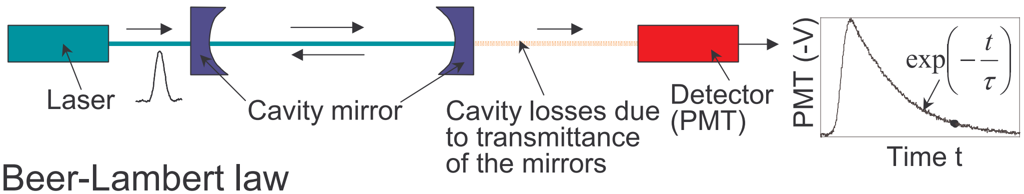

Beer-Lambert law

$$I_t = I_0 \cdot \exp(-\sigma \cdot L \cdot N) = I_0 \cdot \exp(-k \cdot L)$$

Decay time of laser light (Cavity-Ringdown time:τ)

$$i_t = i_0 \cdot \exp\left[-\left(\frac{number\ of\ reflections}{round\ trip}\right)\cdot\left(\frac{loss}{reflection}\right)\cdot(number\ of\ round\ trips)\right]$$

$$i_t = i_0 \cdot \exp\left\{-[(1-R)+k_{Gas}L]\cdot\left(\frac{t\cdot c}{L}\right)\right\} \qquad PMT\ signal = A\cdot\exp\left(-\frac{t}{\tau}\right)$$

Absorption coefficient in an empty cavity

$$k_{Gas}L = \frac{L}{\tau\cdot c} - (1-R)$$

Figure 1.3.1. Schematic of CRDS system.

The system was developed using an injection-seeded Nd:YAG laser at 532 nm and has been tested on gases at various pressures (molecular number densities) and on a particulate solid used as an analog for particulate exhaust matter. Currently, we use a pulsed DPSS system similar to the IS Nd:YAG system, except the light source has a much higher rep rate (2 kHz vs 10 Hz), lower power (1 mJ vs 180 mJ), and is much smaller (laser + power supply is about 150 mm x 150 mm x 150mm vs 2 m x 0.5 m x 1m). This last system proved to be successful and will be pursued into the engine installation. A schematic of the DPSS system is shown in fig. 1.3.2.

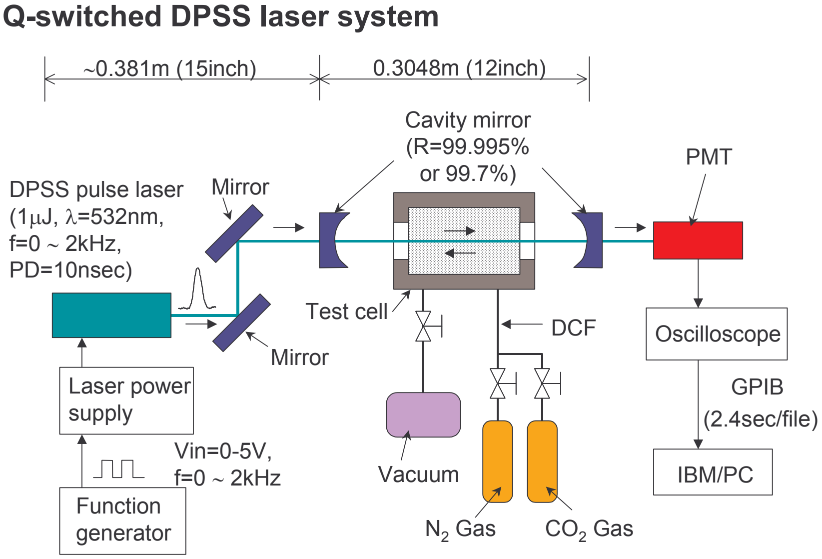

Figure 1.3.2. DPSS configuration for CRDS system

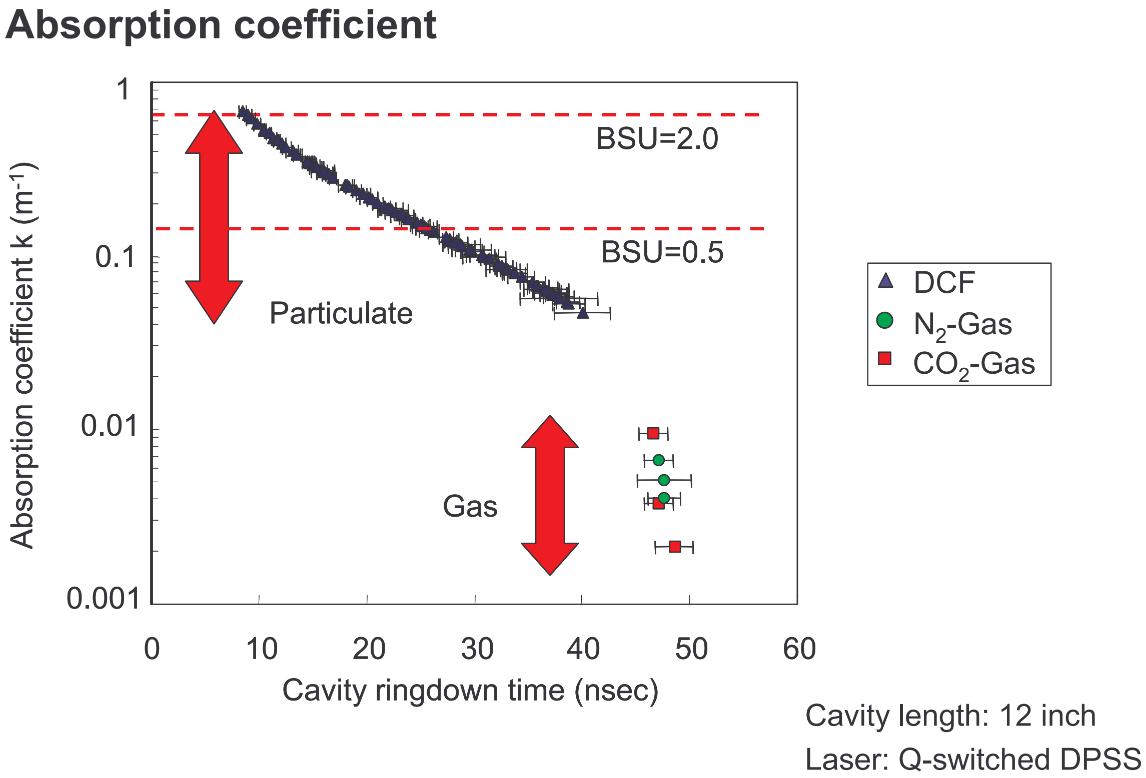

Figure 1.3.3. Absorption measurements using CRDS for DCF and several gases

Figure 1.3.3 shows a sample correlation of DCF weight as a function of ring down time. This type of correlation will be needed to calibrate the ring down time system for soot measurements. As several steady state particulate measurement systems are available in our lab for comparison, we will be able to generate correlations similar to that shown in fig. 1.3.3 for the CRDS system with soot and other engine-generated particulates.

One of goals for this project was to apply P-CRDS to detect small concentrations of particles within a short period of time. We desired to obtain the cavity ringdown time constant, τ, of the testing species after few shots of laser pulses. As a result, shot-to-shot repeatability of the ringdown time constant, τ, and resolution of the decay trace were two concerns throughout the experiments.

Several issues affecting shot-to-shot repeatability include:

1. Optical feedback form cavity to laser source;
2. Mode matching of laser to cavity;
3. Transverse mode excitation;
4. Overall beam shape.

These issues are addressed in the following sections, but even with the results of that effort, we needed to develop tools for filtering mode-matched pulses and ringdown times fro non-mode-matched pulses.

1.3.2 Optical Feedback and Decay Trace Stability

Initially, we constructed a simple optical cavity with a pulsed laser source, which is shown in Figure 1.3.2. The Q-switched diode pumped solid-state green laser system laser was set 38 cm away from the optical cavity and was triggered internally at 2 kHz. Two ultra high reflectivity mirrors, R=99.995%, were used to construct the optical cavity and its cavity length is 45 cm. A photomultiplier tube (PMT) was placed after the cavity to detect the light intensity and transfer the electric signal to the digital oscilloscope, TDS-380.

Eight decay traces plotted as intensity vs. time graph is shown in Figure 1.3.4. The decay trace varies from shot-to-shot. The peak voltage of the traces varies from 0.377 volts to 0.225 volts. After fitting with a least squares curve, the ringdown time constant, τ, for the trace with the highest peak volts is 215.78 ns and τ for the trace with the lowest peak volts is 224.52 ns. The decay trace was also measured with other two settings. One is the cavity with a 30 cm cavity length. The other one is the test cell with W1 windows placed within the 30 cm long cavity. The ringdown time constant, τ, for the 30 cm-long cavity is 145.9 ns and for the test cell (with windows) placed within the cavity is 49.56 ns.

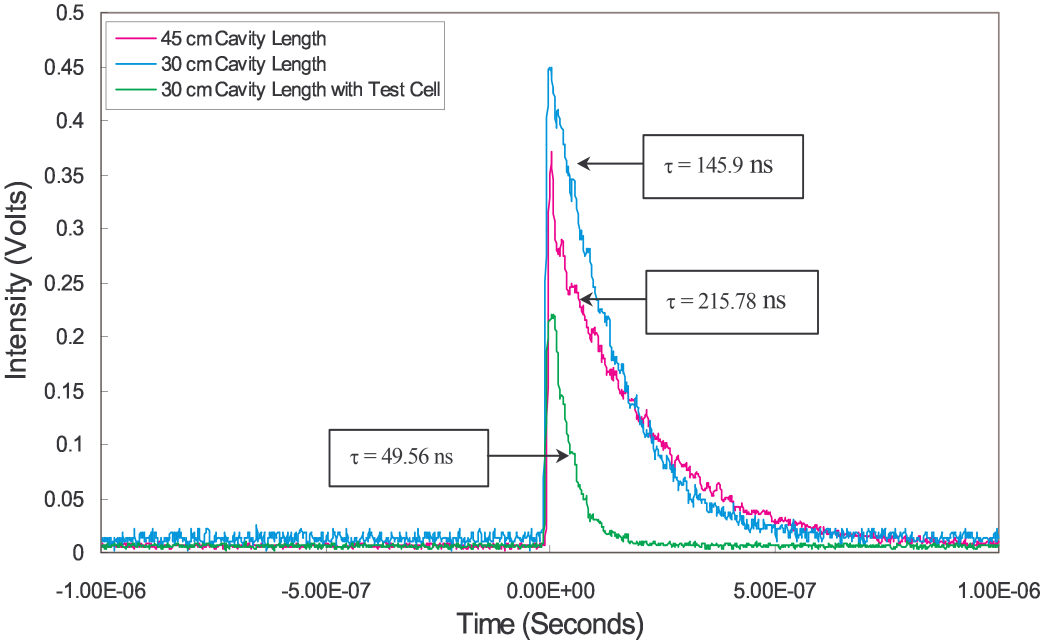

Figure 1.3.4. Decay traces plotted as intensity vs. time from the simple cavities with different setups

By comparing τ of the trace with the highest intensity from each setting, τ for the 45 cm-long cavity, 215.78 ns, is longer than τ for the 30 cm-long cavity, 145.9 ns.

The ringdown time is estimated as

$$\tau = \frac{1}{\left[2\alpha_{window}s + 4r_{window} + (1-R) + \alpha(L' - 2s)\right]}\left(\frac{L}{c}\right)$$

it is relevant that τ is increased as the cavity length, L, is getting longer. Furthermore, with the same 30 cm cavity length, τ for the test cell placed within the cavity is 49.56 ns, which is much shorter than the cavity without the test cell, 145.9 ns. The absorption and reflections of the windows contribute as $2\alpha_{window}s + 4r_{window}$ which can lower down τ value as existing in the denominator of the equation.

1.3.2.1 Cavity with Distant Laser Source

Optical feedback from the cavity and backscattering of stray light into the laser source may affect the decay trace stability. This feedback can cause signal amplitude fluctuation, frequency shift and noise.

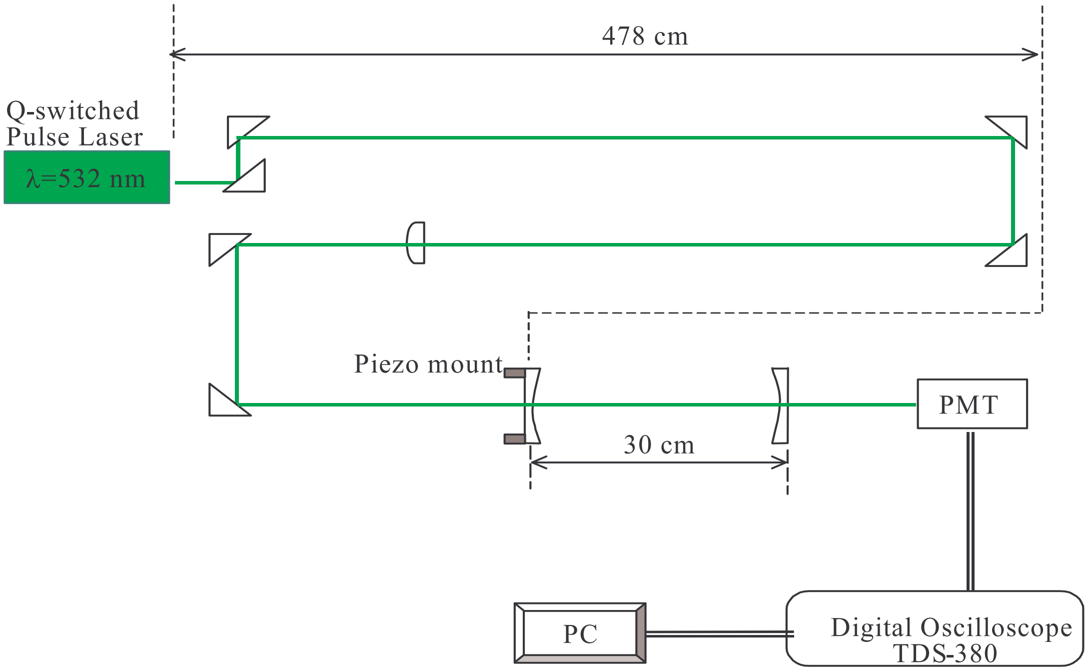

Figure 1.3.5. Schematic diagram of the P-CRD system with the laser source 478 cm away from the cavity

A method to eliminate such feedback is to separate the laser source far from the cavity. By setting enough distance between the laser source and the cavity mirror, the light beam does not have sufficient time to travel the separated distance when reflecting back from the ultra high reflective mirror down to the laser source within the pulse duration period.

The pulse duration for this Q-switched diode pumped solid state green laser system is less than 15 ns. Within the laser pulse duration, 15 ns, the beam travels distance 4.497 m. As a result, if the laser is set more than 4.497 m away from the optical mirrors, after starting the pulse, the reflecting beam from the mirror will not finish traveling 4.497 m back to the laser source before the end of the pulse. As a result, this setting can eliminate the feedback.

We constructed a new experiment of the P-CRD system, which is shown Figure 1.3.5. The laser source was set 478 cm away from the first mirror of the cavity.

One hundred decay traces were collected and recorded. The peak intensity and the ringdown time constant, τ, of all decay traces were exported from a LABVIEW 6 program and processed as EXCEL files, which is illustrated as intensity vs. sample count and τ vs. sample count in Figure 1.3.6. The ringdown time constant, τ, of each trace is plotted as the pink color line and its variation is from 985 ns to 4333 ns. It is obvious that shot-to-shot variation is still substantial in these results. In this new experimental setup, the laser source was placed 478 cm away from the cavity. The laser beam may take 16 ns to travel back to the laser source from the cavity mirrors. Since the laser pulse duration is less than 15 ns, we expect the reflecting beam from the mirror will not have enough time to travel back to the laser source before the end of the pulse duration to cause any feedback. Thus, amplitude fluctuation of the decay trace caused by the feedback should be eliminated. Shot-to-shot variation of decay traces is still observed in this new experiment setup, suggesting feedback is not the source of the variation.

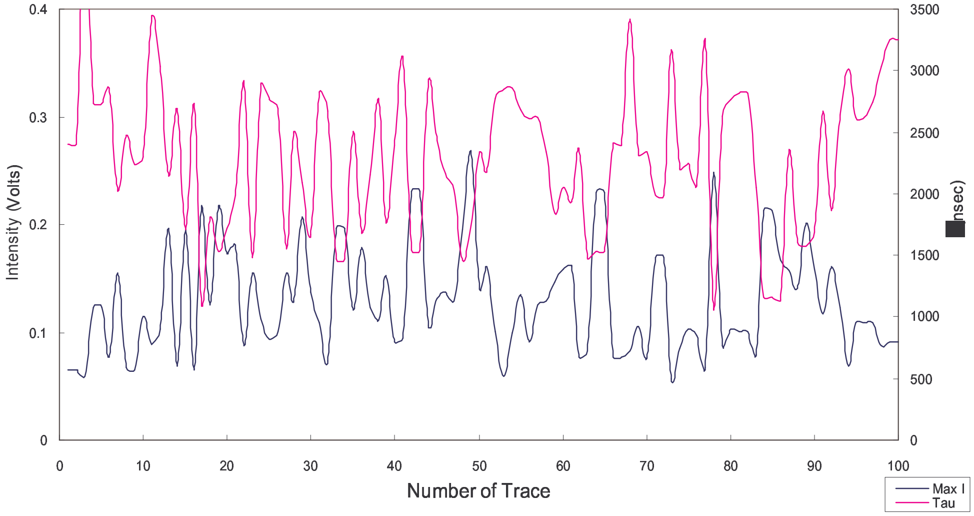

Figure 1.3.6. The peak intensity and the ringdown constant, τ, from the 30 cm length cavity with laser source 478 cm away from the cavity

1.3.2.2 Conclusions for Feedback

In this section, we verified that the ringdown time constant, τ, obtained from simple cavities corresponded to theoretical calculations. Since shot-to-shot variation of the decay trace was observed in results, we suspected that one of its causes was optical feedback. Consequently, the laser source was set 478 cm away from the cavity and the beam reflected by the cavity mirror cannot travel far enough back to the laser source before the end of its pulse duration to cause the optical feedback. However, amplitude fluctuation for the peak intensity and τ recorded in Figure 1.3.6 were apparent. As a result, we confirmed that optical feedback was not the main issue causing shot-to-shot variations of the decay trace.

1.3.3 Cavity Modes Characteristics

In this section, a scanning cavity synchronized with the laser pulse was constructed to verify mode characteristics.

1.3.3.1 Cavity Scanning

For small changes in the cavity length, an optical cavity can be tuned to the axial-mode resonant frequencies. Therefore, altering the cavity length by one half-wavelength, either shortened or lengthened, $\pm \lambda/2$, can shift each of the axial modes. In scanning the cavity, a strong optical signal will be transmitted through the cavity each time as one of its axial-mode resonances coincides with an input laser signal. A decay trace with the high peak intensity will appear as one of the cavity mirrors is moved through 266 nm.

Based on the experiment setup a function generator was coupled with a piezo-driver for moving one of the cavity mirrors. With output of a ramp waveform from the function generator, the cavity mirror mounted on the piezo mount can be moved back and forth in the cavity axial direction as scanning the cavity.

For further investigations of modal phenomenon, as shown in Figure 1.3.7, we integrated the function generator with a digital delay generator to trigger the laser source. This allowed synchronization of the laser pulse with cavity scanning. With control of a delay, the laser pulse could be delayed for a specific time after starting cavity scanning. Through such a setting, the laser would be triggered after the mirror has been moved a specific distance allowing for phase matching of the laser pulse and the cavity mode.

The ramp waveform frequency was 2 Hz, the mirror needed 500 ms to finish one scanning displacement, 1417 nm. Thus, the mirror scanning speed was 2.83 nm/ms. In this experiment, an axial-mode interval, $\lambda/2$, is 266 nm and the mirror may take 79.85 ms to finish scanning one axial-mode interval.

We selected 10 ms as a delay step to trigger the laser pulse after starting the cavity scan. There would be 50 steps to cover one scanning cycle, which was 500 ms. Thus, in terms of cavity length, modal phenomenon would be investigated in 50 different sizes of cavities. We expected to observe resonant axial mode phenomenon, which would be decay traces with highest peak intensity, somewhere in delay range of the laser pulse every 80 ms. Modal phenomenon should be found at 6 of the delay steps since 6 axial mode intervals will fit in 1417 nm scanning distance. The time interval between each resonant axial modes phenomenon step should be about 80 ms.

Figure 1.3.7 shows the peak intensity and the ringdown time constant, τ , of one hundred decay traces recorded by the LABVIEW 6 program from two of the tiem delay measurements the laser pulse delayed 230 ms and the laser pulse delayed 260 ms. The peak intensity is illustrated as the blue color trace and the ringdown time constant, τ , is illustrated as the pink color trace. By selecting 0.25 volts as the threshold for the peak intensity, it is obvious that more data points are above 0.25 volts for the laser pulse delay of 230 ms than the laser pulse delayed of 260 ms. If the peak intensity of a decay trace from the resonant axial modes cavity were above 0.25 Volts, the cavity length as the laser pulse is delayed of 230 ms corresponds to an integral number of axial-mode interval. By investigating all fifty measurements, a similar phenomenon is also observed as the laser pulse delays of 60 ms, 150 ms, 240 ms, 290 ms, 380 ms and 450 ms and the interval among these is 90 ms, 80 ms, 60 ms, 90 ms and 70 ms respectively. By converting each interval to the mirror scanning displacement, the mirror scanning speed is 2.83 nm/ms, the interval to in nm is 254.7 nm, 254.7 nm, 141.5 nm, 254.7 nm and 198.1 nm. By taking the measurement for the laser pulse delay of 60 ms as a reference, and based on a calculated interval as delay of the laser pulse every 80 ms, the resonant axial mode phenomenon should be observed as the laser pulse was delayed 60 ms, 150 ms, 230 ms, 310 ms 390 ms, and 470 ms. These results are listed in Table 1.3.2 for comparison.

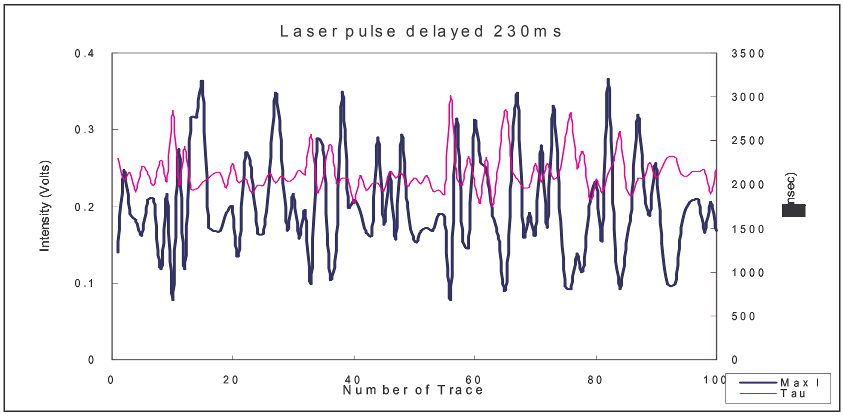

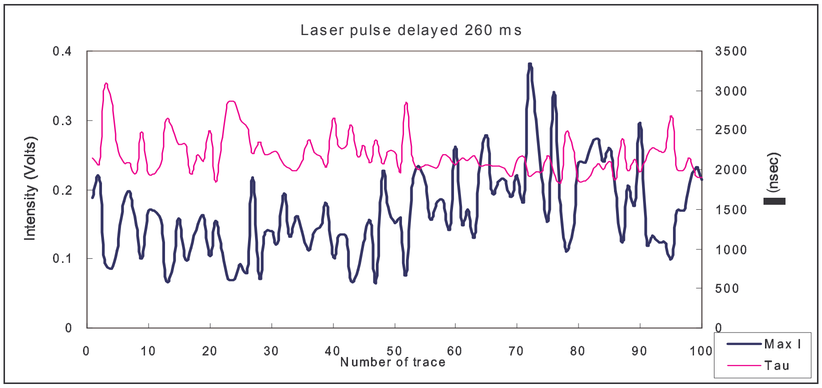

Figure 1.3.7. Modes phenomenon comparisons in two measurements as delay of the laser pulse of 230 ms and 260 ms.

Table 1.3.2. **Resonant axial modes phenomenon measurements from experimental data and calculated data**

Apparent axial mode	1st	2nd	3rd	4th	5th	6th
Experiment delay time	60ms	150 ms	240 ms	290 ms	380 ms	450 ms
Experiment intervals	254.7 nm	254.7 nm	141.5 nm	254.7 nm	198.1 nm	
Calculated delay time	60 ms	150 ms	230 ms	310 ms	390 ms	470 ms
Calculated intervals	226 nm	226 nm	226 nm	226 nm	226 nm	

1.3.3.2 Conclusions for Cavity Mode Experiments

The initial evidence of the cavity modal characteristics is the intensity of the beam output from the cavity altered repeatedly from low to high corresponding to the mirror scanning as the cavity is scanned by one mirror. Furthermore, by synchronizing the cavity scanning with the laser pulse, modal phenomenon was observed in six measurements, which corresponds to six axial-mode intervals that can be fit within the scanning displacement. These results are valuable and important as mode characteristics are observed in the 30 cm long cavity.

1.3.4 Mode Matching Optimization

Any slight misalignment of the cavity mirrors may cause light traveling over slightly different off-axis optical paths and build up transverse modes. The excitation of transverse modes can reduce the transmitted light coupling in and out of the cavity, which also decreases the peak intensity of the decay trace. Furthermore, transverse modes can alter the shape of decay trace and affect the resolution of the P-CRDS. As a result, mode matching should be critical to reducing shot-to-shot variations of decay trace and improve the sensitivity the P-CRDS.

When a pinhole aperture is inserted behind the exit cavity mirror the transverse mode beating will be visible on the decay trace. Precise alignment should be performed to minimize the beat oscillation, and consequently reduce transverse mode excitiation.

For this application, a spatial filter assembly was placed after the laser source to remove spatial noise and produce a beam with a smooth intensity profile. This spatial filter assembly is composed of a 10× microscope objective and a 15 micron pinhole. A 5× microscope objective is used as a beam expander after the spatial filter assembly to collect and collimate the diverging beam with a constant beam radius. The position of the plano-convex lens with 1000 mm focal length placed before the cavity was adjusted to make its focal point at the center of the cavity. After finishing visual alignment of all optical devices with standard technique, an iris as the pinhole aperture was placed behind the exit cavity mirror to observe any transverse mode beating riding on the decay trace. The experiment setup is illustrated in Figure 1.3.8.

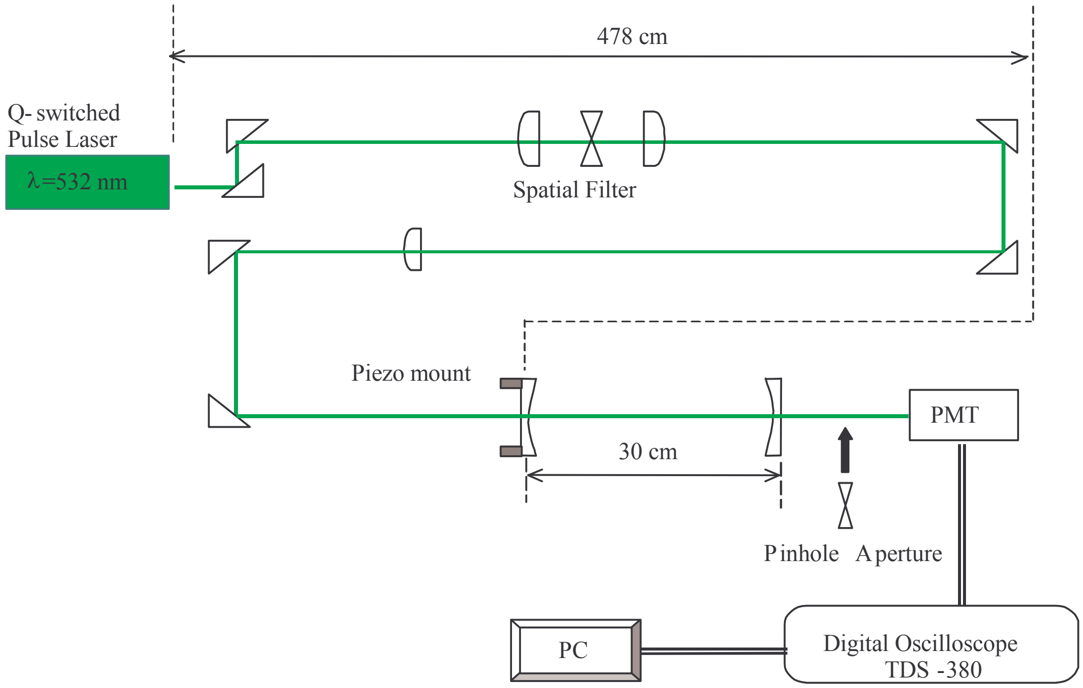

Figure 1.3.8. Schematic diagram of mode matching optimization by placing the pinhole aperture behind the cavity to minimize transverse mode beating.

Figure 1.3.9 shows two decay traces plotted as the intensity vs. time before and after mode matching optimization. After initial alignment was performed, a smooth single-exponential ringdown decay trace was observed, shown as Figure (a). As an iris was placed behind the cavity mirror, small oscillations were shown riding on the decay trace, especially at initial section of the decay trace illustrated in Figure 1.3.9 (b). It is apparent that the transverse mode beating is visible on the decay trace after a pinhole aperture is inserted behind the cavity.

We used the three-channel Piezo-driver, to fine-tune the cavity mirror to minimize oscillation. After the iris was removed, we did not observe any improvement of the ringdown time constant, τ . The shot-to-shot variation of decay trace was still evident, which may cover any improvement in ringdown times.

1.3.4.1 Mode Matching Optimization Conclusions

In the whole, the mode-matching optimization method utilized in the section was simple and inexpensive. The transverse mode beating due to imperfect alignment appeared on the decay trace after placing a pinhole aperture behind the cavity. However, the improvement of the ringdown time constant, τ , was not obvious after minimizing the transverse mode beating. We used this mode-matching optimization method as a technique to optimize the cavity alignment.

1.3.5 Beam Profile Analysis System Investigations

In this section, we used a beam profile analysis system, composed of a CCD camera, to investigate the beam profile at various locations, such as at laser source and after the spatial filter assembly, to check precision of alignment of optical devices.

1.3.5.1 Initial Investigation

The BeamProfiler system used in this research project was composed of a Cohu 4800 CCD camera, ATP-SM variable attenuator, Coherent BCUBE partially reflecting beam sampler and Photon Software..

A consistent attenuation technique is used throughout the whole measurements to

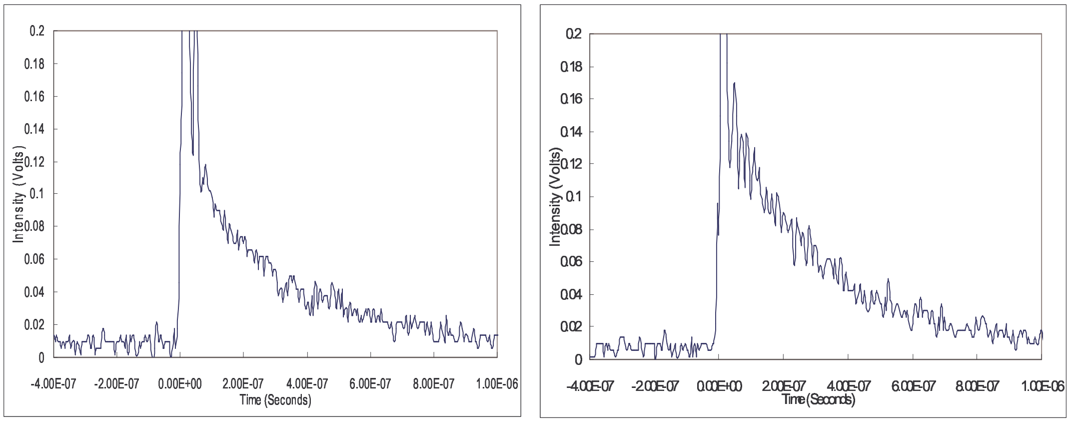

(a) **(b)**

Figure 1.3.9. Difference in decay trace measurement between (a) before placing an iris and (b) after inserting an iris behind the cavity

maximize the CCD dynamic range. That is to attenuate the beam by sliding two wedges on ATP-SM attenuator until the profile peaks are equal to 1 in the two intensity plots at the *Dual Aperture Profile* window and without any flat tops. A flat top intensity curve means a saturated beam, which is out of the CCD dynamic range and can damage the CCD camera.

The Photon BeamPro Analysis Software with *Live Video*, *3D Beam Contours*, *Dual Aperture Profile* and *Beam Statistics* were used to monitor the light beam and acquire the desired data, a sample of which is shown in Figure 1.3.10. The *Live Video* displays the beam image directly from the CCD camera. By observing the beam image in *Live Video*, the intensity and the intensity structure of the beam can be easily understood.

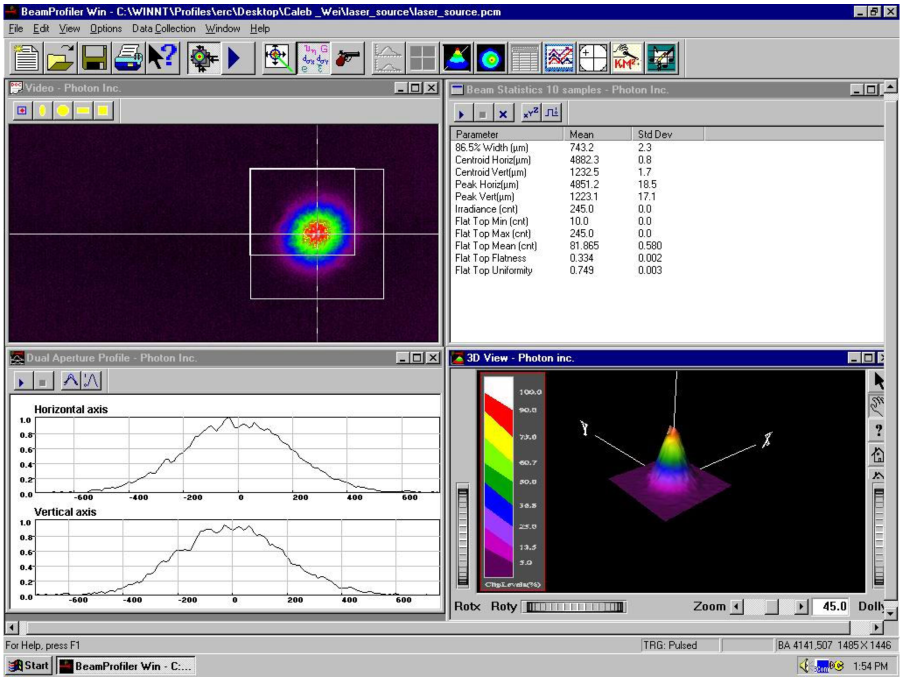

Parameter	Mean	Std Dev
86.5% Width (µm)	743.2	2.3
Centroid Horiz(µm)	4882.3	0.8
Centroid Vert(µm)	1232.5	1.7
Peak Horiz(µm)	4851.2	18.5
Peak Vert(µm)	1223.1	17.1
Irradiance (cnt)	245.0	0.0
Flat Top Min (cnt)	10.0	0.0
Flat Top Max (cnt)	245.0	0.0
Flat Top Mean (cnt)	81.865	0.580
Flat Top Flatness	0.334	0.002
Flat Top Uniformity	0.749	0.003

Figure 1.3.10. The beam image measured by the BeamProfiler system at the laser source.

Meanwhile, the *3D Beam Contours* displays the laser beam image in a “3-dimensional” viewing format with a solid surface.

For an ideal Gaussian beam from a perfect laser source, a circular cross section of the beam with evenly distributed intensity contours would be displayed in the *Live Video* window. A perfect Gaussian curve should be observed in the *Dual Aperture Profile* window. Peak intensities in two-axis scans are normalized at 1 without any flat top. The Gaussian curves would be smooth and without any intensity fluctuation cased by spatial noise. The initial investigations by utilizing the BeamProfiler system were at three locations, which were at the laser source, after the spatial filter assembly and after the optical cavity.

At the laser source, we expected an imperfect beam affected by some spatial noise. Dust in the air or on optical components at the laser head and other optical defects can disrupt the beam and create scattered light. Figure 1.3.10 displays the beam profile analysis results at the laser source. A round cross section of the beam with evenly distributed intensity profiles is seen in the *Live Video* window. The cross section edges and intensity contour edges are not very smooth. In the *Dual Aperture Profile* window, two curves shown in the two intensity plots have some intensity fluctuations. In the *3D Beam Contours* window, the laser beam image is displayed as a right circular cone in a “3-dimensional” viewing format. The cone has a rough surface and its base is shown with rough edges.

The function of the spatial filter assembly is to clean up the beam by removing spatial noise. By comparing the beam profile to the profile at the laser source, the beam after the spatial filter assembly should have a more Gaussian-like beam profile.

Figure 1.3.11 displays the beam profile analysis results after the spatial filter assembly. In *Live Video*, the beam image is an irregular cross section and unevenly distributed intensity contours. In the *3D Beam Contours* window, the laser beam image is displayed as a polyhedron protruded from an irregular shape of base. This 3D image is not even close to a right circular cone.

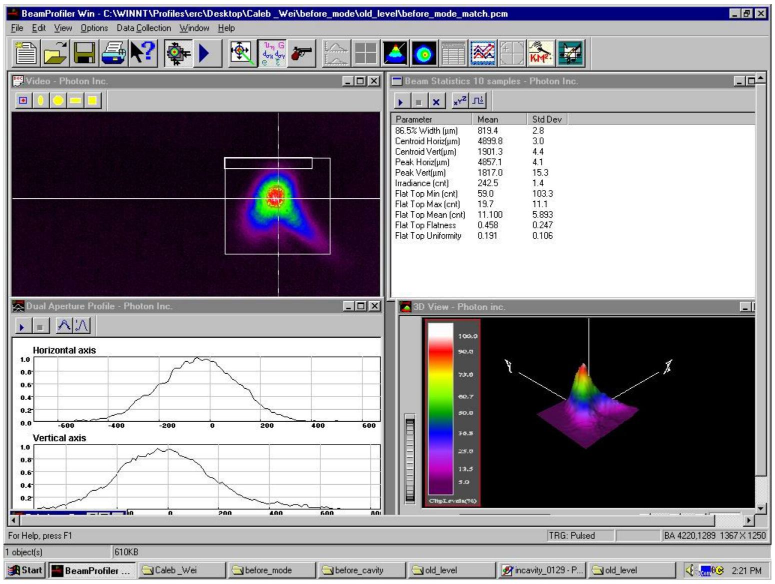

Parameter	Mean	Std Dev
86.5% Width (µm)	819.4	2.8
Centroid Horiz(µm)	4899.8	3.0
Centroid Vert(µm)	1901.3	4.4
Peak Horiz(µm)	4857.1	4.1
Peak Vert(µm)	1817.0	15.3
Irradiance (cnt)	242.5	1.4
Flat Top Min (cnt)	59.0	103.3
Flat Top Max (cnt)	19.7	11.1
Flat Top Mean (cnt)	11.100	5.893
Flat Top Flatness	0.458	0.247
Flat Top Uniformity	0.191	0.106

Figure 1.3.11. The beam image measured by the BeamProfiler system after the spatial filter assembly

It is obvious that the beam profile after the spatial assembly was worse than at the laser source. Apparently, alignment of the spatial filter assembly itself, was poor. The poorly aligned spatial filter assembly contaminates the beam instead of cleaning up the spatial noise.

Two plano-concave mirrors with 6 m radius of curvature compose the cavity. The cavity length is 30 cm. For a well-aligned cavity, the center axis of each mirror will lie on each other and the focal point of one mirror will lie behind the other mirror on its center axis. As the beam is injected into the cavity, the well-aligned cavity makes the beam focus on the center axis of both mirrors. The beam pattern is projected as a circular dot at the center of the inner surface of both two mirrors.

For a misaligned cavity, the center axes of two mirrors will not lie on each other and the focal point of a mirror will not lie on the center axis of the other mirror. As the beam is injected into the cavity, two mirrors focus the injected light beam on their own axis and two-spot pattern will be projected on each inner surface of the cavity mirrors.

When the BeamProfiler system is placed after the cavity, the beam image should be observed as a round well-collimated beam pattern from the well-aligned cavity. A two-spot pattern would be observed from a misaligned cavity.

In previous experiments, alignment was achieved by tuning the optical mirrors to merge two spots into a bright circular dot projected on the inward surface of each cavity mirror. By using a variable iris diaphragm for a rough measurement, the beam projection area on the inner surface of the mirrors is less than 2 mm in its diameter. As aligning the cavity, it is very difficult to monitor the beam pattern visually to discern any slight misalignment of the cavity.

Due to extremely low intensity, the CCD camera was placed directly at exit of the cavity without using the ATP-SM attenuator to measure the beam profile. The cavity mirror would scan the cavity in its axial direction by manually altering input voltage of the Master Scan feature of the Piezo-driver. The voltage variation was 5 volts, which covered about 600 nm scanning distance.

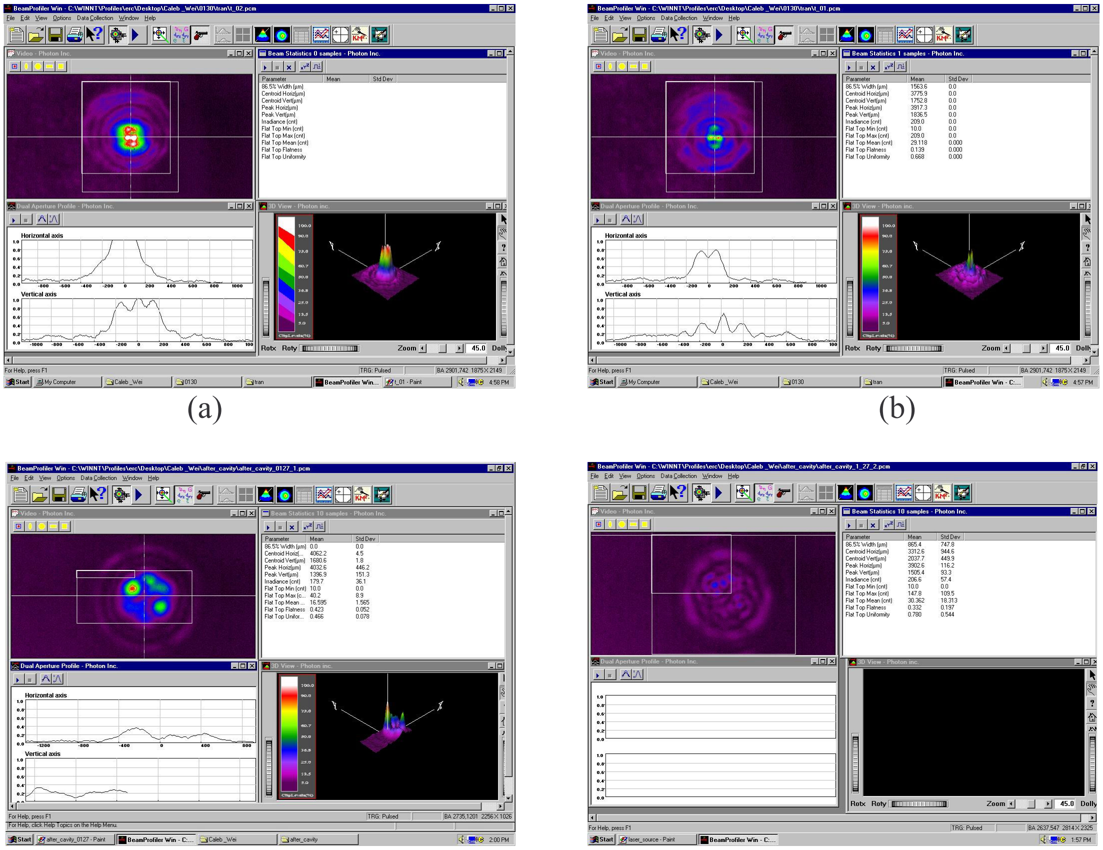

(a)

Beam Statistics 0 samples - Photon Inc.

Parameter	Mean	Std Dev
86.5% Width (µm)		
Centroid Horiz(µm)		
Centroid Vert(µm)		
Peak Horiz(µm)		
Peak Vert(µm)		
Irradiance (cnt)		
Flat Top Min (cnt)		
Flat Top Max (cnt)		
Flat Top Mean (cnt)		
Flat Top Flatness		
Flat Top Uniformity		

(b)

Beam Statistics 1 samples - Photon Inc.

Parameter	Mean	Std Dev
86.5% Width (µm)	1563.6	0.0
Centroid Horiz(µm)	3775.9	0.0
Centroid Vert(µm)	1752.8	0.0
Peak Horiz(µm)	3917.3	0.0
Peak Vert(µm)	1836.5	0.0
Irradiance (cnt)	209.0	0.0
Flat Top Min (cnt)	10.0	0.0
Flat Top Max (cnt)	209.0	0.0
Flat Top Mean (cnt)	29.118	0.000
Flat Top Flatness	0.139	0.000
Flat Top Uniformity	0.668	0.000

(c)

Beam Statistics 10 samples - Photon Inc.

Parameter	Mean	Std Dev
86.5% Width (µm)	0.0	0.0
Centroid Horiz(...	4062.2	4.5
Centroid Vert(µm)	1680.6	1.8
Peak Horiz(µm)	4032.6	446.2
Peak Vert(µm)	1396.9	151.3
Irradiance (cnt)	179.7	36.1
Flat Top Min (cnt)	10.0	0.0
Flat Top Max (c...	40.2	8.9
Flat Top Mean ...	16.595	1.565
Flat Top Flatness	0.423	0.052
Flat Top Unifor...	0.466	0.078

(d)

Beam Statistics 10 samples - Photon Inc.

Parameter	Mean	Std Dev
86.5% Width (µm)	865.4	747.8
Centroid Horiz(µm)	3312.6	944.6
Centroid Vert(µm)	2037.7	449.9
Peak Horiz(µm)	3902.6	116.2
Peak Vert(µm)	1505.4	93.3
Irradiance (cnt)	206.6	57.4
Flat Top Min (cnt)	10.0	0.0
Flat Top Max (cnt)	147.8	109.5
Flat Top Mean (cnt)	30.362	18.313
Flat Top Flatness	0.332	0.197
Flat Top Uniformity	0.780	0.544

Figure 1.3.12. The beam image measured by the BeamProfiler system after the cavity

Twenty screen shots were taken randomly as the cavity length was varied. Four analysis results were selected and displayed in Figure 1.3.12. Since the beam intensity was varied continuously as the cavity was scanned axially, only the beam images in *Live Video* and *3D Beam Contours* were focused for analysis.

Among the twenty records, the intensity contours in *Live Video* of Figure 1.3.12(a) shows much bigger areas for two white spots, which is corresponding much higher intensity amplitude at Z-axis in *3D Beam Contours*. In Figure 1.3.12 (d), the beam image is much weaker in *Live Video* among twenty records Even in *3D Beam Contours*, it is too low intensity to be plotted in a “3-dimensional” viewing format. Figure 1.3.12 (b) and Figure 1.3.12(c) are two results picked at random from among the 20 samples and these exhibit an intensity amplitude between Figure 1.3.12 (a) and (d).

In *Live Video* of Figure 1.3.12 (a), (b), (c), two-circle contours within the measured beam area are observed. In *3D Beam Contours* of 1.3.12 (b) and (c), two-circular contours are displayed as two slim cones protruding from the base areas. It is obvious that two mirrors focus the injected light beam on their center axes and reflect to each other to form two bright spots on their inner surfaces. Such two-spot patterns are shown in *Live Video* and *3D Beam Contours* for all collected images. Based on discussions in previous paragraphs, alignment of the cavity mirrors need to be optimized.

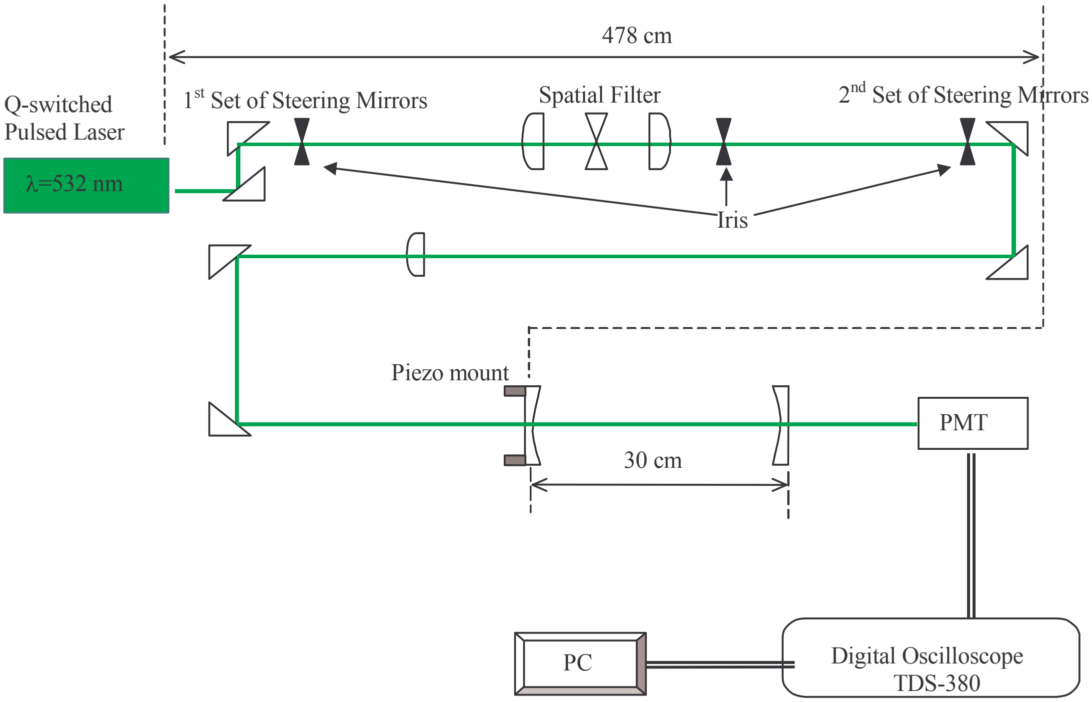

Figure 1.3.13. Diagram of re-alignment by using irises

1.3.5.2 Alignment Optimization

In this section, the BeamProfiler system was adopted as an assistance tool to confirm successful alignment.

Based on the experiment setup shown in Figure 1.3.8, the beam may travel more than 478 cm before entering the optical cavity. Any slight misalignment of the beam near its source can cause tremendous out-of-alignment when entering into the cavity. As a result, it is critical to ensure the 3 dimensional straightness of beam passage at the upstream of the beam path.

While overhauling alignment of all optical devices, variable irises were adopted to insure the straightness of the beam passage in X, Y and Z-axis, which is shown in Figure 1.3.13. Three iris bases were locked on the test bench in a line between the first and the second set of steering mirrors after the laser source, which was the passage where the spatial filter was located.

After the beam was aligned, it could not be altered three-dimensionally, as the spatial filter assembly was added in the passage. While reconstructing the spatial filter assembly, the beam passage was taken as the standard for aligning each optical unit. The BeamProfiler system was used to monitor the beam profile before and after the spatial filter assembly to ensure the beam quality.

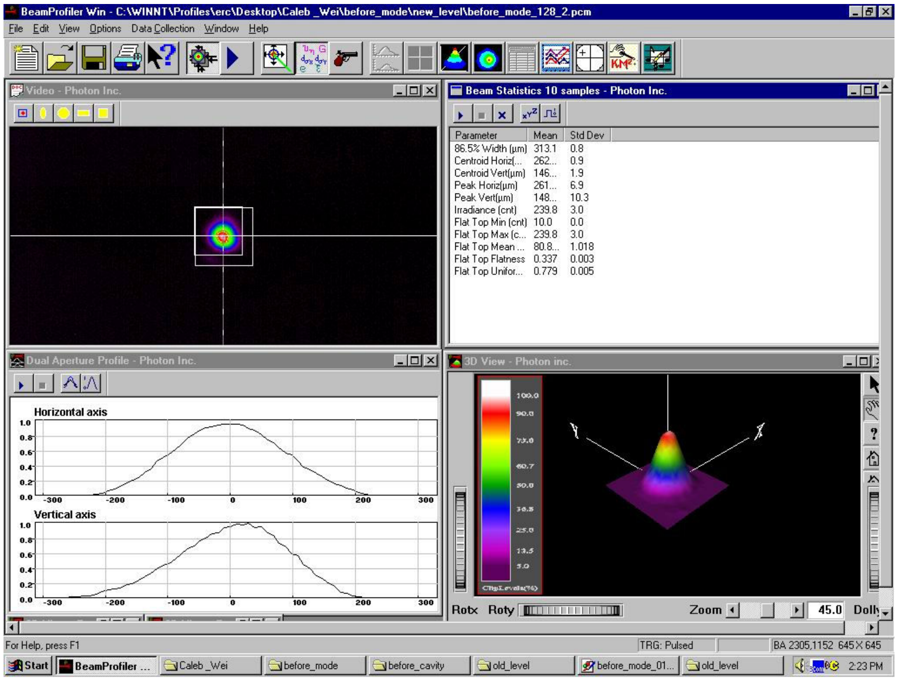

Parameter	Mean	Std Dev
86.5% Width (µm)	313.1	0.8
Centroid Horiz(...	262...	0.9
Centroid Vert(µm)	146...	1.9
Peak Horiz(µm)	261...	6.9
Peak Vert(µm)	148...	10.3
Irradiance (cnt)	239.8	3.0
Flat Top Min (cnt)	10.0	0.0
Flat Top Max (c...	239.8	3.0
Flat Top Mean ...	80.8...	1.018
Flat Top Flatness	0.337	0.003
Flat Top Unifor...	0.779	0.005

Figure 1.3.14. Beam image measured by the BeamProfiler system behind the spatial filter assembly after optimizing alignment.

After new alignment, the beam profile analysis results sampled behind the spatial filter assembly are shown in Figure 1.3.14. In *Live Video*, the beam image is shown as a circular cross section with evenly distributed intensity contours. In *Dual Aperture Profile*, the intensity curves are smooth and without any fluctuation. The shapes of both curves are very close to a Gaussian curve. The beam image displayed in *3D Beam Contours* is a right circular cone protruded from a round base with a very even surface.

1.3.5.3 Alignment Optimization for the Cavity

The CCD camera was placed directly at the exit of the cavity to monitor the projected beam pattern while aligning the cavity mirrors. By using the Peizo-driver to alter the input voltage of three axes on the mirror mounting plate of the Piezo kinematic mount, we could fine-tune the mirror position at the scale of 0.116 µm/volt. After alignment was optimized, the cavity mirror would scan the cavity in its axial direction by manually altering input voltage of the Master Scan feature of the Piezo-driver. The voltage variation was 5 volts, which covered about 600 nm scanning distance.

Twenty screen shots were taken randomly as the cavity length was varied. Since the cavity output intensity varied continuously wiht scanning the cavity axially, only the beam images in *Live Video* and *3D Beam Contours* were examined for analysis. The measuring scale as the display color scheme for the intensity contours was consistent in all twenty records. Two analysis results were selected and displayed in Figure 1.3.15 and Figure 1.3.16.

In *Live Video* of Figure 1.3.15 and Figure 1.3.16, circular contours are observed from the measured beam area. In *3D Beam Contours*, Figure 1.3.15 and Figure 1.3.16 show a single solid cylindrical object protruded from its base. It appears that the alignment of the cavity mirrors is optimized.

1.3.6 Resonant Axial Modes Investigation

In section 1.3.3, the resonant axial mode phenomenon was verified by visual observation of the beam projection on the inner surface of the cavity mirrors. The intensity of the beam projection was altered repeatedly on a regular base from low to high, corresponding to the axial movement of one of the mirrors. In this section, we used the BeamProfiler system to monitor and record the spatial structure of light after the cavity and expect to observe resonant axial mode characteristics.

In a well-aligned cavity, by comparing the beam image in *Live Video*, the contours at the higher intensity amplitude scales, especially the white area, in Figure 1.3.15 is much larger than in Figure 1.3.16; it is also higher than the other records. In 3D *Beam Contours*, as the beam image is displayed in a "3-dimensional" viewing format, the beam image in Figure 1.3.15 has a much larger radius at the highest intensity amplitude at the Z-axis than in Figure 1.3.16. The beam intensity in Figure 1.3.15 is much higher than in Figure 1.3.16 and higher than most of the other samples.

A similar comparison was also applied to the results from a not-well-aligned cavity shown in Figure 1.3.12. It is obvious that the beam image in Figure 1.3.12(a) shows much higher intensity than the others. Consequently, the beam image was obtained when the cavity was in a resonant axial mode in Figure 1.3.12 (a).

1.3.7 Resonant Axial Mode Locking

The BeamProfiler system gives us visual realization of resonant axial mode characteristics. By comparing the beam contours and intensity in *Live Video* and *3D Beam Contours*, we are able to discern wheatear the cavity is in a resonant axial mode when the scanning mirror was moved to certain position.

We tried to lock the scanning mirror as the cavity was in a resonant axial mode to verify if the cavity length could be fixed to mode-match the to laser source. The cavity mirror would scan the cavity by manually by altering input voltage of the Piezo-driver. As a beam image with higher intensity amplitude was observed in *Live Video* and *3D Beam Contours* on the Bemaprofiler system, we stopped scanning of the cavity immediately and observe any change of the beam image. However, the beam image varied by itself after a very short period of time without changing any experimental parameters. The intensity amplitude dropped irregularly as if the cavity were moved out of a resonant axial mode position by itself. The same procedure was repeated extensively as the mirror was moved at different position. Since the beam intensity could not be maintained as the cavity was in a resonant axial mode, it is obvious that the cavity could not be locked to mode-match the laser source.

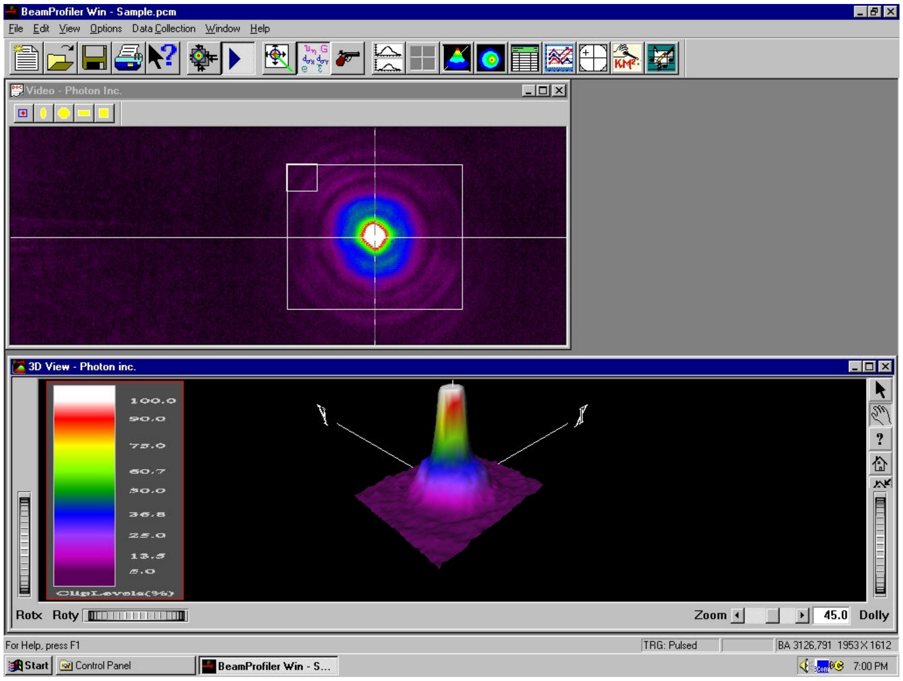

Figure 1.3.15. The beam image measured by the BeamProfiler system behind the cavity after optimizing alignment with the highest intensity.

The laser that we used is a Q-switched diode pumped solid-state green laser system. Its pulse duration is less than 15 ns. According to its specification from INTELITE, Inc, this is not a mode-locking laser. The company does not specify its line width. For a mode-locking laser, the longitudinal modes have fixed phase as a short pulse is generated within the optical cavities of the laser, which produces a single mode pulse with stable intensity. Since the longitudinal modes of this laser are not locked, disparity exits as each pulse is generated. Thus, by its nature, it is a broadband laser. The line width causes variation of its wavelength as every pulse is generated by the laser. Therefore, the optical cavity of the P-CRDS system cannot be locked to mode-match the laser source.

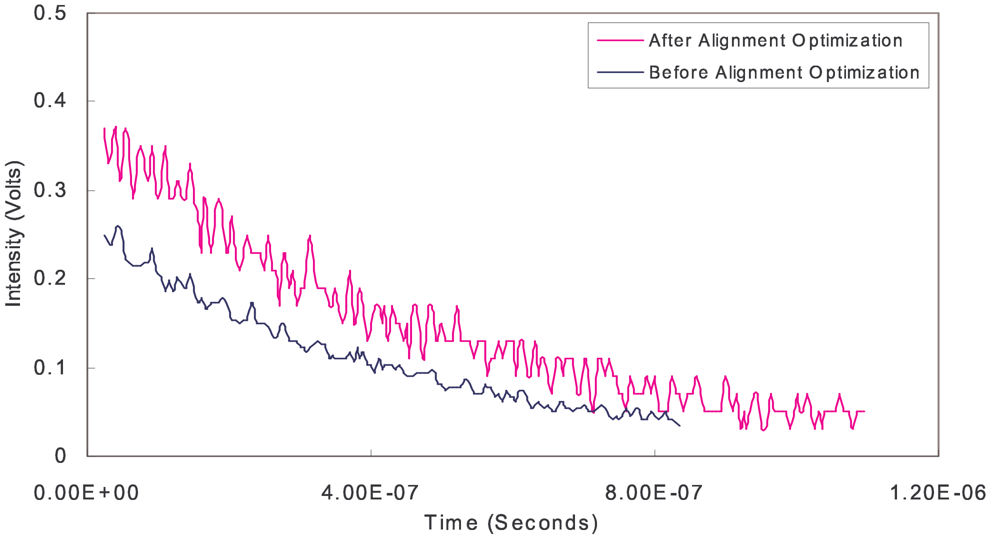

Figure 1.3.16. Decay traces plotted as intensity vs. time from cavities before alignment optimization and after alignment optimization

1.3.7.1 Resonant Axial Mode Locking Conclusion

As discussions in the previous section, by using the BeamProfiler system, we can optimize alignment of the cavity to eliminate transverse modes, which cause the transverse modes beating and generate intensity fluctuations. Since the laser source of this P-CRDS system is short-pulsed free running laser, the interactivity between the laser mode shape and cavity mode shape can not be controlled by locking the cavity to mode-match the laser source. We observed shot-to-shot variation of decay trace and could not acquire consistent repeatability of the ringdown time constant, τ . Data selection methods must be introduced in order to confirm that the decay trace only measured as the cavity is in the same resonance behavior.

1.3.8 Decay Trace Measurements after Alignment Optimization

Based on the conclusions discussed in Section 1.3.7, after the cavity was aligned with assistance of the BeamProfiler system, transverse mode beating could be controlled. The experimental setup shown in Figure 1.3.8 was adopted for decay trace comparisons after alignment was optimized. The cavity length of this setup was 30 cm. Each decay trace was recorded by the LABVIEW 6 program and was interpreted for the ringdown constant, τ . The peak intensity for each decay trace was also recorded for comparison of shot-to-shot variations. The scanning displacement of the mirror was about 700 μm in the cavity axial direction, which could cover three axial-mode intervals.

Two hundred data were collected. Since the laser source is not a single mode laser, the cavity cannot be locked to mode-match the laser source. In order to compare similar cavity conditions, we need to select decay traces from the same cavity resonance behavior. Since the decay trace will have a high peak intensity when the cavity is in a resonant axial mode, by picking the twenty highest peak intensity decays from the total data collection, the selected twenty decay traces should be measured from a similar cavity resonance condition.

The decay traces with the highest peak intensities were selected and plotted in Figure 1.3.16 as the pink color trace, which is labeled as “after alignment optimization”. Decay traces with highest peak intensity were also selected from the results in Section 1.3.4, which is the cavity aligned visually with standard techniques. This trace is plotted as the blue trace in Figure 1.3.16 and labeled as “before alignment optimization”.

The peak intensity of the decay trace measured after alignment optimization was 0.378 Volts. The peak intensity of the decay trace measured before alignment optimization was 0.25 Volts.

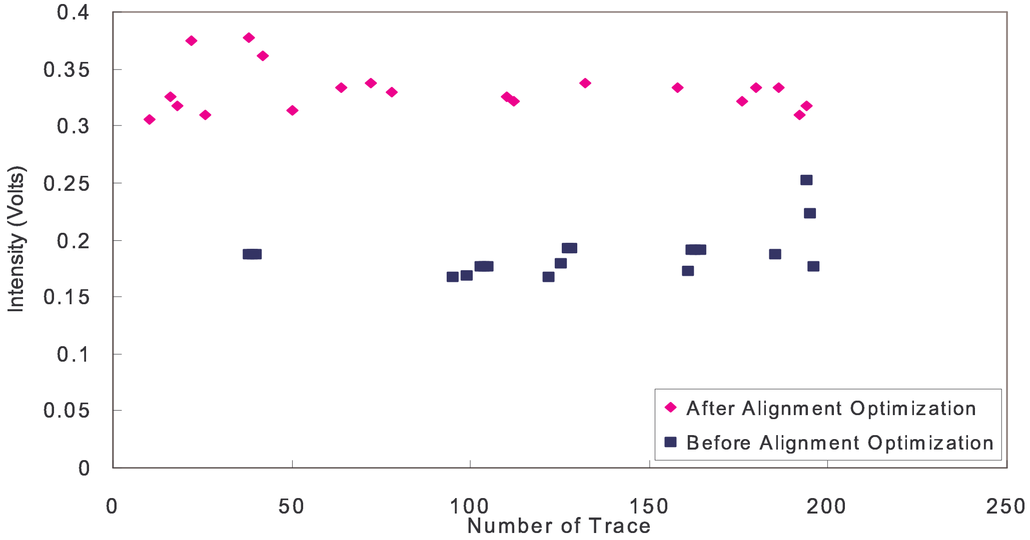

Figure 1.3.17. Top twenty highest peak intensity data from cavities before alignment optimization and after alignment optimization

In Figure 1.3.17, the twenty peak intensity values from the cavity with optimized alignment are plotted as pink color dots with an average intensity of 0.331 Volts. Twenty traces from the cavity aligned visually are plotted as blue color dots with an average intensity of 0.187 Volts.

In Figure 1.3.18, the ringdown time constant, τ , of the twenty highest peak intensity decay traces from the cavity with optimized alignment are plotted as pink color dots with an average τ of 465.01 ns. The ringdown time constant, τ , of the twenty highest peak intensity decay traces from the cavity aligned visually are plotted as blue color dots with average intensity of 593.76 ns.

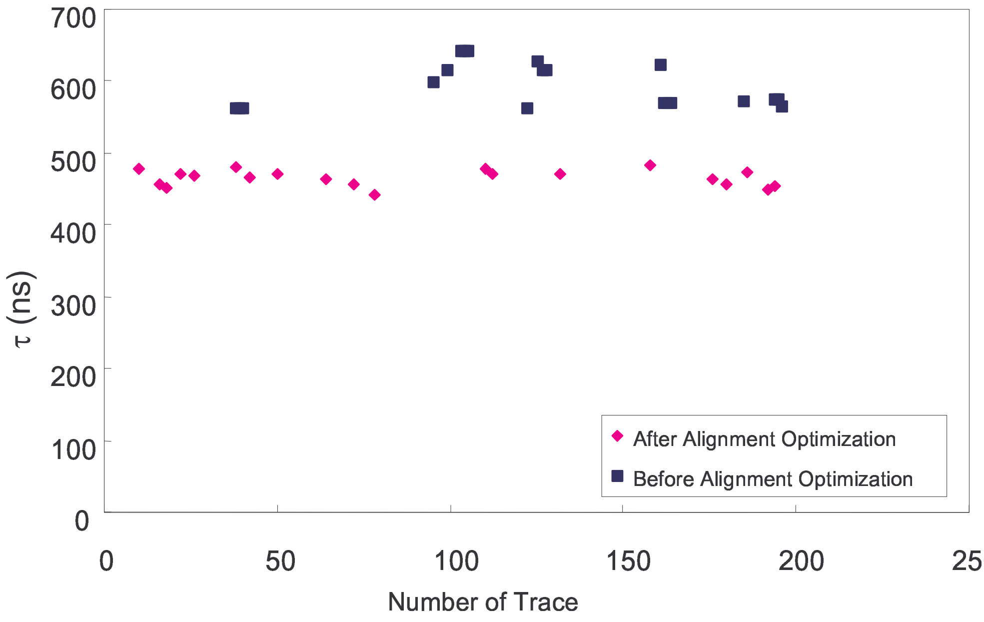

Figure 1.3.18. The ringdown time constant, τ , of twenty highest peak intensity data from cavities before alignment optimization and after alignment optimization

In a not well-aligned cavity, the beam path is slightly off the center axis of the cavity. It can be considered as the beam is injected into a cavity with slightly longer cavity length and with longer decay time constant, τ . As alignment is optimized, the beam path is closer to the center axis of the cavity, which is the shortest distance between two cavity mirrors. As the beam is injected into a cavity with slightly shorter cavity length, its decaying time constant, τ , is smaller. That is why the ringdown time constant, τ , is decreased as the cavity is in resonant axial modes after alignment is optimized.

1.3.9 Measurements Using P-CRDS System

To test the P-CRDS system, we performed measurements for Nitrogen, Carbon Dioxide and 2’,7’- Dichlorofluorescein (DCF) in the test cell, instead of measuring diesel exhaust directly. The advantage of these substitutes is that test species chemical properties and concentrations in the test cell can be measured and controlled with some confidence. Based on the above results, the resolution of the decay trace is optimized when the cavity is resonant in an axial mode. For the measurements in this section, two strategies are introduced to select data obtained from decay traces measured when the cavity is in a resonant axial mode. Two different windows were tested at the two ends of the airtight test cell. Losses caused by the absorption and reflections of the windows are also discussed.

1.3.9.1 Data Selection

According to the discussions in Section 1.3.8, since the laser source is not a single mode laser, the cavity can not be locked to mode-match the laser source. For measurement analysis, we need to select decay traces with similar cavity resonance behavior. Further, when the cavity is in a resonant axial mode, the decay trace is has a high intensity profile, with optimal resolution for measurements. Thus, two selection strategies are introduced to distinguish the decay traces to be measured from the not-resonant-axial-mode cavity cases. One strategy is setting the selection intensity at certain voltage level, which is called mode selection threshold. When the peak intensity of a decay trace is higher than the selection threshold, the decay trace is considered as measured from a resonant axial mode for the cavity. This selection is valid only when the absorption of the testing species is constant. The other strategy for trace selection relies on the absolute slope of the initial part of the decay trace, which we have called the index slope. The traces with high intensity profile typically have very steep absolute slope at the initial part, which is an indication the cavity is in a resonant axial mode. This selection method can be applied to measure the testing species with variable absorption.

1.3.9.2 Data Selection by Intensity Threshold

The *g* parameter for this cavity is $g_1 = g_2 = 1 - \frac{L}{R_1} = 1 - \frac{L}{R_2} = 0.95$. The product of $g_1 g_2$ is, 0.9025. As $g_1 g_2$ is close to 1, the transverse mode spacing is much smaller than the axial mode spacing. The axial mode spacing for this cavity is 500 MHz while the transverse mode spacing for this cavity is 51 MHz. If transverse modes are excited in the cavity, they will fill the gaps between axial modes.

This selection strategy was already applied in Section 1.3.8, where two hundred data were collected from a well-aligned cavity. Only decay traces with the twenty highest peak intensity were selected for comparisons. The average peak intensity for these twenty data is 0.335 volts and its standard deviation in terms of percentage was 5.82 %.

1.3.9.3 Data Selection by Index Slope

The selection strategy by setting the mode selection threshold works only when absorption of the testing species is constant during the testing period. For measuring the species with variable absorption, such as particles suspended in the test cell, a different selection method, called the index slope selection, must be introduced.

In Figure 1.3.19, two decay traces are plotted as intensity vs. time. The blue color trace at a high intensity profile was measured when the cavity was in a resonant axial mode and the green color trace at lower intensity profile was measured when the cavity was not in a resonant axial mode. A linear equation was fitted to the first twenty points of the decay traces and labeled with its fitting equation. The index slope was the absolute value of the slope of the linear fit line for each decay trace. By observing two decay traces in Figure 1.3.19, it is evident that the absolute slope of the fitting line of the blue color trace is higher than of the green color trace, which is $|-870303|$ volts/second $>|-339394|$ volts/second . Therefore, by comparing the index slope of decay traces, we can determine if a decay trace is measured from the in-resonant-axial-mode cavity.

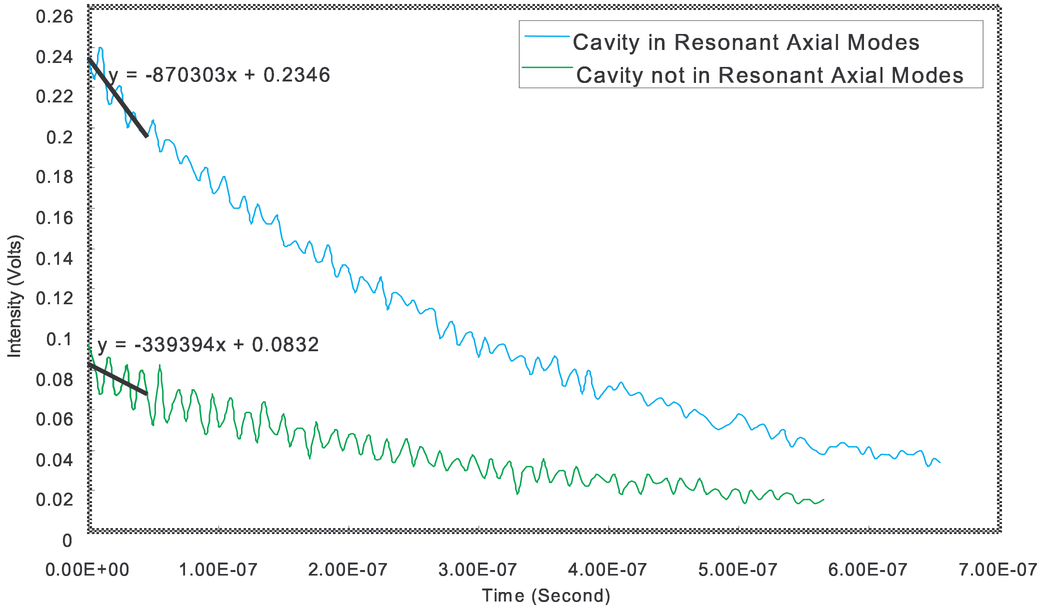

Figure 1.3.19. Comparison of initial slopes for resonant and non-resonant cavity ringdown

For further confirmation, five hundred decay traces were collected from a 30 cm long cavity with the same experimental setup as in Section 1.3.8. We selected the data from the visually aligned cavity with standard techniques. In this data collection, the τ variation between in resonant axial mode and not in resonant axial mode is more relevant, to the applications of interest. The peak intensity, the ringdown time constant, τ , and the index slope of each trace was interpreted and reordered. All five hundred collected data were plotted as the τ vs. index slope graph in Figure 1.3.20(a) and the τ vs. peak intensity graph in Figure 1.3.20(b). Both graphs had very similar trend shapes. One set of twenty data with the highest index slope was selected and compared with another set of twenty data with the highest peak intensity. The average τ for the selected data based on the highest index slope is 663.7 ns and its standard deviation in percentage is 2.29%. The average τ for the selected data based on the highest peak intensity is 665.1 ns and its standard deviation in percentage is 2.29%. The Pearson correlation coefficient of these two sets of τ is $r = 98.67\%$, which means two sets of τ are strong positive associated. The selected data as the ringdown time constant, τ , from these two methods are plotted in Figure 1.3.20 for comparison.

1.3.10 Measurements for Test Cell Windows

The test cell is an airtight metal chamber with two parallel windows at its two ends. Both window surfaces are coated with a specific anti-reflection coating to improve transmittance. Although the absorption and reflection of the windows are very small, they can cause tremendous loss in the optical cavity as the laser beam bounces back and forth within the cavity hundreds times. As a result, it is important to select the proper windows improving the resolution of decay trace.

Two sets of commercial windows were used. One, W1, set is from Quantum Optics Company with a diameter of 25.4 mm and thickness of 1 mm. The window is made of BK7 and both sides are coated with narrowband AR coatings for 532 nm. The other, W2, is from the same company, with a diameter 25.4 mm and thickness of 2 mm. The window is made of BK7 and both sides are coated with broadband AR coatings, 400 ~ 700 nm.

In this section, test cell windows were placed in the cavity for four spectroscopic measurements. The first measurement was for an empty cavity as reference. The second measurement was one W2 window and the third measurement is one W1 window. The forth measurement was for two W1 windows, which total thickness was equal to one W2 window thickness, 2 mm. Two hundred decay traces were collected from each case. The interpretations of the ringdown time constant, τ, for each decay trace was consistent with previous sections. Ten decay traces with the highest peak intensity were picked up from each data collection. The program took three seconds to process one decay trace. For collecting two hundred decay traces, the testing period was more than 10 min. The results were plotted as τ vs time, which was the τ variations within the testing period.

The results are shown in Figure 1.3.21. The average τ for an empty cavity plotted as yellow color dots is 380.59 ns with 15.48 ns as its standard deviation. For the second case, the average τ for one W2 window plotted as blue color dots is 101.80 ns with 5.37 ns as its standard deviation. For the third case, the average τ for one W1 window plotted as pink color dots is 107.75 ns and its standard deviation is 6.21 ns. For the fourth case, the average τ for two W1 windows plotted as green color dots is 43.70 ns and its standard deviation is 1.87 ns. The standard deviations as in percentage are 3.94%, 5.31%, 5.76% and 4.28% respectively.

The total glass thickness in the second case and the fourth case are the same, 2 mm, which should also cause the same absorption loss by the glass. However, we find that the average τ of the second case, 101.80 ns, is higher than of the fourth case, 43.70 ns. It is obvious that higher loss in the fourth case is contributed by reflections of additional two surfaces of W1 window.

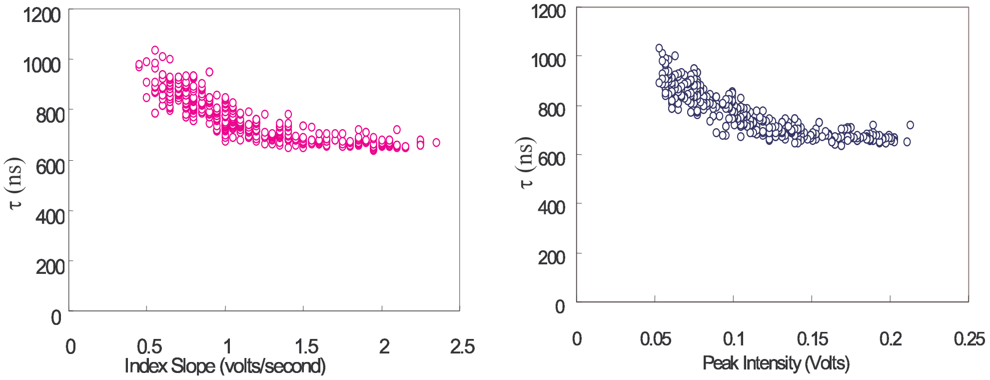

(a) (b)

Figure 1.3.20. Data selection comparisons between (a) the index slope method and (b) the modes selection threshold method

Meanwhile, the average τ for the second case is very close to the average τ for the third case and the difference is only 5.95 ns. Although the thickness of one W2 window is two times thicker than the thickness of one W1 window, glass absorption may contribute a nominal loss. The other possible cause of different loss as is from the different AR coatings for these two windows. Based on this comparison, the average τ of one W1 window is higher than of one W2 window, which means less loss is contributed by one W1 window as placing within the cavity. We will select W1 windows as the test cell widows for the following measurements.

Finally, comparing the average τ for the empty cavity, 380.59 ns, with the other three cases, 101.80 ns, 107.75 ns and 43.70 ns, the difference is at least 70 %. The sensitivity of this P-CRDS system is relative high especially compared to applications, the absorption and reflections of the windows can be neglected.

The results obtained in this section are important. From these four measurements, we found that the window surface reflection contributes a significant loss, which is much more than the glass absorption. Meanwhile, the τ measurement value was decreased at least 70 % by placing one W1 window, with 1 mm thickness, in the cavity.

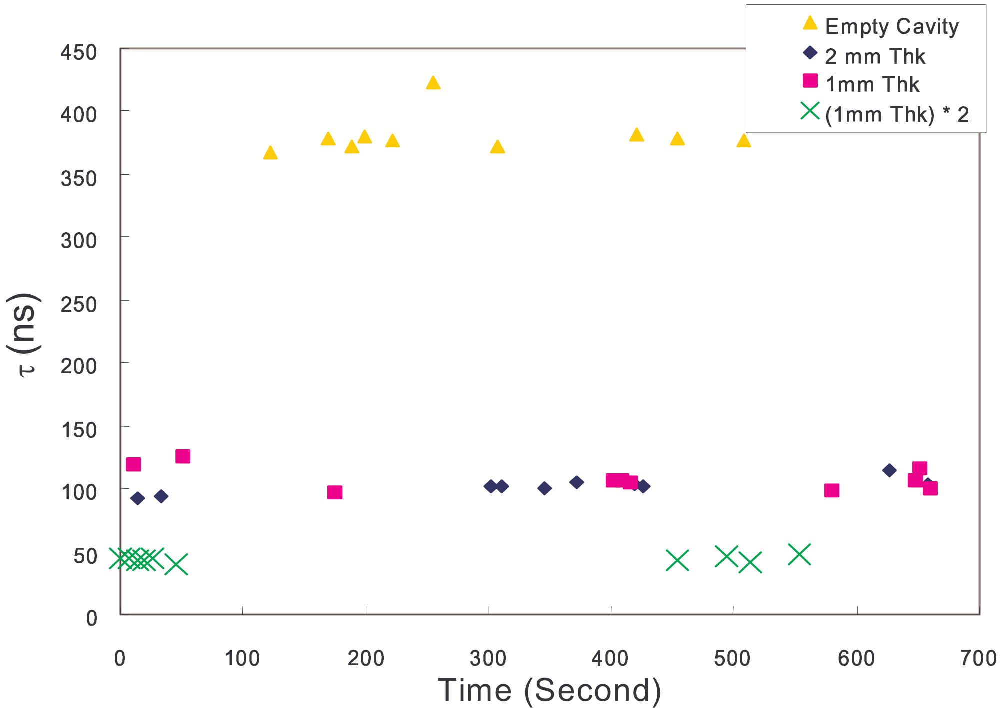

Figure 1.3.21. Measurements for test cell windows

1.3.11 Measurements for Particles

In this project, instead of measuring diesel exhaust directly, 2',7'-Dichlorofluorescein (DCF) mixed with Nitrogen gas was selected for particle spectroscopic measurements within the test cell. The advantage of this substitute is that its chemical properties and concentration in the test cell can be realized and controlled with confidence, unlike typical diesel exhaust.

According to its material data sheet from the Sigma-Aldrich Corporation, 2',7'-Dichlorofluorescein (DCF) is listed as a low hazard and stable chemical compound. Its molecular formula is $C_{20}H_{10}Cl_2O_5$ and its formula weight is 401.21. The melting point is 280 °C. The wavelength for maximum absorption is 509 nm, which is ideal for our P-CRDS system with the laser wavelength at 532 nm. DCF particle diameter distribution evaluated by Hasegawa$^{)}$ is illustrated in Figure 1.3.22 (a) and Sauter mean diameter , D_{32}, of DCF is 13.36 μm. Its absorption and emission spectra is also in Figure 1.3.22 (b).

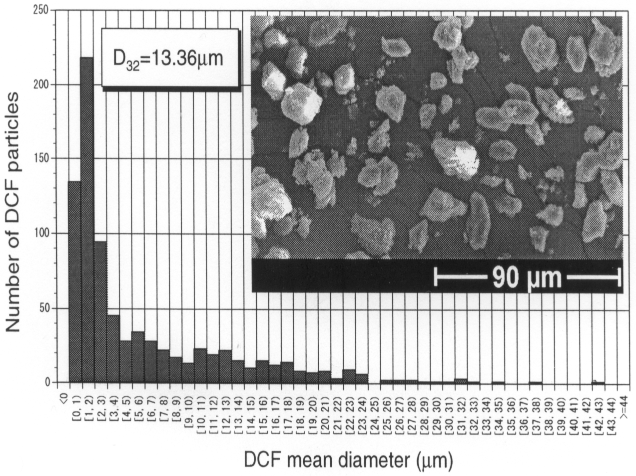

(a)

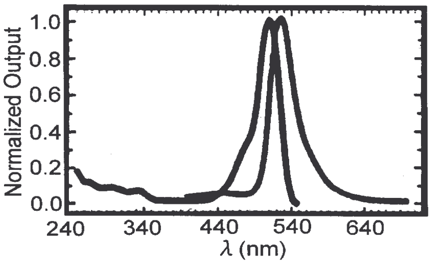

(b)

Figure 1.3.22. DCF characteristics (a) DCF particles size distribution (b) DCF absorption and emission spectra.

The W1 test windows, with 1 mm thickness, were used as the test cell windows. The cavity length was set at 30 cm. After the test cell was placed and locked within the

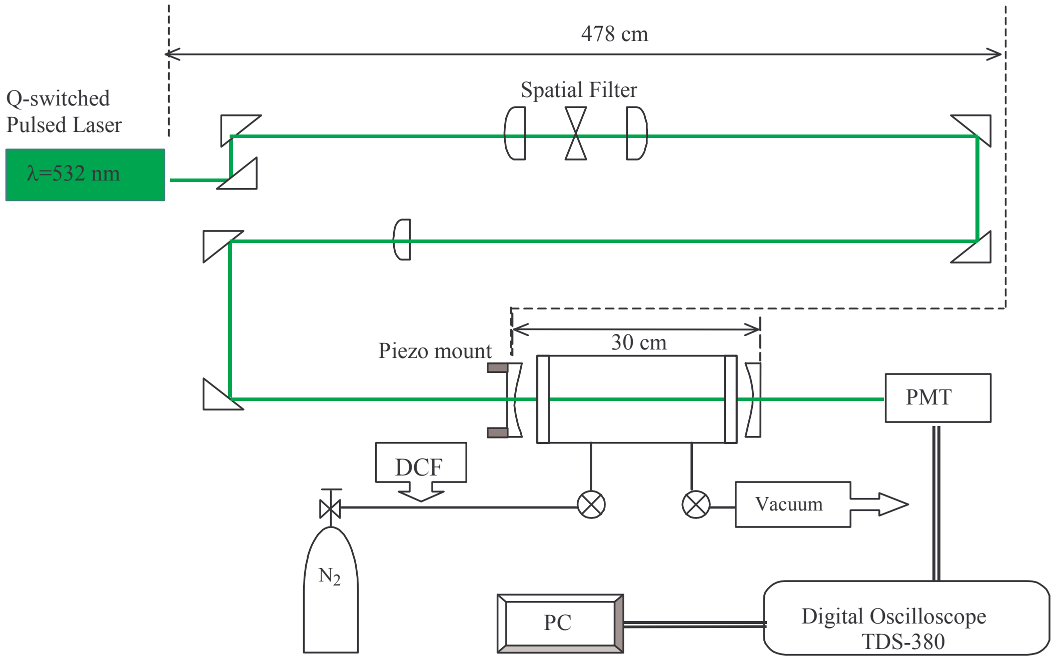

Figure 1.3.23. Schematic diagram of experiment setup for DCF spectroscopic measurements.

cavity, the BeamProfiler system was used at the cavity exit to optimize alignment. Then, the PMT would replace the BeamProfile system to measure the decay trace.

Before the DCF measurement, we measured the ringdown time constant, τ, for the empty test cell as reference. Two hundred decay traces were collected. Decay traces with ten highest peak intensity were selected to acquire average τ for the empty test cell. It is used as a reference, τ_0, for analyzing the absorption of DCF.

As shown in Figure 1.3.23, two air hoses were installed on the test cell. One was hooked up with a vacuum pump. The other one was connected to the Nitrogen cylinder with an opening, which allowed DCF to be added into the system. The valve on the hose connected to the Nitrogen cylinder is closed first. The vacuum pump was used to evacuate air out of the test cell. The vacuum was maintained at 14 psig of vacuum within the test cell. As valve on the hose connecting to the vacuum pump was closed, the DCF with desired weight was added into the opening. When the valve in the hose connected to the Nitrogen cylinder was open, the test cell was rapidly charged with Nitrogen gas and DCF particles. The filling pressure of the test cell was fixed at 14 psig of pressure. We created a pressure difference up to 28 psi before and after DCF injection into the test cell to make sure a homogeneous charge of DCF particles was in the test cell.

Data sampling begins 10 seconds after the DCF particles were injected into the test cell. Four hundred decay traces were recorded for each measurement, which covered the testing period up to 22 minutes. For data selection, any decay trace with τ higher than the reference, τ_0, measured from of the empty test cell with only air, was eliminated. Then, decay traces with twenty highest index slopes were selected for analysis. The results were plotted as τ vs. time.

Two measurements were performed, one is for an initial 10.8 mg of DCF particles and the other is for an initial 5.7 mg of DCF particles. After acquiring the reference, τ_0, the measurement for 10.8 mg of DCF particles was performed first. Then, the tested particles were blown out of the test cell and evacuated by the vacuum pump. The reference ringdown time constant is measured again. Finally, 5.7 mg of DCF particles were injected into the test cell for measurement.

The results are plotted in Figure 1.3.24. Each line is estimated by a power function curve. τ_0 for the case of 10.8 mg was 51.26 ns and τ_0 for the case of 5.7 mg was 43.47 ns. In Figure 1.3.24, it is obvious that initially, each curve is rising rapidly. Later, the 5.7 mg curve approaches to its steady state and only increases very gradually after that. By comparing two curves to each other, the curve for the 5.7 mg case takes shorter time to reach its steady state than the 10.8 mg case and its initial increase is also more rapid than the 10.8 mg case.

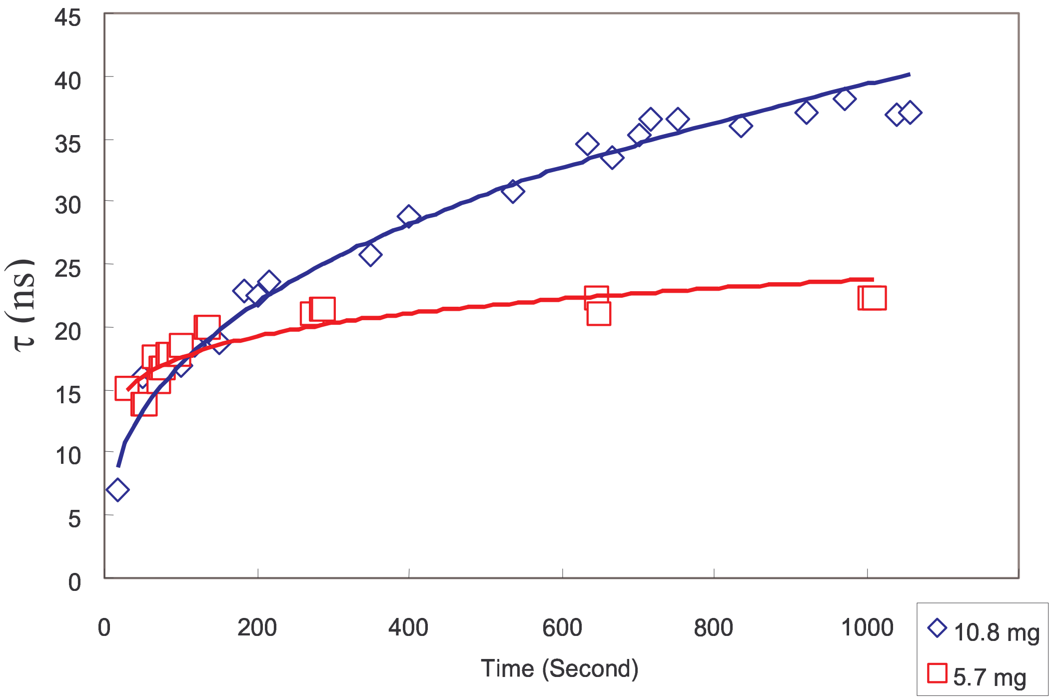

Figure 1.3.24. DCF spectroscopic measurement as the ringdown time constant, τ, variation within the testing period

In the Figure 1.3.24, the curves cross each other and the difference between two curves gets bigger. The reasons is that when measuring 10.8 mg of DCF, some particles may deposit on the test cell windows and can not be fully evacuated out of the cell by the vacuum pump. The particles deposited on the test windows cause additional absorption loss for the subsequent 5.7mg experiment. The τ measurement reading is smaller as more particles stick to the windows. Thus, the reference τ_0 for the case of 10.8 mg is 51.26 ns, which is larger than the reference τ_0 for the case of 5.7 mg, 43.47 ns. More, as performing second measurement for 5.7 mg of DCF particles, even more particles may deposit on the test cell windows, which can cause more absorption loss and lower τ reading. Thus, in the graph, we see 5.7 mg curve is beneath 10.8 mg curve after approaching to the steady state, which is caused by window fouling.

By knowing two ringdown time constants, the absorption of testing species can be determined using:

$$\alpha = \frac{1}{(L' - 2s)} \left(\frac{t_r}{2} \right) \left(\frac{1}{\tau_1} - \frac{1}{\tau_0} \right)$$

Since L', s and t_r are constant, the absorption of the testing species, α, is proportional to the difference between the inverse of the measured ringdown time constant, τ_1, and the inverse of the reference ringdown time constant, τ_0,

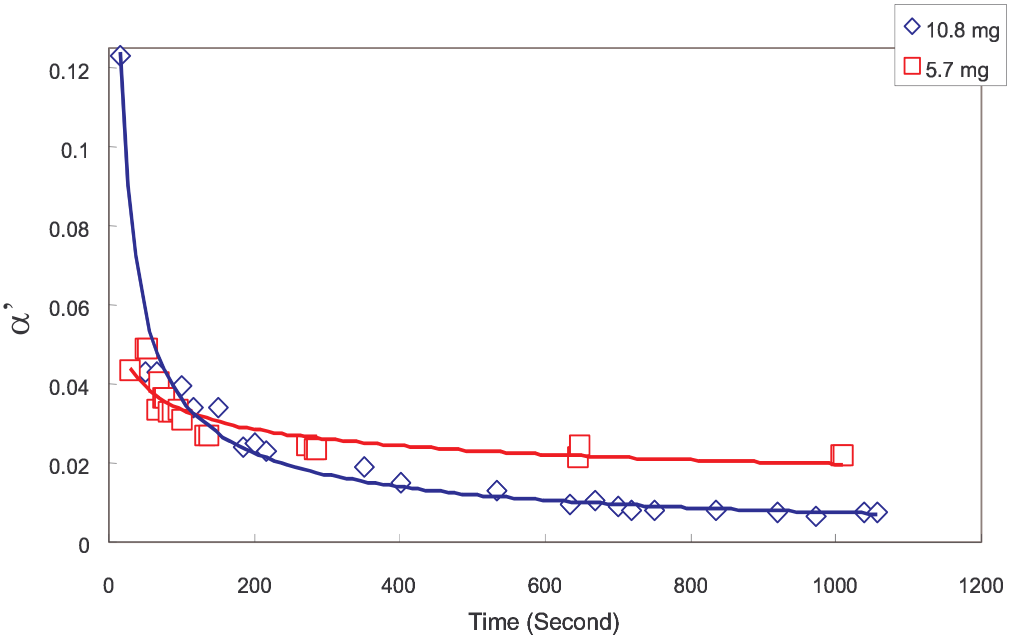

Figure 1.3.25. DCF spectroscopic measurement as the absorption variation within the testing period

$$\alpha \propto \left(\frac{1}{\tau_1} - \frac{1}{\tau_0} \right)$$

Assuming absorption is proportional to its volume fraction, f_v, by plotting $\left(\frac{1}{\tau_1} - \frac{1}{\tau_0} \right)$, which is shown as α', vs. time, we can envision the volume fraction, f_v vs. time.

DCF spectroscopic measurement as α' vs. time of theses two measurements is shown in Figure 1.3.25. Initially, each curve decreased rapidly. Afterward, each curve approached to a steady state and decreased more gradually. By comparing the two curves to each other, the curve of the 5.7 mg case took a shorter time to reach its steady state than the 10.8 mg case. After approaching the steady state, the curve for the 5.7 mg case was slightly above the curve for the 10.8 mg case by about 0.01 of α'. The additional absorption was caused by particle deposit on the test windows while performing each measurement.

To interpret the two curves in terms of absorption measurement, as DCF particles are injected into the test cell, most of particles are suspended by Nitrogen gas and cause a large absorption for spectroscopic measurement. Thus, the ringdown time constant τ is small and absorption, α', is high at initial stage. Shortly after that, a significant number of particles start to sink to the bottom of the test cell and the absorption is decreased rapidly; the ringdown time constant τ increases and so the absorption, α', decreases. Then, most of the particles are down at the bottom of the test cell at the approach to the steady state. Gradually, only few particles, mostly smaller particles, are still suspended in the test cell and may take a long time to sink to the bottom of the test cell. Thus, τ is increased very slowly and the absorption, α' is decreased later in the experiment. Since more particles are injected into test cell in the case of 10.8 mg, it may take a longer time to let majority of particles sink down to the bottom of the test cell. Therefore, from the graph, we see its curve in both τ vs. time and α' vs time takes longer time to reach its steady state than the case of 5.7 mg.

In each case, only twenty highest peak intensity data were selected for analysis from four hundred collected data. This is a great limit to plot and interpret the curves in the τ vs. time and α' vs. time graphs precisely, especially in the case of 5.7 mg. The major cause is that the actual transfer rate of the data acquisition system was 3 seconds/decay trace, which is a great hindrance for acquiring τ in real time, especially compared to the laser pulse rate at 2 kHz. A data acquisition system with higher data transfer rate should be used to improve the resolution of curves in both τ vs. time and α' vs time.

1.3.12 References

1. J. J. Scherer, D. Voelkel, D. J. Rakestraw, J. B. Paul, C. P. Collier, R. J . Saykaly, and A. O'Keefe, " Infrared cavity ring down laser absorption spectroscopy (IR-CRDS)" Chemical Physics Letters 245, pp. 273-280 (1995).
2. J. T. Hodges, J. P. Looney, and R. D. vanZee, "Laser Bandwidth effects in quantitative cavity ring-down spectroscopy", Applied Optics 35, pp. 4112-4116 (1996).
3. K. Lehmann and D. Romanini, "The superposition principle and cavity ring-down spectroscopy", J. Chem Phys. (105) pp. 10263-10277 (1996).

Thrust 2: Engine Simulation and Powertrain Modeling

2.1 A Numerical Model for Jet Primary Breakup

A numerical study was performed to develop a spray model for predicting the atomization and mixing processes in diesel engines. The model was validated for both low- and high-speed jets and was applied to diesel engine simulations. To simulate the spray and mixing in a diesel engine, a Lagrangian approach is employed using the discrete particle concept. The primary breakup of each particle is predicted by a Eulerian method.

2.2 LES Turbulent Combustion Modeling

The work under this project is part of a larger effort at the ERC to develop large eddy simulation (LES) models for engine simulations. Under the ARO program, models for the scalar transport and the turbulence spray models were developed. These are based on the Dynamic Structure tensor coefficient approach developed at the ERC (Pomraning and Rutland, 2002).

2.3 Parallelization for Engine CFD Models

Our goal was to create an efficiently parallel version of the KIVA code. KIVA is a two-phase computation consisting of repeated iterations of a mesh-based phase followed by a particle-based phase. In its current form it executes in a serial, or sequential, manner. Thus, researchers making use of this engineering "tool" are unable to utilize of the latest advances in supercomputing – parallel processing. We have written a message-passing based wrapper which allows the code to be executed on an arbitrary number of processors. This allows DoD scientists and engineers to perform larger simulations which will capture more of the physics and chemistry of unsteady combustion-- exhibiting a higher fidelity to real-world engines. Two strategies were considered; one was eliminated and the other implemented. The first technique was the parallelization via domain decomposition and MPI. The results of the implementation has resulted is two problems, high communication loading and accuracy errors. The communication loading is a result of the numerous variables that must be broadcasted (copied) from the master processor to the slaves, and then gathered (copied) from the slaves to the master. This repetitions has caused wallclock times to increase with the number of processors. The second technique was to utilize OpenMP to parallelize KIVA. OpenMP is a parallel programming model for shared memory multiprocessors. OpenMP directives are instructional notes to any compiler supporting OpenMP. They take the form of source code comments to non-OpenMP environments.

2.4 Advanced Thermal Component Modeling

The primary goal was to develop a diesel engine simulation code suitable for advanced engine cooling system control design, including an all electric cooling system. The two-phase approach was to first improve MTU's existing Vehicle Engine Cooling System Simulation (VECSS), followed by the creation of the Enhanced Vehicle Engine Cooling System Simulation (E-VECSS) by combining the cooling system aspects of VECSS with the engine cycle analysis of a commercial, off-the-shelf code (GT-Power). During both phases, model validation was performed using existing over-the-road engine data as well as control system design. Control system design focused on using electrical components (coolant by-pass valves, electric coolant pumps, and electric fans) to increase performance as defined by fuel economy and engine component temperature criteria. The contributions of this work were not only the development of enhanced diesel engine simulation tools, but also fundamental knowledge on active control of vehicle cooling systems. The remainder of this section has three parts. First, a brief overview of VECSS is provided since it forms the basis for the E-VECSS simulation code. Second, the phase I activity of adding an EGR model to VECSS, in addition to a model based control strategy, is described. Third, the development of E-VECSS and the subsequent all-electric, controlled cooling system study is summarized.

2.5 Incorporation of CFD in System Simulations

The ERC has developed techniques for using artificial neural networks in system simulations that take advantage of CFD results. This approach is well developed and has been used to improve combustion and emissions models in system simulations. Efforts are focused on using optimization techniques to optimize diesel engine combustion and thermal operation

2.5.1 Modeling and Optimization of HSDI Diesel Engines

A combustion chamber geometry design optimization study was performed on a high-speed direct-injection (HSDI) automotive diesel engine at a part-load medium-speed operating condition using both modeling and experiments. A model-based optimization was performed using the KIVA-GA code. This work utilized a newly developed 6-parameter automated grid generation technique that allowed a vast number of piston geometries to be considered during the optimization.

2.5.2 Engine Optimization using Engine System Models

The CFD trained neural networks for engine heat release and emissions are used in cycle simulation codes to simulate full test procedures. These were used in an optimization procedure to obtain the best engine operating parameters (boost level, %EGR, start of injection timing, % fuel in the first pulse of a split pulse injection). These parameters were optimized over a full federal test procedure and used to generate operating maps over the full speed-load range.

2.6 System Robustness Analysis

This document outlines a methodology whereby the robustness of the overall dynamic system of interest to various inputs or effects can be analyzed and displayed graphically. Input data to this methodology could come from test vehicles, test cell experiments, dynamic models, or from functional understanding of proposed designs. The data and models are not linearized, so the operational relationships between variables are preserved. The methodology describes how data sets are handled mathematically for analysis, statistically merged, or specific data sets removed from the overall data that is used for analysis. The output displays system performance data in a statistical format, and compares this format with known or perceived limits on variables of interest. The user can visually see the system robustness, and quickly spot the sensitivity of these constrained variables to other inputs, variables, or even know levels of disturbances that may affect the system.

Thrust 2: Engine Simulation and Powertrain Modeling

2.1 A Numerical Model for Jet Primary Breakup

A one-dimensional model was explored to predict the breakup characteristics of liquid jets. Initial disturbances were imposed on the jet surface at the nozzle exit due to the turbulent and cavitating flow inside the nozzle. The surface disturbances grow up due to the interaction of the liquid and gaseous phases, and the wave growth is tracked using a one-dimensional model that describes mass and momentum conservation. The surface structure is then resolved by a Fast Fourier Transform (FFT), which provides the wavelength composition of the waves. The drop size distribution is evaluated from the Fourier series based on the argument that the drop size is proportional to the wave's wavelength, and the mass associated with a given drop size is proportional to the amplitude of the corresponding wave. For high-speed jets the multi-dimensional surface structure is obtained by mapping the wave composition found in the axial direction to the peripheral direction, based on experimental observations. The liquid core and the surrounding mixing layer that exist in dense spray regions are simulated by a multi-layer drop-stripping model. An area-based breakup criterion is used to predict the breakup time.

The new breakup model was applied to fuel spray simulations using a multi-dimensional CFD code (KIVA3v), where the primary breakup is calculated from a library built from the one-dimensional breakup model. Secondary breakups are calculated using a hybrid KH-RT model. Drop collision is calculated using the model of O'Rourke. The predicted breakup length, spray liquid tip penetration and drop size were compared with experimental data and good agreement was found. The effects of multi-component fuel vaporization were also investigated.

As a final application of the models, a direct-injection compression-ignition engine was simulated to study the air-fuel mixing processes. The prediction of in-cylinder pressure, heat release rate and NOx and soot emissions were compared successfully with experimental data, as shown in Figs. 2.1-1 and 2.1-2. The present results demonstrate that the primary atomization model has a significant effect on NOx and particulate, soot emissions, but has a lesser effect on cylinder pressure, heat release and liquid jet penetration lengths.

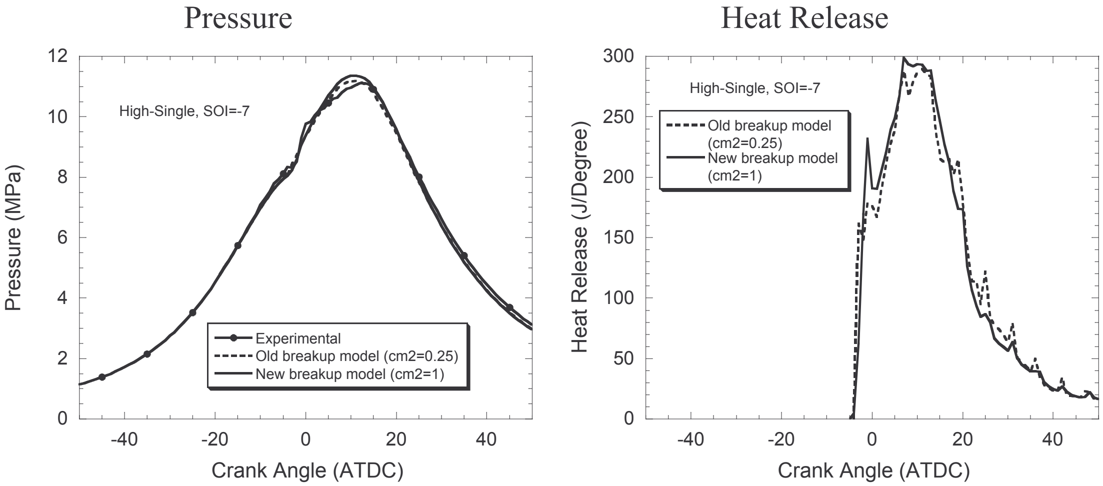
Pressure

Heat Release

Figure 2.1-1 Comparison of in-cylinder pressure and heat release for high-load single-injection with SOI=-7.

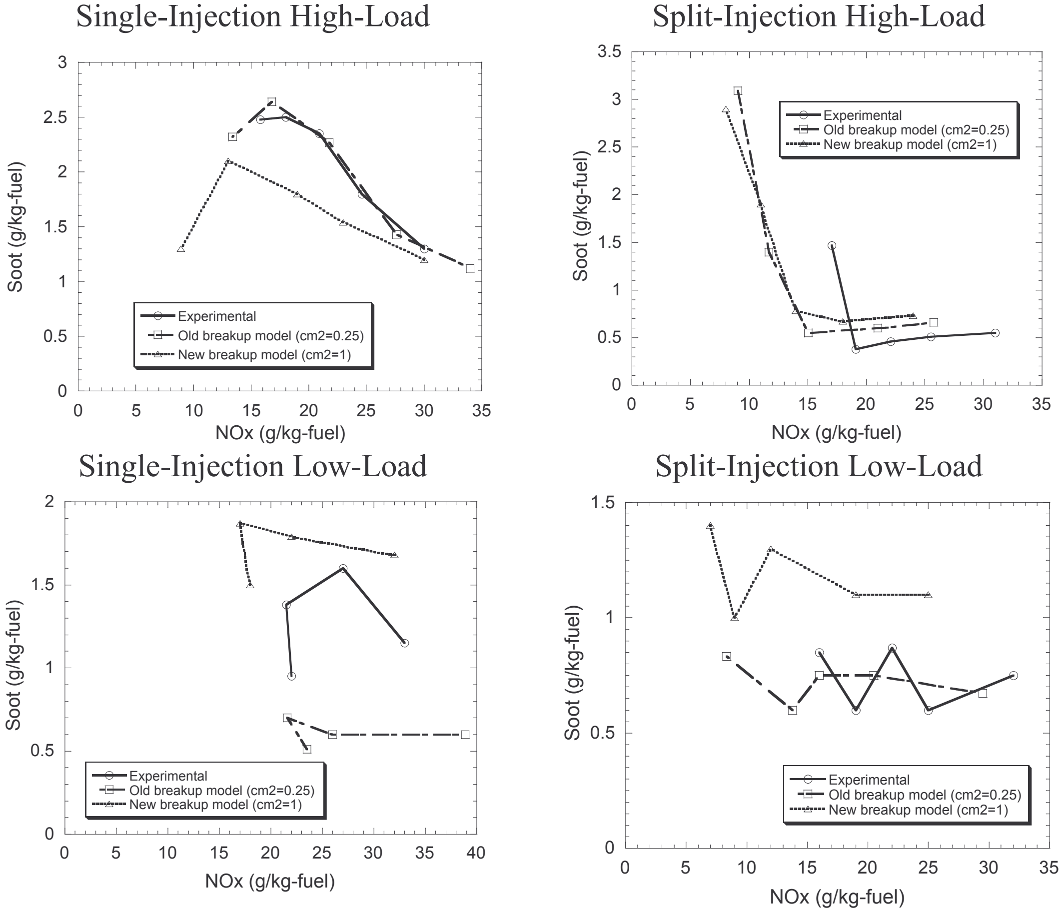
Single-Injection High-Load

Split-Injection High-Load

Single-Injection Low-Load

Split-Injection Low-Load

Figure 2.1-2 Comparisons of emissions for other operating conditions. (HD: high-load split-injection; LS: low-load single-injection; LD: low-load split injection)

2.2 LES Turbulent Combustion Modeling

The dynamic structure approach developed at the ERC uses a tensor coefficient and the dynamic procedure that results in a mathematically sound and robust sub-grid turbulence model (Pomraning and Rutland, 2002). This has been expanded under this program to include scalar transport and spray modeling for combustion modeling.

The major terms that require modeling in scalar transport are the sub-grid scalar flux and the scalar dissipation. The following dynamic structure (DS) model for the subgrid flux term was implemented in KIVA. :

$$\tau_{i,\phi} \approx \frac{\theta}{\Theta} L_{i,\phi} \equiv \frac{\overline{\phi\phi} - \bar{\phi}\bar{\phi}}{\widehat{\bar{\phi}\bar{\phi}} - \hat{\bar{\phi}}\hat{\bar{\phi}}} \left[\widehat{u_i \bar{\phi}} - \hat{\bar{u}}_i \hat{\bar{\phi}} \right]$$

Here, ϕ is taken to be one of the following: the mass fraction of every species including passive scalars, SGS kinetic energy, resolved mixture fraction, and SGS mixture fraction variance. The DS approach for the scalar dissipation leads to the following model:

$$\chi_\phi = C \left[\widehat{\frac{\partial\bar{\phi}}{\partial x_i} \frac{\partial\bar{\phi}}{\partial x_i}} - \frac{\partial\hat{\bar{\phi}}}{\partial x_i} \frac{\partial\hat{\bar{\phi}}}{\partial x_i} \right]$$

where the coefficient, *C*, can be obtained either dynamically or as a constant. A comparison of the scalar flux model with a traditional eddy viscosity model against DNS results in shown in Fig. 2.2-1a. The DS model clearly out performs the eddy viscosity model. In Figure 2.2.-1b the error obtained from comparison with DNS results of the DS scalar dissipation and a simple mixing length model are shown. Again, the DS model has a significantly smaller error.

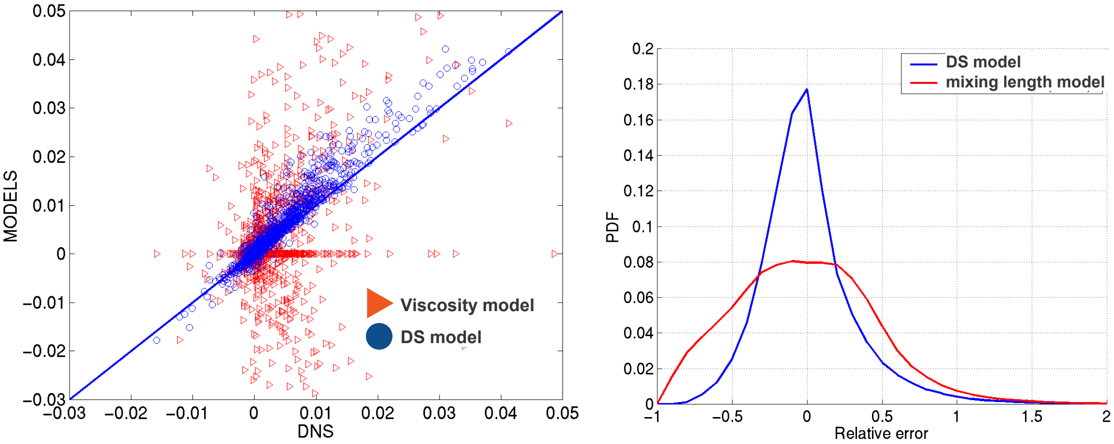

Figure 2.2-1: Comparison of DS models with traditional models using DNS results: (a) sub-grid scalar flux on left, (b) scalar dissipation on right.

To test the models in an application an LES of coaxial combustor following the experiments of Spadaccini et al. (1976) was performed. For the chemistry, the LES Flamelet Timescale Model developed at the ERC (Rao and Rutland, 2003) was implemented. Several configurations of computational grid were used: cylindrical meshes with 90, 180 and 360-degree sector, and a Cartesian mesh. The latter seemed to give the best results since sector meshes as they are implemented in KIVA-3V do not facilitate mixing near the central axis. Figures 2.2-2 and 2.2-3 show an example of temperature contours and a plot comparing the simulation results with the experimental results for the radial profile of the CO2 concentration.

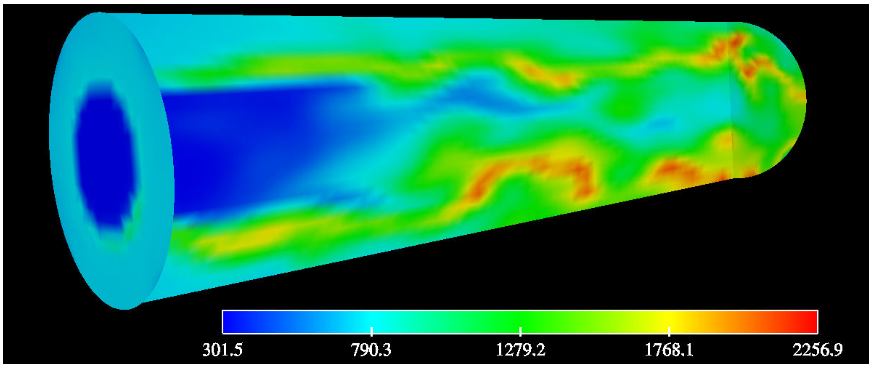

Figure 2.2-2. Temperature distribution in the LES KIVA-3V simulation of coaxial combustor. Fuel and air enter from the left in a co-flow configuration.

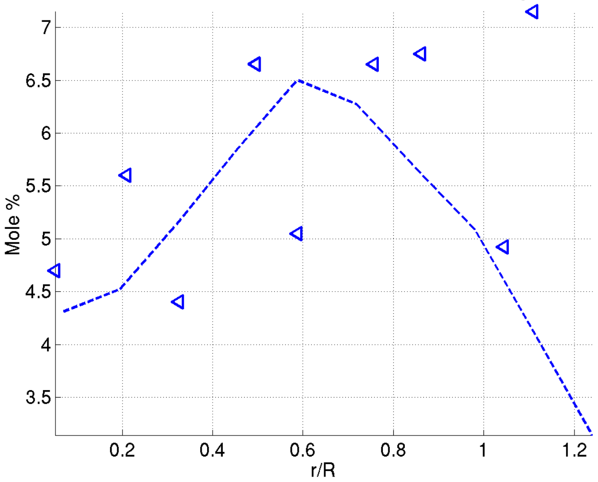

Figure 2.2-3. Radial profiles of CO2 molar fraction: experimental results (triangles) and LES simulation (dashed line).

A Sub-Grid Droplet Source (SGDS) Spray model, which takes into account the effect of droplet existence on the sub-grid scales of a two-phase turbulent flow, was developed and implemented into the KIVA-3V engine simulation code. This approach simulates the particles in a Lagrangian manner and the continuous phase in an Eulerian manner with two-way coupling of interactions between spray droplets and the carrier gas. The SGDS spray model is used in conjunction with a Dynamic Structure Large Eddy Simulation (LES) turbulence model (Pomraning and Rutland, 2002) for the momentum transport. The dynamic structure model is a dynamic, one equation, non-viscosity model, which uses a transport equation for the sub-grid kinetic energy of the flow field. This dynamic structure model can capture the flow field more accurately than conventional viscosity-based models and gives better estimates of the quantities such as the sub-grid kinetic energy that are needed for spray modeling.

In the SGDS model, the production term in the sub-grid kinetic energy equation due to spray droplets is modeled to include the interaction of droplets with the continuous phase via the drag force. The model also considers the effect of both the sub-grid and resolved scales on the spray droplets. A method is adopted for the determination of sub-grid continuous phase velocities at the droplet locations. This approach assumes a Gaussian distribution for the sub-grid turbulent velocities and that each droplet interacts with these fluctuations for its ‘eddy residence time’.

Direct Numerical Simulation (DNS) data of high Reynolds number ($Re_p = 102$) two-phase turbulent flow with high-speed spray droplets from the S3D code simulation is used for a priori testing of the model. Comparison between the exact and modeled spray droplet source terms in the sub-grid kinetic equation shows very good results as indicated by the example in Figure 2.2-4. The simulated results for liquid penetration length and spray dispersion are also presented in comparison to the diesel spray experiments conducted by Siebers, 1998 and Kim and Ghandhi, 2001 (for example see Figures 2.2-5 and 2.2-6).

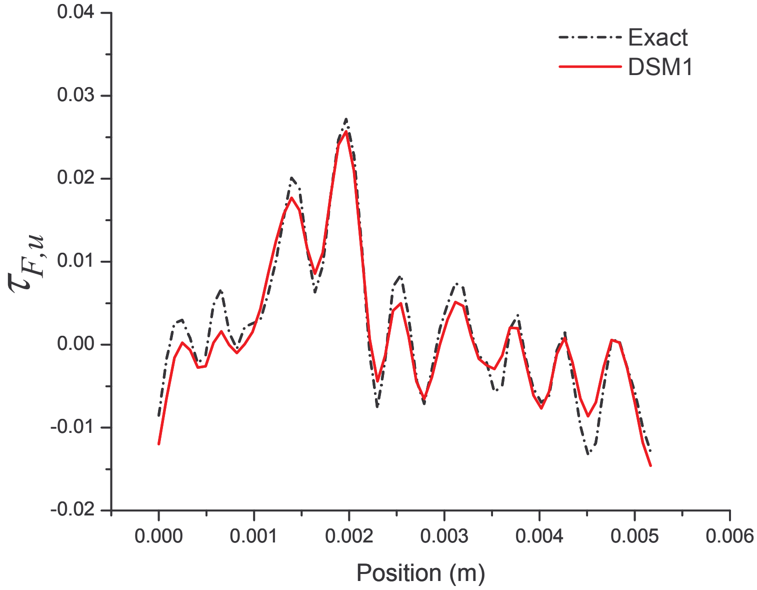

Figure 2.2-4: Comparison of DNS results (dashed line) and LES model for spray source term in sub-grid kinetic energy equation.

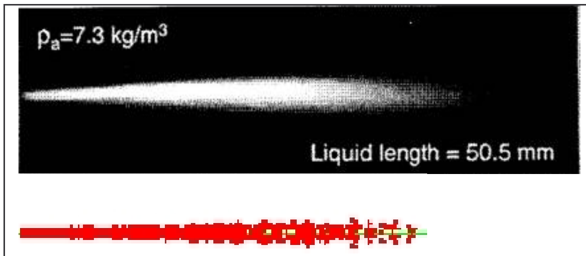

Figure 2.2-5: Experimental (top) and predicted spray images (bottom) for DF2. The chamber temperature, density, injection pressure and orifice diameter are 1000K, 7.3 kg/m^3, 135 MPa and 246 *u*m respectively

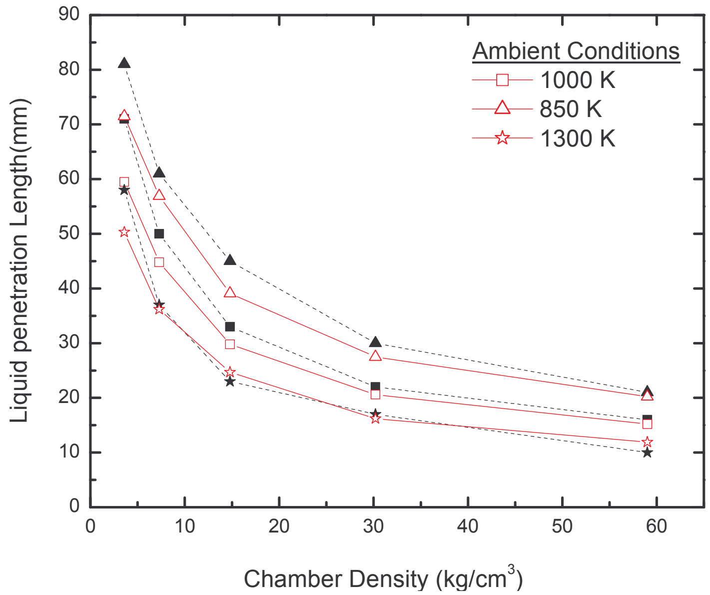

Figure 2.2-6: Liquid penetration length as a function of chamber density for DF2. The values in the legend are ambient temperature. The orifice diameter and injection pressure were 0.246 mm and 135 MPa respectively. Solid lines represent the simulation results and dotted lines represent the experimental results.

2.3 Parallelization for Engine CFD Models

KIVA has been parallelized. The KIVA code now runs on an arbitrary number of processors. Parallelization accomplished via platform-independent OpenMP. Accuracy, precision and consistency tests were performed and the solutions were shown to be identical to those of the serial KIVA code. Our results indicated that parallelization was not beneficial for small problems. Parallelization is beneficial with large problems of 100,000+ vertices.

2.4 Advanced Thermal Component Modeling

VECSS Summary The Vehicle Engine Cooling System Simulation software (VECSS) predicts the performance of a heavy duty (HD) truck with an emphasis on modeling all fluid and air handling components and systems [Arici, et al., 1999a, Arici, et al., 1999b]. This includes models for the engine, radiator, charge air cooler, turbocharger, cab, engine compartment airflow, oil circuit, and the coolant circuit.

The VECSS is composed of various subroutines each representing a different component of the engine or truck, including models for the engine, radiator, EGR cooler, turbocharger, charge air cooler (CAC), fan, ram air/engine compartment airflow circuit, coolant circuit, cab heater, cab, thermal control devices (radiator thermostat, fan control, oil thermostat), oil circuit, oil cooler, and oil filter. These components are modeled with transient or quasi-steady governing equations in order to predict the steady state as well as the transient operation since the models are updated each second of truck running time. The models are designed to have the flexibility to be replaced with models with different features as the components are specified through data files relating the physical dimensions and attributes. This systematic approach makes it possible to vary components in parametric studies and to make future improvements, additions and updates to VECSS.

The principal inputs to VECSS are the fuel flow rate, engine speed, vehicle speed, wind speed, and ambient temperature, pressure and humidity and are illustrated in Figure 2.4-1. The fuel flow rate, engine speed, and vehicle speed are specified through the input files as either run-time data files or as step inputs. The ambient conditions are specified in an input file and are held constant during the simulation.

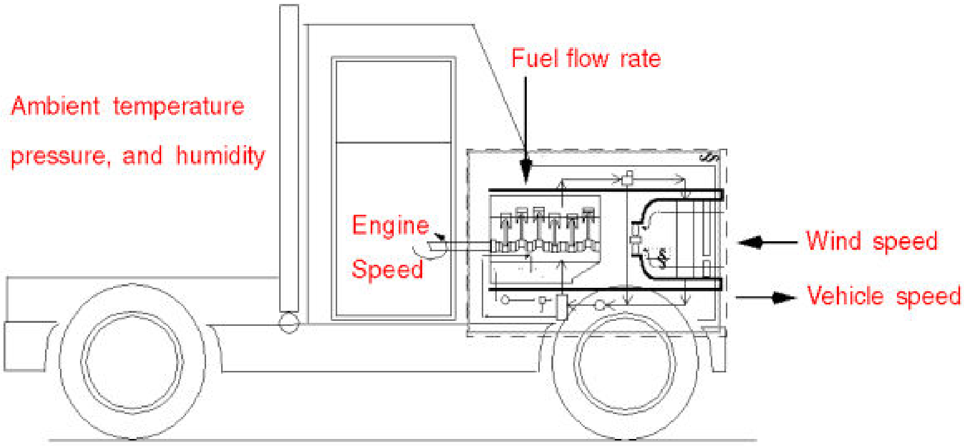

Figure 2.4-1. Overview of the VECSS time-history inputs.

<u>Phase I – Incorporation of EGR and EGR Control into VECSS</u> The goals of this phase were to design, model, and simulate a controlled cooling system with an electric water pump to regulate the EGR cooling. First, EGR was modeled in the VECSS so that the effects of EGR on the cooling system could be analyzed. The research proceeded with the design of an advanced control system integrating a secondary variable-flow electric water pump to control the EGR cooling. The performance of this electronic controlled EGR cooling system was then compared to the performance of an uncontrolled EGR cooling system. Finally, in order to realize the full benefits of controlled cooling, the controlled EGR cooling system was combined with a previously developed controlled engine cooling system.

Simulation results indicated that a controlled EGR cooling system could maintain the EGR cooler outlet exhaust temperature at 130□8C, as compared to 110□60C for an EGR cooling system without coolant flow control [Chalgren, 2000, Chalgren, et al., 2002]. This was an important result for two reasons. First, by reducing large temperature variations, EGR cooler service life can be increased by reducing fouling caused by sulfuric acid production during low temperature excursions. Fouling deposits can also degrade the performance of the valves, cylinder liner, piston, and the valve guides, stems, and seals. Second, high EGR cooler outlet exhaust temperatures are not as effective at reducing NOx and can increase the operating temperature of the engine and decrease fuel economy.

In addition to maintaining consistent EGR cooler outlet exhaust temperatures, the controlled EGR cooling, combined with a controlled engine cooling system, decreased warm-up times for fast warmup of aftertreatment devices, decreased power consumption, and provided better engine temperature control. In the remainder of this section, the details of the model development are summarized. This is followed by a description of the EGR control strategy and its performance results.

EGR Model Two different EGR coolers were modeled in VECSS. One was based on full coolant flow with the cooler located between the conventional water pump and the oil cooler, herein referred to as uncontrolled EGR cooling (UCEGRC) and is shown in Figure 2.4-2. This cooler was designed to offer sufficient flow area for a low water pressure drop, since the coolant flowing through this cooler must also flow through the oil cooler, engine block and cylinder head. The overall heat transfer coefficient and heat transfer area values for this cooler were based on the analysis of EGR cooler performance data using the NTU method (number of transfer units). The other heat exchanger model, shown in Figure 2.3-3, was a low coolant flow design and used a secondary electric pump to control the water flow rate to the cooler. The product of the overall heat transfer coefficient and the heat transfer area of this cooler was 14% larger than the full-flow cooler of the UCEGRC. This size increase was necessary for increased effectiveness, especially at lower coolant flow rates.

Gas and coolant outlet temperatures were computed through energy balances, allowing for changing mixture compositions and temperatures. Any chemical reactions or phase changes in the cooler were assumed not to be of significance to the heat transfer and outlet temperatures. Also, the cooler was assumed to have the same performance characteristics over time (no fouling). A 1 second time lag was incorporated into the cooler model to approximate the dynamics associated with transient heat transfer in the cooler.

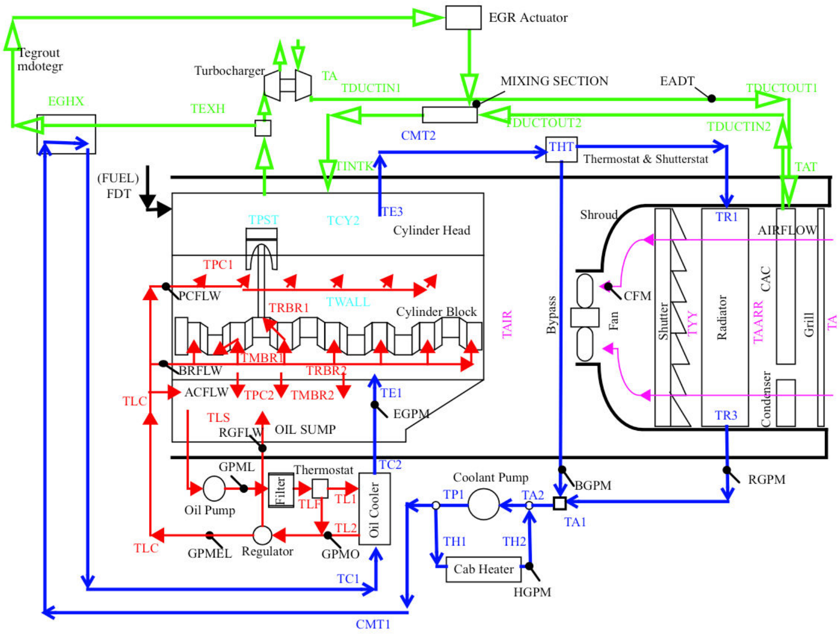

Figure 2.4-2. Uncontrolled EGR cooling system (UCEGRC) schematic.

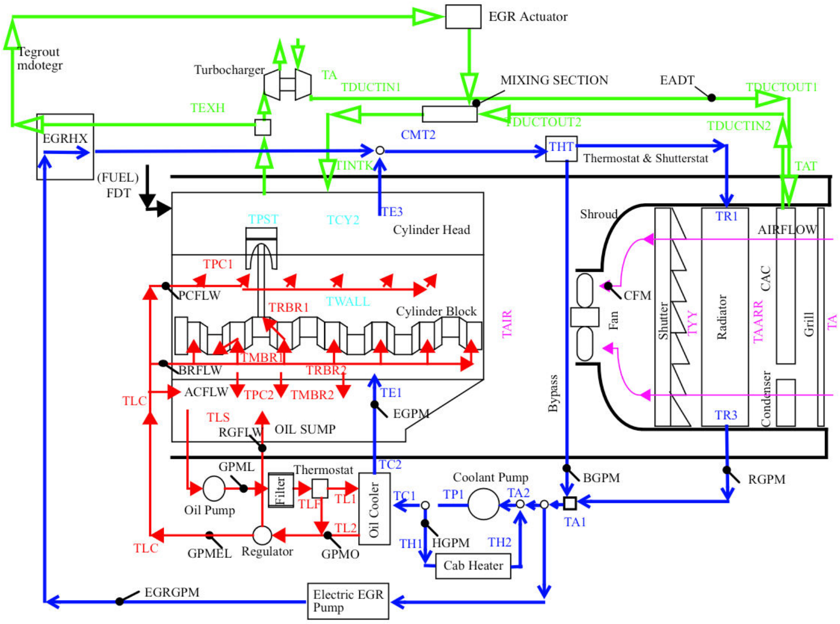

Figure 2.4-3. Controlled EGR cooling system (CEGRC) schematic.

EGR Control Strategy and Results The control objective was to maintain the EGR cooler outlet exhaust temperature (TEGROUT) to a set value of 130C using the secondary electric coolant pump shown in Figure 2.3-3. VECSS was used to model a Freightliner FLD12064ST heavy duty truck with a Detroit Diesel Corporation Series 60 12.7 liter engine. A gain scheduled Proportional-Integral-Derivative (PID) controller was used in conjunction with a feed-forward pump speed command as shown in Figure 2.4-4.

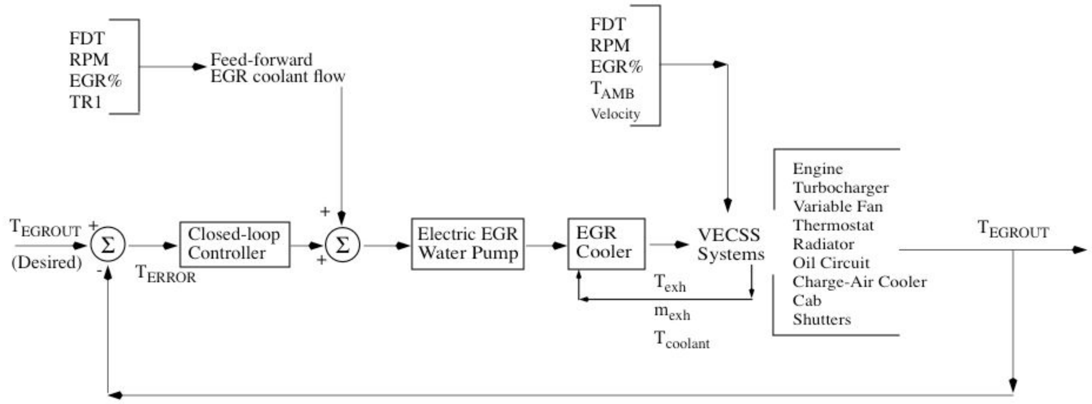

Figure 2.4-4. Controlled electric EGR coolant pump block diagram.

It should be noted that engine exhaust temperatures change rapidly with changes in the fueling rate. The high amplitude/high frequency characteristics of the exhaust temperature variation necessitate a fast response from the water pump to adjust the heat transfer rate in order to maintain TEGROUT. As simulation results showed, accurate feed-forward actuation of the coolant pump was necessary to maintain a sufficiently constant EGR cooler outlet exhaust temperature due to the high amplitude random disturbances, characteristic of the exhaust gas temperature.

The conventional engine coolant pump was kept in the CEGRC of Figure 2.4-3 for several reasons. First, the mechanical pump is durable and is established in the heavy-duty industry. Second, the electric pump will only require electrical power to pump coolant through the EGR cooler, radiator, and bypass with this setup. The electrical power specifications for electric pump(s) to power the entire coolant system are too great for current alternators and 24V electrical systems. Third, the controlled EGR cooling system provided more coolant flow through the radiator and bypass than the UCEGRC, thus the radiator rejected more heat with the CEGRC provided there was enough airflow passing through the radiator. The variable flow rate of the electric water pump enabled it to run at the speed necessary for the particular engine operating condition, whereas mechanically driven pumps would need to be sized to provide adequate cooling under extreme conditions since the pump flow rate is coupled with engine speed.

As mentioned above, there were two main components to the EGR coolant pump control strategy: (1) a feed-forward command and (2) a gain-scheduled PID generated command. The feed-forward command was generated based on the steady-state heat exchanger equations, and required a real-time numerical solution since closed-form solutions did not exist. The PID gain-scheduling was based on the coolant flow rate and captured a wide variety of different engine operating conditions from warm-up, to heavy-load.

The controlled EGR cooling system (CEGRC) was compared to the uncontrolled case (UCEGRC) for a variety of operating conditions. Experimentally obtained, over-the-road time-histories were used to “drive” the simulations. A typical comparison of the ability to maintain TEGROUT at a consistent level is shown in Figure 2.4-5. The uncontrolled

TEGROUT was approximately 110C with 60C dispersions. In contrast, the controlled TEGROUT maintained 130C with only 8C dispersions. While the EGR pump consumed roughly 40W, the fan power was decreased.

The final study combined the CEGRC with a previously developed Controlled Engine Cooling system (CEC) [Arici, et al., 2001]. The resulting system consisted of not only the electrically controlled EGR coolant pump, but also an electrically controlled main coolant pump and an electric bypass valve. The combination of the CEGRC with the CEC resulted in additional power savings due to fan on-time reductions and improved cylinder wall temperatures. The results of this study, in terms of fan and pump power consumption (Figure 2.4-6) and engine warm-up time (Figure 2.4-7) are shown below.

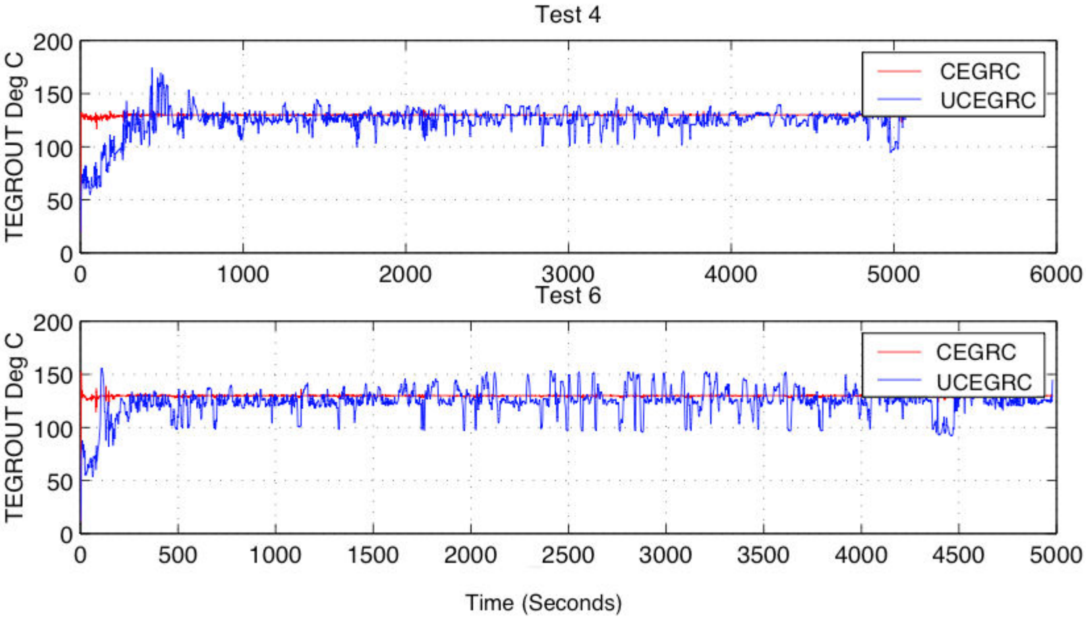

Figure 2.4-5. Comparison of controlled versus uncontrolled EGR exhaust outlet temperature (TEGROUT). The “Test 4” case was at 55% load while the “Test 6” case was a 100% load case.

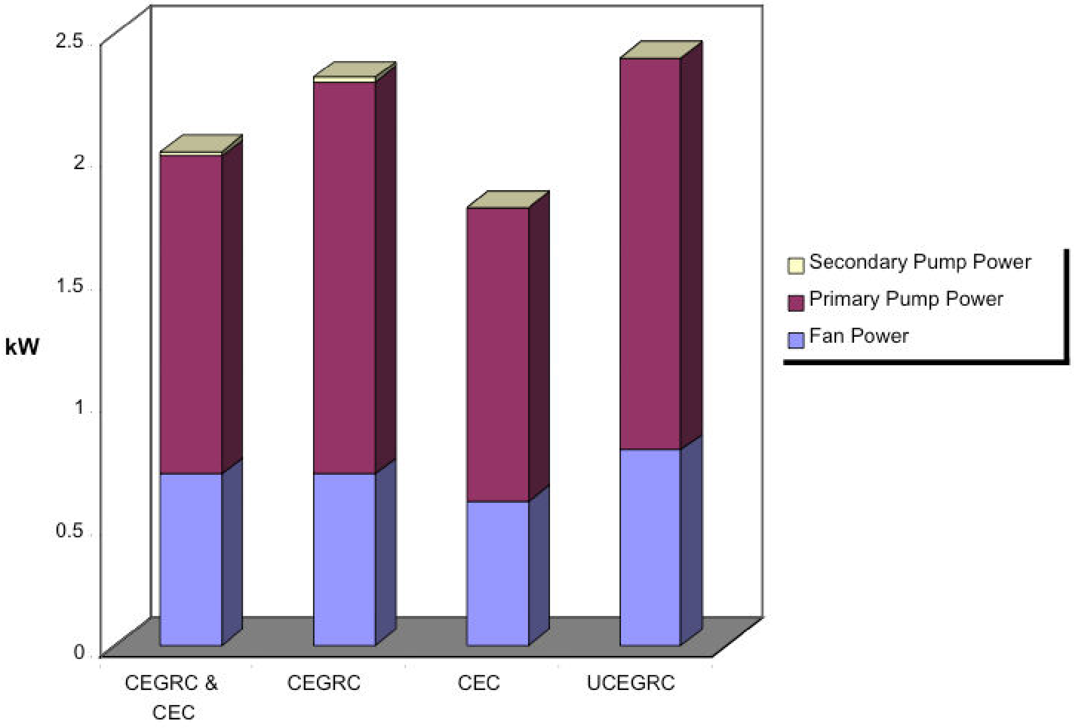

Figure 2.4-6. Steady state power consumption of both pumps and the fan at 1500 rpm, 50% load and 55 mph.

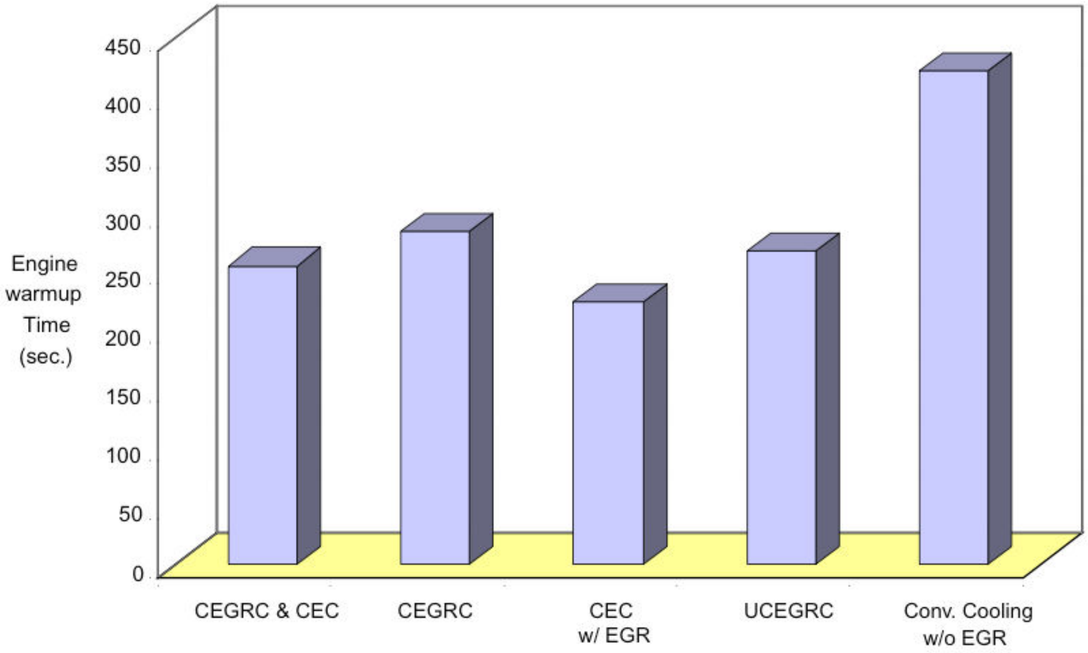

Figure 2.4-7. Engine warm-up times for different cooling system configurations at 1500 rpm, 50% load and 21C ambient temperature.

Phase II – Development of E-VECSS and All-Electric Cooling System Control The Vehicle Engine Cooling System Simulation (VECSS) was enhanced by linking it with GT-Power, via MATLAB/Simulink, for the engine/cycle analysis and is shown in Figure 2.4-8. Enhanced VECSS (E-VECSS) predicted the effects of cooling system performance on engine performance including accessory power and fuel conversion efficiency. Along with the engine cycle, modeled components included the engine manifolds, turbocharger, radiator, charge-air-cooler, engine oil circuit, oil cooler, cab heater, coolant pump, thermostat, and fan. Such a model can be used for conventional cooling system design as well as controlled cooling system development and evaluation.

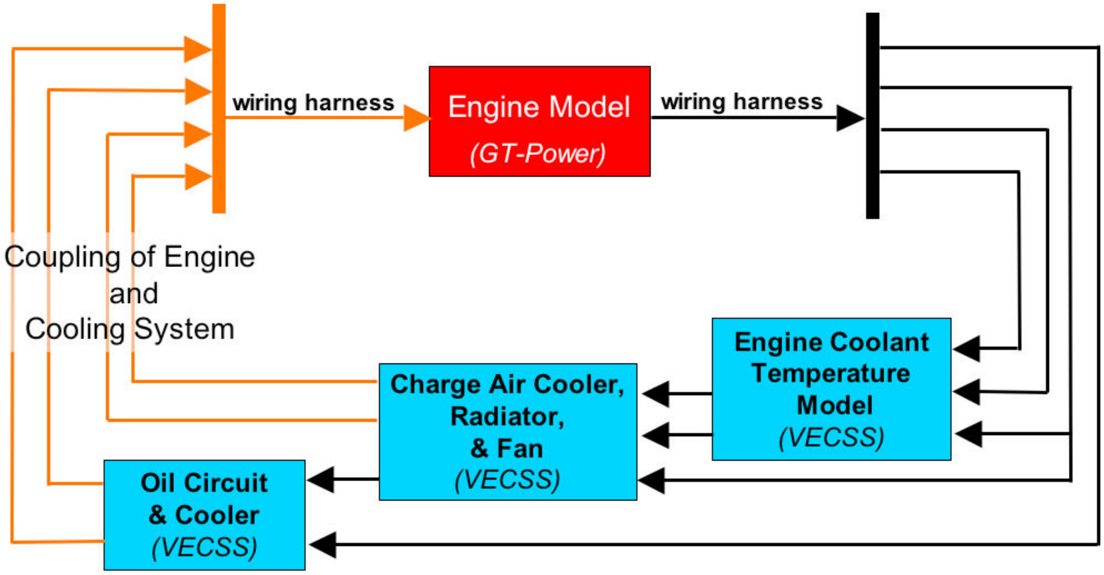

Figure 2.4-8. Illustration of E-VECSS showing the incorporation of GT-Power for cycle analysis.

The Enhanced Vehicle Engine Cooling System Simulation (E-VECSS) was used to develop and simulate an actively controlled electric cooling system for a Freightliner FLD120 with a Detroit Diesel Series 60 engine. The conventional pump, fan, and thermostat models where replaced by an electric pump, electric fans, and an actuator as shown in Figure 2.4-9.

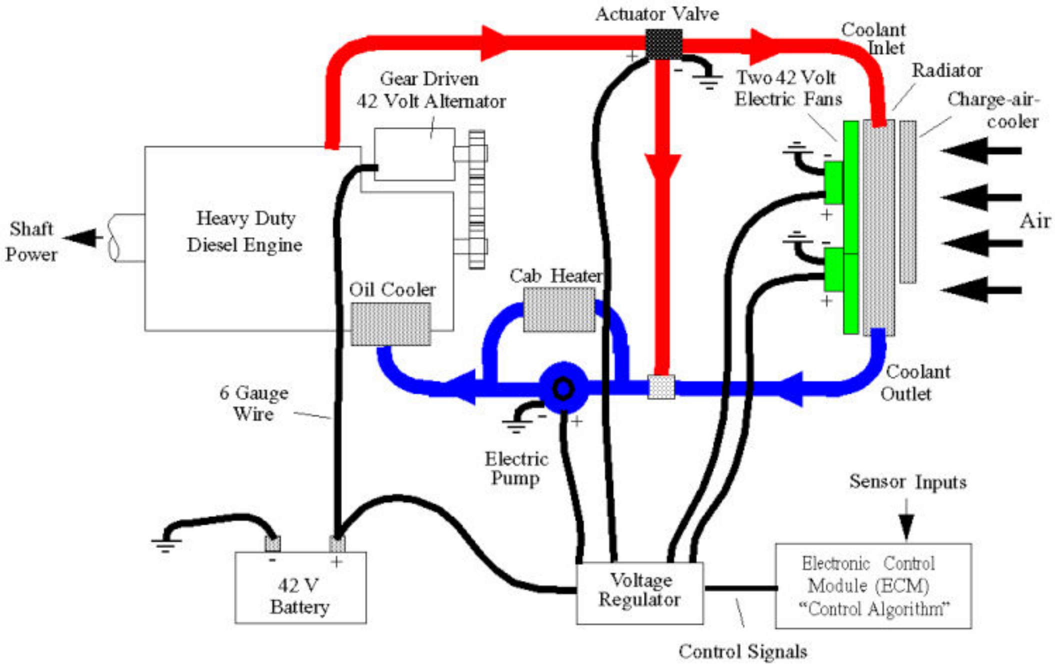

Figure 2.4-9. All electric 42 volt cooling system layout.

A two mode active control scheme was developed and used both feed-forward and feedback loops for management of energy in the cooling system based on vehicle and operating conditions. With active control, engine metal temperatures were maintained while simultaneously minimizing accessory power. Accessory power savings ultimately translated into a fuel consumption reduction. Compensation for coolant transport delays and transient radiator operation was found to be an important issue and was compensated by the control strategy. Results of E-VECSS simulations showed the controlled cooling system improved gas side cylinder wall temperature control, as compared to the conventional system, while still reducing fan on time and fuel consumption. In the remainder of this section the E-VECSS model is summarized. This is followed by a description of the 42 volt, all-electric controlled cooling system and its performance.

E-VECSS Model Development Data from a Freightliner FLD12064ST heavy duty truck with a Detroit Diesel Corporation Series 60 12.7 liter engine was used to develop the engine in E-VECSS within the GT-Power framework. Rated to 370 hp at 1800 rpm, the turbocharged and aftercooled DDC S60 is the same engine which was previously modeled in VECSS. The engine is a six cylinder in-line configuration with four valves per cylinder and direct injection. All six cylinders of the engine were modeled independently. Models of the intake and exhaust manifolds are also included in GT-Power. Integration of continuity, energy, and momentum equations were performed over time for discretized volumes of the manifolds to solve for the airflow rate, pressure drop, temperature, and pressure waves throughout the flow passage. A turbocharger model, including the turbine and compressor inertia, was linked to the intake and exhaust manifolds.

The general configuration of the heat exchangers in the airflow path of the Freightliner FLD120 truck is shown in Figure 9. The modeled Freightliner configuration included a charge-air-cooler in series with a radiator and a puller fan downstream of the heat exchangers.

The conventional mechanical fan was modeled using a standard performance curve (fan static pressure vs. airflow rate). Fan data was only available for one fan speed (2000 rpm). The conventional fan was coupled to the engine speed and coolant temperature by pulleys and a variable speed viscous fan clutch. The flow rate, fan pressure, and power was approximated at fan speeds other than 2000 rpm using well-established fan laws.

The radiator heat transfer model was very similar in structure and methodology to the charge-air-cooler model, with only a few subtle differences [Luptowski, 2003].

Engine cycle analysis was done in GT-Power while the cooling system was incorporated into MATLAB/Simulink S-functions. For a fully coupled simulation, the two models were dynamically linked together. This is made possible by the `WiringHarness' component in GT-Power which allows signals to be sent between GT-Power and MATLAB/Simulink while both are running.

Given adequate boundary conditions, the engine model calculates a heat transfer rate to the coolant from the cylinder wall and head. These values are then sent through the wiring harness to the cooling model. Four differential equations are then solved in the cooling system model to determine the engine coolant temperatures and the bulk temperature of the external block metal and external head metal [Luptowski, 2003].

After completing the E-VECSS model development, its results were compared to existing experimental cooling system data and to the output of the VECSS for a variety of operating conditions.

All-Electric Controlled Cooling System and Results The advent of 42-volt automotive systems offers the possibility of a fully electric cooling system in a heavy duty diesel truck. Electric cooling components alone, however, offer little benefit without a proper control strategy. The Enhanced Vehicle Engine Cooling System Simulation (E-VECSS) was used to develop and simulate an actively controlled electric cooling system for the Freightliner FLD120 with a Detroit Diesel Series 60 engine model described above. The conventional pump, fan, and thermostat models where replaced by an electric pump, electric fans, and an actuator. A two mode active control scheme used both feed-forward and feedback loops for management of energy in the cooling system based on vehicle and operating conditions. With active control, engine metal temperatures were maintained while simultaneously reducing accessory power. Accessory power savings ultimately translated into a fuel consumption reduction. Compensation for coolant transport delays and transient radiator operation was needed as these quantities, often neglected in the existing literature, were found to be non-negligible.

A simple 1-D heat transfer model was used for feed-forward calculation of the coolant flow rate required for the engine as shown in Figure 2.4-10. For the calculations, the gas side cylinder wall temperature was assumed to be 187C and the engine coolant outlet temperature was assumed to be 90C. The fan and bypass actuator feed-forward commands were generated by minimizing fan power. A detailed description of this approach is described by Luptowski [2003]. As mentioned above, coolant passage time delays were found to be significant. A Smith-Predictor approach was used to mitigate their destabilizing effects. The entire control strategy is shown in Figure 2.4-11.

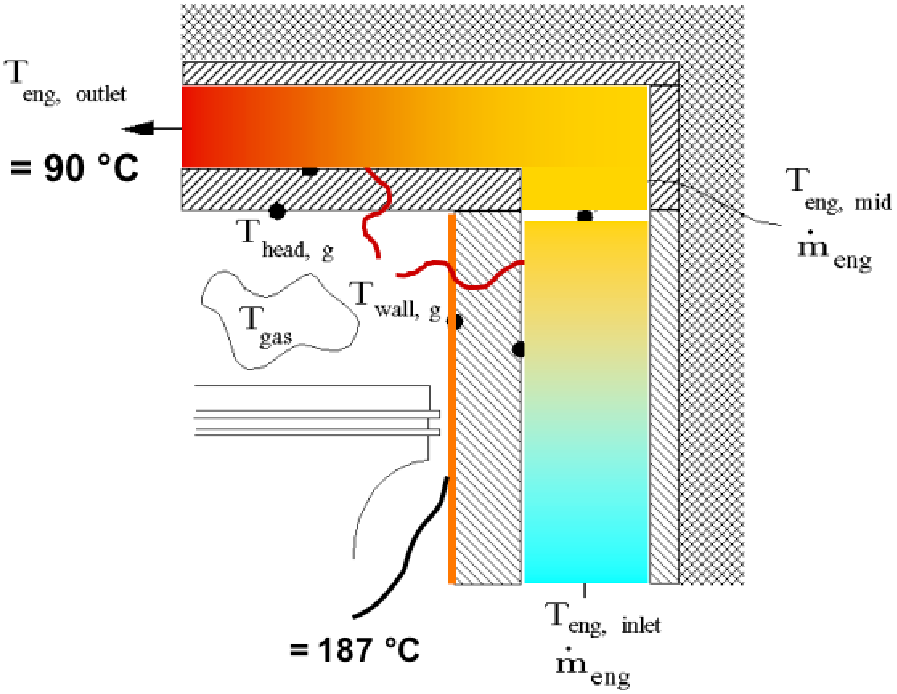

Figure 2.4-10. Cylinder and coolant passages used for development of the feed forward control law for coolant pump commands.

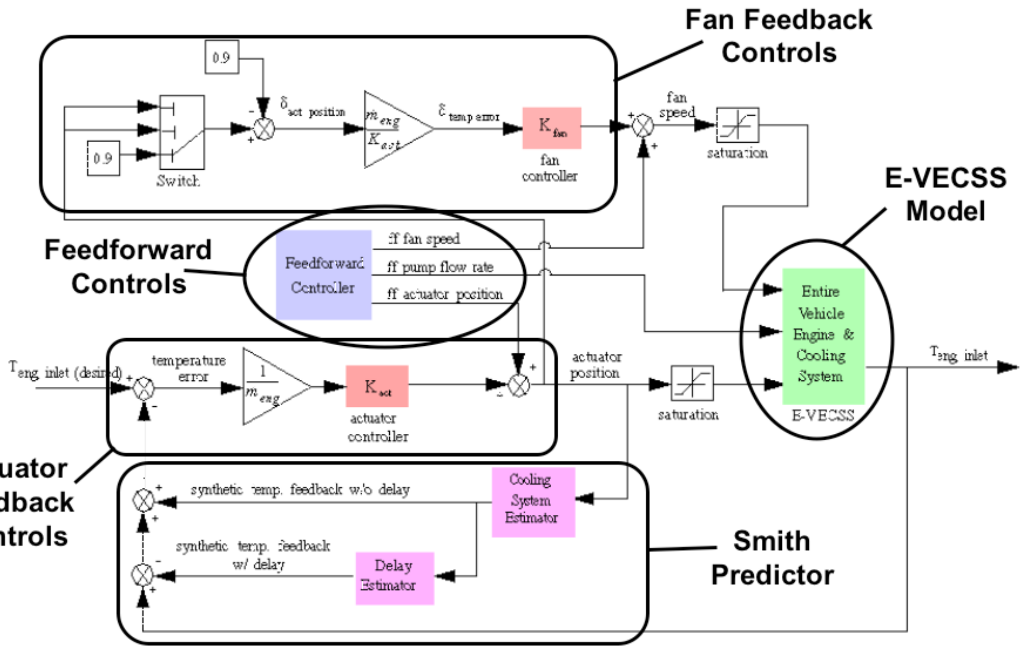

Figure 2.4-11. Complete control strategy including both feed forward and feedback elements.

Typical closed-loop control results are shown in Figure 2.4-12. As in the Phase I work, the simulation was "driven" using experimentally obtained, over-the-road data. In this case the truck was operated at 67% load and –20C ambient temperature. For this case, the average accessory power savings was 1.52 kW and the predicted fuel consumption savings was 1.47%. This illustrated the ability of the all-electric cooling system to yield savings in some operating regimes, mainly by reducing fan on-time.

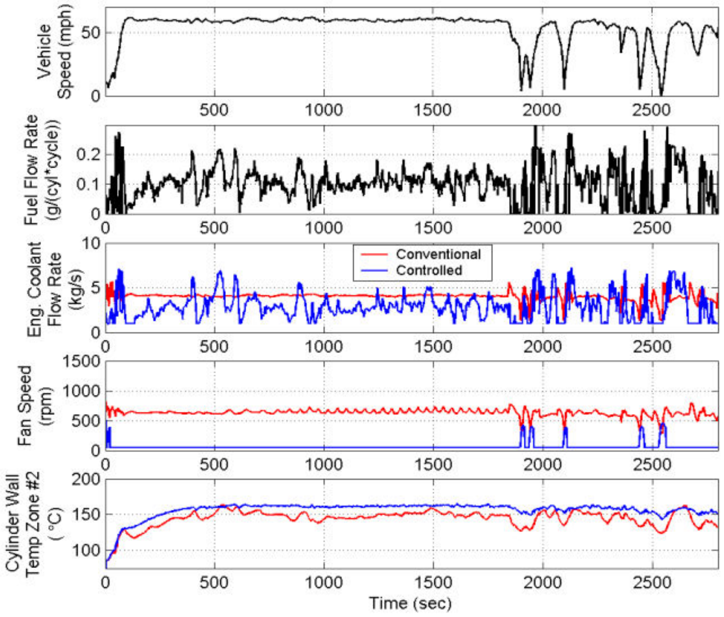

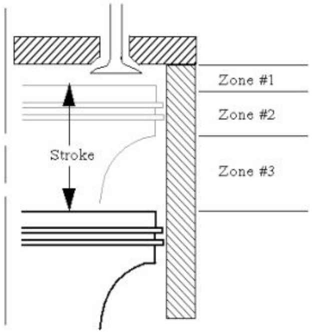

Figure 2.4-12. Controlled versus uncontrolled simulated engine data. The truck is operating at 67% load with an ambient temperature of –20C.

2.5 Incorporation of CFD in System Simulations

2.5.1 Modeling and Optimization of HSDI Diesel Engines

A model-based combustion chamber geometry design optimization was performed using the KIVA-GA code. This work utilized a newly developed 6-parameter automated grid generation technique that allowed a vast number of piston geometries to be considered during the optimization. Other salient parameters were included that are known to have an interaction with the chamber geometry. They included the start of injection (SOI) timing, swirl ratio (SR), exhaust gas recirculation percentage (EGR), injection pressure, and the compression ratio (CR). The measure of design fitness used included NO_x, soot, unburned hydrocarbon (HC), and CO emissions, as well as the fuel consumption. Subsequently, an experimental parametric study was performed using the piston geometry found by the numerical optimization. The model-based optimum design parameters were used as a starting point for the experiments. Parameters varied included the SOI timing, EGR, SR, boost pressure, and injection pressure. The resulting design features a novel chamber geometry that was demonstrated to be able to achieve low emissions, as described by Wickman et al. SAE 2003-01-0348.

2.5.2 Engine Optimization using Engine System Models

This project expands on the use of neural networks for engine computations. One reason for using neural networks is to capture the accuracy of multi-dimensional CFD calculations or experimental data while saving computational time, so that system simulations can be performed within a reasonable time frame. A schematic of the technique is shown in Fig. 2.5.2-1.

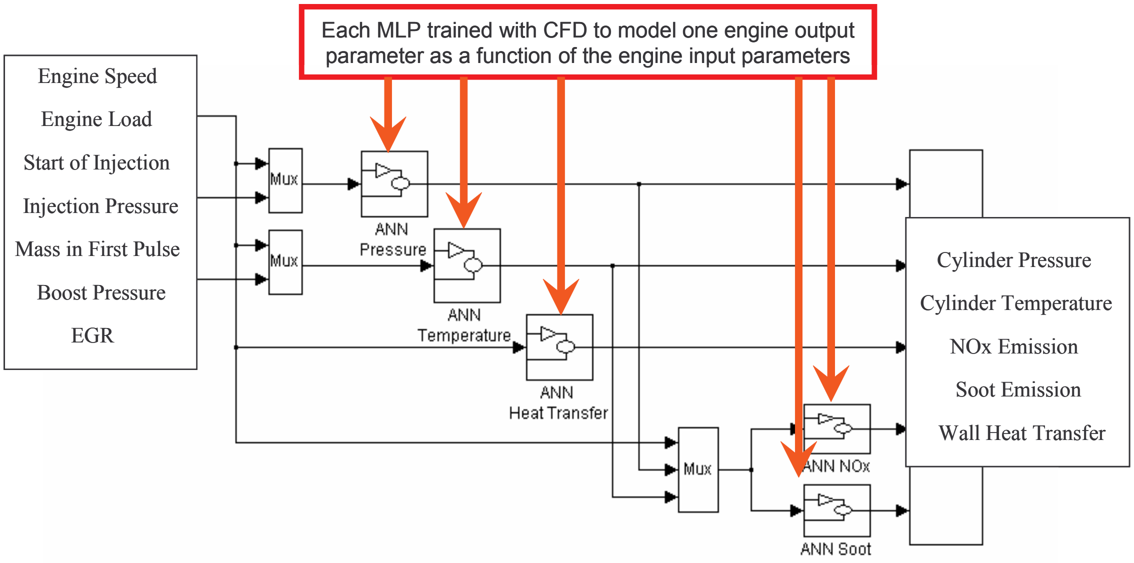
Each MLP trained with CFD to model one engine output parameter as a function of the engine input parameters

Figure 2.5.2-1: Schematic showing Simulink based model that uses Multi-Layer Perceptron (MLP) neural networks to model the major in-cylinder processes. This model is also used within GT-Power for a full system cycle simulation.

Three methods to improve upon neural network predictions were recently developed. Improvement is demonstrated for in-cylinder pressure predictions in particular. The first method incorporates a physical combustion model within the transfer function of the neural network, so that the network predictions incorporate physical relationships as well as mathematical models to fit the data. The second method shows how partitioning the data into different regimes based on different physical processes, and training different networks for different regimes, improves the accuracy of predictions. The third method shows how using an ensemble of different networks based on engine operating parameters can provide greater accuracy than each of the individual networks. Although these methods have been implemented for engine computations, they might hold promise for other applications too.

Neural networks are useful tools for optimization studies since they are very fast, so that while capturing the accuracy of multi-dimensional CFD calculations or experimental data, they can be run numerous times as required by many optimization techniques. A set of neural networks trained on a multi-dimensional CFD code to predict pressure, temperature, heat flux, torque and emissions, have been used by a genetic algorithm in combination with a hill-climbing type algorithm to optimize operating parameters of a diesel engine over the entire speed-torque map of the engine.

The optimized parameters are mass of fuel injected per cycle, shape of the injection profile for dual split injection, start of injection, EGR level and boost pressure. These have been optimized for minimum emissions. These optimized parameters were used as inputs to another set of neural networks that were then trained to predict the optimized operating conditions for each speed-torque point of the engine (see Fig. 2.5.2-2). These networks can be thought of as ‘engine maps’ and have been used to simulate the emissions of the engine over the FTP heavy duty diesel cycle. Improvements resulting from the optimization were observed. The entire process of getting optimized parameters for an engine, starting from raw engine data or CFD results is capable of being automated and has been shown to take a reasonably small amount of computational time.

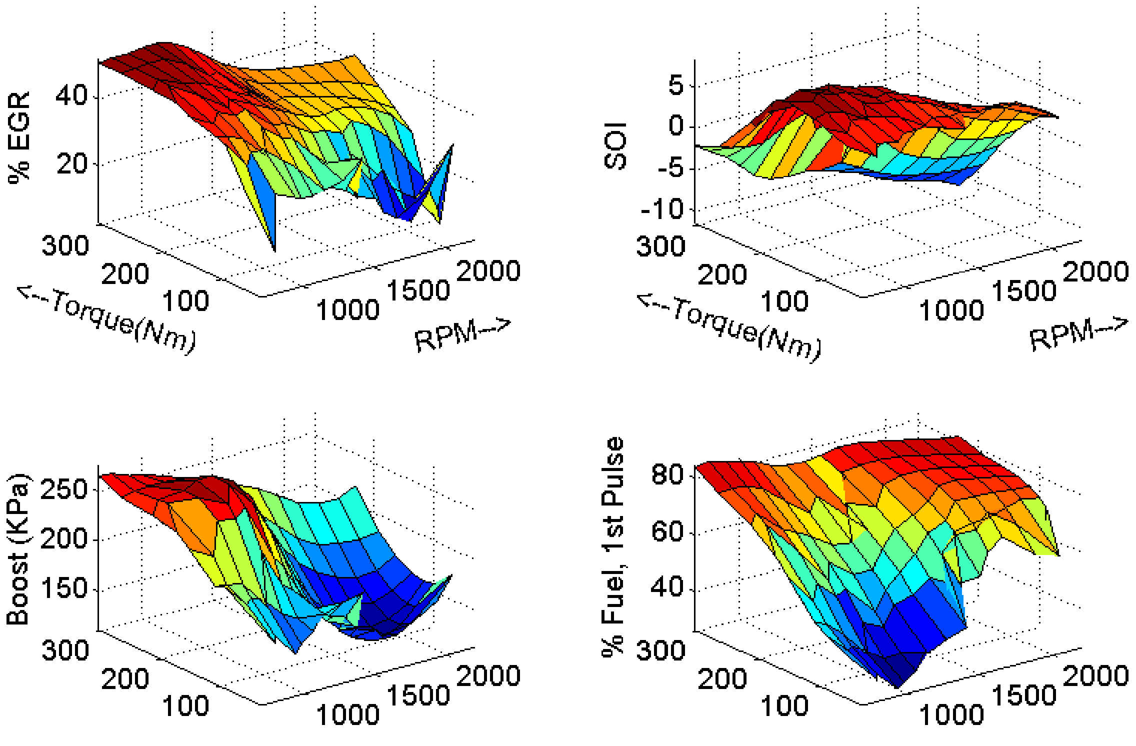

Figure 2.5.2-2: Optimized engine operating maps developed using neural network based simulations.

References Sections 2.1-2.5

Arici, O., Johnson, J.H., Kulkarni, A.J., "The Vehicle Engine Cooling System Simulation, Part 1 – Model Development," SAE Paper 1999-01-0240, 1999.

Arici, O., Johnson, J.H., Kulkarni, A.J., "The Vehicle Engine Cooling System Simulation, Part 2 – Model Validation Using Transient Data," SAE Paper 1999-01-0241, 1999.

Arici, O., Johnson, J.H., Lehner, C.W., Parker, G. G., "Design and Development of a Model Based Feedback Controlled Cooling System for Heavy Duty Diesel Truck Applications Using a Vehicle Engine Cooling System Simulation," SAE Paper 2001-01-0336, 2001.

Chalgren, R.D., "The Modeling of Exhaust Gas Recirculation in the Vehicle Engine Cooling system Simulation for Designing a Controlled EGR Cooling System," Master's Thesis, Michigan Technological University, 2000.

Chalgren, R.D., Parker, G. G., Arici, O., and Johnson, J. H., "A Controlled EGR Cooling System for Heavy Duty Diesel Applications Using the Vehicle Engine Cooling System Simulation," SAE Paper 2002-01-0076, 2002.

Kim T., and Ghandhi J. B., Quantitative 2-D fuel vapor concentration measurements in an evaporating diesel spray using exciplex fluorescence method, SAE Technical paper 2001-01-3495, 2001.

Luptowski, B.J., “Development and Evaluation of an All Electric Active Cooling System in a Heavy Duty Diesel Truck Using the Vehicle Engine Cooling System Simulation Enhanced with GT-POWER,” Masters Thesis, Michigan Technological University, 2003.

Pomraning E. and Rutland C. J., “Dynamic one-equation nonviscosity large eddy simulation model,” AIAA Journal, 40, 4, April 2002

Rao, S. and Rutland, C.J., 2003, “A Flamelet Time Scale Model for Non-Premixed Combustion Including Unsteady Effects,” Comb. and Flame, Vol 133, pp. 189-191.

Siebers D. L., Liquid phase fuel penetration in diesel sprays, SAE technical paper 980809, 1998.

Spadaccini L.J., Owen F.K., and Bowman C.T., (1976), “Influence of aerodynamic phenomena on pollutant formation in combustion (Phase I. Gaseous fuels), Report EPA-600/2-76-247a.

2.6 A Methodology For Powertrain System Robustness Analysis

by John J. Moskwa & James A. Bedrosian, Powertrain Control Research Laboratory, Department of Mechanical Engineering, University of Wisconsin-Madison

2.6.1 Introduction

For robust design, it is necessary to first identify noise and disturbance factors early in the design process, and to understand their relationships to operating variables. These disturbance factors may include noise signals in system inputs, outside environmental factors acting on the system that vary considerably, manufacturing variations of individual components of the system or the effects of aging components of the system [2]. This includes the uncertainty of internal system parameters as well as any anticipated outside noise and disturbances acting on the system. After identifying noises and disturbances, the range of each disturbance factor needs to be characterized. Once the disturbance ranges are characterized, information on the sensitivity of system behavior to these anticipated variations needs to be sought out. With this information, the amount system behavior will deviate from desired function as a result of these disturbance variations can be assessed. These deviations from ideal function can then be compared to allowable limits of system behavior, providing information on how “robust” system behavior is to these disturbances. This information can be then be taken into consideration in making design process.

Design specifications establish thresholds, limitations, or relationships on or between external system outputs and internal operating states to ensure that appropriate function is achieved with the desired reliability for the life of the system designed. The range of all anticipated disturbances, the sensitivity of the system to each disturbance, the variance in behavior caused by these disturbances, and the required thresholds behavior must be constrained within are all necessary considerations in robustness analysis. The goal of this project is to develop a visualization tool to display all this information graphically to a design engineer from the sources of information that may be available. The earlier this type of information can be presented to the designer, the earlier in the design process robust design decisions can be made. This prevents expensive prototype failures due to robustness issues in later development phases and costly and embarrassing failures after product release.

Traditional methods of robustness analysis include Failure Modes and Effects Analysis (FMEA), fault tree analysis, Taguchi and other methods. All of these focus on one or more of the following goals; to devise a method to identify system influences, to assess the effects and magnitudes of these influences on the system, to put this information in a form that is easily understood, and to deliver this information to the people that can make the appropriate decisions to improve system robustness [1,14].

The 'Design Robustness System' (or 'DRS') is a development and extension of fundamental ideas developed by the second author [1], to produce a set of tools to assess system design robustness. The basis for this approach is to provide a tool to utilize information available to the designer and to present this information in a form from which robustness decisions can be made. The system methodology was designed to be general and flexible to assess system behavior and robustness of a wide range of different types of systems. It is a graphical, user-interactive approach to help a design engineer visualize system behavior and robustness to anticipated system disturbances [1]. Large amounts of information can be explored graphically to improve understanding of system behavior, compare system design options, assess current system robustness, or lead to recommendations for future design improvements.

The DRS is also flexible for use in various phases of product development or design [1]. It can be used early in the design process to evaluate robustness of system designs to anticipated noises and disturbances by examination of data from dynamic system models. It can be used in later development to examine experimental data from prototype hardware to re-assess actual behavior of these developed systems, or for initial robustness analysis if developed system models are not available. Existing production hardware can also be analyzed from experimental data to develop suggestions for robust design improvements.

Data from any of these sources are formatted from time-domain data into a statistical form where the behavior of the desired parameter to be constrained can be evaluated as system parameters that affect this constrained parameter vary. The variables that affect the constrained parameters can include the system inputs, current operating states, system noises and disturbances, or system design parameters. The mean values and variance of the constrained parameter behavior is characterized at each observed combination of the affecting variables. Behavior of the examined system parameters can then be explored as a function of the affecting variables, not time, and information about the sensitivity of system behavior to these disturbances is available. This information can be used to assess robustness over the range of conditions tested.

The graphical output of this tool is comprised of plot that display whether thresholds established by system requirements are met or violated [1]. The sensitivity of the constrained system parameter can be evaluated with respect to varying levels of disturbances inputs, commanded system inputs, system operating states and changes in system design parameters. The user can graphically explore the tolerable levels of disturbances and how this may change with varied system inputs, operating conditions or changes in system design parameters. Plots also display how behavior of the examined system output varies as any of the affecting variables are varied individually about any combination of these parameters. This type of information presents how much disturbance levels may need to be reduced or how system design parameters may need to be changed to make the system less sensitive to these disturbances in order to maintain robust operation.

The data formatting and graphics presented are generated using Graphical User-Interfaces (or 'GUIs') developed in MATLAB. This makes data formatting and exploration a quick, user-friendly process. Appropriate time-domain modeling or experimental data must first be collected and imported into MATLAB for analysis. The user then specifies the necessary information in GUI figure windows, providing the required inputs and cues for the developed MATLAB programs that automate data formatting and display the data in a manner specified by the user. The user can then manipulate the user-interface controls within the GUI to update and change the graphical displays to examine system behavior over the entire operating range tested. This provides a graphical, user-interactive method to help a design engineer visualize system behavior in order to assess design robustness.

2.6.2 Discussion

This report details the fundamentals of data collection, data formatting, and the graphical form in which this information is displayed to the user for robustness analysis. This robustness assessment methodology is flexible and can be applied to diverse projects and tasks in various phases of design and development. Fundamentals of the data formatting and the graphics used to display robustness information will be illustrated using a simple theoretical system example with three variables.

2.6.3 System Variable Nomenclature

The following terminology will be adopted in discussing the system variables selected for robustness analysis. The system parameter that is to be constrained to meet the design specifications for robut operation will be referred to as the Dependent Variable (DV). The variables that affect the DV behavior will be referred to as the Independent Variables (IVs). The IVs may include System Inputs (SI), Disturbances (D), Operating States (OS), or Design Parameters (DP). IVs may be referred to generically by number (e.g. if four IVs are identified they may be referred to as IV1, IV2, IV3 and IV4). This nomenclature is summarized in Table 1.

Table 1 System Variable Nomenclature

Systesm Variable Type	**Nomenclature**
Dependent Variable	DV

Independent Variable	IV
-System Input	*SI*
-Disturbance	*D*
-Operating State	*OS*
-Design Parameter	*DP*

2.6.4 Data Sources and Data Collection Fundamentals

The Design Robustness System is capable of formatting data from a number of different sources, allowing the user to visualize system behavior and analyze robustness for designs in various phases of product development. Data can be analyzed from dynamic system models developed for in early product development, from pre-production hardware and experimental prototypes to assess current design robustness, or from production hardware to assess behavior for next generation system improvements. If instrumented experimental or production hardware exists, experimental tests can be designed and run to collect time-domain data from sensors which can be analyzed. If earlier in the design phase, hardware has not yet been produced, or if instrumentation to measure the desired system parameters is difficult or too expensive, time-domain data from dynamic system models can be used.

2.6.5 Data Formatting Fundamentals

Formatting Time-Domain Data into Functional Form

The data input into the Design Robustness System (DRS) for analysis is in the form of time-domain data arrays obtained from system simulations or hardware testing. These time-domain data arrays are formatted and transformed into a functional form where the values of user-specified variable to constrain (DV) are expressed as a function of the affecting variables (IVs).

$$(\mathrm{DV},\mathrm{IV1},\mathrm{IV2},\mathrm{IV}n\ldots) = \mathrm{f}(\mathrm{t})\ldots \Rightarrow \mathrm{DV} = \mathrm{f}(\mathrm{IV1},\mathrm{IV2},\mathrm{IV}n\ldots) \qquad (1)$$

This transformation, from time domain data to functional data, is done by establishing the mean DV value and variance statistics at each combination of the independent (input, disturbance, state & design) variables. This transforms large time-domain data strings into more compact and concise data matrices or arrays in a functional format with DV behavior characterized in each operating mode or condition. These data arrays can be examined and explored graphically displaying how DV behavior is affected with changes in the IVs. This data format requires less storage space and in this format multiple datasets can be merged and evaluated together, or individual datasets can be extracted from previously merged datasets.

Defining the Operating Space

The operating space consists of all possible operating points or combinations of the IVs. The minimum and maximum values of each time-domain IV data array are first identified. The range of values for each IV is then split into a smaller number of discrete "bins" and the IV value range within each bin is referred to as the "binlength". Each possible combination of IV bins is referred to as an operational "cell" and the full set of possible operational cells is referred to as the system "operating space". The simplest example is that for a system with 1 DV and 2 IVs (referred to as a 1x2 System), as displayed in Figure 1. The total number of cells in the operating space is equal to the product of the number of bins specified for each IV. In this example, both IV1 and IV2 have 10 bins resulting in 100 cells of possible operating conditions in the operating space. For the 1x2 operating space in Figure 1, DV behavior throughout the operating space can be represented in matrix with each element of a 10x10 matrix corresponding to DV behavior within the corresponding operating cell. In general, the operating space for a 1x2 system can be represented as a matrix of size (# IV1 bins) x (# IV2 bins).

The "binlength", or range of IV values within each bin, is equal to the range of a particular IV divided by the number of bins specified for that IV. The number of bins chosen sets the resolution of the operating space with respect to each IV. The numbers of bins are selected to obtain an appropriate resolution for each IV relative to its affect on DV behavior.

DV Mean, Variance, and Data Density for each Cell

Dependent variable behavior can now be characterized for system operation where each IV is within the range specified for a cell of the operating space. All time domain data samples which occur within the IV ranges of particular operating cell can be grouped together and DV behavior examined. The mean DV value and the statistical variance (in standard deviations) for these samples, occurring in the same cell of the operating space, are then calculated. The number of occurrences or data points in this cell is also identified and stored. This procedure is repeated recursively to characterize system behavior within each cell of the operating space. This creates a map of the DV behavior over the operating space and characterizes system behavior as a function of the IVs instead of time. This process is shown in Figure 2.

This information can be stored in matrices the size of the operating space (10x10 for the example in Figure 1) with each cell of each matrix corresponding to system behavior within the appropriate operating range of the operating space. Mean DV values, statistical variance, and number of data points can each be stored individually in matrices the size of the operating space.

2.6.6 Data Storage Fundamentals

Data Structure

Time domain data strings are not used for generating the graphical output after initial formatting and can be set aside and archived. The mean, variance, and number of data points (referred to as "points per cell" or "ppc") are now stored in three concise matrices of the same dimensions. These matrices are quickly generated in MATLAB and the corresponding elements of each matrix hold the mean DV value ("Emean" matrix), statistical variance ("Estd" matrix), and ppc ("Eppc" matrix) for the corresponding cell of the operating space. This functional format of the statistical data provides more useful information on how DV behavior changes, relative to IV changes, over the entire system operating range. It also condenses lengthier time-domain data arrays into a simpler, more efficient form for data storage and analysis. One additional data character array (named

"PlotData") is required to save information from formatting, which includes the DV chosen, which IVs are represented in which matrix dimension, and the necessary information to determine the IV ranges which serve as the boundaries of each cell of the operating space. These four data arrays are generated and then stored in the MATLAB workspace. These data arrays are unique to the user-specified formatting parameters and the same time-domain data can be re-formatted and examined for operating spaces defined with different IV resolutions. These four data arrays can also be saved and examined at a later time. Graphics displaying the information in these data arrays can be manipulated and updated from these four data arrays without having to refer back to the original archived time-domain datasets.

Data Merging

Multiple datasets can also be merged and examined together as combined data arrays of the same size without the necessity to return to the time-domain data. This enables the data collection process to be completed in stages, if necessary, or the tested operating space to be expanded by adding new datasets without the need to re-collect or re-format the original data. Additional data can be collected and added to the analysis based on the statistics from analysis of the original dataset. This process requires that each dataset be formatted such that the cells of each operating space correspond to the same IV ranges in each matrix dimension.

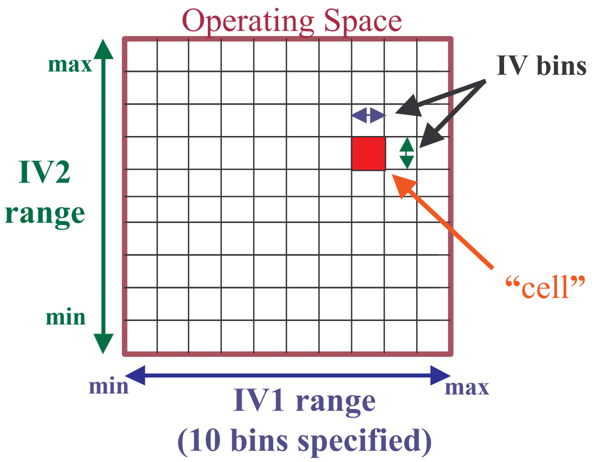

Figure 2.6.1 Discrete cells of the system operating space for a 2 IV (1x2) system

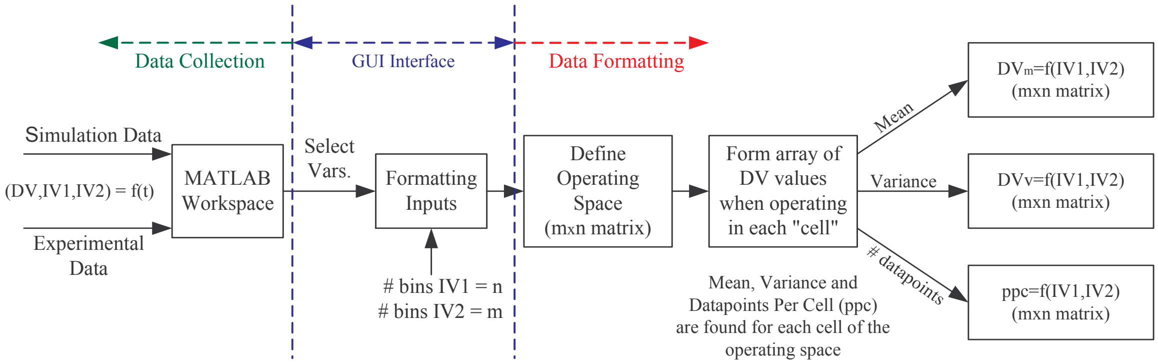

Figure 2.6.2 1x2 data formatting: schematic of data formatting from time-domain data, statistically to Dv = f(IV1,IV2) [14].

The data within each cell can then be statistically merged based on the following expressions derived from the definition of the statistical mean and variance [1]. Two datasets **X** and **Y**, whose data are described by the mean (σ_x^2, σ_y^2), variance (μ_x, μ_y), and ppc (ppc_x, ppc_y), can be merged to form dataset **Z** = **X**∪**Y** (described by σ_z^2, μ_z, ppc_z) as follows:

$$\mu_z = \left(\frac{ppc_x}{ppc_z}\right)\cdot\mu_x + \left(\frac{ppc_y}{ppc_z}\right)\cdot\mu_y \tag{2}$$

$$\sigma_z^2 = \left(\frac{ppc_x}{ppc_z}\right)\cdot\sigma_x^2 + \left(\frac{ppc_y}{ppc_z}\right)\cdot\sigma_y^2 + \left(\frac{ppc_x}{ppc_z}\right)\cdot\left(\frac{ppc_y}{ppc_z}\right)\cdot\left(\mu_x - \mu_y\right) \tag{3}$$

$$ppc_z = ppc_x + ppc_y \tag{4}$$

The definition of variance used to derive these relationships is the fundamental definition provided in typical statistical texts [3,4]:

$$\sigma^2 = \sum_{i=1}^{n}(x_i-\mu)^2\cdot p(x_i) = \sum_{i=1}^{n}(x_i-\mu)^2\cdot\left(\frac{1}{n}\right) = \left(\frac{1}{n}\right)\cdot\sum_{i=1}^{n}\left(x_i-\mu\right)^2 \tag{5}$$

Only the final statistical descriptions are needed to later combine or remove data to or from the final analysis set.

Data Extracting

If the original statistically formatted datasets are saved for each set of time-domain data collected, any individual dataset in this merged dataset can also be extracted. If analysis of the merged datasets, or any other knowledge were to identify issues with data integrity of a particular experimental or modeling dataset, this problematic dataset can be statistically extracted from a merged dataset. If the final merged dataset and an individual dataset it was comprised of is known, equations 2-4 can be solved for the statistical description of the remaining datasets (e.g. the three data matrices for **X** (μ_x, σ_x^2, ppc_x) can be extracted from the merged **Z** matrices (μ_z, σ_z^2, ppc_z) to obtain the matrices for the remaining **Y** datasets (μ_y, σ_y^2, ppc_y)). These equations can be solved cell by cell and the desired 'Emean', 'Estd' and 'Eppc' matrices generated and saved in the MATLAB workspace. To examine any combination of datasets (with identical formatting parameters) only the original formatted statistical datasets for each individual data run and the final combination of these datasets needs to be saved.

2.6.7 Graphical Fundamentals

The basic fundamentals of the Design Robustness System (DRS) graphical output will be presented below. With the data formulated as described in the previous sections, the user can now explore this functional information graphically. The DRS graphics display DV behavior over the operating space, specifically identifying where in the IV space the DV meets the required specifications, or thresholds, defined by the user. To illustrate the fundamentals of the graphical output, again consider a simple 1x2 System, where the DV is a function of two IVs and the operating space is defined as depicted in Figure 1. This simple example was chosen to allow these concepts to be illustrated most easily in three-dimensional space.

DV Thresholds

The target DV value and minimum and maximum tolerable DV thresholds for robust system operation can be plotted on three dimensional axes as a function of the IVs. This is depicted in Figure 3 for the 1x2 System example. Upper thresholds are presented in blue (high) and lower thresholds presented in red (low). These thresholds are commonly a constant value but each may also vary independently over the operating space, such that (DVThesh,min, DVThesh,max) = f(IV1,IV2). For the examples that follow, the DV thresholds have been chosen such that they remain constant and do not varying as a function of the operating space. Some system requirements may only have one threshold (i.e., a maximum or a minimum) and similar concepts apply to these one-sided constraints. For this particular system parameter, the required constraints for robustness remain the same regardless of the system inputs (SI), disturbance (D), operating states (OS) or design parameters (DP) examined. The acceptable operating region of this system is defined as the region where DV output is constrained between these thresholds.

DV Surface and Variance Surfaces

Within each cell of the operating space, the DV data is not single-valued, but is represented by the mean DV value and statistical variance from the mean. The IV operating space for a 1x2 System can be thought of as being located on the horizontal (IV1-IV2) plane. The mean DV values and variance information are available within each cell on this plane, representing all data obtained over the range of operating conditions contained within each cell. The mean values within each cell can be plotted as a mean DV surface, and the statistical variance of the DV values within each cell can be thought of as a statistical data distribution of DV values along the vertical axis. It can be conceptualized that the actual values of the DV vary from this mean surface in the positive and negative vertical directions with decreasing probability as described by the DV variance statistics. For example, consider a case with a parabolic mean DV data surface, $DV_m = f(IV1,IV2)$, as shown Figure 4.

Considering the simplest case, if the DV variance is identical within each cell, the range of the DV can be represented as being within two identical parabolic surfaces offset from the mean statistical surface by plus or minus the appropriate variance, or confidence interval (specified in standard deviations), as shown in Figure 4. In reality, variance of

DV values from this mean surface will most likely differ within each cell of the operating space and the upper and lower statistical surfaces will not be parallel, but will be defined based on the data statistics. Within each cell, the values that comprise the statistical surfaces are defined as:

$$DV_{upper} = DV_{mean} + \text{Confidence Interval [\# std dev]} * DV_{variance} \tag{6}$$

$$DV_{lower} = DV_{mean} + \text{Confidence Interval [\# std dev]} * DV_{variance} \tag{7}$$

The probability that the DV values fall on and within the range between the upper and lower DV statistical surfaces is established by the specified confidence interval (stated in standard deviations). For example, if one or two standard deviations are chosen, the statistical surfaces will be drawn such that approximately 68% or *95%* of the data examined fall on or between the upper and lower statistical surfaces, respectively. If two standard deviations are chosen, this is referred to as a *95%* confidence interval, and statistically only the remaining 5% percent of the DV values would lie outside of the region between the upper and lower statistical surfaces. It can be said that the DV values will lie within these surfaces with 95% confidence. An appropriate confidence level is to be chosen such that DV values will only be expected to exceed the upper and lower statistical surface the maximum allowable percentage of the time. These rare occurrences may likely be from quick, transient system responses.

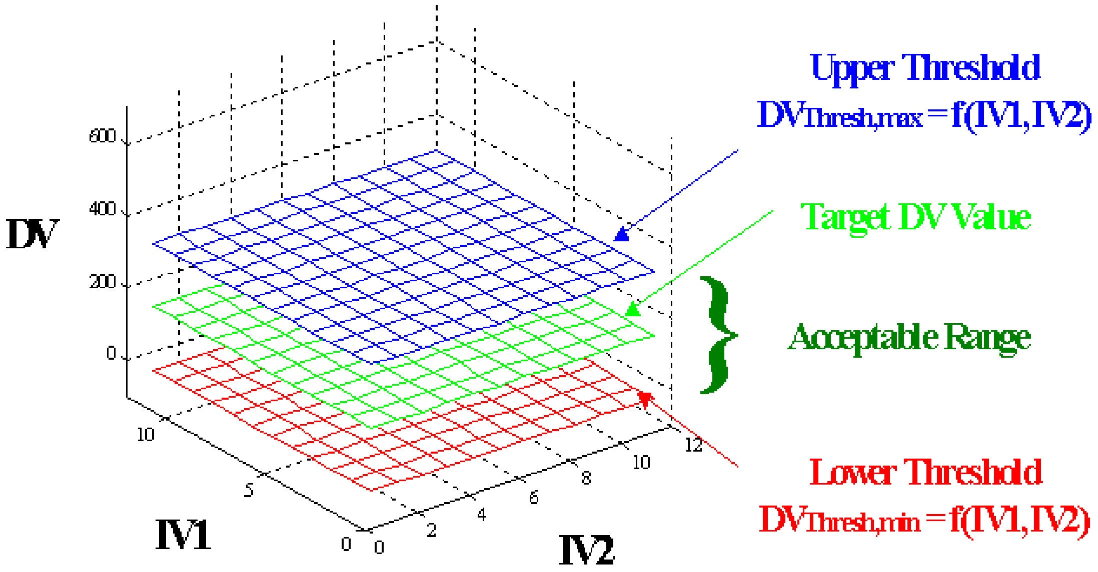

Figure 2.6.3. Dependent variable desired target value and upper and lower thresholds [14].

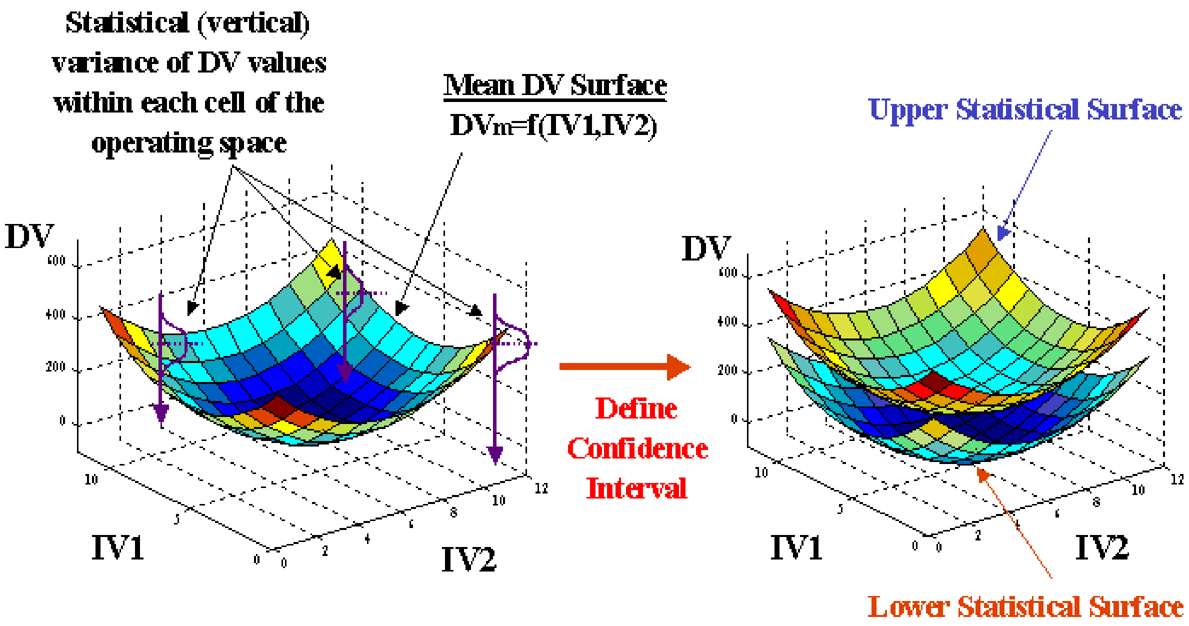

Figure 2.6.4. Mean statistical DV surface and DV statistical surfaces [14].

Threshold Violation Contours

Figures 5 and 6 illustrate how the information discussed thus far is combined to form threshold violation contours, which are the output of the Design Robustness System. Data is first formatted such that the mean and variance of the DV is found within discrete regions of the independent variable combinations (constituting the system operating space). Threshold functions and the statistical confidence desired by the user are selected next, and the thresholds and statistical DV surfaces are defined accordingly from this data. The concepts of the upper and lower threshold surfaces and the upper and lower statistical surfaces can now be combined to display at what combinations of the IVs (or cells of the operating space) the DV thresholds are satisfied and violated within the specified confidence level. Where the upper statistical surface and the upper threshold intersect constitutes the upper threshold violation contour. Likewise, where the lower threshold surface and the lower statistical surface intersect constitutes the lower threshold violation contour. These contours display where in the operating space the upper and lower thresholds are met and violated, respectively, with the statistical confidence specified.

These threshold violation contours can be projected in the plane of the operating space, as seen in Figure 6, displaying more clearly at which IV combinations each threshold was met and violated, respectively.

The upper thresholds and upper threshold violation contours are represented in blue (signifying high), and the lower threshold and threshold violation contours are represented in red (signifying low), this color scheme will be used continuously. The color green will be used to specify where the thresholds are satisfied. In this example, the lower threshold is violated in the center region of the operating space (region I), the upper threshold is violated outside the upper threshold violation contour (region III), and both thresholds are satisfied in the circular ring between the violation contours (region II). It is possible that both thresholds be simultaneously violated in operating regimes with high levels of variance relative to the acceptable DV operating range. These threshold violation contours can be examined to identify problematic combinations of the IVs and to identify which regions in the operating space will provide operation where the required DV constraints and threshold specifications are met.

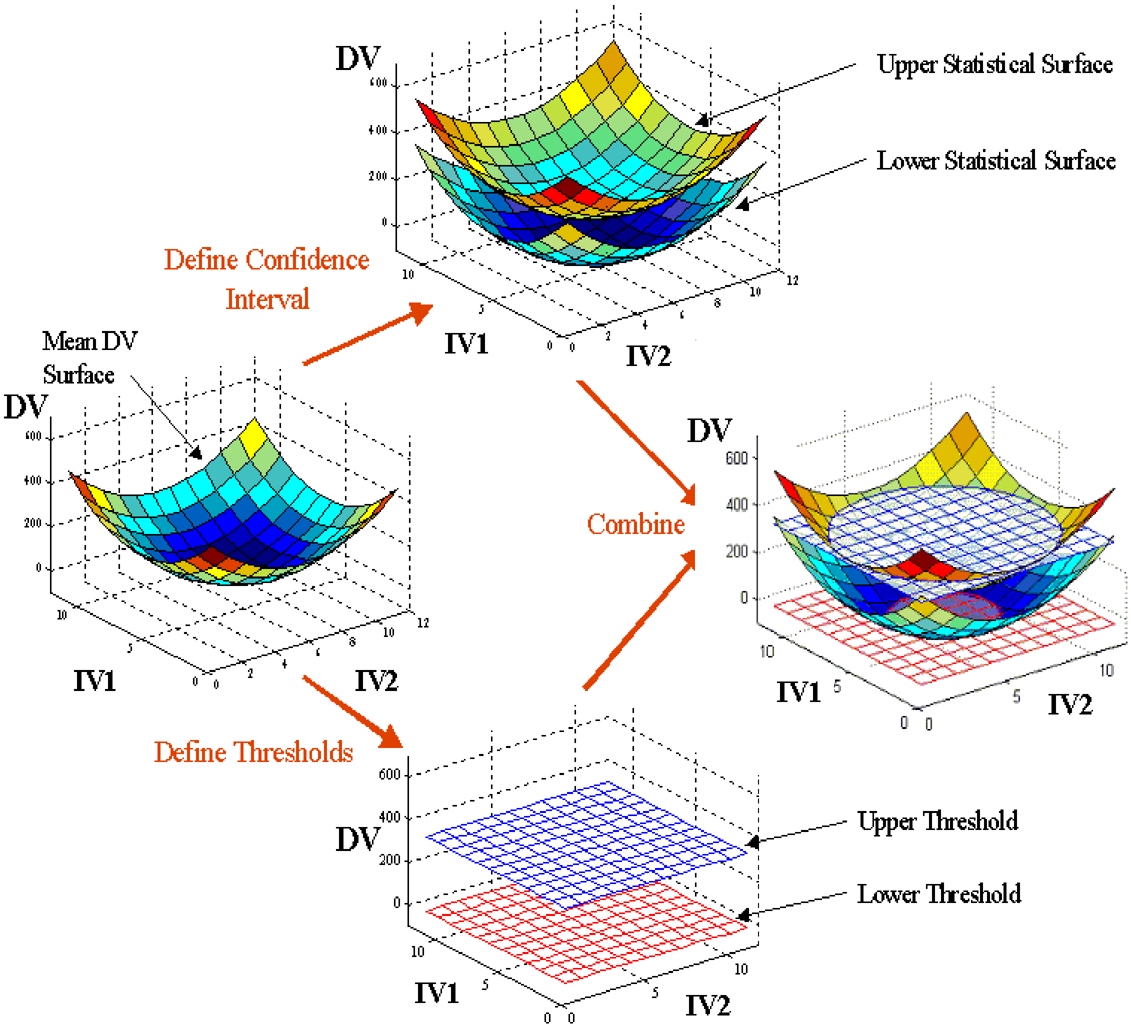

Figure 2.6.5. Graphical illustration of the intersection of dv statistical surfaces with the thresholds to form threshold violation contours [14].

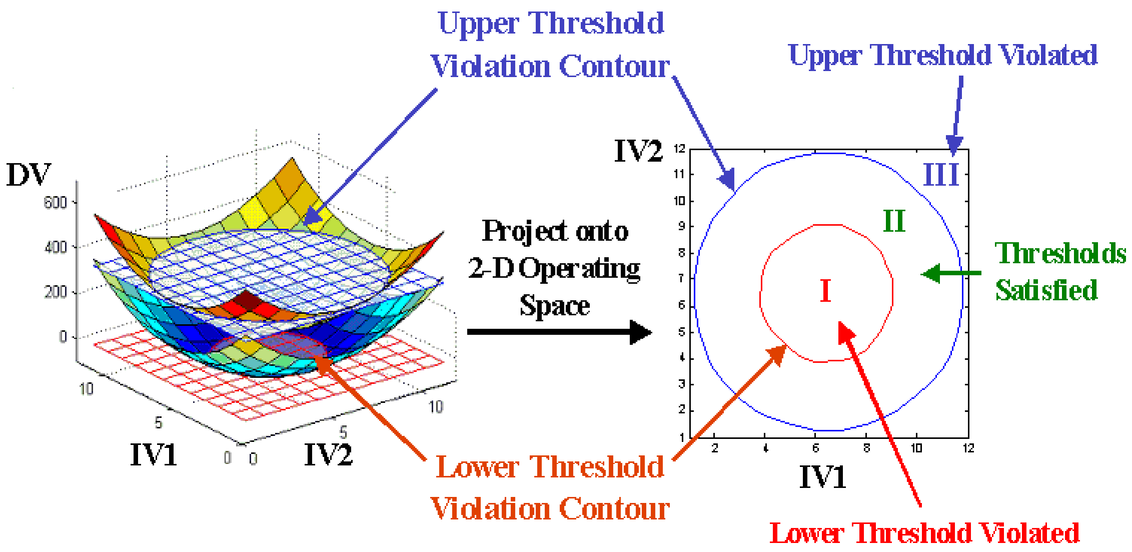

Figure 2.6.6. Projection of threshold violation contours onto the operating space [14].

Robustness Slices

Threshold violation plots provide useful information on where in the operating space the DV thresholds are violated within the specified level of confidence. This enables system behavior to be understood quickly and easily, allowing important generalizations to be made from one simple plot. But information on actual DV behavior within each threshold violation region cannot be obtained with the data presented in this form. More detailed information on DV behavior within each region can be evaluated by examining plots of DV behavior at specified cross-sections through the operating space, referred to as “robustness slices”. Robustness slices are drawn through a cross-section of the operating space at a constant level of all but one IV. The mean, upper and lower statistical DV surfaces and the upper and lower thresholds are each plotted on the same axes as a function of one IV (at the specified values of the remaining IVs). Figure 7 illustrates a robustness slice for the same parabolic data example used in the previous figures.

In Figure 7, a value of 6 was selected for IV1, and the robustness slice (right) represents the intersection of the black plane at IV1=6 with the mean, upper and lower statistical surfaces, and the upper and lower threshold surfaces. Changes in DV behavior, DV variance and regions of threshold violations can now be viewed solely as a function of IV2 where IV1 = 6. This allows the user to view how changes in each IV individually affect DV behavior.

From either the threshold violation contours or the robustness slices it can be ascertained how robust system behavior is to variation in each IV, or how much variance in each IV level can be tolerated without exceeding the specified DV thresholds. This allows the user to explore and understand the relationships between each of the variables. The robustness slices provide additional information on how the actual DV levels and variances change within each threshold violation region. This information can be useful in determining the most robust operating condition within the operating space. The robustness slices provide information on how quickly DV values approach and/or exceed the thresholds (e.g., the slopes or partial derivatives of the robustness slices), by how much the thresholds are violated, and if the mean values are in violation or if it is an occasional violation due to observed DV variance.

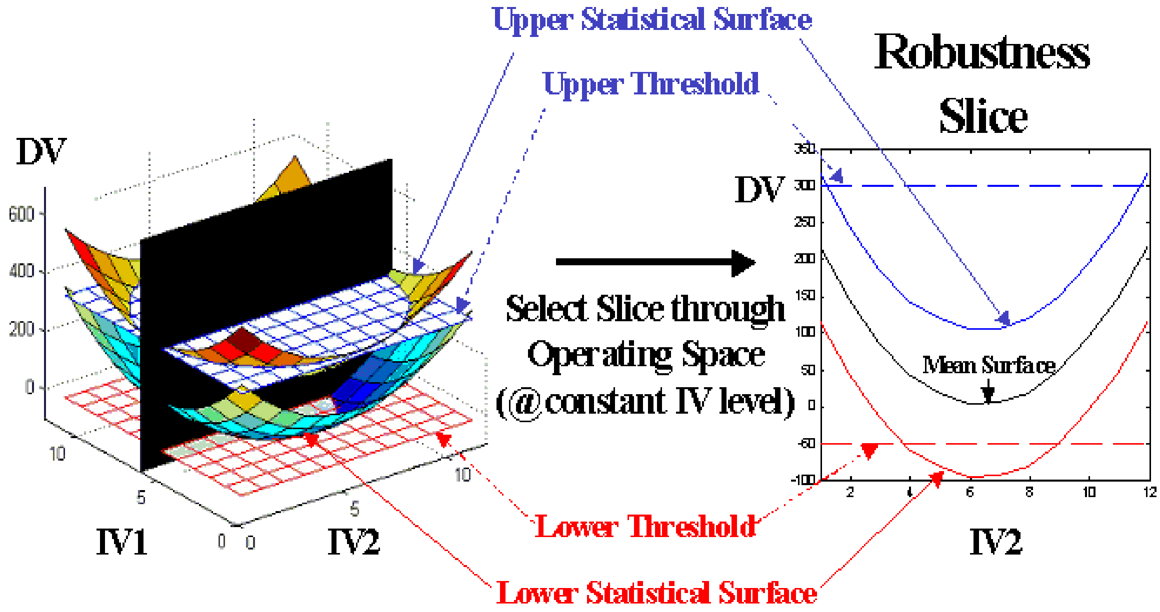

Figure 2.6.7. Graphical illustration of a robustness slice through the operating space [14].

Selection of an Operating Point for Robustness Analysis

Robustness slices can be drawn at specified levels of each IV of the system. Any operating point within the operating space can be specified and robustness slices drawn as a function of each IV individually about this operating point.

In Figure 8, the operating point of IV1 = 6 & IV2 = 6 was selected, and robustness slices can be viewed through the cross-sectional planes at IV1 = 6 (top right) with DV = f(IV2), and where IV2 = 6 (bottom right) with DV = f(IV1). From these plots, the effects on the DV of either IV can be viewed about the selected operating point.

At this operating point, the relationship of how each IV individually affects DV behavior is now readily available for analysis. It can easily be identified if the relationship between DV behavior with each IV is linear or non-linear or perhaps linear over some of the IV range and non-linear in other regions. If non-linear, the nature of the relationship between the DV and each IV can be characterized from the appropriate robustness slice. Different operating points in the operating space can be selected to view the robustness slices of how DV behavior varies with changes or variations in each IV about a new operating condition. This can be repeated, exploring behavior over the entire range of the operating space, enabling the used to assess robustness of system behavior to each IV about any operating point.

Identifying the Operating Point on Threshold Violation Contour Plots

The cross-sectional planes at each constant IV level of the specified operating point can also be projected into the plane of the operating space, as the threshold violation contours were in Figure 6. The projections onto the operating space of both the threshold violation contours and planes of constant IV levels for each robustness slice are displayed in Figure 9. In this plot, each IV value is represented as a line of constant value on the appropriate axis, and the selected operating point is represented at the intersection of these lines. The operating point about which robustness slices are evaluated can be selected by individually identifying the IV levels for each axis or by selecting any operating point within the operating space by specifying the intersection of these lines of specific IV values.

Fundamental Format of GUI Graphical Display

System design robustness can be examined graphically by combining the graphical concepts presented in Figures 8 and 9. Threshold violation contours can be examined on a mapping of the operating space to assess problematic combinations of the IVs (as in Figure 9); displaying regions in the IV space where DV values are not within the thresholds with the specified statistical confidence required for robust system behavior. Any operating point within the operating space can then be selected on this plot to obtain more detailed information from robustness slices (as in Figure 8); displaying how DV mean and variance change as each IV value is varied about the selected operating point. This graphical format is presented in Figure 10.

A graphical user-interface (GUI) has been developed to allow the user to easily format, plot, and explore system behavior using the graphics as displayed in Figure 10. Provisions can be in the GUI made allowing the user to select different operating points and IV values, to explore system behavior over the range of the operating space, by manipulating the GUI graphics. Once the data is formatted as discussed, the statistical data can be plotted and manipulated graphically by selecting and modifying the appropriate controls in a GUI figure windows. These graphical displays are then automatically updated based on the user selections.

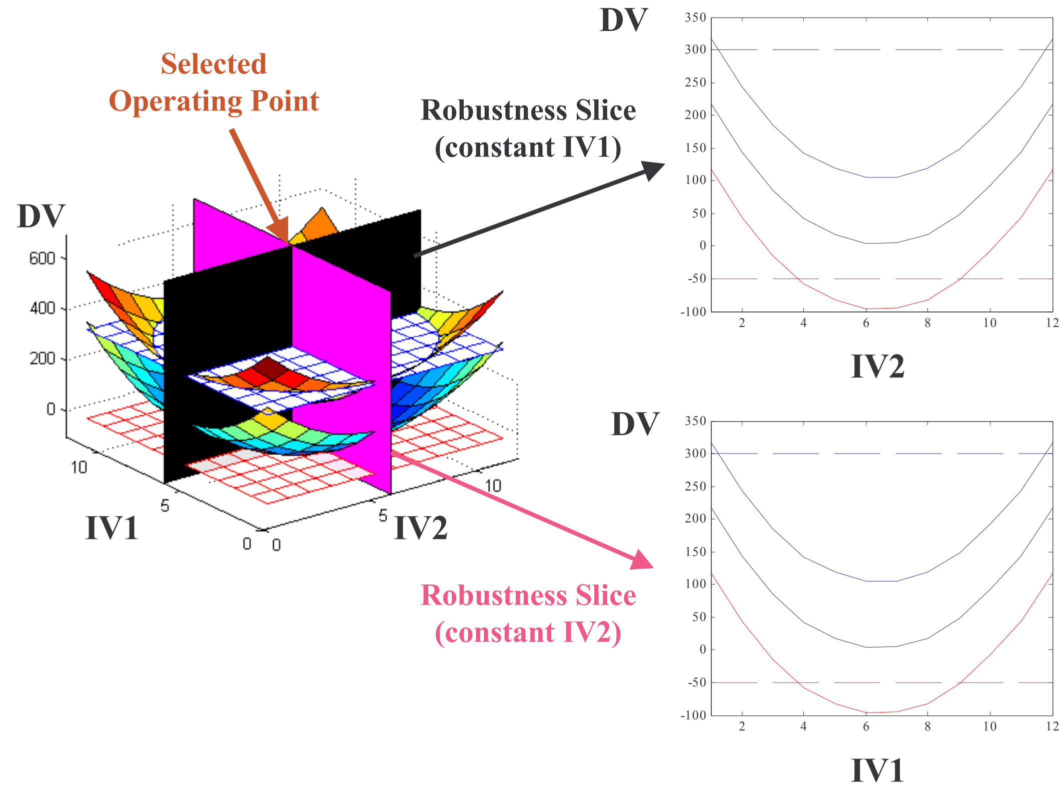

Figure 2.6.8. Robustness slices about a selected operating point in the operating space [14].

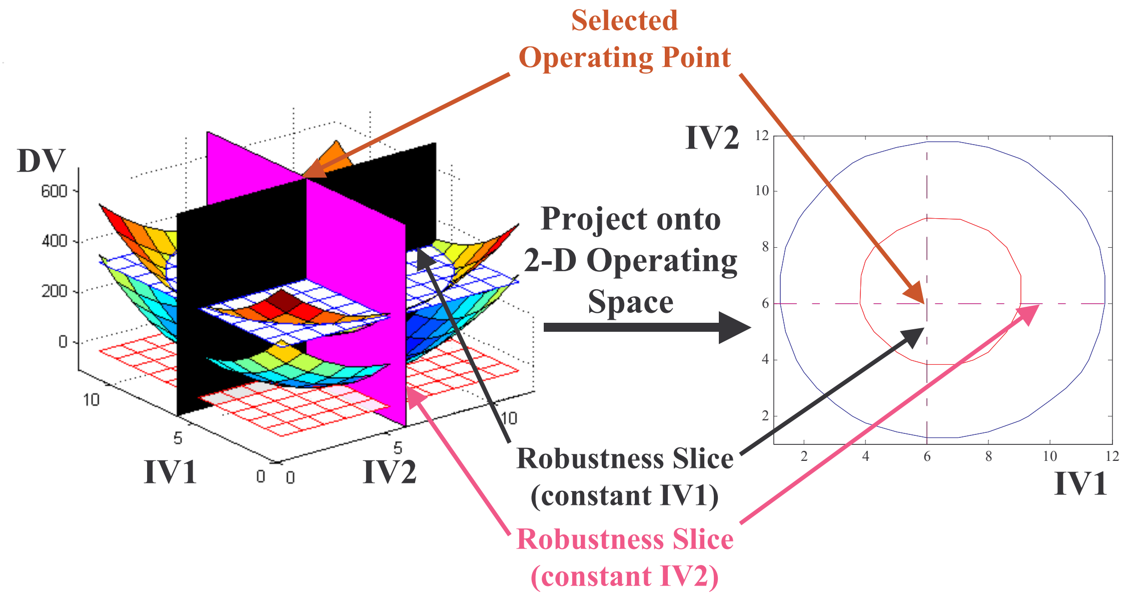

Figure 2.6.9. Threshold violation plot with robustness planes projected.

The concepts presented for the 1x2 system GUI have been coded into MATLAB [7, 14], and one variation of the front end of this robustness analysis software is shown in Figure 11. The software is very flexible, and the user can choose which attributes are displayed, and the method of displaying them (contour plots, gradients, etc.). In this way the user can tailor the GUI for his/her own needs and visualization skills. These same data formatting and graphical principles can also be extended to more complex systems with an increased number of IVs. Examples of this extension are shown in Figure 12 (extension of the 1x2 principles) and Figure 13 (a 1x3 system GUI with robustness slices). If the user has strong visualization skills and can absorb higher dimensional relationships in the system of interest, these concepts can be extended further as shown in Figure 14 (1x5 example), and if there are several outputs to be constrained there may be multiple contour plots in each variable. However, in most situations it is assumed that the user will analyze smaller subsets of the system robustness relationships, looking at one output at a time. The final Figure 15 provides a broad overview as to how the DRS can be used to assess the robustness of a dynamic system. While this work was focused on powertrain system robustness, this approach can be used to analyze the robustness of any dynamic system through its data.

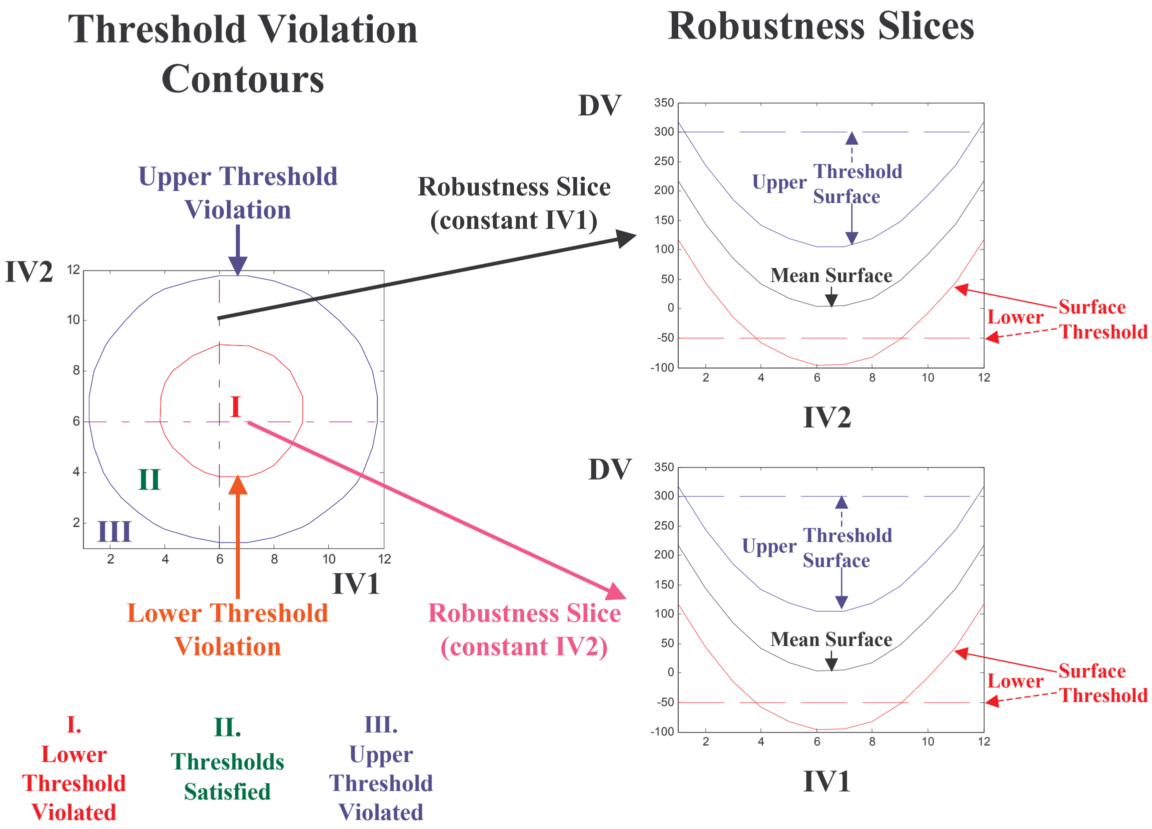

Figure 2.6.10. Graphical exploration of operating space using threshold violation contours and robustness slices [14].

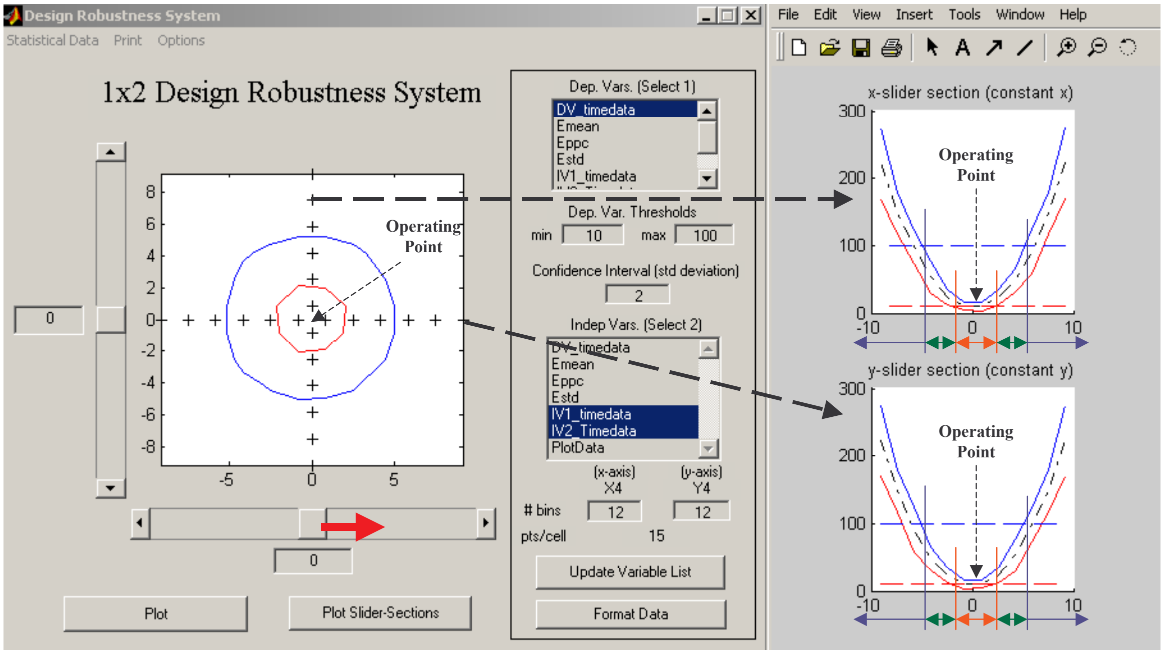

Dep. Vars. (Select 1)
DV_timedata
Emean
Eppc
Estd
IV1_timedata

Dep. Var. Thresholds
min 10 max 100

Confidence Interval (std deviation)
2

Indep Vars. (Select 2)
DV_timedata
Emean
Eppc
Estd
IV1_timedata
IV2_Timedata
PlotData

(x-axis) X4 (y-axis) Y4
bins 12 12
pts/cell 15

Figure 2.6.11. Illustration of exploring the DV behavior over the operating space [14].

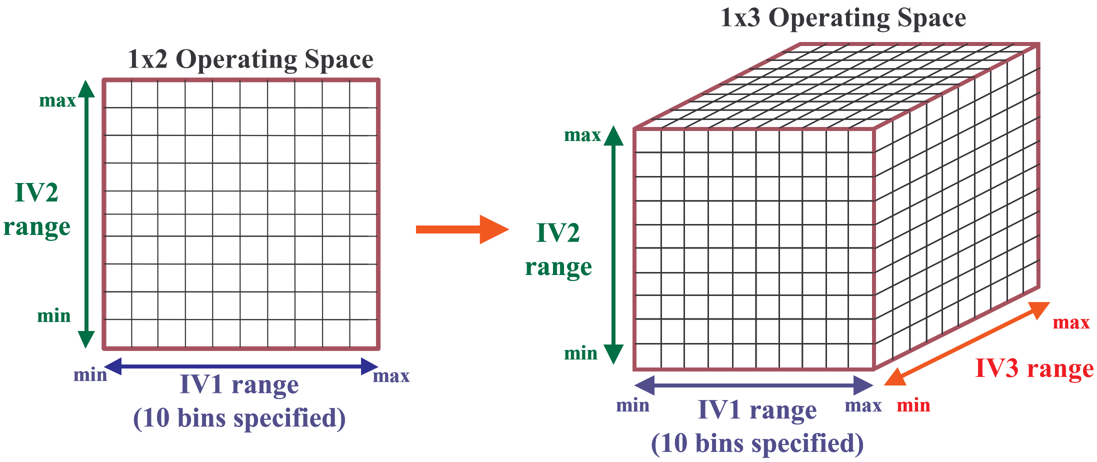

Figure 2.6.12. Illustration of the operating space and operating cells of 1x2 & 1x3 systems [14].

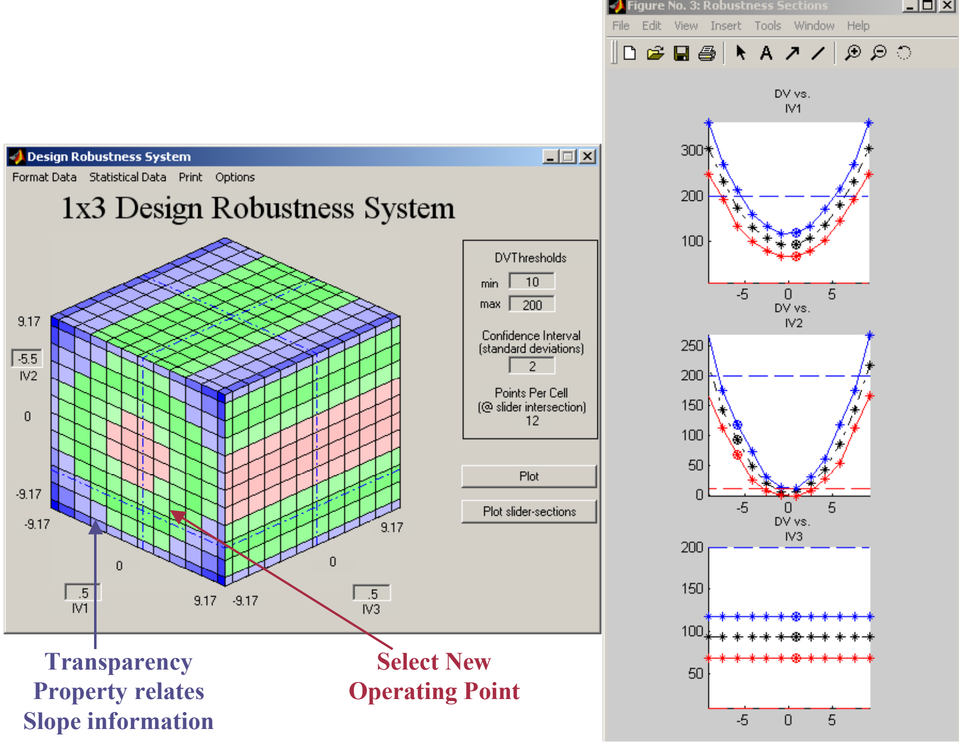

DVThresholds
min 10
max 200
Confidence Interval (standard deviations) 2
Points Per Cell (@ slider intersection) 12

Transparency Property relates Slope information

Select New Operating Point

Figure 2.6.13. Illustration of the enhanced 1x3 system GUI graphical output [14].

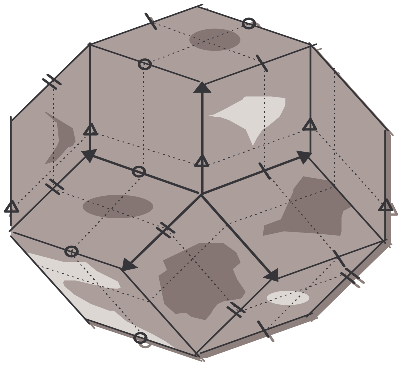

Figure 2.6.14. An example of a 1x5 robustness GUI (5 sliders representing each independent variable)[14].

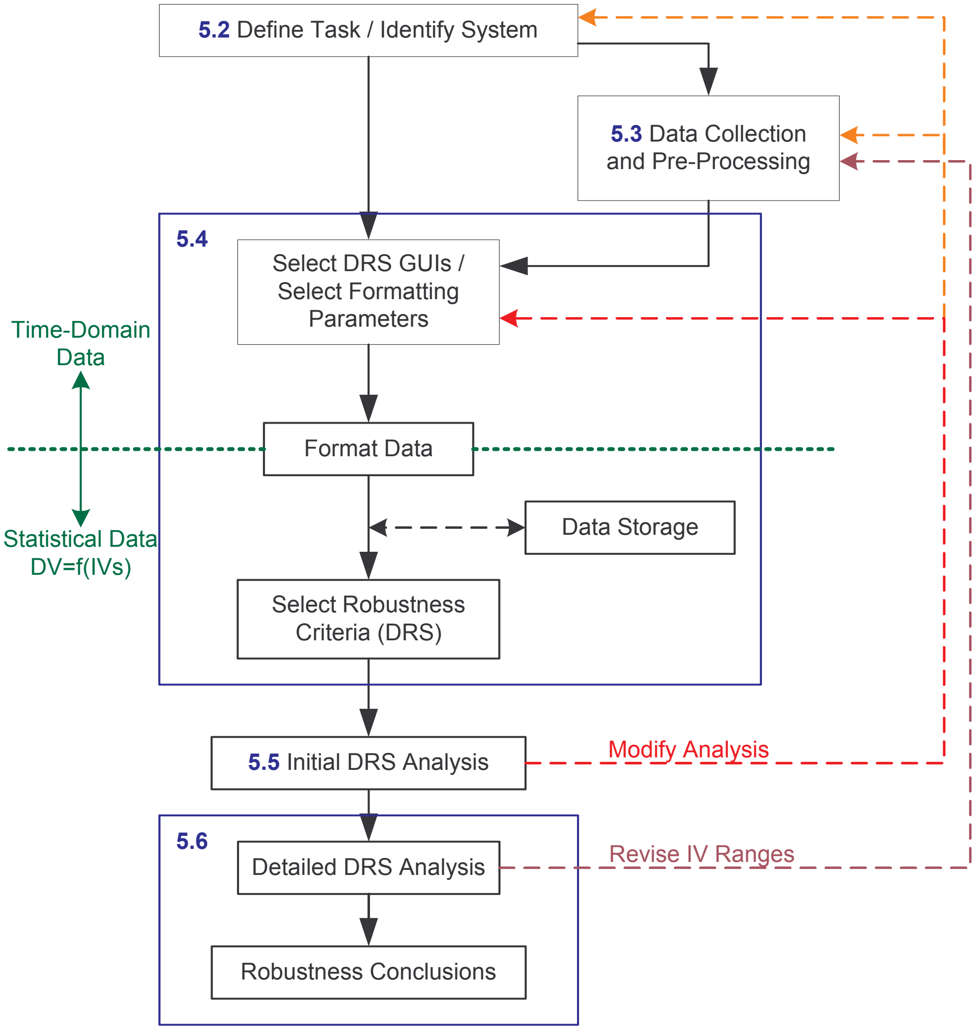

Figure 2.6.15. Overview of the DRS robustness analysis process [14].

2.6.8 Acknowledgments

The authors would like to thank both the Ford Motor Company and the U.S. Army Research Office for their support of this research.

2.6.9 References Section 2.6

[1] Moskwa, John J., Scarisbrick, Andrew D., and Eade, Derek, "Design Robustness System (DRS): New Concepts for Robustness Analysis." Proceedings of the 1999 American Control Conference, San Diego, June 1999

[2] Davis, T.P., "Robustness Thinking and Robust Engineering Design." Proceedings of the IMechE Conference, April 1997.

[3] Papoulis, A. Probability, Random Variables, and Stochiastic Processes. McGraw-Hill, Inc.,1984.

[4] Breipohl, A.M. Probabilistic Systems Analysis, an introduction to probabilistic models, decisions, and applications of random processes. John Wiley & Sons, Inc., 1970.

[5] MathWorks website: http://www.mathworks.com/

[6] Marchand, Patrick. Graphics and GUIs with MATLAB. Second Edition. CRC Press, 1999.

[7] Herniter, Marc E. Programming in MATLAB. Brooks/Cole, 2001.

[8] Hanselman, Duane, and Littlefield, Bruce. Mastering MATLAB 6; A Comprehensive Tutorial and Reference. Prentice Hall, 2001.

[9] Rahman, Sadek, and Sun, Richard, "Robust Engineering of Engine Cooling System." SAE Paper 2003-01-0149. 2003.

[10] Gu, L., and Yang, R.G., "Recent Applications on Reliability-Based Optimization of Automotive Structures." SAE Paper 2003-01-0152. 2003.

[11] Zou, T., Mahadevan, S., Mourelatos, Z.P., and Meernik, P., "Reliability Analysis of Systems with Nonlinear Limit States; Application to Automotive Door Closing Effort." SAE Paper 2003-01-0142. 2003.

[12] Six Sigma website: http://www.isixsigma.com/me/taguchi/

[13] Dorey, R.E., and Scarsbrick, A.D., "Rapid Prototyping Methodology Applied to the Powertrain Control System." IEE Colloquium into System Control Integration and Rapid Prototyping in the Automotive Industry. 9/12/1997.

[14] Bedrosian, James A., "Design Robustness System-Development of a Graphical, User-Interactive Software Tool for Visualization of System Design Robustness," M.S. Thesis, Department of Mechanical Engineering, University of Wisconsin-Madison, June 2003.

(5) “Technology transfer” (any specific interactions or developments which would constitute technology transfer of the research results). Examples include patents, initiation of a start-up company based on research results, interactions with industry/Army R&D Laboratories or transfer of information which might impact the development of products.

Brian Luptowski started work at Gamma Technologies in June of 2003 in the area of engine/cooling system simulation and is working on the integration of engine and cooling system software for commercial and research applications.

Thrust 3: Detailed Chemical Characterization of Diesel Engine Exhaust:

3.1 Scientific Progress and Accomplishments During the Reporting Period:

The research effort in this task can most easily be described via three objectives: development of methods that integrate advanced air pollution sampling and analysis techniques with state of the art engine research facilities; investigate the effects of changes in engine design, operating conditions, lubricants and fuels on the physical and chemical properties of emissions: use these data to gain an enhanced understanding of the fundamental combustion phenomena occurring within the engine. Furthermore, it is anticipated that this advanced understanding can be incorporated into our state of the art 3-D and system simulations for use in gaining further insight into the complex interaction between the fuel, lubricant and operating conditions and the resulting engine performance and environmental impact.

A schematic showing the different aspects of the research and how they fit together is given below in Figure 3-1.

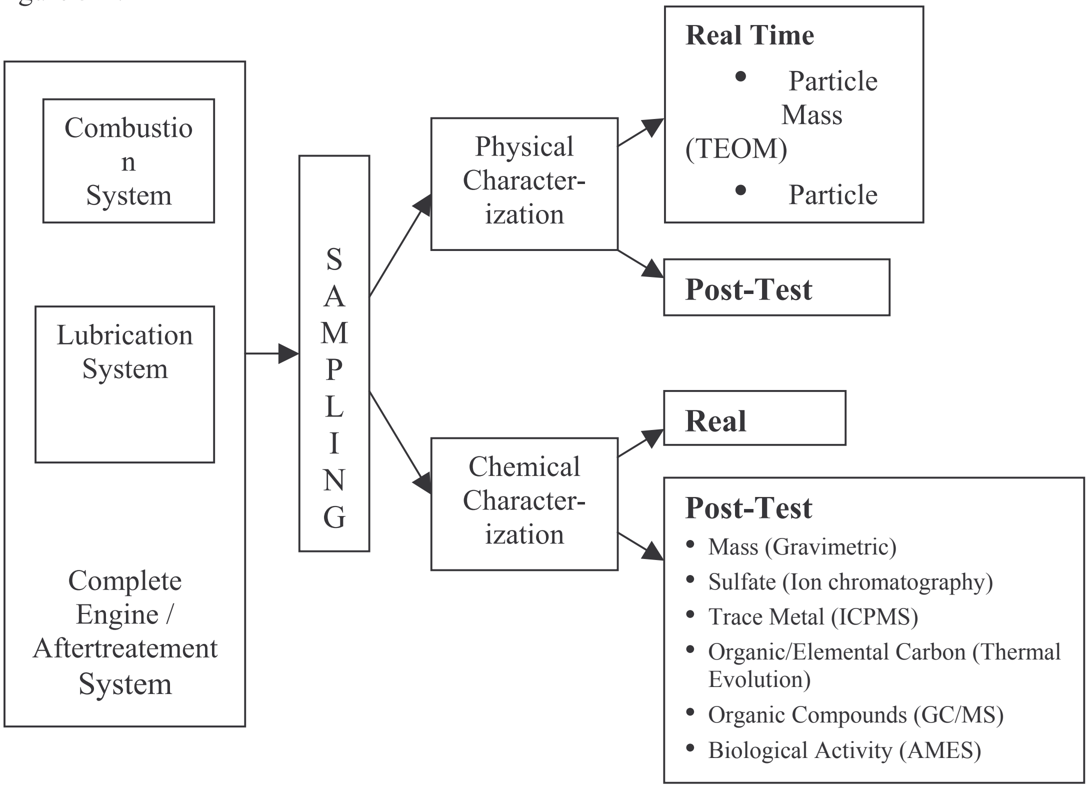

Figure 3-1: Schematic of overall research program

The research being performed was a collaborative effort between the Engine Research Center (UW), the Civil and Environmental Engineering-State Hygiene Laboratory of the University of Wisconsin – Madison and Michigan Technological University. At the University of Wisconsin Madison the physical and chemical characterization of the exhaust was performed, with an emphasis on the engine combustion and lubrication systems. The work at Michigan Technological University focused on the complete engine system. The State Hygiene Laboratory interfaced with all experimental efforts in performing the detailed analysis of the samples provided.

The single cylinder combustion study at the ERC was an investigation of the effects of engine operating conditions and fuel characteristics on the detailed chemical compositions of diesel particulates and gaseous emissions and understanding how lubricating oil participates in the in-cylinder processes. This work was done on a Cummins N14 research engine in the Engine Research Center (ERC).

The schematic of the research engine bench is shown in Figure 3-2. The engine employed in the experiment is a research single-cylinder direct-injection (DI) 4-cycle diesel, adapted from an in-line six-cylinder Cummins N14-series engine, which has a low swirl, turbo-charged, 4-valve, centrally located direct-injection combustion system. The combustion chamber of the engine is a quiescent, shallow dish type and it uses a CELECT unit injector. The specification of the engine is given in Table 3-1.

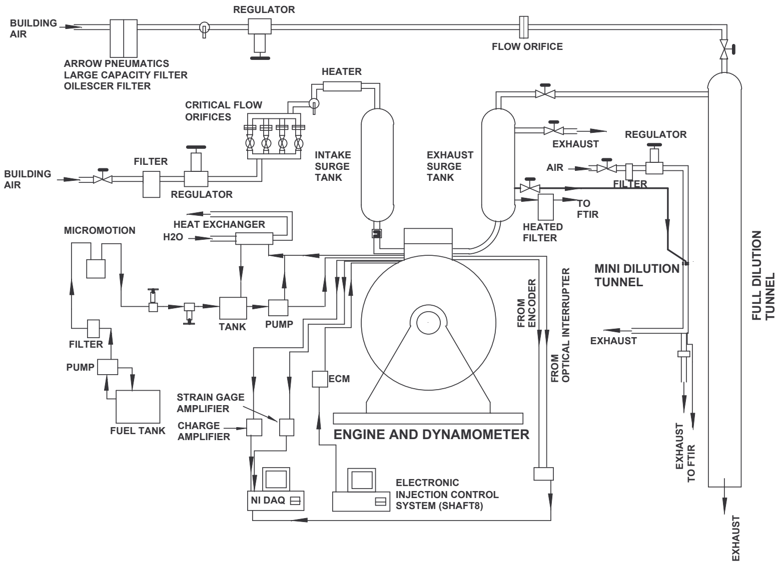

Figure 3-2. Schematic of the research single-cylinder Cummins N14 engine bench layout.

The laboratory has a full-dilution tunnel system to collect particulate samples from the engine. Gaseous emissions such as nitrogen oxides (NOx), carbon monoxide (CO), total hydrocarbon (THC), and carbon dioxide (CO2) are measured using with either an FT-IR spectrometer or California Analytical Emission bench.

Table 3-1. The research single-cylinder Cummins N14 engine specification.

Engine Type	Research Single-Cylinder Diesel
Cycle	4-stroke
Combustion Chamber	Quiescent
Piston Chamber	Shallow Dish
Number of Intake Valves	2
Number of Exhaust Valves	2

Compression Ratio	13.1:1
Swirl Ratio	1.4
Displacement	2333 cc
Bore/Stroke	139.7 mm / 152.4 mm
Combustion Chamber Diameter	97.8 mm
Connecting Rod Length	304.8 mm
Piston Pin Offset	None
Injection System	Unit Injector, Direct Injection
Nozzle Dimension	8 × ϕ 0.2 mm
Length/Diameter of holes (l/d)	4.1
Spray Angle	152°

AUGMENTED FULL DILUTION TUNNEL SYSTEM

For the current study an augmented sampling system, which was designed and installed according to the EPA ambient air quality measurement protocol, was used. Specifically, the secondary dilution tunnel of a typical full dilution tunnel was enhanced to allow more detailed assessment of the individual chemical components of the particulate matter. The design of the augmented sampling system was based on the study by Hildemman et al. [4] and Schauer et al. [5,6,7]

Figure 3-3 shows the schematic of the augmented sampling system, which consists of a primary dilution tunnel (PDT), secondary dilution tunnel (SDT), residence time chamber (RTC), and subsystems such as a 142 mm filter holder, two PM2.5 cyclones, several 47 mm filter holders, vacuum pumps, etc.

Because diesel particles are naturally charged, as a result of the combustion process, which can cause electrostatic deposition in the sampling system, the current sampling system was made with electrically non-chargeable materials, such as 304, 316, and 316L stainless steels. Thermophoretic deposition is caused by asymmetric forces, which arises from a temperature gradient. To minimize the temperature gradient inside the sampling line, its main body was made with a thin 304 stainless steel tube (thickness = 0.16 cm) and insulated. In addition, the surface temperature of the residence time chamber can be controlled to be approximately the same temperature as the inside gas temperature by using four rows of heated bands and respective temperature controller. The sampling system inlet, which supplies the secondary dilution tunnel, was made thin and sharp to facilitate isokinetic sampling, and its diameter was gradually increased to minimize inertial deposition of particles in bends of the pipe.

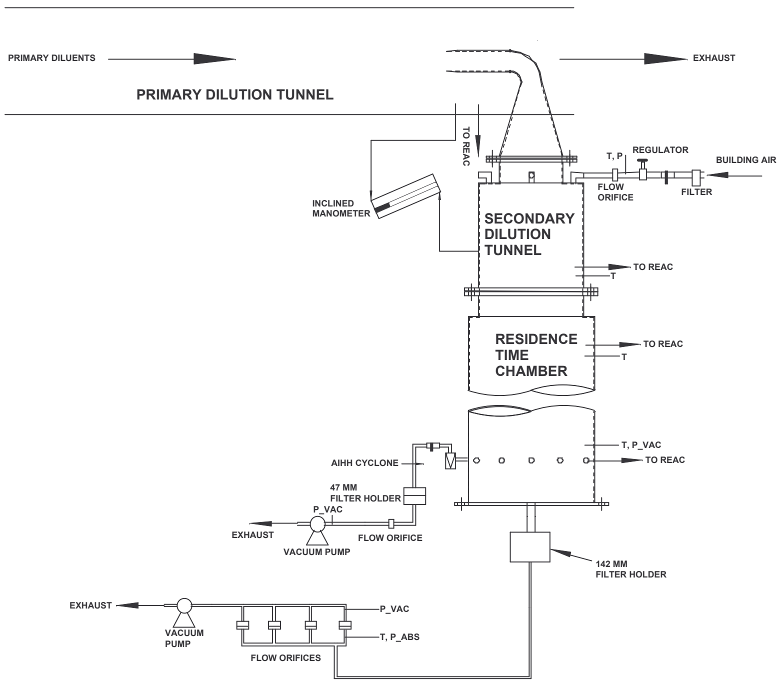

Figure 3-3. Schematic of the augmented sampling system in the Cummins N14 engine bench.

The residence time chamber was designed to give a residence time of between 30 and 60 seconds, under isokinetic sampling, which is believed to be sufficient time to allow all the condensation processes to take place for the current system [8].

At the bottom of the residence time chamber, a 142 mm filter holder is attached. It has two functions. First, the 142 mm filter holder allows a large range of sample flow rates, which enables us to control the residence time in the residence time chamber, while maintaining isokinetic flow from the primary dilution tunnel. Second, a large amount of sample can be collected for the analyses such as soluble organic fraction (SOF).

The augmented sampling system has many extra sampling ports to collect many different kinds of samples. The relative humidity (RH) of the diluted gases is measured with dry- and wet-bulb thermometers installed in one of the available sampling ports. All the flow rates of air and diluents are controlled by critical flow orifices.

DETAILED CHEMICAL COMPOSITION

The two types of sampling trains that were used are shown in Figure 3-4. These are attached to the residence time chamber and are operated in parallel. All the flow rates are controlled with critical flow orifices located downstream of the filter holders. The first component of each sampling train is an AIHH aluminum Teflon coated PM2.5 cyclone, which is operated at a flowrate of 24 liter/min.

As shown in Figure 3-4 (top), the first sampling train consists of a cyclone followed by three Teflon membrane filters (47 mm diameter, Gelman Teflo, 2 μm pore size) and one baked quartz fiber filters (47 mm diameter, Pallflex Tissuequartz 2500 QAO). The first Teflon membrane filter is used for gravimetric determination of the PM and is analyzed for sulfate ions by ion chromatography (IC). The second is for a duplicate PM concentration measurement, and the third is used for an analysis of trace metals by ICP-mass spectrometry (ICP-MS). The quartz fiber filter is for determination of elemental and organic carbon (ECOC), which is analyzed with a Sunset Laboratories Carbon Analyzer, the operation of which follows NIOSH method 5040.

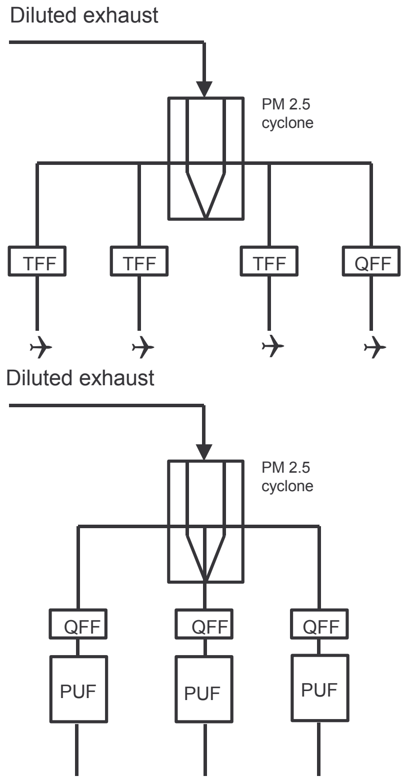

Figure 3-4. Sample trains of four (top) and three (bottom) filter holders with respective PM2.5 AIHH cyclone.

The second sampling train shown in Figure 3-4 (bottom) is composed of a cyclone followed by three baked quartz fiber filters operated in parallel, which are then followed by a polyurethane foam (PUF) cartridge (Atlas Foam; density = 0.022 g/cm3, ILD = 30, 5.7 cm diameter by 7.6 cm long) in series. The PUF cartridge is pre-cleaned with solvent. The particle-phase organic compounds are collected on the three quartz fiber filters and the PUF cartridges downstream of the filters collect semi-volatile organic compounds. The sampled filters and PUF cartridges are analyzed with a HP5973 gas chromatography/mass spectrometry (GC/MS) with a 30-meter HP-5MS GC column.

PARTICLE NUMBER AND SIZE DISTRIBUTION

A TSI 3936L10 Scanning Mobility Particle Sizer (SMPS) is connected to one of the sampling ports of the residence time chamber to measure particle size distributions of the particulates. The 3936L10 SMPS consists of a TSI Model 3081 Electrostatic Classifier, a TSI Model 3077 Kr-85 Aerosol Neutralizer, and a TSI Model 3010 Condensation Particle Counter (CPC). This instrument measures particle number concentrations and size distributions in terms of number-, mass-, volume-, and surface area-weighted.

EXPERIMENTAL OPERATING CONDITIONS AND RESULTS OF DETAILED CHEMICAL ANALYSIS OF ENGINE EXHAUST

For this research effort data was taken for a wide range of engine operating conditions with three different fuels. The engine's run conditions were set to those of the CARB 8-mode test. The specific values of the different engine parameters used to establish the individual operating modes are shown in Table 3-2. In addition, we were successful in using an Atmospheric Time of Flight Mass Spectrometer (ATOFMS) to analyze the particulate matter in approximately "real time" on a basis of chemical composition and particle size.

Table 3-2. Values of Engine Operating Parameters Used in Achieving the CARB 8-Mode Operation

	Mode 1	Mode 2	Mode 3	Mode 4	Mode 5	Mode 6	Mode 7	Mode 8
Speed	1800	1800	1800	1200	1200	1200	1200	700
Load [%]	100	75	50	25	100	75	50	10 (idle)
Remark	High rated speed				Peak torque			Low rated speed
Intake P [kPa]	179.3	179.3	179.3	179.3	175.2	179.3	177.9	175.2
Intake T [°C]	49	48.3	48.3	48	48.3	49	48.1	48.7
Exhaust P [kPa]	174.1	188.5	184.4	157.9	150.7	217.6	187.9	161.7
Equi. Ratio, ϕ	0.69	0.50	0.34	0.21	0.82	0.69	0.41	0.09
Peak Incylin. P [MPa] @ aTDC	7.15 13.25	7.21 14.0	7.08 7.25	7.63 8.5	10.58 10.75	7.85 15.5	7.77 13.25	7.31 3.75
Peak Incylin. T [K] @ aTDC	1958 30.75	1856 26.25	1588 22.75	1362 15.25	2212 20.75	2140 28.75	1728 20.75	1024 3.75
ISFC [kg/ihp-hr]	0.172	0.146	0.14	0.131	0.168	0.160	0.141	0.219
IMEP [MPa]	1.083	0.922	0.671	0.524	1.491	1.225	0.878	0.150
SOI [CA aTDC]	-5	-5	-5	-2	-11	-2	-2	-6
Inj. Duration [CA]	25	20	13	10	27	22	15	3.5
Peak Injec. P [MPa]	121	113	106	62	96	80	70	42

For each of the operating conditions listed in Table 3-2 complete sets of filters were obtained. The mass of the particulate matter was evaluated through both gravimetric analyses of filters and by summing the mass of the measured elemental carbon, organic carbon and sulfates plus trace metals. The agreement was very good, which we interpreted as an indication of the accuracy of your experimental technique.

Three different fuels were used throughout the course of this research. The fuels were nominally classified according to their sulfur content, although other characteristics such as aromatic content and cetane number, for example, varied as well. The fuels used were a standard 350 ppm sulfur fuel, a low sulfur fuel, 14 ppm, and a zero sulfur fuel, Fischer Tropsch. A more detailed description of the fuels is given in Table 3-3.

Table 3-3. Test Fuel Properties

	Fuel A	Fuel B	F-T
Density, 15°C	865 kg/m^3	830.5 kg/m^3	768.0 kg/m^3
API Gravity, 16/16°C	31.4	38.8	52.7
Viscosity @ 40°C	2.595 mm^2/s	2.43 mm^2/s	1.98 mm^2/s
Flash Point	70°C	65°C	58°C
Cetane Number	39.1	52.9	74
Sulfur	352 ppm	14 ppm	< 1 ppm
Gross Heating Value	43506 kJ/kg	45652 kJ/kg	47239 kJ/kg
SFC Aromatics	49.2 wt%	22.1 wt%	< 1 wt%
Mono-Aromatics	29.6 wt%	19.4 wt%	
PNA's	19.6 wt%	2.7 wt%	
H/C	1.69	1.89	2.16
Selected Trace Metals	All below detection limit	Assumed all below detection limit	All below detection limit
Magnesium (Mg)	< 0.1 ppm		< 0.1 ppm
Calcium (Ca)	< 0.1 ppm		< 0.2 ppm
Manganese (Mn)	< 0.1 ppm		N/A
Iron (Fe)	< 0.1 ppm		< 0.1 ppm
Lead (Pb)	< 0.1 ppm		< 0.4 ppm
Sodium (Na)	< 0.1 ppm		< 1.0 ppm
Chromium (Cr)	< 0.1 ppm		< 0.1 ppm

The mass of the elemental carbon, organic carbon and the sulfate contained within the particulate changes significantly as the engine load is changed. These trends are shown in Figure 3-5. It can be seen in the figure that as the load increases the proportion of the particulate matter that is elemental carbon increases and the proportion of the particulate matter that is organic carbon decreases. The proportion of the particulate matter that is sulfates also increases as the load increases, except for operation at Mode 5, which has an advanced injection timing. This can be seen in Figure 3-6. In these figures one can also see the impact reducing sulfur has on the characteristics of the particulate matter. The lower sulfur in the fuel yields combustion characteristics which reduce particulate matter, both in terms of elemental carbon and organic carbon. This could be the result of a lower sulfate composition in the particulate matter, see Figure 3-6, or the result of combustion differences resulting from the differences in fuel properties, such as cetane number, see Table 3-3.

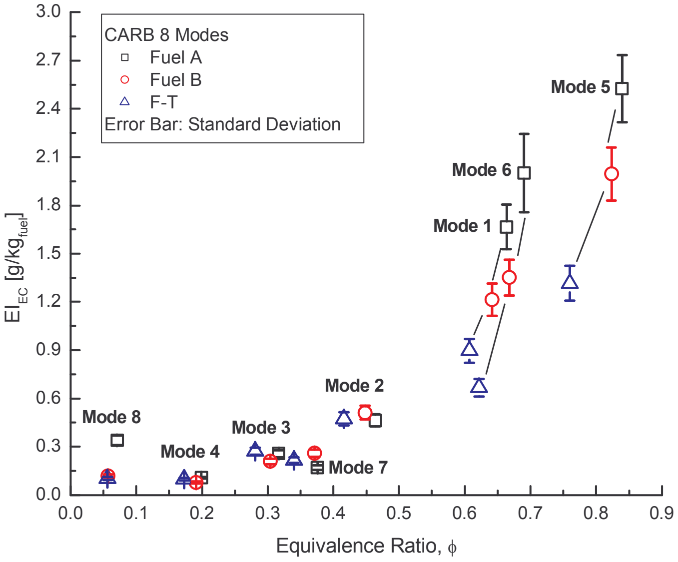

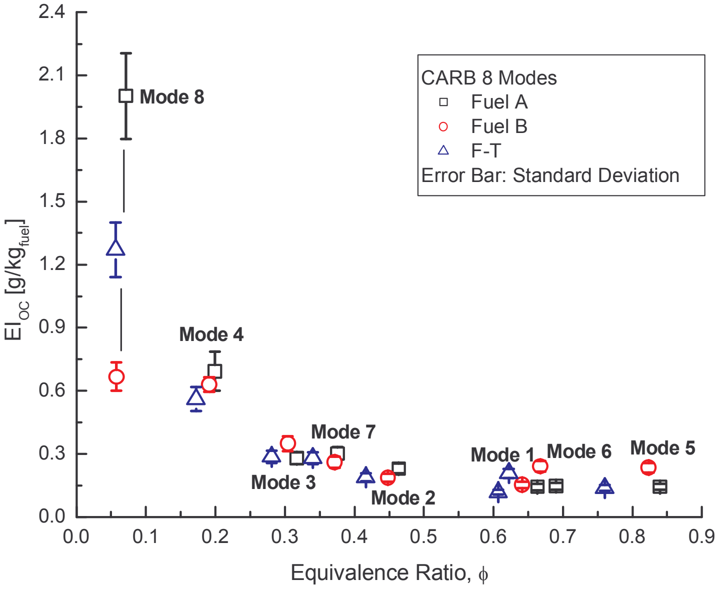

Figure 3-5 Distribution of Elemental Carbon and Organic Carbon within the Particulate versus Equivalence Ratio (Load)

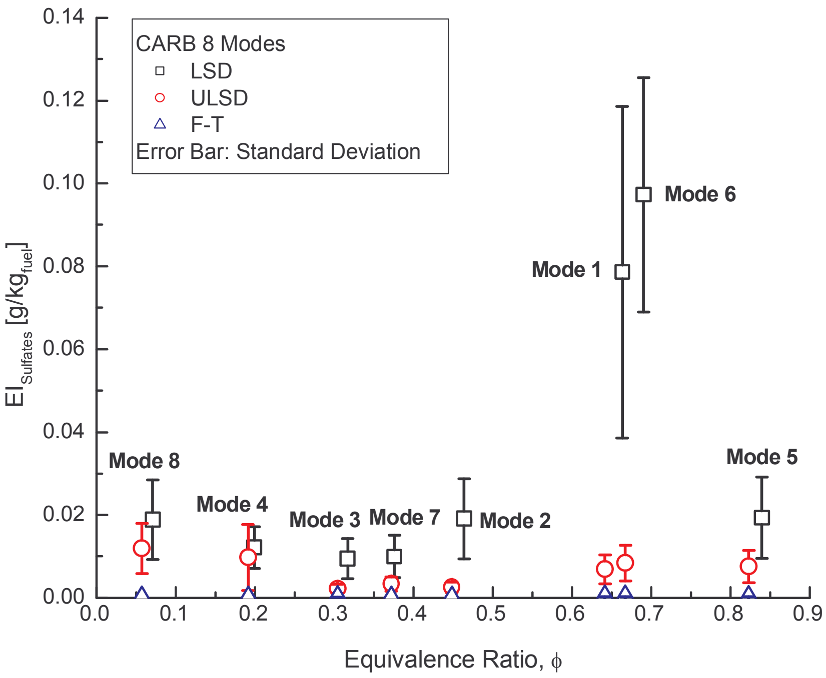

Figure 3-6. Distribution of Sulfate within the Particulate versus Equivalence Ratio (Load). Mode 5 has lower sulfate because of the advanced injection timing of this operating condition.

These data were correlated to the global combustion characteristics of the engine and the results are shown in Figure 3-7. It appears that there is a correlation between the fraction of premixed burn and the proportion of the particulate matter that is organic carbon. The larger the premixed burned fraction, the larger the organic carbon content.

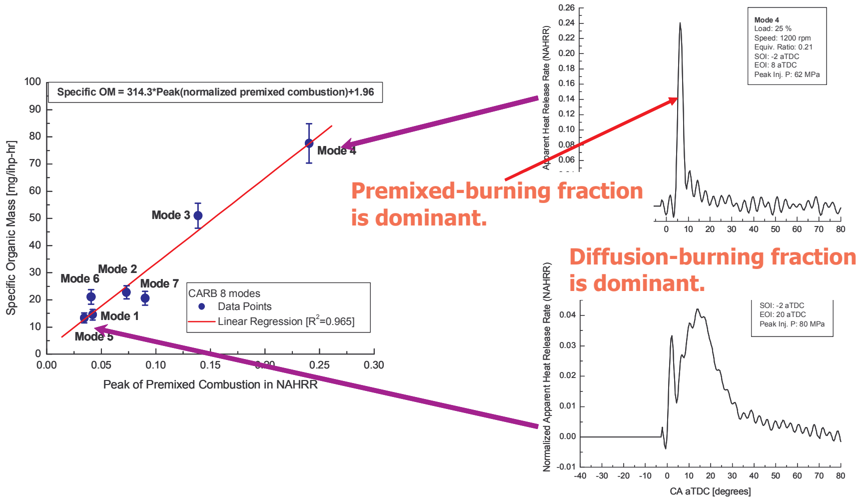

Figure 3-7. Correlation between premixed burn fraction and organic carbon content in the particulate Fuel A.

The data for trace metals, magnesium, calcium, manganese, iron and lead, for different engine loads at speeds of 1200 RPM and 1800 RPM are shown in Figure 3-8. Note the values of calcium are divided by 20, in order to display them on the same scale as the other trace metals. That is, calcium is the dominant trace metal measured in these experiments. Calcium is not present in the fuel, so these data can be used to assess the participation of the lubricating oil in the combustion process and show that the lubrication oil contributes to the particulate matter in different amounts at different engine operating conditions. The iron measured in the particulate is most likely from engine wear.

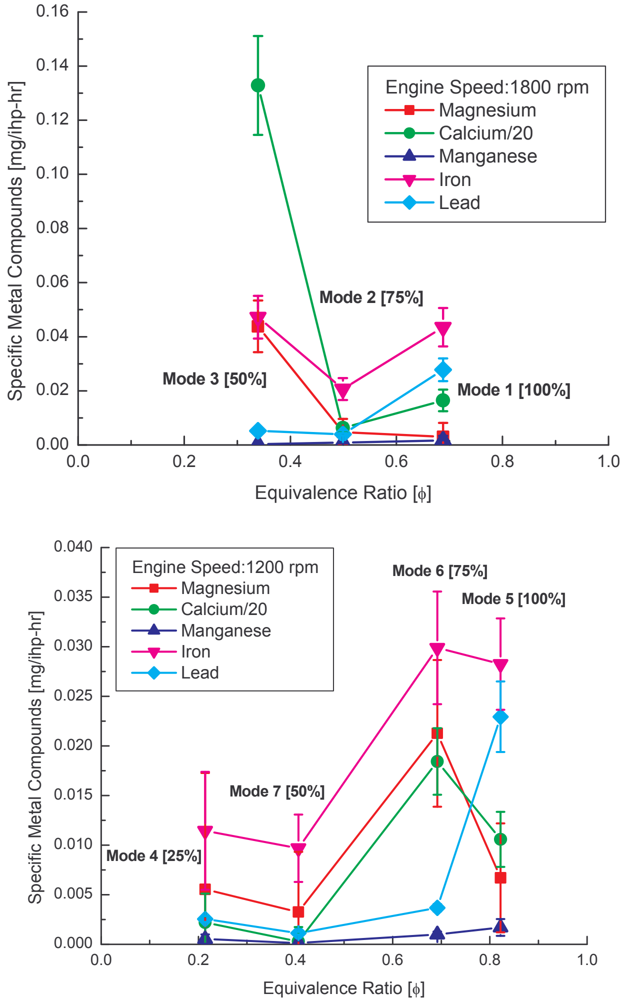

Figure 3-8, Trace metal concentration in the particulate matter for different engine loads, at speeds of 1200 RPM and 1800 RPM. Fuel A

When the premixed burn fraction is small, the organic carbon content will probably be small. Typically, the premixed burn fraction correlates with the ignition delay; shorter ignition delays have smaller premixed burn fractions. It appears that this also correlates with the chemical composition of the particulate matter. Highly turbocharged, high power density diesel engines will most likely have particulate matter that is primarily elemental carbon, with contributions of trace metals coming from the lubricating oil

It has also been observed that for different engine operating conditions, the chemical composition of the particulate matter can be quite different, even though the mass loading of the particulate, as measured with the typical gravimetric filter technique, is very much the same. This phenomenon is shown in Figure 3-9.

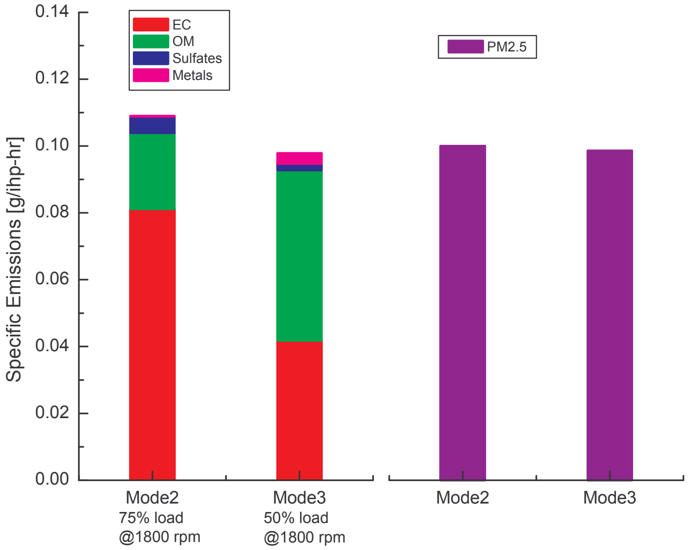

Figure 3-9. Comparison of the distributions of elemental carbon, organic carbon, sulfate and trace metals for two different engine operating conditions (left hand bar graphs) for which the gravimetric particulate measurement (right hand bar graphs) are approximately equal. Fuel A.

These data indicate that the details of the combustion process are quite different for these two engine conditions, even though the mass of particulate emission is the same. As the particulate emission is indicative of incomplete air utilization, and hence an indication of approaching the limit of the power density, these data indicate that the details of the chemical energy conversion processes at these power limiting conditions, are different for these two operating conditions.

During this research, we were fortunate to have the opportunity to use an atmospheric time of flight mass spectrometer (ATOFMS). The instrument was brought to the Engine Research Center as part of a NSF collaborative equipment use research grant. The instrument is capable of sampling individual particles at a rate of up to 150 particles per minute and measuring their size (within a size range of 0.15 to 5.0 μm) and chemical composition. An example of these data is shown in Figure 3-10, which shows the percentage of particles containing organic carbon versus particle size for three different loads at 1200 RPM. It appears that there is a tendency for organic carbon to be found in the smaller particles. This is consistent with the conceptual picture that the organic carbon originates from semi-volatile organics which nucleate, forming small particles, which dominate the smaller size distribution.

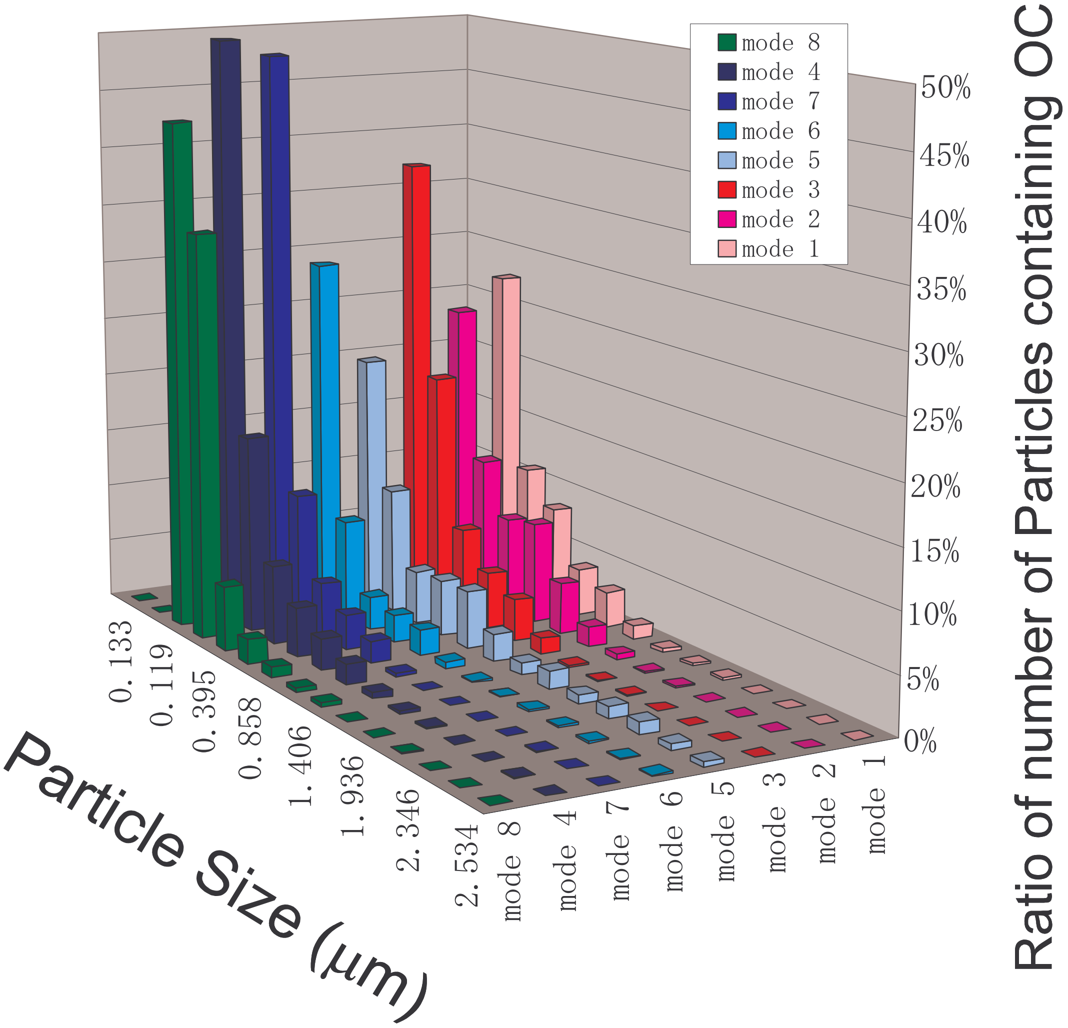

Figure 3-10 An Example of ATOFMS data. The partitioning of the particulates into size categories and the percent of particles in each size category that contain organic carbon. Fuel A – D2

Detailed chemical analysis was done on the particulate samples in an attempt to identify the origin of the organic carbon found in the particulate matter. The relative distribution by carbon number of elutable hydrocarbon is given in Figure 3-11. From Figure 3-11, it is seen that the proportioning of the organic carbons covers a range carbon numbers and that the relative proportion of the types of species changes with engine operating condition.

The fraction of carbon compounds that would most likely be attributed to lubricating oil, carbon numbers greater than 30, only constitutes a small portion, less than approximately 25%, of the organic carbon found in the particulate. It cannot be determined whether the smaller carbon number molecules are fragments of the larger oil molecule, or originate from the fuel. This will be discussed in more detail later in the report.

Further resolution of the organic carbon species is shown in Figures 3-12 and 3-13. As shown in Figure 3-12, the chemical compounds have been classified by their structural groups. The results are plotted as specific emissions, μg/ihp-hr, so one should not correlate the magnitude of the bar graph with the actual mass of the emission from the engine. What can be seen from this plot is the range of chemical compounds that are found in the particulate matter. For example, the families of compounds of hopanes and steranes are only found in the lubricating oil. The n-alkanes can be found in either the lubricating oil or the fuel, depending on the size of the base chain. The alkylcyclohexanes and the polycyclic aromatic compounds are probably from pyrolysis reactions during combustion. One trend that is seen in studying Figure 3-12 is that the relative contribution of fuel, lubricating oil and combustion pyrolysis products changes with engine operating conditions.

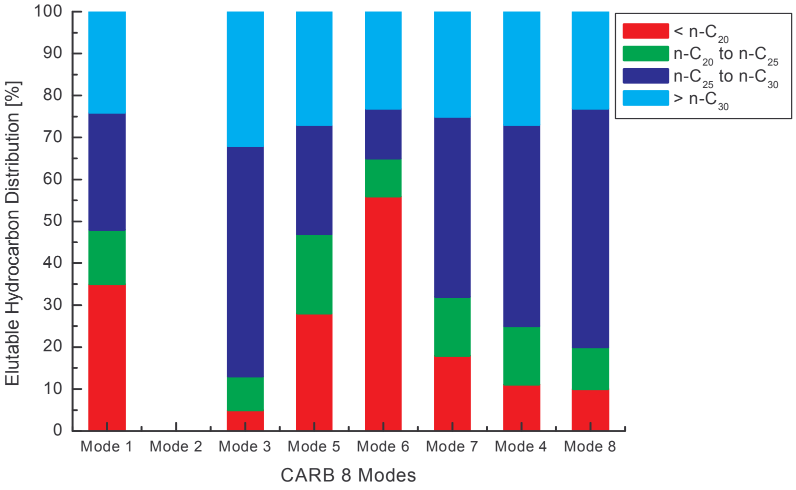

Figure 3-11. Distribution of elutable hydrocarbons within the particulate matter in terms of carbon number for the different engine operating modes.

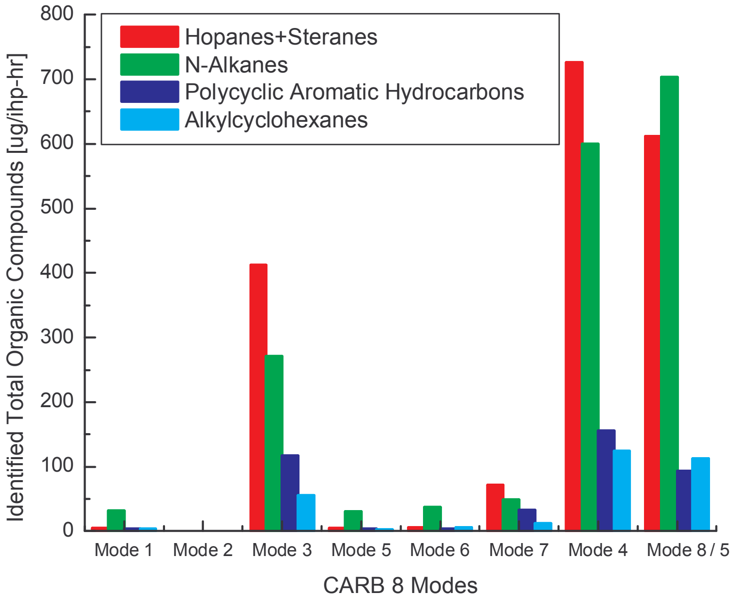

Figure 3-12. Summary of the distribution of chemical structural groups observed in diesel particulate matter. Fuel A

An even more detailed analysis of the polycyclic aromatic hydrocarbon (PAH) compounds is shown in Figure 3-13. It is seen from the data that the PAH are only present for the in the light load conditions, where the organic carbon proportion of the particulate matter is high.

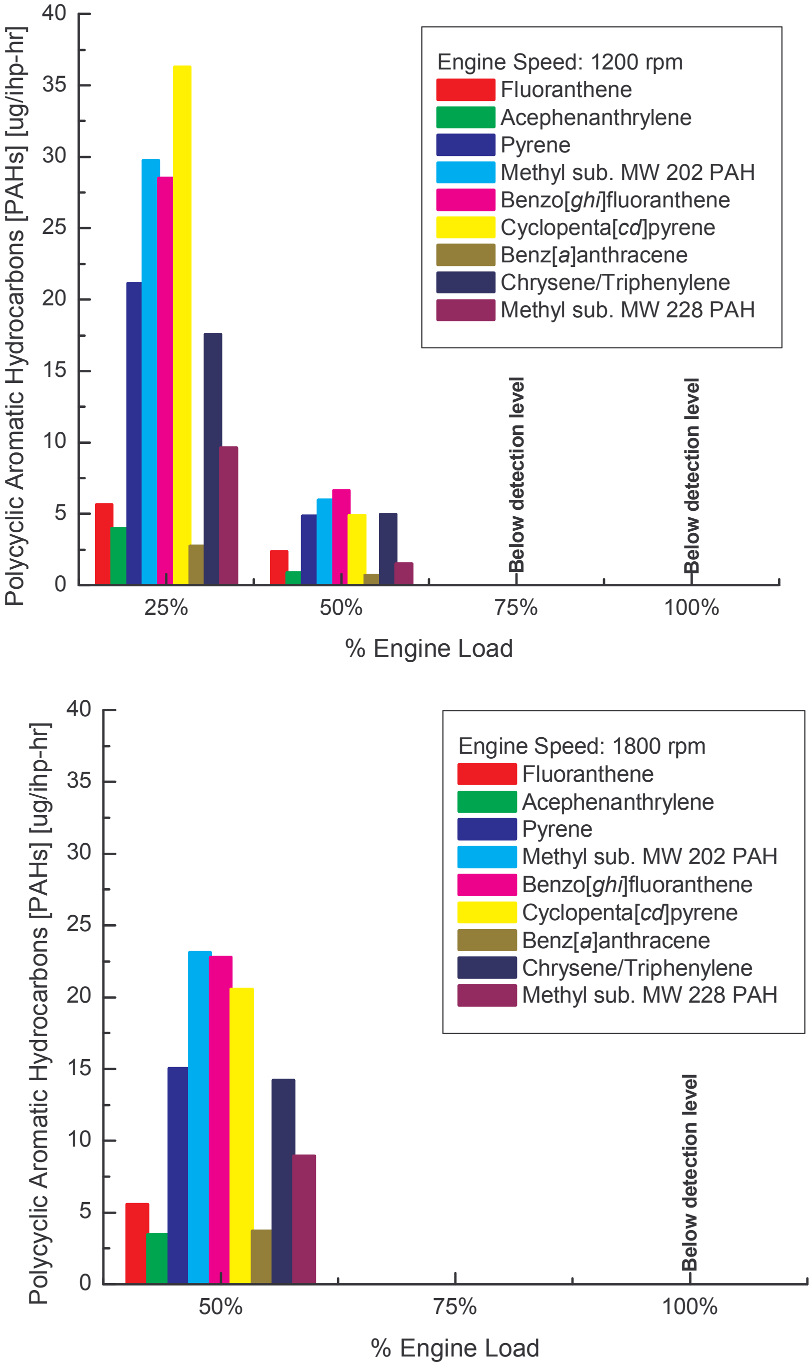

Figure 3-13 Particle phase PAH versus engine load and speed. Fuel A – D2

Particle size distributions were measured using an SMPS for a wide range of operating conditions. One can see that at idle and light load conditions the particle distribution is skewed towards the smaller particles. These small particles contribute very little to the total mass loading, even though their number density is very high. At the heavier loads the number of nano-sized particles deceases and more accumulation mode particles are present. From the distributions shown in Figure 3-14 it is readily observed that the increase in particulate mass emissions from the engine with increases in load is the results of a larger number of accumulation mode particles being emitted.

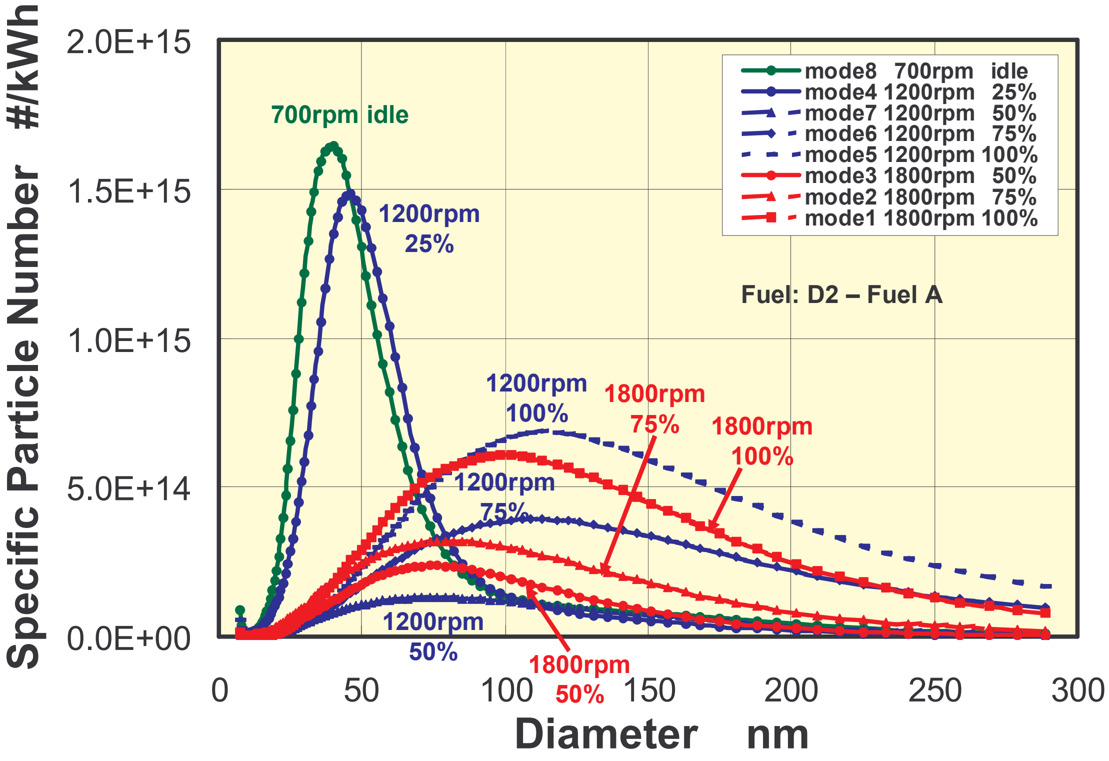

Figure 3-14. Particle size distributions for a range of engine speeds and loads.

The data shown in Figure 3-14 can be cast in a different light. Figure 3-15 shows the median particle size and number for the different operating conditions tested. The data is plotted as median particle size and number versus peak injection pressure. With the unit injector used on this engine, the peak injection pressure also correlates with load. Note that, in general, as the load increased, the median particle size and number also increased. The exceptions to this trend are the mode 4 and mode 8 operating conditions. The median particle number exhibits a pronounced increase for these operating conditions relative to the other conditions. These are light load conditions, mode 8 is idle, for which the premixed burn fraction was relatively high. As seen above, when the premixed burn fraction is high, the proportion of the particulate that is organic carbon increases. Closer analysis of the SMPS data showed that the particle number is high because of a very high number of nucleation, or nano, particles. This is a direct result of the predominance of organic carbon contributing to the particulate at these operating conditions.

As one pushes to higher power density, the limiting condition for air utilization, as evidenced by increases in particulate emissions, the result will be larger particles that are predominantly elemental carbon. At idle conditions; there will be a very large number of nano particles which are largely organic carbon. The chemical kinetic processes occurring at the air utilization limits for the two engine operating conditions are different.

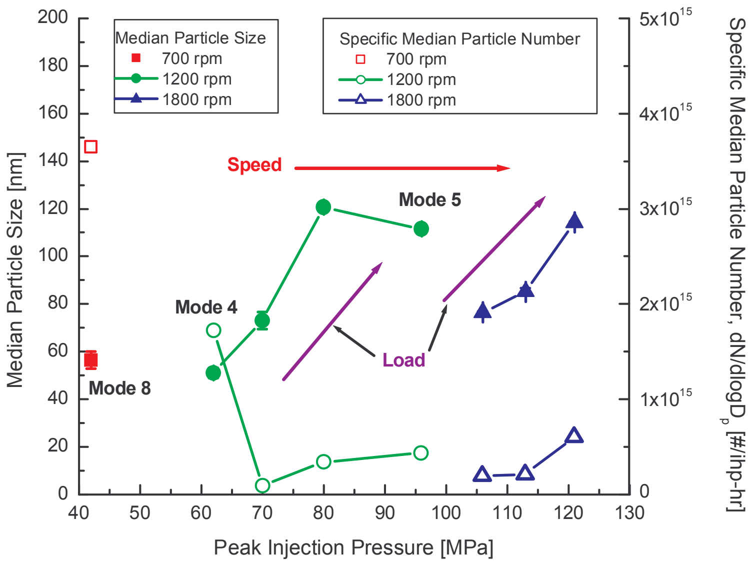

Figure 3-15. Median Particle Size and Specific Median Particle Number for the different engine operating conditions. The results are plotted against peak injection pressure, which is indicative of the engine load.

Impact Of Lubricating Oil On Particulate Composition And Tracing Lubricating Oil Consumption Via Detailed Chemical Analysis Of The Exhaust

Oil consumption is naturally regarded as one of the indices to evaluate the engine performance. Unreacted lubricating oil may contribution to the nucleation of nanoparticles [1]. Particulates from unburnt lubricating oil may be significant especially at low load engine operating conditions [2]. Consequently the reduction of oil consumption becomes important in its own right, as well being a component of reducing PM.

For the measurement of oil consumption, many methods have been used. The weighing methods and the volumetric methods, including the “drain method”, the “constant weight method”, and the “constant oil level method”, require considerable engine operating time to acquire reliable results. In addition to the time requirements, the accuracy can be problematic because of oil hang-up and fuel dilution. To compensate for such defects, tracer methods have been used [3]. Tracer methods involve exhaust sampling, typically using filters. In the work reported here detailed chemical composition of the particulate matter was determined through exhaust sampling, hence the potential exists to extract oil consumption information from these measurements, similar to a tracer technique.

In this research, Inductively Coupled Plasma Mass Spectrometer (ICPMS) and Aerosol Time-of-Flight Mass Spectrometer (ATOFMS) measurements were applied to the diesel exhaust. ICPMS, which uses the filter sampling technique, gives a detailed chemical composition of PM. Via its trace metal concentration, we can determine the relative lubricating oil consumption using a chemical mass balance, which then allows us to examine the effect of engine operating condition on lubricating oil consumption.

Experiments were performed at selected points of the California Air Resources Board (CARB) 8 mode test cycle. Figure 3-16 shows an engine map with the eight operating modes identified. The arrows on the figure depict the operating conditions evaluated in this research effort, modes 1, 4 and 5.

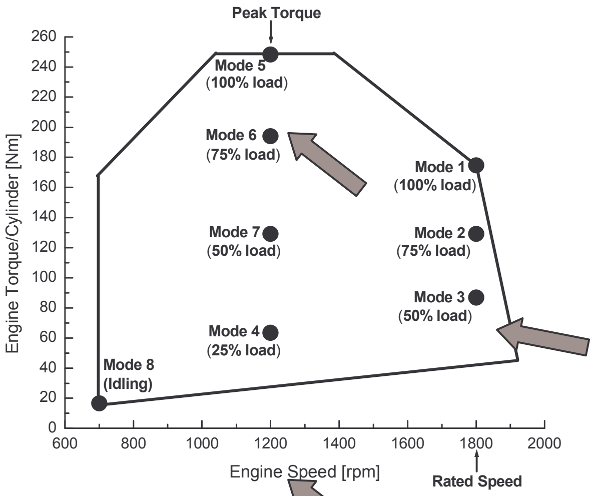

Figure 3-16. California eight mode test cycle with modes, 1, 4 and 5 identified. These were the conditions studied in this research.

The operating conditions for the conditions chosen are described in Table 3-2. The fuel used was a low sulfur EPA 2006 compliant fuel, Fuel B.

The purpose of this program was to assess the impact of different lubrication consumption mechanisms and rates on the resultant particulate and exhaust gas composition and characteristics. There are several avenues by which lubricating oil can be consumed during engine operation. Figure 3-17 shows a schematic of these different mechanisms.

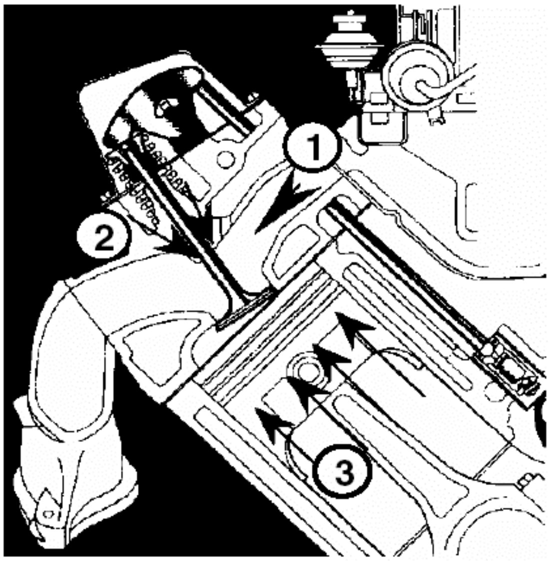

Figure 3-17. Schematic of different mechanisms for oil consumption. (From SAE 1999-01-3460)

As shown in the figure, lubricating oil can be consumed via: 1. blowby gases which are reintroduced into the intake flow by the PCV system; 2. leakage past the valve stem seals; 3. leakage past the rings; and 4. (not shown in the figure) leakage at the turbocharger.

In this experiment, we did not have a turbocharger and the crankcase was ventilated directly into the test cell exhaust system. Consequently we only investigated mechanisms 2 and 3, valve stem seal leakage and leakage past the rings, for their impact on diesel exhaust composition.

The oil consumption was determined through the measurement of the trace metals in the particulate [9, 10]. The most prominent trace metal in the particulate was found to be calcium. Analysis of the fuel indicated that there was no calcium in the fuel, so this should be a good indicator of lubricating oil consumption. By measuring the calcium concentration in the oil one could then calculate the oil consumption that would be necessary for the different calcium levels to exist in the particulate. This was the approach taken in the results reported here. As an internal check we also calculated, using the same procedure, the oil consumption using the zinc concentration measured in the particulate. Figure 3-18 shows a comparison of the oil consumption determined using the two different markers, calcium and zinc. The agreement between the two techniques is very good.

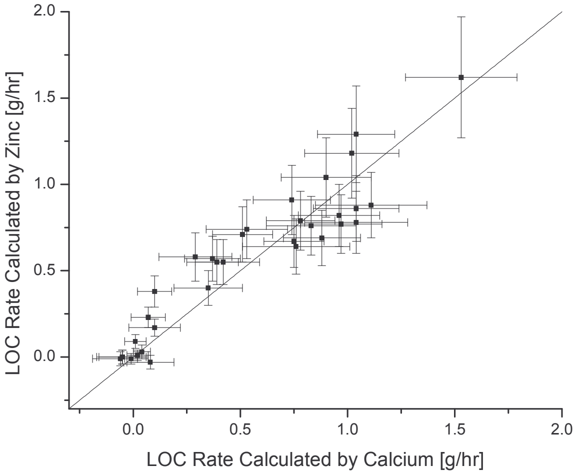

Figure 3-18. Lubricating Oil Consumption (LOC) as determined using calcium and zinc as tracers

Lubricating Oil Comsumption – Discussion

Various approaches were taken to vary the oil consumption of the engine. Engine runs were made with the intake valve stem seals removed, with the exhaust valve stem seals removed, with both intake and valve stem seals removed and with the oil control ring pressure spring reduced by 50 percent. Duplicate runs were made for several test conditions.

Figure 3-19 shows the oil consumption for the different test cases examined in the research. The data are plotted as a percent difference from the base case, which is the normal engine configuration. In looking at Figure 3-19 one is immediately struck by the fact that for the situation of no intake and exhaust valve stem seals and for the case of no exhaust valve stem seals the oil consumption was measured as less than the base case. This occurred for both mode 1 and mode 5 operating conditions. These data repeated. It is the authors' opinion that leakage past the exhaust valve stem, enhanced by the absence of the valve stem seal, is responsible for this observation. In a normal engine these gases would be routed back into the intake manifold via the crankcase ventilation system. In our engine, these gases would be directed into the building exhaust system. Consequently the oil and particulate matter would not exit the engine in the exhaust and would not be measured in our analysis.

Note that for the case of no intake valve stem seal there was a measured increase in the oil consumption. Likewise for the case of a 50% reduction in oil control ring pressure there was a measured increase in oil consumption. When the oil consumption increase was caused by the absence of the intake valve seals there was no relative impact for the two different engine operating conditions. However, for the case of the oil control ring pressure reduction there was a dependence of lubricating oil consumption on the engine operating condition. The maximum power condition resulted in higher oil consumption.

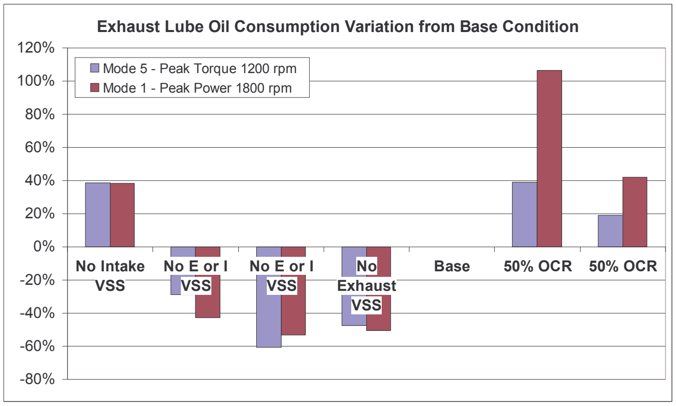

Figure 3-19. Relative oil consumption for different approaches of altering oil consumption.

It is important to put the relative oil consumptions into perspective in terms of their absolute magnitudes. Based on the measurements of calcium in the particulates and the calcium concentration in the oil the lubricating oil consumption was determined. The consumption rates were shown in figure 6 but are repeated here in Table 3-4 for emphasis.

The magnitudes of oil consumption given in Table 3-4 are for our experiment in which the engine was run under steady state conditions. Also shown in Table 3-4 are typical in-use oil consumption rates for engines. The typical in-use oil consumption rates are general values for engines operating over a range of conditions, which includes transient operation. It is striking the difference between the oil consumption rates measured in this experiment and those typical for in-use operation. The principle difference between our operating conditions and those of in use operation is the prevalence of engine transients. As such, one would conclude that a very important operational characteristic that impacts oil consumption is transient operation.

Table 3-4.
Oil Consumption For Steady State Engine Operation and "Typical" Values of In-Use Oil Consumption

N14 Steady State Oil Consumption - Modes 1 & 5	0.3 - 1.5 g/hr
N14 Steady State Oil Consumption - Mode 4	< 0.1 g/hr
Typical "in-use" oil consumption	0.1 - 0.5% full load fuel consumption: 7.0 - 40 g/hr

We have some data that supports this premise. Figure 3-20 shows the results obtained from an Aerosol Time of Flight Mass Spectrometer (ATOFMS). These data were obtained using a TSI Inc., Model 3800 ATOFMS during a step change in operating conditions. The data are qualitative but trends are discernible. Even though the data is qualitative, the sudden spike in Ca is quite apparent. This sudden spike occurs at the time of the step change in load. Again, even though the data is qualitative, it is interesting that the magnitude of the number of particles containing calcium during the transient is approximately an order of magnitude larger than the number of particles containing calcium during the steady state operation before and after the transient step. This observation is consistent with the premise that oil consumption is linked to transient operation.

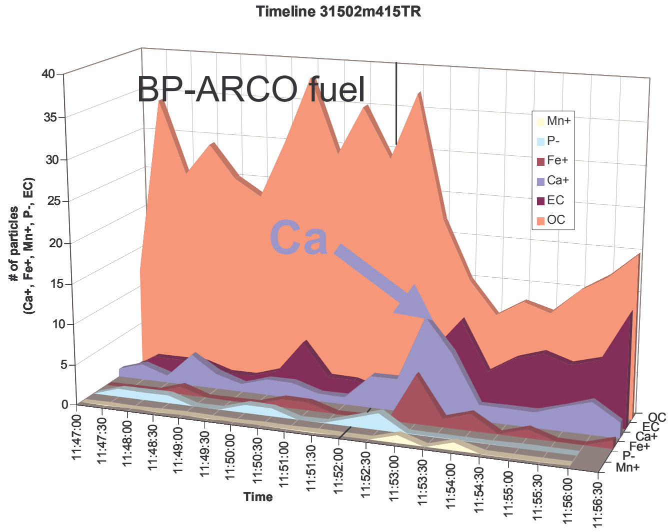

Figure 3-20. ATOFMS data of number of particles containing various trace metals as the engine moves through a step load change.

It seems apparent that for this engine operating in steady state operating conditions the oil consumption is very small. However, it was decided to continue with the data analysis to determine if differences in the detailed composition of the particulate could be correlated with variation in oil consumption rates.

To make this assessment, the mass based measurements of organic and elemental carbon and trace species were examined more closely. Since the measurements of the total particulate mass and resolved components, i.e. elemental carbon, organic carbon, trace metals and sulfates were done on separate filters, we first verified the consistency of the data by comparing the total mass measured on the particulate filters with the sum of the mass of the individual components, measured on individual filters. This comparison is shown in Figure 3-21. As seen in the figure, we get good agreement between the total mass of particulate and the sum of the individual components.

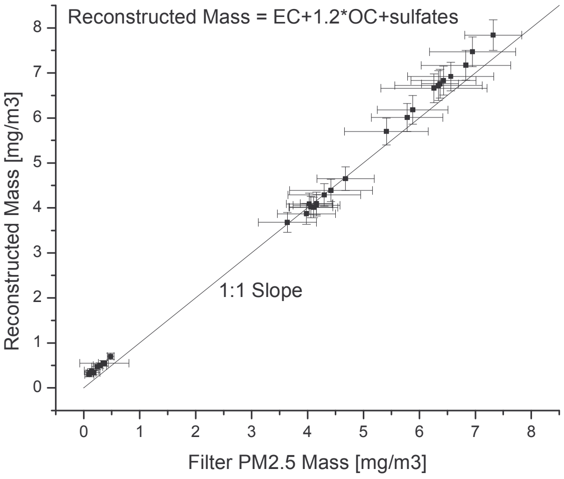

Figure 3-21. Comparison of the reconstructed mass, the sum of the individual components - each measured on separate filters, with the total filter PM 2.5 mass measurements.

Figure 3-22, a, b, and c show the partitioning of the particulate matter into elemental carbon (EC), organic matter (OM), sulfates and ash for the three different engine conditions run in this research. As seen previously, there is significant variation in particulate composition with changes in engine operating conditions.

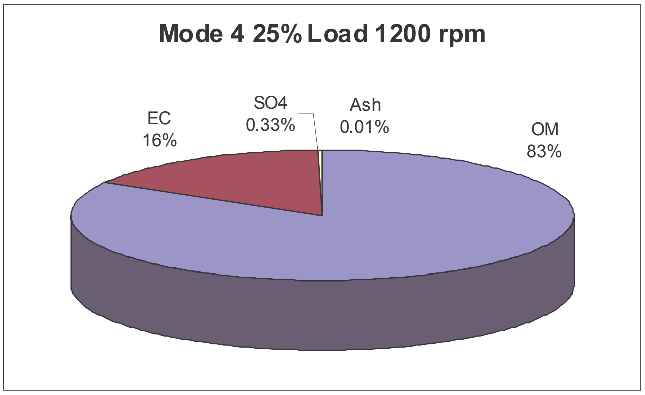

Figure 3-22 a. Particle composition distribution for Mode 4, 25% load, 1200 rpm

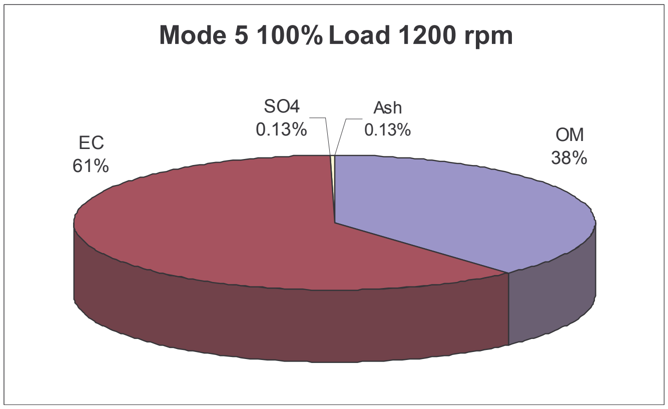

Figure 3-22b. Particle composition distribution for Mode 5, 100 % load, 1200 rpm

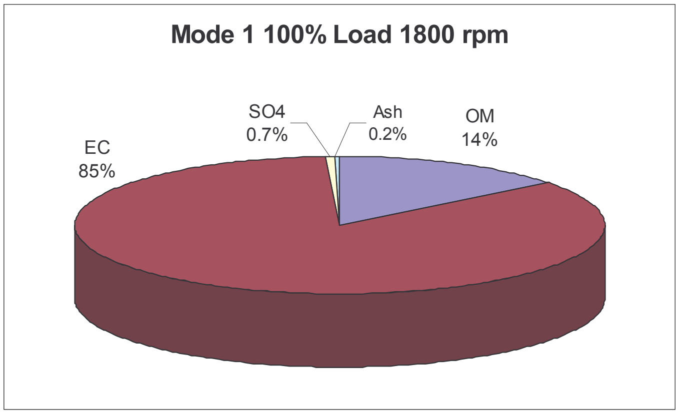

Figure 3-22c. Particle composition distribution for Mode 1, 100 % load, 1800 rpm

What is not shown in Figures 3-22 a-c is that the relative partition of the particulate composition did not change appreciably with changes in lubricating oil consumption. The variation in the distribution of the components of the particulate matter at any particular operating condition was within 5 percent, plus or minus, for the different oil consumption builds of the engine.

These results are shown as bar graphs in Figures 3-23 a-c. In viewing Figures 3-23 a-c, notice the discontinuity in the ordinate axes. For mode 4, 25% load, 1200 rpm, the majority of the particulate is composed of organic matter. Within the measurement variation for a given oil consumption build, there is no significance different between the organic matter with changes in the steady state oil consumption. The elemental carbon composition is approximately an order of magnitude less than the organic material, and like the organic material, the variation in EC between the different oil consumption engine builds is statistically insignificant. The variation of the sulfate composition is at the detection limit of our measurement.

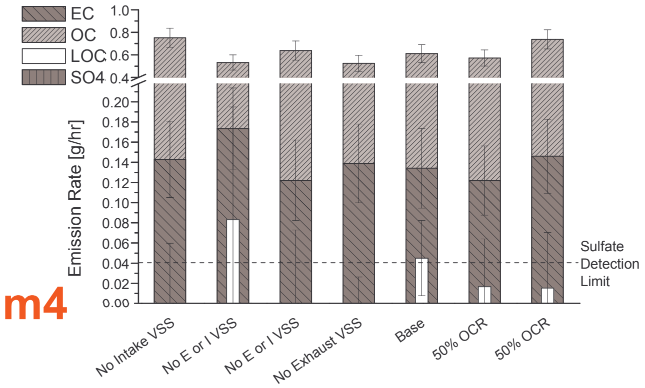

Figure 3-23a. Variation in particle composition at mode 4 operating condition versus different oil consumption engine builds.

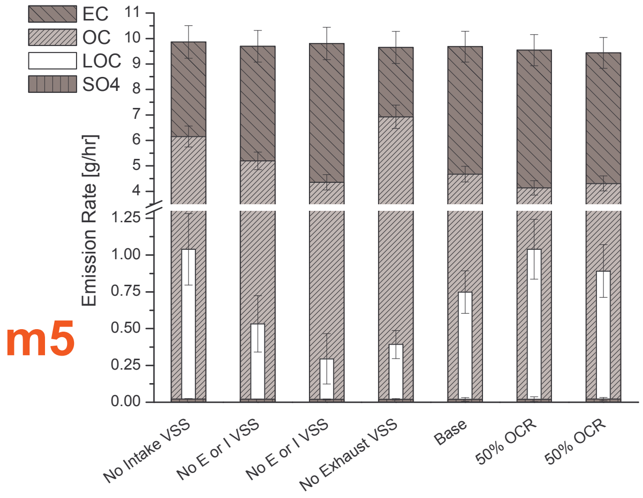

Figure 3-23b. Variation in particle composition at mode 5 operating condition versus different oil consumption engine builds.

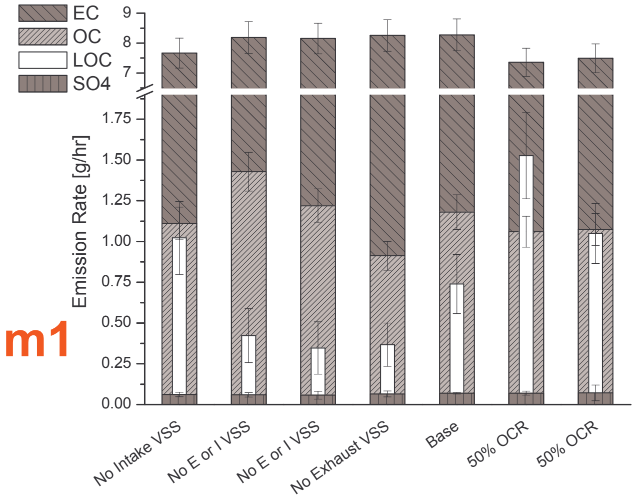

Figure 3-23c. Variation in particle composition at mode 1 operating condition versus different oil consumption engine builds.

For the operating conditions at heavier load, mode 5 and mode 1 - shown in Figures 3-23 b and c, the elemental carbon is the dominant component of the particulate matter. In both cases there appears to be no statistically significant difference in the mass loading of the particulate which is elemental carbon for the different oil consumption engine builds. However, we see that there is a difference in the proportioning of the particulate that is organic matter, or sulfate, with changes in oil consumption engine builds. Furthermore, although the organic matter composition is less than the elemental carbon its magnitude is on the same order as that of the elemental carbon.

The fact that these differences in organic matter are not correlated with differences in oil consumption is shown in Figures 3-24 a and b. In this figure the proportion of the particulate that is organic is plotted versus oil consumption. This is shown for both modes 5 and 1.

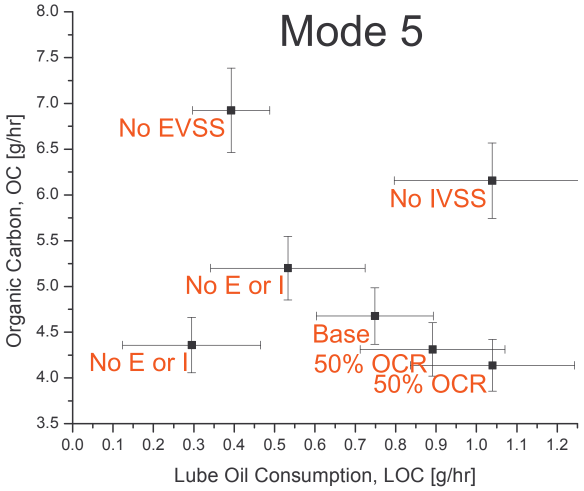

Figure 3-24a Comparison of organic carbon content of the particulate versus oil consumption for Mode 5. The different oil consumption rates were obtained via different oil consumption engine builds.

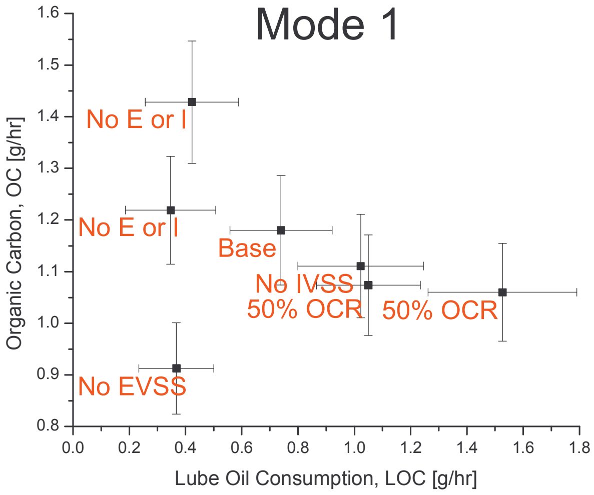

Figure 3-24b Comparison of organic carbon content of the particulate versus oil consumption for Mode 1. The different oil consumption rates were obtained via different oil consumption engine builds.

In looking at the figures, it is immediately apparent that for the conditions tested there is no correlation between the steady state lubricating oil consumption and the organic carbon content of the particulate. This seems surprising as it is commonly stated that the soluble component of the particulate, which would be measured here as organic matter, is readily attributed to the oil consumption. This may indeed be the case. But as shown above, the steady state oil consumption for this engine is very low, and indications are that transient operation is the primary contributor to increased oil consumption. At the low oil consumptions measured in this work, variations in the organic material that could be attributed to the lubricating oil are probably below the resolution of the data.

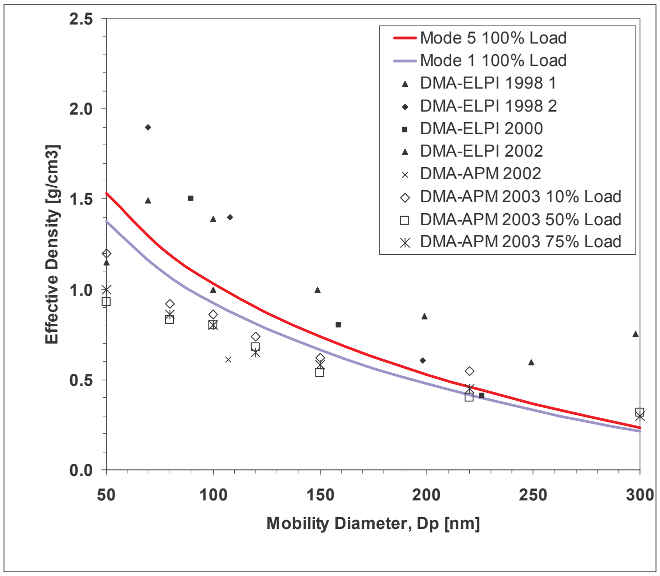

Figure 3-25. Density versus diameter, mode 5, mode 1 and different literature values.

The final aspect of our investigation was the examination of the particulate size distribution and whether it was impacted by changes in the engine operating condition. We also determined a functional fit for the particle density versus diameter for the different operating conditions. Using literature data for particle density versus diameter, we established a generalized empirical form for the density versus diameter. We then fit our data to this form, adjusting the proportionalities so that the total mass of particulate measured in our experiments would be obtained when the density - diameter correlation was integrated over the particle size distribution measured using the SMPS.

These results are shown in Figure 3-25. Data from the literature are shown as points on the plot, while the fit for mode 5 and mode 1 are shown as solid lines. Both of these fits adhere to the general functional form of density versus diameter that is observed in the literature and will yield the same particulate mass measured on the filter when integrated over the particulate size distribution measured in the experiments.

It is interesting to observe that the density versus diameter is different for different operating conditions. In particular, mode 5, which has a larger organic mass concentration than mode 1, 38 percent versus 14 percent, has a higher density at each particle diameter. Figure 3-26 shows the variation in particulate size distribution for modes 1 and 5, for the 50% oil control ring build.

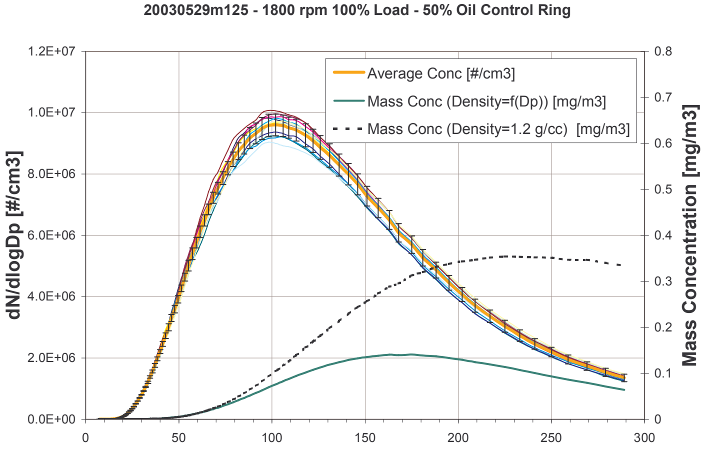

Figure 3-26 a. Particle number and mass distribution versus diameter, mode 1

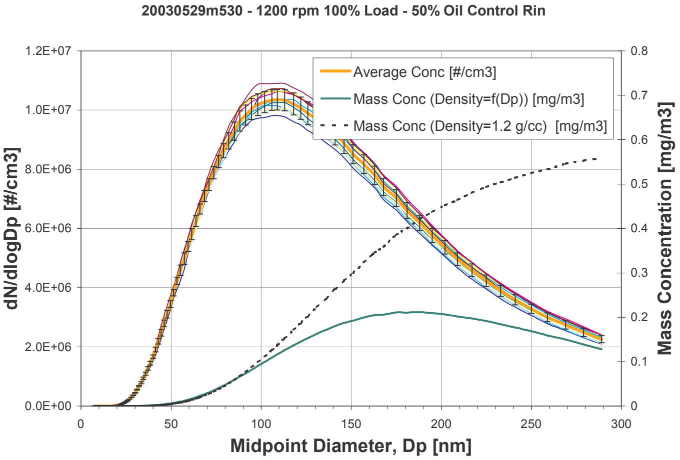

Figure 3-26 b. Particle number and mass distribution versus diameter, mode 5

The data shown in figures 26 a, and b indicate that there is very little variation in the particulate size distribution with changes engine operating condition. This observation also held for the different oil consumption builds at these operating conditions. The two mass concentration curves show the results of using the density versus diameter correlation obtained from Figure 13, which is the lower curve in each figure, and the results of assuming a constant density regardless of particle diameter, which is shown in the upper curve. It is easily seen that the calculation of particulate mass from size distribution would be in error if a constant density were used.

Conclusions: Single Cylinder Research Engine

As a result of this research effort we reached the following conclusions:

1. Subtle details of combustion change significantly as the engine operating conditions and fuels are changed, as witnessed by differences in the chemical composition, size and number concentrations of the particulates.
2. Operating conditions with similar macroscopic output parameters can have very different chemical composition make-up of the exhaust.
3. Significant shift in number concentrations between nuclei mode and accumulation mode with changes in engine load and fuel, indicating a difference in in-cylinder species compositions.
4. There appears to be interrelationships between the particle size and their composition, which can be to be related to the characteristics of the fuel and heat release and in-cylinder temperature histories.
5. Sulfate composition in the particulate matter changed with fuel and engine operating conditions, notably injection timing.
6. Ca can be used as a tracer for lubricating oil consumption
7. Lube oil consumption for steady state operation has insignificant effect on diesel particulate matter
8. It appears that transient operation is responsible for the majority of the lubricating oil consumption.
9. Under steady state operation, lubricating oil makes only a small contribution to the organic matter in the particulate
10. Effective density calculations provide insight into the importance of the engine operating conditions and the relative composition of the particulate matter on the density versus diameter relationship, and ultimately on the mass loading.

11. There was no apparent change in particulate size distribution with the small changes in lubricating oil consumption measured in this research.

3.2 The Complete Engine System - Mtu

The research at MTU focuses on emission characterization of the complete multi-cylinder engine with exhaust gas aftertreatment systems in place. This research was done in conjunction with the Wisconsin State Hygiene Laboratory. The experiments for Phases I and II were conducted with a 1995 Cummins M11-330E and a turbocharged in-line 6-cylinder engine having electronically controlled injection and manually controlled EGR. Similar operating conditions were used with the MTU and ERC engines, at 25, 50, 75 and 100% loads, in conjunction with comparable conventional low and ultra low sulfur fuels. Catalyzed particulate filters (CPFs) were used as the aftertreatment devices. Catalyzed particulate filters have the potential to increase the ability of Army vehicles to accelerate from idle faster and for reoptimizing the combustion system for power density and lower brake specific fuel consumption while at the same time maintaining low particulate and HC emissions. The work at MTU consists of three phases. Phase I consisted of emission characterization experiments with a CPF (catalytic loading of 5 gms/ft^3, designated as CPF III) and conventional low sulfur fuel (CLSF, fuel sulfur content of 375 ppm). Phase II consisted of emission characterization experiments with a different CPF having a heavier catalytic loading (50 gms/ft^3, designated as CPF V) and ultra low sulfur fuel (ULSF, fuel sulfur content of 0.57 ppm). Both Phase I and Phase II experiments were conducted at four load conditions and rated speed (Table 3-5). The experiments were conducted upstream and downstream of the CPF. The experimental set up for these Phases are shown in Figure 2 of the ARO annual report 2002.

Table 3-5: Load conditions at rated speed for Phases I and II

Mode	Load at 1800 rpm rated speed
11	311 Nm (25 %)
10	622 Nm (50 %)
9	933 Nm (75 %)
8	1133 Nm (100 %)

Phase III of the emission characterization experiments was conducted with a new experimental set up. A 2002 Cummins ISM-330 engine with a variable area gas turbine (VGT), electronically controlled fuel system and optimized cooled EGR subsystem was used for the experiments. The effects of a new aftertreatment device, a continuously catalyzed regenerating trap (CCRT®), which consists of an oxidation catalyst (OCC) followed by a CPF, with ultra low sulfur fuel (ULSF sulfur content of 0.4 ppm) were studied. The experimental set up is shown in Figure 3-27. The CCRT® was made by Johnson Matthey and is preceded by a mixer, which will assist in the mixing of injected fuel during active regeneration experiments. The gaseous emissions were taken at three locations, upstream CCRT®, downstream OCC and downstream CCRT®. Three pneumatically controlled high temperature bellows valves were installed in series for fast switching between these locations. These valves were very important components in the system to study the conversion efficiency of the OCC during the active regeneration experiments. Laboratory upgrading was done for better data collection and analysis. A high efficiency particulate air (HEPA) filter was installed upstream of the dilution tunnel to remove ambient particles and improve background particulate concentration for better particle size distribution data. Data storage capacity was increased by installing two 20 GB hard disks in the laboratory computers. LabVIEW software was upgraded to version 6.1 from version 3.1 and a new NI 6052E data acquisition board was installed to improve the data collection. A Mettler Toledo AX105DR balance and a digital hygrometer/thermometer were purchased to comply with the 2007 EPA measurement systems. To measure axial and radial temperature distribution across the CCRT®, new thermocouples were purchased.

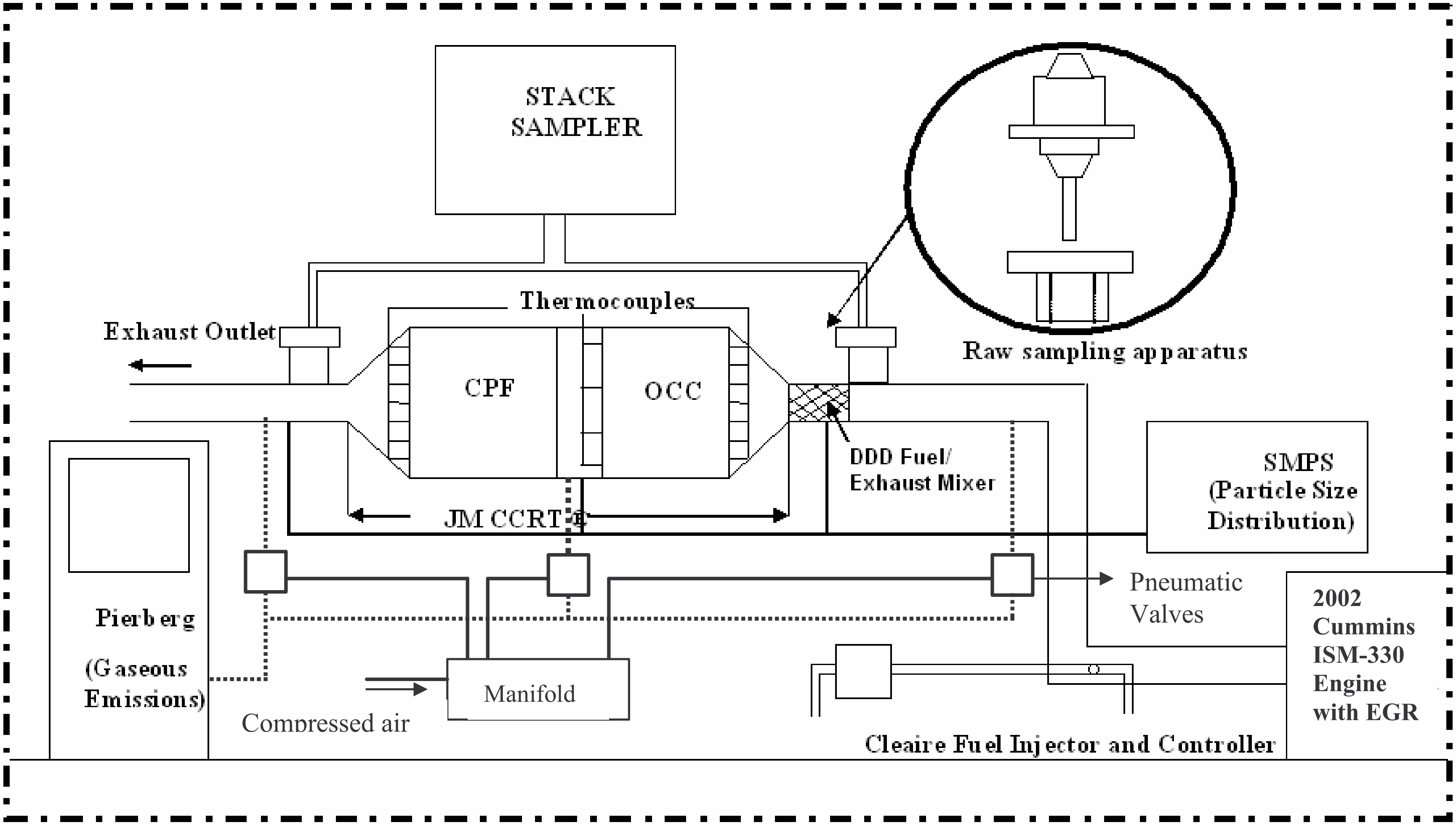

Figure 3-27: Phase III experimental Set-up

The TPM, XOC and particle numbers were measured upstream and downstream of the CCRT® at two loads. The load conditions for Phase III are shown in Table 3-6. Table 3-7 shows the comparison of technology in the two engines

Table 3-6: Load Conditions at Rated Speed for Phase III

Mode	Load at 2100 rpm, rated speed
11	280 Nm (25 %)
9	840 Nm (100 %)

Table 3-7: Comparison Of The Technology Of The Engines Used In This Study

Model	1995,Cummins M11–330 E	2002, Cummins ISM-330
Type	4-stroke cycle	4-stroke cycle
Cylinders	6, in-line	6, in-line
Bore and Stroke	125 mm x 147mm	125 mm x 147mm
Aspiration	Turbocharged & Charge Air Cooled	Turbocharged & Charge Air Cooled
Aftercooling	Separate cooler, cooled with water in lab	Separate cooler, cooled with water in lab
Turbocharger	Constant Area Turbine	Variable Area Turbine
Displacement	10.8 L	10.8 L
Rated Power & Rated Speed	246 kW & 1800 rpm	246 kW & 2100 rpm
Peak Torque	1841Nm at 1231 rpm	1697 Nm at 1200 rpm
Timing	Electronic (Cummins CELECT system)	Electronic
Peak Fuel Injector Pressure	~154 Mpa	Data not available
EGR system	Manually controlled EGR	Electric EGR Valve and programmed EGR

Phase I Results (with CPF III and the CLSF)

Gaseous Emissions: Table 3-8 shows the gaseous emissions concentrations at four loads and Table 3-9 shows the reduction efficiencies of the gaseous emissions in Phase I. Oxides of nitrogen (NOx) emissions are typically increased with load as a result of increased combustion temperatures which facilitate the formation of nitric oxide (NO) and nitrogen dioxide (NO_2). NOx reductions across the CPF were generally statistically significant. Total hydrocarbon (HC) emissions are typically formed as a result of over-leaning and under-mixing. Carbon monoxide (CO) is typically formed as a result of incomplete combustion and is a by product of the combustion of fuel. HC and CO emissions showed statistically significant reductions at each of the operating conditions ranging from 61.5 to 80.9% and 79.2 to 84.6%, respectively. The CO_2 and O_2 changes are mainly attributed to day-to-day experimental variations resulting from upstream and downstream experiments being performed on separate days.

Table 3-8: Phase I Gaseous Emissions at Four Loads

Emissions	Mode 11		Mode 10		Mode 9		Mode 8	
	Us	Ds	Us	Ds	Us	Ds	Us	Ds
HC (ppm)	71	27	40	9	31	7	27	5
NOx (ppm)	246	238	250	239	258	239	271	249

CO (ppm)	133	28	92	14	90	15	100	18
CO2 (% Vol)	5.12	5.14	6.95	7.18	8.36	8.60	9.11	9.31
O2 (% Vol)	13.2	13.2	11.1	10.7	9.14	8.79	8.08	7.75

Table 3-9: Phase I Reduction Efficiencies of Gaseous Emissions[a]

Emissions	Mode 11	Mode 10	Mode 9	Mode 8
HC	61.5	78.5	79.0	809
NOX	3.28	4.31	7.20	7.99
CO	79.2	84.6	83.1	82.3
CO2	-0.3	-3.3	-2.9	-2.2
O2	0.2	4.0	3.8	4.1

a Presented as emission reduction (%) = [(Upstream – Downstream)/Upstream] x 100.

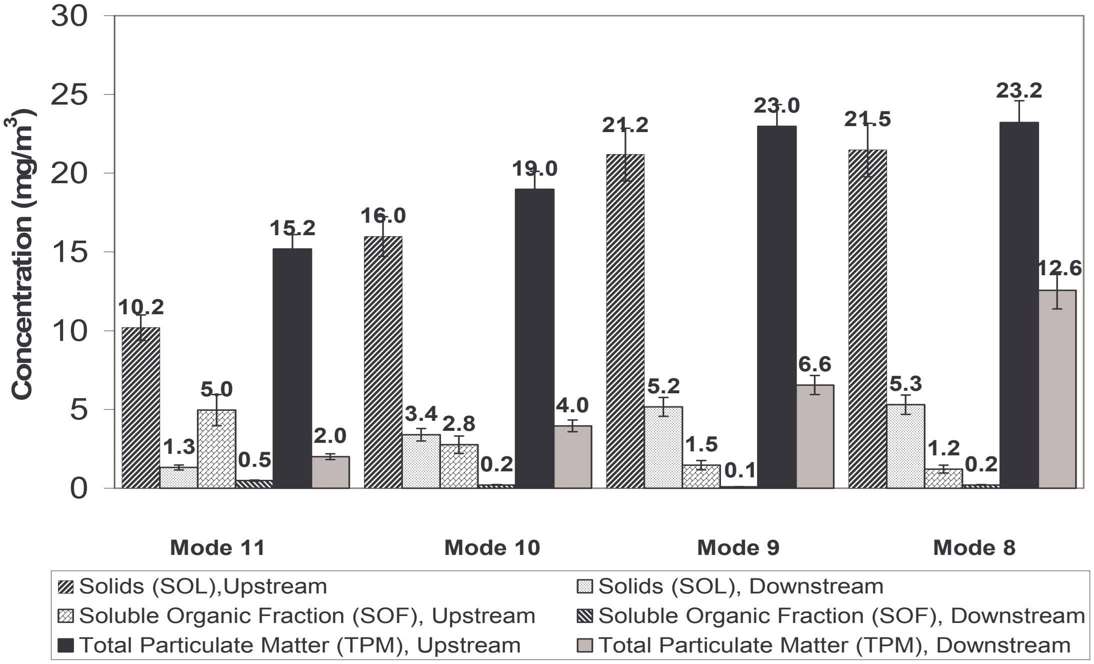

Figure 3-28: Phase I total particulate matter, solid and soluble organic concentrations.

Total Particulate Matter (TPM): As shown in Figure 3-28, TPM levels increased with increasing load. This was primarily due to the increase in solids (SOL) as a result of longer injection durations, which tend to increase diffusion combustion by increasing the fuel injected after the start of ignition. The increase in the TPM downstream at full load is attributed to an increase in the sulfates (shown in Figure 3-29). Sulfates also tended to increase with increasing load, which is attributed to the increase in sulfur dioxide (SO_2) in the combustion chamber due to increased fuel rate. The TPM and SOL showed significant reductions across the CPF at all operating conditions. Sulfates increased at all conditions, with significant increases at Mode 11 and Mode 8. SOL concentrations were significantly reduced across the filter medium between ~87 to 75% for the range of operating conditions. This indicates that the filter medium is effectively removing particles at all of the operating conditions.

Soluble Organic Fraction (SOF) and Vapor Phase Organic Fractions (XOC): In contrast to the TPM and SOL, the SOF and XOC levels decreased with increasing load and were significantly reduced across the CPF (as shown in Figure 3-30). These decreases were related to decreases in HC (shown in Table 3-8). For the SOF there would be less HCs, which on dilution, would adsorb on the surface of the carbonaceous SOL to form SOF. The XOC decreases are related to the decrease in gas phase HCs.

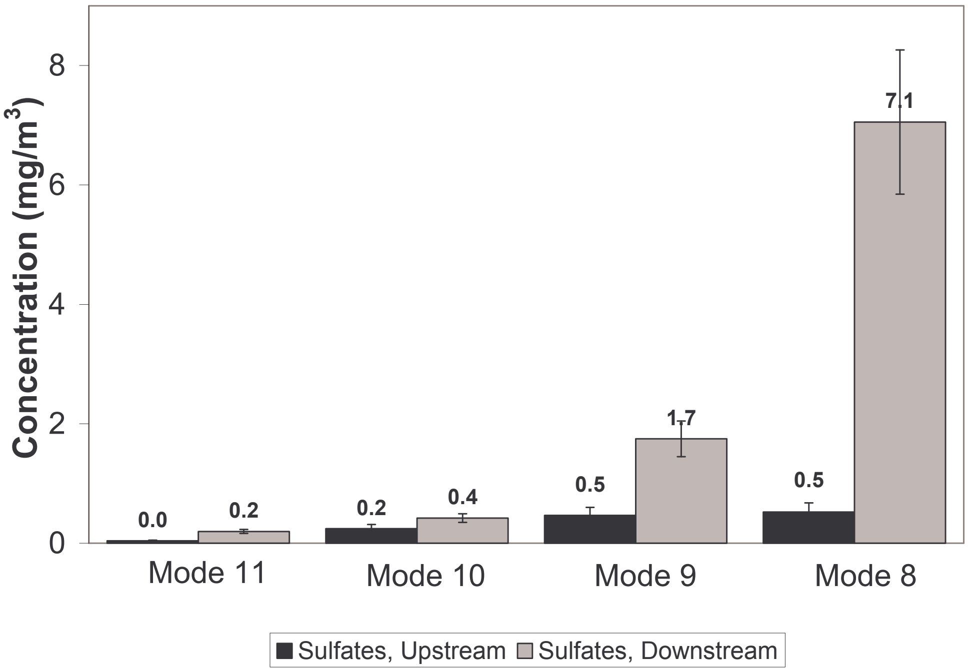

Figure 3-29: Phase I sulfate concentrations.

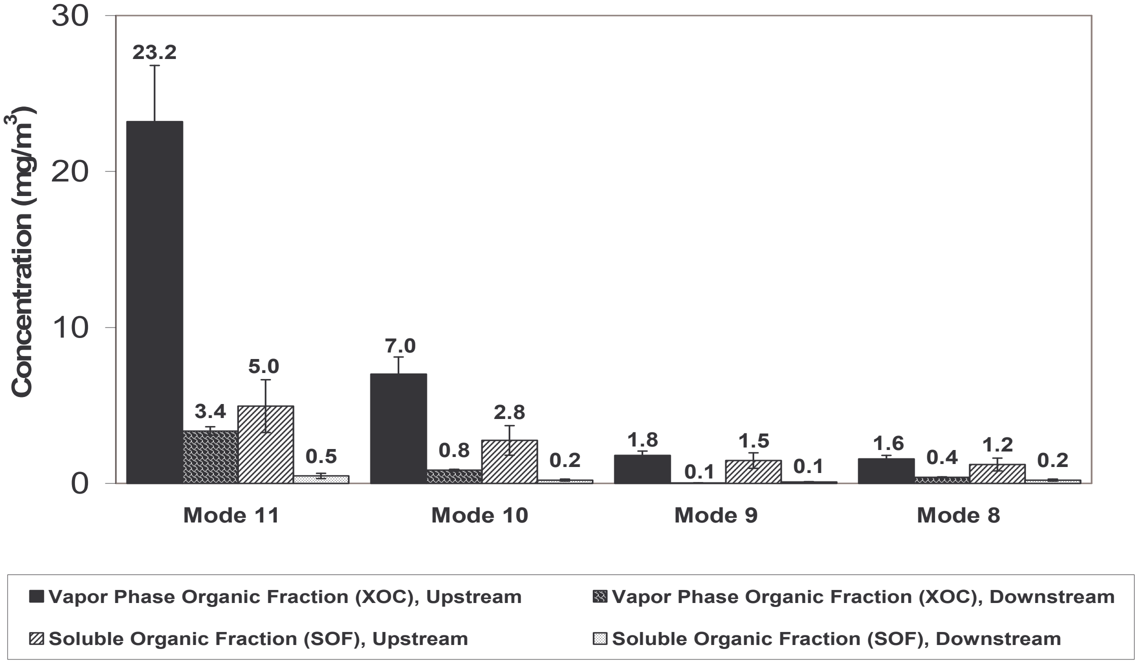

Figure 3-30: Phase I SOF and XOC concentrations

Elemental Carbon (EC), Organic Carbon (OC) and Total Carbon (TC): TC, EC, and OC were all significantly reduced across the CPF for each of the operating conditions (Figure 3-31). TC and EC increased over the entire range of engine conditions from Mode 11 to Mode 8 (lowest to highest load). These results were similar to those found with the TPM and SOL, indicating that the same types of materials are being measured by these different techniques. The OC levels did not display as consistent a trend, with a significant increase found only at the highest load (Mode 8). This is different from the trend with the SOF (Figure 4). The EC is the more abundant portion of the TC and shows high reduction efficiencies across the CPF at each of the loads ranging from 93.8 and 96.7%. The OC portion of the TC was reduced between 84.8 and 97.8% for the range of operating conditions as shown in Table 3-10.

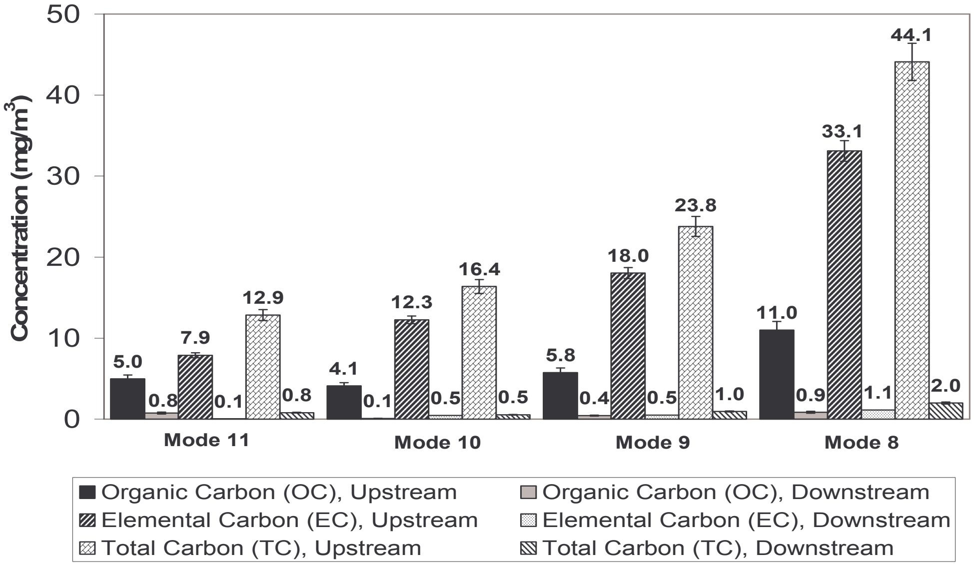

Figure 3-31: Phase I EC, OC and TC concentrations

Table 3-10: Phase I Reduction Efficiencies of TC, EC and OC[a].

Emissions	Mode 11	Mode 10	Mode 9	Mode 8
TC	93.8	96.7	95.5	93.9
EC	99.5	96.3	97.1	94.7
OC	84.8	97.8	92.4	92.2

[a] Presented as emission reduction (%) = [(Upstream – Downstream)/Upstream] x 100.

Particle size emissions: Particle size data were taken under three sampling conditions including; the normal dilution ratio (NDR), which was approximately 12:1, the higher dilution ratio (HDR), which was approximately 45:1, and at the NDR using a thermodenuder. The thermodenuder removes all the HC, sulfates and water allowing only the solid particles to enter the scanning mobility particle sampler (SMPS). The particle size distributions were taken at the NDR and HDR to take into account effect of primary dilution ratio on nanoparticle size formation, which has been shown to have an effect on particles in the nuclei mode. The accumulation mode particles (particles > 50 nm) were nearly unaffected for the two indicated dilution ratios, while the nuclei mode particles (particles < 50 nm) were increased at the NDR as compared to the HDR. This result indicates that dilution can substantially affect the nuclei mode particles. The particle number results, with and without the thermodenuder at the NDR and HDR, upstream and downstream of the CPF for Mode 11 is shown in Figure 3-32. Data are available in the SAE paper No 2003-01-0049 for the other modes.

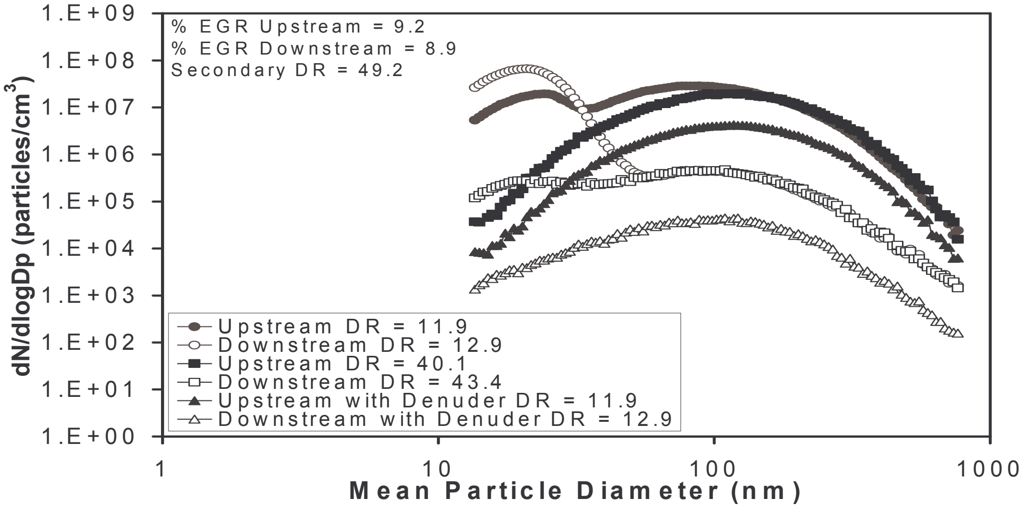

Figure 3-32: Phase I Particle size number distribution at Mode 11

Phase Ii Results (With Cpf V And Ulsf)

Gaseous Emission Results: Table 3-11 shows the gaseous emissions and Table 3-12 shows the reduction efficiencies of the gaseous emissions in Phase II. The catalyst affected the gas phase emissions downstream of the CPF. The HC, NOx and CO emissions were reduced significantly across the CPF. The downstream gas phase emissions showed significant reductions for HC, NOx and CO emissions with increase in load from Mode 11 to Mode 8. The downstream NOx and CO_2 emissions increased with load from Mode 11 to Mode 8. The CO_2 and O_2 changes are mainly due to day-to-day experimental variations resulting from upstream and downstream experiments being performed on separate days.

Table 3-11: Phase II Gaseous Emissions at Four Load Conditions

Emissions	Mode 11		Mode 10		Mode 9		Mode 8	
	Us	Ds	Us	Ds	Us	Ds	Us	Ds
HC (ppm)	63	22	50	8	41	5	37	5
NO_x (ppm)	232	227	239	231	250	236	266	247
NO (ppm)	211	201	218	203	227	205	239	207
NO_2 (ppm)	21	26	22	28	22	32	27	40
CO (ppm)	146	36	95	16	94	15	98	17
CO_2 (% Vol)	5.10	5.13	6.64	6.97	8.19	8.53	8.90	9.20
O_2 (% Vol)	13.5	13.4	10.9	10.4	9.3	8.74	8.10	7.70

Table 3-12: Phase II Reduction Efficiencies of Gaseous Emissions at Four Load Conditions[a]

Emissions	Mode 11	Mode 10	Mode 9	Mode 8
HC	66	84	87	88

NO_x	2.0	3.6	5.4	7.1
NO	4.8	6.8	9.9	13
NO_2	-26	-29	-40	-48
CO	75	83	84	83
CO_2	-0.5	-5.0	-4.2	-3.4
O_2	0.9	4.7	5.6	4.9

[a] Presented as emission reduction (%) = [(Upstream – Downstream)/Upstream] x 100

The HC emissions are oxidized by the catalyst in the CPF to form H_2O and CO_2 and the CO is oxidized to form CO_2. The equations below describe these reactions:

$$CH_2 + 3/2\ O_2 \longrightarrow H_2O + CO_2$$

$$CO + 1/2\ O_2 \longrightarrow CO_2$$

The NOx showed slight reductions across the CPF at all the four operating conditions. The NO also showed a slight decrease across the trap at the four operating conditions. The NO_2 however showed a significant increase across the trap at all four operating conditions. This is attributed to the oxidation of the NO across the trap to form NO_2. The increase in the NO_2 with increase in load is due to the oxidation of NO to NO_2 being facilitated by higher temperatures. The NO_2 formed helps in the oxidization of the carbonaceous particulate matter in the CPF. Some of the incoming NO_2 is consumed in the oxidation reaction with the particulate matter and additional NO_2 is produced from the oxidation of NO across the catalyst. The increase in the NO_2 across the CPF is higher than its usage for the oxidation of the particulate matter across the CPF leading to a net increase in NO_2 across the CPF.

Total Particulate Matter (TPM) and Vapor Phase Compounds (XOC): Figure 3-33 shows the comparison of the TPM, SOL, SOF and sulfates at the four operating conditions. The SOL concentrations increased with increase in the load from Mode 11 to Mode 8. This increase in the SOL is due to the decrease in the A/F ratio with increasing loads. The SOF concentrations decreased with increase in load. This is due to the decrease of the gaseous HC emissions (shown in Table 3-11) with increase in load, thereby leading to lower HC adsorbed onto the solid particles. The XOC and SOF emissions are shown in Figure 3-34. The XOC emissions also decreased with increase in load. This is attributed to the decrease in the gas phase HC emissions with increase in load (shown in Table 3-11).

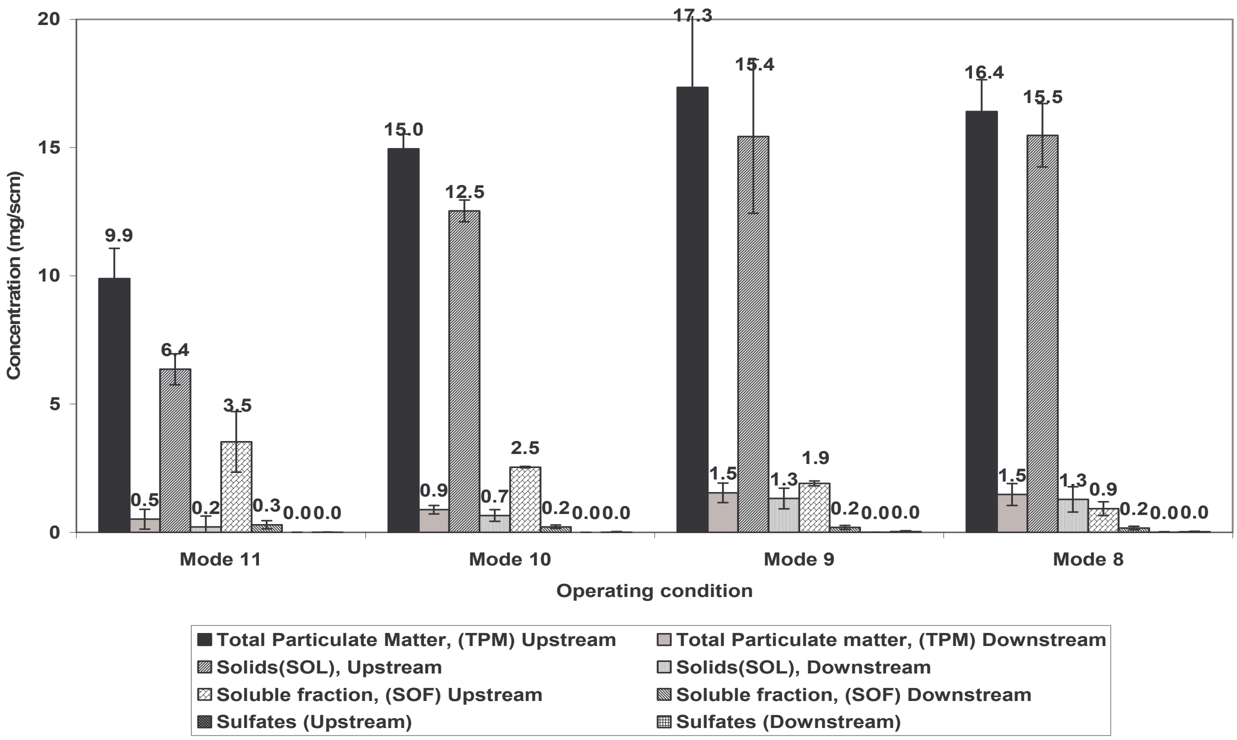

Figure 3-33: Phase II TPM, SOL, SOF and Sulfate emissions upstream and downstream of the CPF at the four load conditions

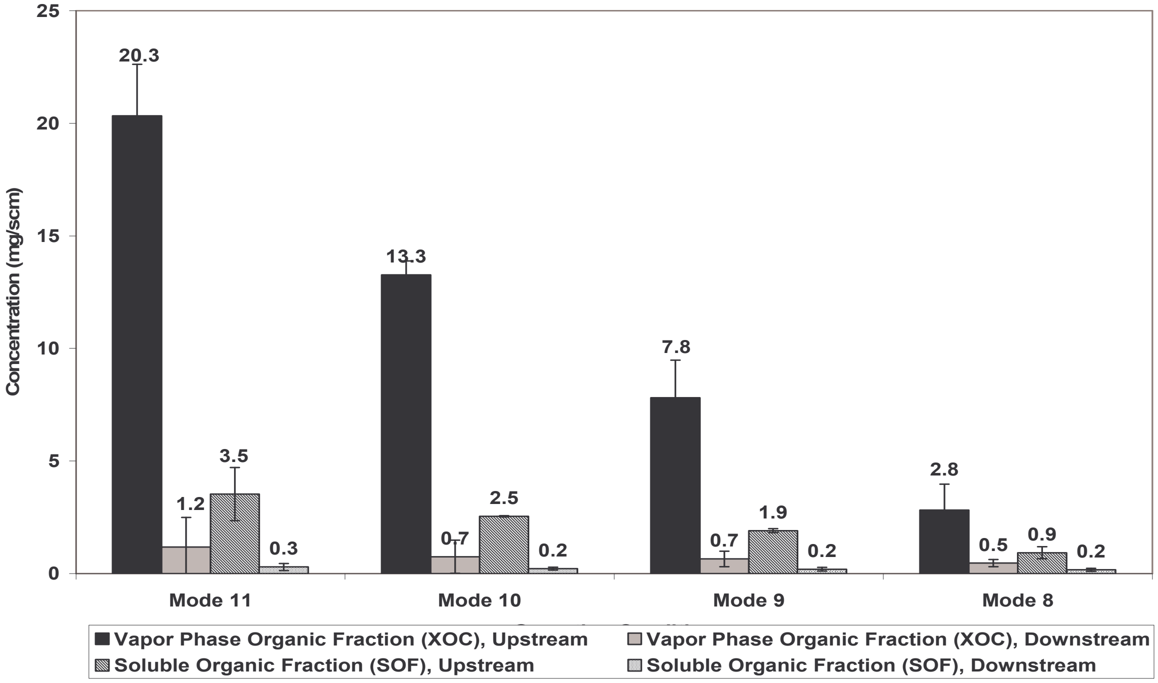

Figure 3-34: Phase II XOC and SOF at the four operating conditions

The sulfate emission concentrations are shown in Figure 3-35. The sulfate concentrations both upstream and downstream of the CPF were extremely low. This is due to the low (0.57 ppm) sulfur concentration in the fuel. The sulfate emission concentrations tended to increase both upstream and downstream of the CPF, as a function of load except for Mode 10 upstream and Mode 8 downstream. The reduction of sulfates with load for Mode 10 upstream and Mode 8 downstream can be attributed to the difficulty in measuring the very low levels of sulfates. The sulfates in the TPM are directly related to the sulfur content of the fuel. The sulfur in the fuel reacts with the O2 in the combustion chamber to form SO_2. The SO_2 is oxidized to SO_3, which combines with water to form sulfuric acid. Increasing the engine loads leads to increased fuel flow rates, higher SO_2 levels and higher temperatures, which in turn assists SO_3 formation. On dilution, the SO_3 combines with water molecules to form H_2SO_4. There is an increase in the sulfate concentrations downstream of the CPF due to catalytic conversion of SO_2 to SO_3 leading to the formation of H_2SO_4.

TPM, SOL, SOF, sulfates and XOC were all significantly affected by the CPF. The reduction efficiencies of the TPM, SOL, SOF and XOC are shown in Figure 3-36. The TPM showed reduction efficiencies of 95, 94, 91, and 91 % at Modes 11, 10, 9 and 8 respectively. The SOL also showed high reduction efficiencies of 97, 95, 91, and 92 % at Modes 11, 10, 9 and 8, respectively.

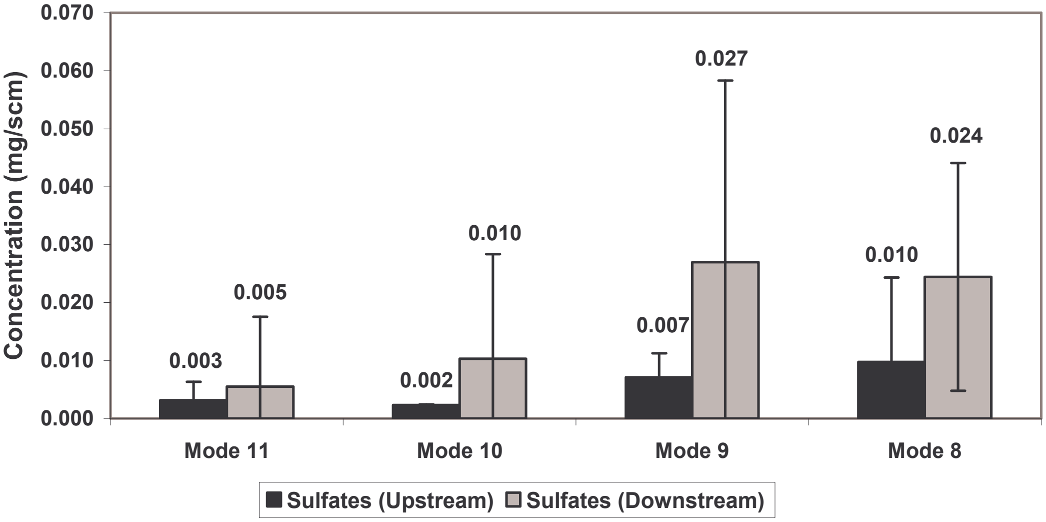

Figure 3-35: Phase II sulfate emissions at four operating conditions

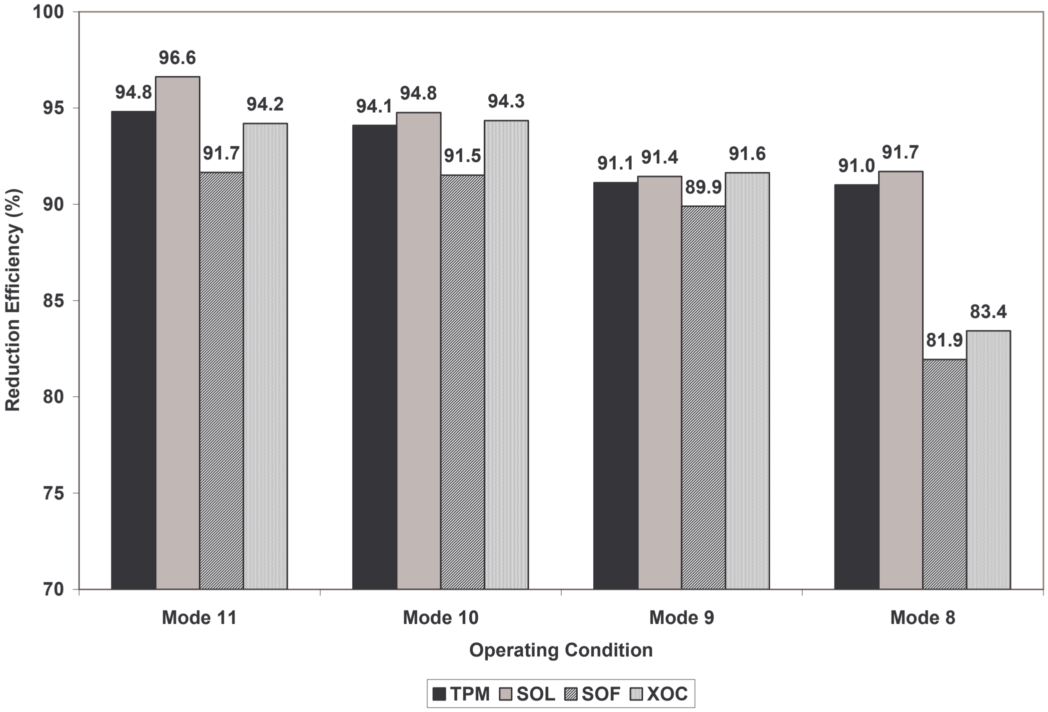

Figure 3-36: Phase II reduction efficiencies across the CPF for TPM, SOL, SOF, and XOC at the four operating conditions

Elemental Carbon, Organic Carbon and Total Carbon: Figure 3-37 shows the TC, EC and the OC emission concentrations. The TC and the EC emissions increased with load from Mode 11 to Mode 8. The TC increased with the same trend as the TPM and the EC increased with the same trend as the SOL. The OC emissions however showed a different trend as compared to the SOF, which decreased with increase in load.

The reduction efficiencies of the TC, EC and the OC are shown in Figure 3-38. The reduction efficiencies for the TC were 89, 95, 92 and 88 %, at Mode 11, 10, 9 and 8, respectively. The reduction efficiencies of the EC are 97, 97, 90 and 87 % at Mode 11, 10, 9 and 8, respectively. The reduction efficiencies of the OC are 85, 91, 97 and 90 % at Mode 11, 10, 9 and 8, respectively. These reductions were significant for the TC, EC and OC at all the four conditions. The reduction of the EC fraction depends on the filtration efficiency of the CPF whereas the reduction of the OC fraction depends on the catalyst.

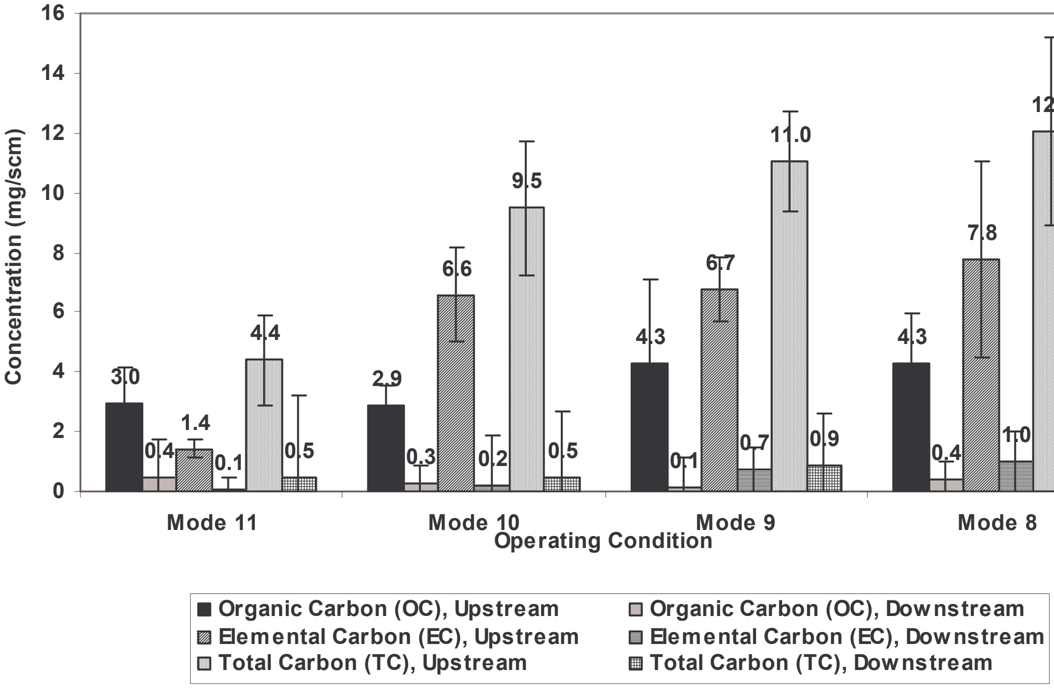

Figure 3-37: Phase II TC, EC and OC emissions concentrations upstream and downstream of the CPF at the four operating conditions.

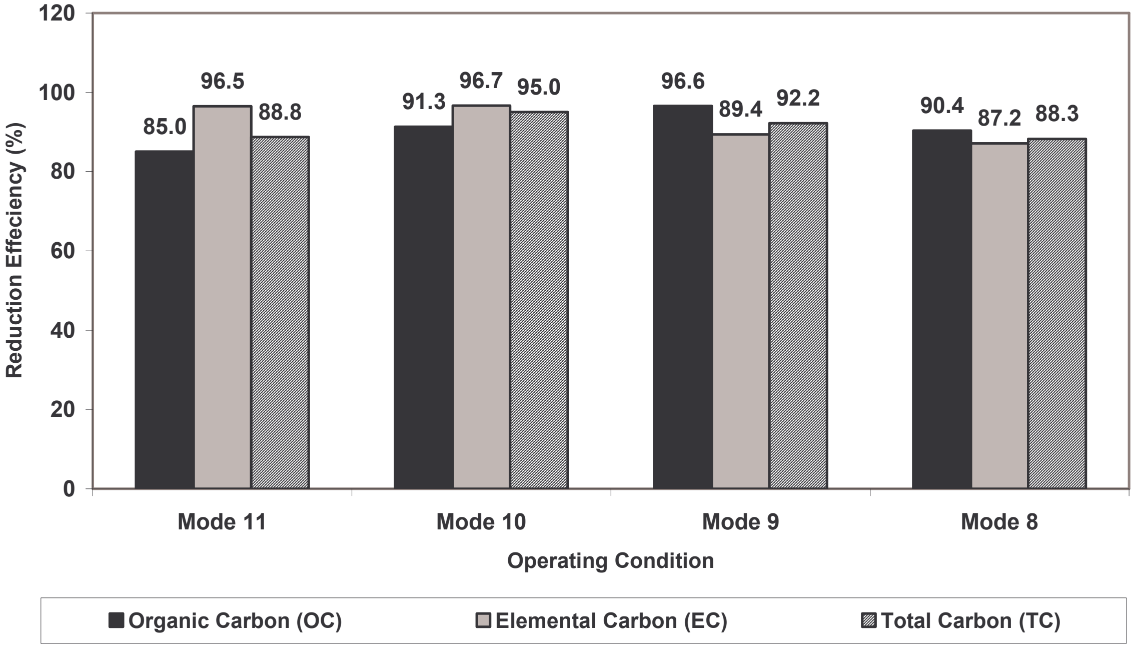

Figure 3-38: Phase II reduction efficiencies of the TC, EC and the OC at the four operating conditions

Particle Size Distributions: The particle size data were taken in the tunnel at the NDR between 10:1 and 15:1 and at an HDR between 40:1 to 55:1. The particle sizes were also measured at the NDR using a thermodenuder. The particle size distributions at Mode 8 are shown in the Figure 3-39.

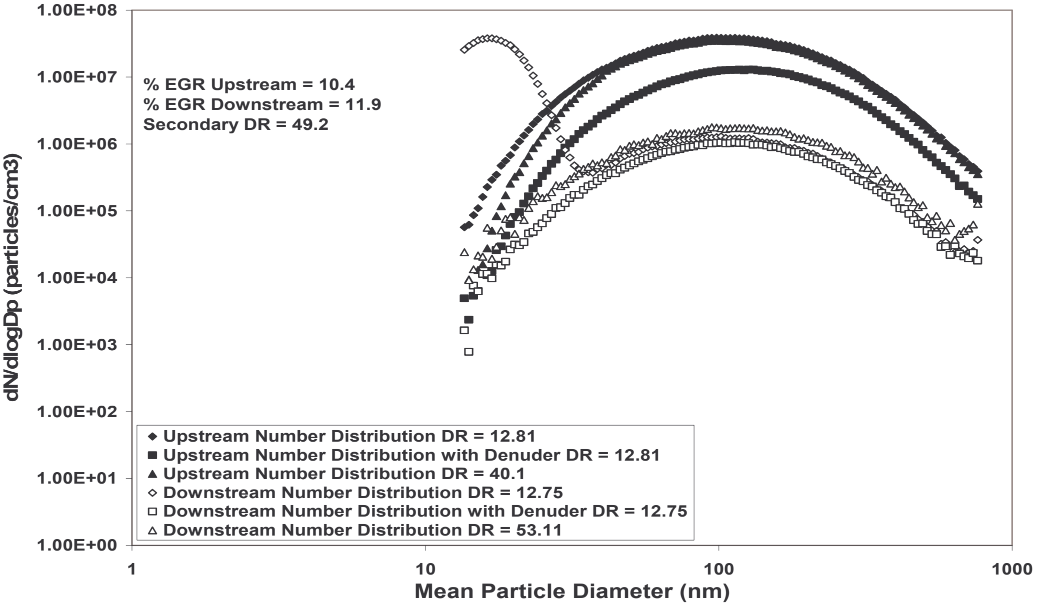

Figure 3-39: Phase II particle size distribution at Mode 8

The particle size distribution was measured across a range of 13.6 nm to 763.5 nm. This range was chosen so as to collect data ranging from the nuclei mode to the maximum diameter possible in the accumulation mode. The effect of the NDR and HDR on the particle size distribution can be seen with more nuclei mode particles at NDR. The lower nuclei mode particles at HDR as compared to that at NDR can be attributed to more nucleation at NDR. There is not much of a difference in the accumulation mode particles between the NDR and the HDR. There is also a substantial reduction in the accumulation mode particles across the CPF at NDR. The removal of the carbonaceous particles by the CPF is the reason for the reduction in the accumulation mode particles. The carbonaceous particles allow the HC and sulfates to adsorb on them, and since the CPF removes the carbonaceous particles, the HC and the sulfates form nuclei mode particles. At higher loads there is an increase in the nuclei mode particles. This is due to the formation of sulfates downstream of the CPF. Other particle size data, PAH and mutagenicity test results for phase I and phase II will be available in the SAE papers titled "A Study of the Effects of a Catalyzed Particulate Filter with a High Loading of the Catalyst and Ultra Low Sulfur Fuel on Heavy Duty Diesel Engine Emissions" and "A Study of the Effects of Two Catalyzed Particulate Filters on Exhaust Emissions from a Heavy Duty Diesel Engine: Filtration and Particulate Matter Oxidation Characteristics Studied Experimentally and Using a 1-D 2-Layer Model".

Table 3-13 shows the reduction efficiencies of various emissions across the CPFs for Phase I and Phase II. It was observed that the catalyst loading, CPF formulation method and fuel composition were the most important variables in the CPF performance. CPF V / ULSF generally has higher reduction efficiencies as compared CPF III / CLSF. The higher catalyst loading in CPF V is responsible for this. CPF V also has lower sulfur conversion which is due to the difference in the application of catalyst on the CPF substrate. However the TC/EC/OC reduction efficiencies are generally equal or higher for CPF III except for TC at mode 11.

Phase III Results (With Ccrt® And Ulsf)

Gaseous Emissions: Table 3-14 shows the gaseous emissions at two loads and three locations and Table 3-15 shows the reduction efficiencies of the CCRT®, the OCC and the CPF. Both HC and CO have large reductions across the CCRT®. The OCC had a major effect on CO, with 100% reductions at both modes. HC has large reductions of 77.1% and 82.8% across the OCC for mode 11 and mode 9, respectively. NO has major reductions across the OCC for both mode 11 (52.4%) and mode 9 (24.2%), due to oxidation of NO to NO_2. Oxidation of NO to NO2 caused a large increase at mode 11 (211%) and mode 9 (246%) across the OCC. The CPF has minor effects on all the gaseous emissions. Overall across the CCRT®, there are major reductions at both mode 11 and mode 9 in the concentrations of HC (89.3% and 91.4%), CO (100% and 100%) and NO (56.2% and 26.8%) and a large increase in NO2 levels (235% and 255%). The change in NOx, CO2 and O2 concentrations were very low; the differences are mainly attributed to experimental variation during sampling at different times.

Table 3-13: Comparison of Phase I and Phase II Reduction Efficiencies[a]

Emission	Mode 11		Mode 10		Mode 9		Mode 8	
	CPF V / ULSF	CPF III / CLSF	CPF V / ULSF	CPF III / CLSF	CPF V / ULSF	CPF III / CLSF	CPF V / ULSF	CPF III / CLSF
TPM	95	87	94	79	91	71	91	46
SOL	97	87	95	79	91	75	92	75
SOF	92	90	92	92	90	96	82	83
Sulfates	-75	-381	-349	-73	-280	-276	-150	-1249
XOC	94	86	94	87	92	85	83	75
TC	89	85	95	98	92	92	88	92
EC	97	100	97	96	89	97	87	95
OC	85	94	91	97	97	96	90	94
HC	66	62	84	78	87	79	88	81
NOx	2.0	3.5	3.6	4.3	5.4	7.2	7.1	8.0
CO	75	79	83	85	84	83	83	82

a Presented as emission reduction (%) = [(Upstream – Downstream)/Upstream] x 100

Table 3-14: Phase III Gaseous Emissions at Two Loads

	Mode 11			Mode 9		
	OCC Us	OCC Ds	CPF Ds	OCC Us	OCC Ds	CPF Ds
HC (ppm)	81	18	9	65	11	6
CO (ppm)	177	0	0	122	0	0
NO2 (ppm)	201	199	202	339	334	333
NO (ppm)	161	77	71	310	235	227
NO2 (ppm)	39	122	131	29	100	103
CO2 (%)	4.81	4.83	4.84	7.58	7.62	7.57
O2 (%)	13.6	13.6	13.5	10.2	10.1	10.1

Table 3-15: Phase III Reduction Efficiency of Gaseous Emissions

	Mode 11			Mode 9		
	OCC	CPF	CCRT	OCC	CPF	CCRT
HC	77.1	53.5	89.3	82.8	50.3	91.4
NOX	0.83	-1.49	-0.65	1.36	0.42	1.77
NO	52.4	8.1	56.2	24.2	3.4	26.8
NO2	-211	-7.5	-235	-246	-2.7	-255
CO	100	0	100	100	0	100
CO2	-0.46	-0.15	-0.60	-0.49	0.60	0.11
O2	0.43	0.36	0.79	0.34	0.09	0.43

a Presented as emission reduction (%) = [(Upstream – Downstream)/Upstream] x 100

Total Particulate Matter (TPM) and Vapor Phase Organic Fraction (XOC): The upstream CCRT® TPM levels are lower at mode 9 (6.48 mg/m3) than at mode 11 (13.2 mg/m3) (Figure 3-40). Higher EGR at mode 11 (16.2%) than at mode 9 (9.4%) may be responsible for this as the engine was programmed for higher EGR to reduce the NOx emissions at mode 11. A higher back pressure at mode 11, coupled with higher EGR levels could have affected the engine performance resulting in higher TPM levels. The downstream TPM levels are higher at mode 11 (0.75 mg/m3) compared to mode 9 (0.61 mg/m3). A higher exhaust temperature at mode 9 (484 - 498oC) resulted in complete regeneration of the particulate matter (PM), resulting in low PM collected in the CCRT ® in both upstream and downstream experiments as shown in Table 3-16. The high temperatures in the CPF oxidized nearly all of the incoming PM.

Table 3-16: Mass in Grams in CPF at End of the Run

Mode	Run Time (hrs)	Mass (g)
11 Upstream	7.65	81
11 Downstream	6.75	76
9 Upstream	3.94*	0
9 Downstream	5.62	8

* Test run stopped early due to mechanical problems.

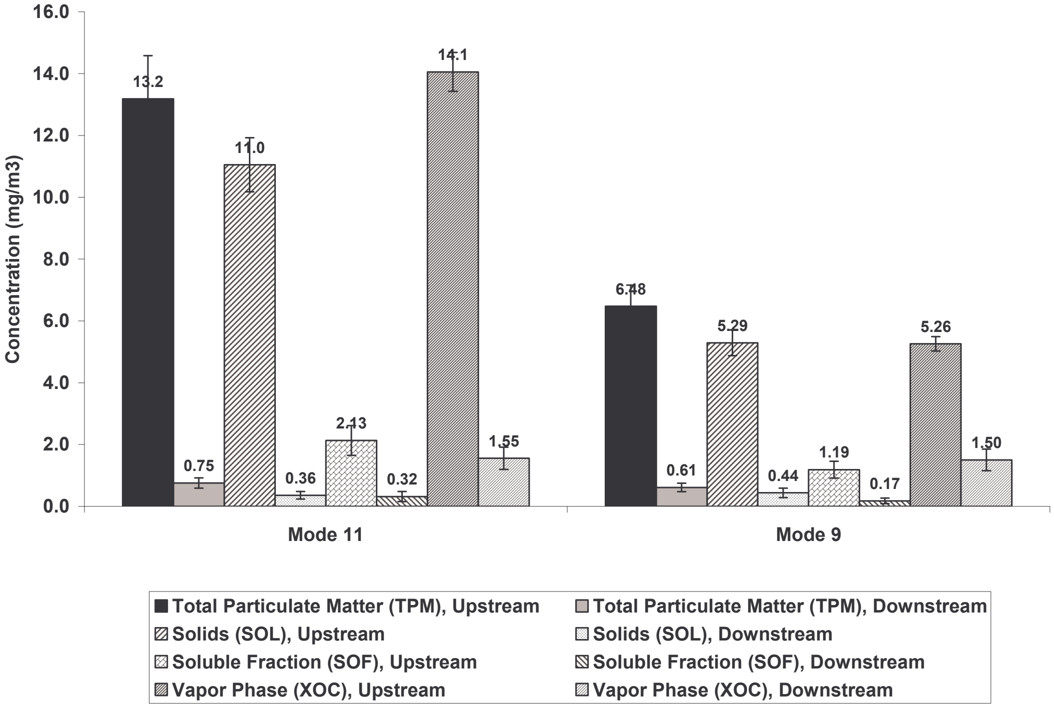

Figure 3-40: Phase III Particulate and Vapor Phase Emissions

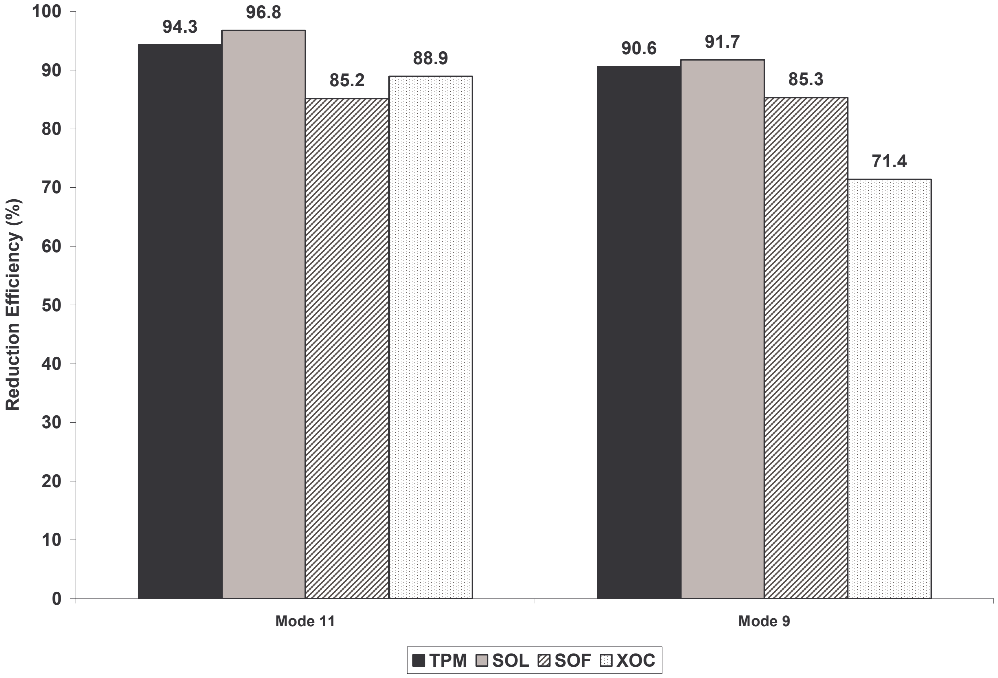

Figure 3-41: Phase III Reduction Efficiencies of TPM and XOC across the CCRT®

Figure 3-40 shows the TPM, SOL, SOF and XOC levels and Figure 3-41 shows the reduction efficiencies. Mode 11 has a higher reduction efficiency for TPM (94.3%) and SOL (96.8%) as compared to mode 9 (90.6 and 91.7 % respectively) so that the downstream concentrations for mode 11 and 9 are close.

The SOF at the upstream CCRT® remained a fairly constant proportion of the TPM at both modes (16.2% and 18.1% at modes 11 and 9) but is a greater fraction of the TPM in the downstream CCRT® concentrations at mode 11 (53.8%) than at mode 9 (28.5%). The upstream SOF values were 2.13 mg/m3 for mode 11 and 1.19 mg/m3 for mode 9. The higher SOF concentration at mode 11 is due to higher HC concentration at mode 11 (shown in Table 3-14). The SOF reduction efficiency across the CCRT® is equal at both modes with very low downstream concentrations at both mode 11 (0.32 mg/m3) and mode 9 (0.17 mg/m3). The XOC has higher upstream emissions (14.1 mg/m3) at the low temperature conditions of mode 11 and lower emissions (5.26 mg/m3) at the high temperature conditions of mode 9. This is again due to lower HC concentration at mode 9 compared to mode 11. However, the XOC reduction efficiency is higher at mode 11 (88.9%) than at mode 9 (71.4%), resulting in similar downstream concentrations for both modes.

The sulfate concentrations are less than 4 µg/m3 for this engine, even across the CCRT®. The CCRT® may have been designed to suppress the sulfate formation, resulting in low sulfur conversion rates. The particle size distribution data are still being analyzed.

Technology Transfer:

We have presented an SAE papers at the SAE Congress, the spring and fall sectional meetings, JSAE, and at the American Association of Aerosol Researchers (AAAR) in Charlotte NC. See publication and theses list.

References:

9. John H. Johnson, Susan T. Bagley, et. al., ”A Review of Diesel Particulate Control Technology and Emissions Effects 1992 Horning Memorial Award Lecture”, SAE paper No.940233
10. Kent Froelund, Ed C. Owens, et al., “Impact of Lubricant Oil on Regulated Emissions of a Light-Duty Mercedes-Benz OM611 CIDI-Engine”, SAE paper No.2001-01-1901
11. Brent K. Bailey, Susumu Ariga, “On-Line Diesel Engine Oil Consumption Measurement”, SAE paper No.902113

12. Hildemann, L.M., Cass, G.R., Markowski, G.R., "A Dilution Stack Sampler for Collection of Organic Aerosol Emissions: Design, Characterization and Field Tests", Aerosol Science and Technology Vol. 10, pp. 193-204, 1989.
13. Schauer, J.J., Kleeman, M.J., Cass, G.R., and Simoneit, B.R.T., "Measurement of Emissions from Air Pollution Sources. 1. C1 through C29 Organic Compounds from Meat Charbroiling", Environmental Science and Technology, Vol. 33, No 10, pp. 1566-1577, 1999.
14. Schauer, J.J., Kleeman, M.J., Cass, G.R., and Simoneit, B.R.T., "Measurement of Emissions from Air Pollution Sources. 2. C1 through C30 Organic Compounds from Medium Duty Diesel Trucks", Environmental Science and Technology, Vol. 33, No 10, pp. 1578-1587, 1999.
15. Kleeman, M.J., Schauer, J.J., and Cass, G.R., "Size and Composition of Fine Particulate Matter Emitted from Motor Vehicles", Environmental Science and Technology, Vol. 34, No 7, pp. 1132-1142, 2000.
16. Private Communication with Schauer, J.J., 1999
17. Andrews, G. E., Elamir, I. E., Abdelhalim, S., Ahamed, F. M., and Shen, Y., "The Measurement of Lubricating Oil Combustion Efficiency Using Diesel Particulate Analysis", SAE Technical Paper 980523, 1998.
18. Okada, S., Kweon, C., Stetter, J. C., Foster, D. E., Shafer, M. M., Christensen, C. G., Schauer, J. J., Schmidt, A. M., Silverberg, A. M., and Gross, D. S., "Measurement of Trace Metal Composition in Diesel Engine Particulate and its Potential for Determining Oil Consumption", SAE Technical Paper 2003-01-0076, 2003.

(6) List of papers submitted or published under ARO sponsorship during this reporting period:

a. Papers published in peer-reviewed journals

Chalgren, R.D., Parker G.G., Johnson J.H., Arici, O., 2002, "A Controlled EGR Cooling System for HD Diesel Applications Using the Vehicle Engine Cooling System Simulation," SAE Paper 2002-01-0076.

He, Y, and Rutland, C.J., 2004, "Application of Artificial Neural Networks in Engine Modeling," to appear: *J. of Engine Research*.

He, Y, and Rutland, C.J., 2004, "Application of Artificial Neural Networks in Engine Modeling," *J. of Engine Research*, , Vol. 5, No. 4, pp 281-296.

Indranil, B. and Rutland, C.J., 2003, "Improvement of neural network accuracy for engine simulations," SAE Paper 2003-01-3227, Powertrain and Fluid Systems Conference, Oct.27-30, Pittsburgh, Pennsylvania.

Indranil, B. and Rutland, C.J., 2003, "Optimization of diesel engine operating parameters using neural networks," SAE Paper 2003-01-3228, Powertrain and Fluid Systems Conference, Oct.27-30, Pittsburgh, Pennsylvania. *SAE 2003 Transactions Journal of Fuels and Lubricants*, pp. 2521-2529.

Johnson, J. H., Bagley, S. T., Shende, A. S., Thalagavara, A. M., "A Study of the Effects of a Catalyzed Particulate Filter with a High Loading of the Catalyst and Ultra Low Sulfur Fuel on Heavy Duty Diesel Engine Emissions", to be presented at the SAE Powertrain & Fluid Systems Conference & Exhibition, Oct 2004.

Kweon, C-B., Okada, S , Stetter, J., Bae, M-S., Christensen, C. G., Shafer, M. M., Schauer, J. J., and Foster, D.E., "Effect of Fuel Composition on Combustion and Detailed Chemical/Physical Characteristics of Diesel Exhaust," JSAE 20030098, SAE 2003-01-1899

Kweon, C-B., Okada, S , Stetter, J., Bae, M-S., Christensen, C. G., Shafer, M. M., Schauer, J. J., and Foster, D.E., "Effect of Injection Timing on Detailed Chemical Composition and Particulate Size Distributions of Diesel Exhaust," JSAE 20030099, SAE 2003-01-1794

Kweon, C-B., Okada, S , Stetter, J., Foster, D.E., Shafer, M. M., Christensen, C. G., Schauer, J. J., and Gross, D. S. "The Effect of Operating Conditions on the Chemical Composition of Diesel Particulate Matter," AAAR Annual Conference, 2002.

Kweon, C-B., Okada, S. , Stetter, J., Foster, D.E., Shafer, M. M., Christensen, C. G., Schauer, J. J., and Gross, D. S., Overview of Detailed Chemical Speciation and Particle Sizing for Diesel Exhaust, Both Real Time and Filter Based Measurements, DEER 2002 .

Kweon, C-B. , Foster, D.E., Schauer, J. J., and Okada, "Detailed Chemical Composition and Particle Size Assessment of Diesel Engine Exhaust," SAE 2002-01-2670

Kweon, C-B. , Foster, D.E., Okada, S., Schauer, J. J., and Bae, M-S, "Effect of Engine Operating Conditions on Particle-Phase Organic Compounds in Engine Exhaust of a Heavy-Duty Direct-Injection (D.I.) Diesel Engine," SAE 2003-01-0342

Okada, S , Kweon, C-B., Stetter, J., Foster, D.E., Shafer, M. M., Christensen, C. G., Schauer, J. J., Schmidt, A. M., Silverberg, A. M., and Gross, D. S., "Measurement of Trace Metal Composition in Diesel Engine Particulate and its Potential for Determining Oil Consumption : ICPMS (Inductively Coupled Plasma Mass Spectrometer) and ATOFMS (Aerosol Time of Flight Mass Spectrometer) Measurements, SAE 2003-01-0076

Shende, A. S., Johnson, J. H., Yang, S. L., Bagley, S. T., and Thalagavara, A. M., “A Study of the Filtration and Particulate Matter Oxidation Characteristics of a Highly Loaded Catalyzed Wall-flow Diesel Particulate Filter: Experimental and 1-D 2-layer Model Results,” to be presented at the SAE Powertrain & Fluid Systems Conference & Exhibition, Oct 2004.

Stetter, J., Forster, N., Ghandhi, J., and Foster, D. E., “The Impact of Oil Consumption Mechanisms on Diesel Exhaust Particle Size Distributions and Detailed Exhaust Chemical Composition,” DEER 2003.

Thalagavara, A. M., Shende, A. S., Triana, A., Johnson, J. H., Yang, S. L., and Bagley, S. T “A Study of the Effects of Two Catalyzed Particulate Filters on Exhaust Emissions from a Heavy Duty Diesel Engine: Filtration and Particulate Matter Oxidation Characteristics Studied Experimentally and Using a 1-D 2-Layer Model,”, to be presented at the SAE Powertrain & Fluid Systems Conference & Exhibition, Oct 2004.

Warner, J. R., Johnson, J. H., Bagley, S. T., and Huynh, C. T. “Effects of a Catalyzed Particulate Filter on Emissions From a Diesel Engine: Chemical Characterization Data and Particulate Emissions Measured with Thermal Optical and Gravimetric Methods,”, SAE 2003-01-0049

Warner, J. R., Johnson, J. H., and Bagley, S. T., “Effects of a Catalyzed Particulate Filter on Emissions from a Diesel Engine: Chemical Characterization Data and Particulate Emissions Measured with Thermal Optical and Gravimetric Methods,” SAE Paper No 2003-01-0049. Presented March 3 - 6, 2003, SAE World Congress

Yi, Y., and Reitz, R.D., "Modeling the Primary Breakup of High-speed Jets," Atomization and Sprays, Vol. 14, No. 1, pp. 53-80, 2004.

Yi, Y., and Reitz, R.D., 2004, “Modeling the Primary Breakup of High-speed Jets,” to appear *Atomization and Sprays*.

Yi, Y., and Reitz, R.D., “Modeling the Primary Breakup of High-speed Jets," Atomization and Sprays, Vol. 14, No. 1, pp. 53-80, 2004.

b. Papers published in non-peer-reviewed journals or in conference proceedings

He, Y, and Rutland, C.J., 2003, “Neural Cylinder Model and Its Applications in Transient Engine Simulations,” SAE Paper 2003-01-3232, Powertrain and Fluid Systems Conference, Oct.27-30, Pittsburgh, Pennsylvania.

Indranil, B. and Rutland, C.J., 2003, “Improvement of neural network accuracy for engine simulations,” SAE Paper 2003-01-3227, Powertrain and Fluid Systems Conference, Oct.27-30, Pittsburgh, Pennsylvania.

Indranil, B. and Rutland, C.J., 2003, “Optimization of diesel engine operating parameters using neural networks,” SAE Paper 2003-01-3228, Powertrain and Fluid Systems Conference, Oct.27-30, Pittsburgh, Pennsylvania.

Yi, Y., and Reitz R. D., “A New Jet Primary Breakup Model and its Application to Diesel Combustion,” Published in Conference Proceedings, Presented at ILASS-2003, Monterey, CA, May 18-21, 2003.

c. Papers presented at meetings, but not published in conference proceedings

d. Manuscripts submitted, but not published

Smitha Nagaraj and Susan T Bagley, "Application of Ames Tester Strains TA102, YG1021, and YG1024 for Detection of New Classes of Mutagens Associated with Diesel Exhaust." To be submitted to Environmental and Molecular Mutagenesis.

e. Technical reports submitted to ARO

Interim report for DAAD19-00-1-0487 for CY 2001

Interim report for DAAD19-00-1-0487 for CY 2002

Interim report for DAAD19-00-1-0487 for CY 2003

(7) Scientific personnel supported by this project and honors/awards/degrees received

a) Personnel supported:

a. Thrust 1:

Prof. Patrick Farrell (PI—UW Madison)
Prof. Michael Corradini (PI—UW Madison)
Millicent Coil (Research Associate-UW Madison)
Mike Feist (Research Associate-UW Madison)
Hyungsuk Kang (Graduate Student-UW-Madison)
Caleb Wei (Graduate Student-UW-Madison)

Prof. Carl Anderson (PI-MTU)
Scott Miers (Graduate Research Assistant-MTU)
Koray Inal (Graduate Research Assistant-MTU)

b. Thrust 2:

Prof. Christopher J. Rutland (PI—UW Madison)
Prof. Rolf Reitz (PI—UW Madison)
Prof. John Moskwa (PI—UW Madison)
James A. Bedrosian (Graduate Research Assistant- UW Madison)
Indranil Brahma (Graduate Research Assistant- UW Madison)
Sergei Chumakov (Graduate Research Assistant)
Yongsheng He (Graduate Research Assistant)
Amol Kulkarni (Graduate Research Assistant- UW Madison)
Zac Nagel (Graduate Research Assistant)
Wei Ning (Graduate Research Assistant- UW Madison)
Eric Pomraning (Post-doc)
Bret RempelEwert (Graduate Research Assistant- UW Madison)
David Wickman (Graduate Research Assistant- UW Madison)
Yong Yi (Graduate Research Assistant- UW Madison)

Prof. John Johnson (PI-MTU)
Prof. Oner Arici (PI-MTU)
Prof.. Gordon Parker (PI-MTU)
Brian J. Luptowski (Graduate Research Assistant-MTU)

Prof. Sean Garrick (PI-UMinn)
Prof. George Karypis (PI-UMinn)
Scott Miller (Graduate Research Assistant-UMinn)
Irene Moulitsas (Graduate Research Assistant-UMinn)

c. Thrust 3:

Prof. Dave Foster (PI—UW Madison)
Prof. Jaal Ghandhi (PI—UW Madison)
Prof. James Schauer (PI-UW Madison, Water Chemistry, CEE, and State Hygiene Lab)
Chol Bum Kweon (Graduate Research Assistant- UW Madison)
Nathan Forester (Graduate Research Assistant- UW Madison)
John Stetter (Graduate Research Assistant- UW Madison--since 6/2002)

Prof. John Johnson (PI-MTU)
Prof. Susan Bagley (PI-MTU)
James Warner (Graduate Research Assistant-MTU)
Smitha Nagaraj (Graduate Research Assistant-MTU)
Abishek M Thalagavara (Graduate Research Assistant-MTU)
Venkata R. Lakkireddy (Graduate Research Assistant-MTU)

b) Degrees granted:

James A. Bedrosian, "Design Robustness System-Development of a Graphical, User-Interactive Software Tool for Visualization of System Design Robustness," M.S. Thesis, Department of Mechanical Engineering, University of Wisconsin-Madison, June 2003.

Chalgren, R.D., The Modeling of Exhaust Gas Recirculation in the Vehicle Engine Cooling system Simulation for Designing a Controlled EGR Cooling System, Masters Thesis, Michigan Technological University, 2000.

Sergei Chumakov, "Large Eddy Simulation Models for Sub-Grid Scalar Transport", MS Degree, University of Wisconsin-Madison, 5/9/2001

Nathan Forster, "The Effects of Lubricating Oil Consumption on the Detailed Characteristics of Diesel Particulate Matter," M.S. Mechanical Engineering, University of Wisconsin – Madison, August 2003

Chol Bum Kweon, "The Effects of Engine Operating Conditions and Fuel Composition on the Detailed Characteristics of Diesel Exhaust," Ph.D. ME, University of Wisconsin - Madison, December 2002.

Kulkarni, Amol, "A Sub-Grid Droplet Source Model for High Speed Sprays using Large Eddy Simulation," MS Thesis, University of Wisconsin-Madison 8/19/2003.

Luptowski, Brian, "Development and Evaluation of an All Electric Active Cooling System in a Heavy Duty Diesel Truck using the Vehicle Engine Cooling System Simulation Enhanced with GT-Power," MS Thesis, Michigan Technialogial University, 5/14/03.

Miller, Scott "Direct numerical simulation of nanoparticle coagulation in a planar jet," PhD Thesis, University of Minnesota, 2002

Smitha Nagaraj, "Refinement of the Salmonella/Microsome Microsuspension Assay to Apply Tester Strains TA102, YG1021 and YG1024 for Mutagenicity Testing of Diesel Emissions", MS Thesis, MTU, 2003

John Stetter, "Sensitivity of the Detailed Characteristics of Diesel Particulate Matter Emissions Under Steady State, Light –Load Engine Operation," M.S. Mechanical Engineering, University of Wisconsin – Madison, January 2004

Abishek M. Thalagavara, "A Study of the Effects of Two Catalyzed Particulate Filters with Different Loadings of the Catalyst on Exhaust Emissions from a Heavy Duty Diesel Engine with EGR", MS Thesis, MTU, 2003

J R Warner, "Effects of a Catalyzed Particulate Filter on Emissions from a Diesel Engine: Chemical Characterization Data and Particulate Emissions Measured with Thermo Optical and Gravimetric Methods", M. S. Thesis, MTU, 2002

Caleb Wei, "CDRS Development for Soot Measurements", MS Thesis, Department of Mechanical Engineering, University of Wisconsin-Madison, June, 2004.

Yi, Y., “Numerical Modeling of Spray Primary Breakup with Application to Diesel Engines” PhD. Thesis, University of Wisconsin-Madison, 9/27/2002

Yongsheng He, “Development of a Diesel Engine Simulation Tool Using Artificial Neural Networks”, Ph. D Thesis, University of Wisconsin-Madison, 7/6/2002.

(8) Report of inventions

none